Contents

| Abstract |
|--|
| 1.1 Some General Issues Related to Black Hole Astrophysics |
| 1.1.1 Formation of Black Holes |
| 1.1.2 Fueling Active Galactic Nuclei |
| 1.1.3 Evolution of Galactic Centers |
| 1.1.4 Black Holes in Galactic Halos? |
| 1.1.5 Some Signatures of Black Holes |
| 1.2 Difference between Motions around a Newtonian Star and a Black Hole 16 |
| 1.3 Basics of Pseudo-Newtonian Geometries |
| 1.4 Remarks About Units and Dimensions |
| 2: Spherical Accretion |
| |
| 2.1 Bondi Accretion on a Newtonian Star |
| 2.1.1 Basic Equations 25 |
| 2.1.2 Phase Space Behaviour of the Bondi Flow |
| 2.2 Bondi Flow on a Black Hole |
| 2.2.1 In Schwarzschild Geometry |
| 2.2.2 In pseudo-Newtonian Geometry 31 |
| 2.3 Bondi Flow with Simple Radiative Transfer |
| 2.4 Bondi Flow with General Radiative Transfer 32 |
| 2.4.1 Single Temperature Solutions |
| 2.4.2 Two Temperature Solutions 35 |
| 2.4.3 General Relativistic Optically Thick Bondi Flow |
| 2.4.4 Inclusion of Pair Production and Preheating |
| 2.5 Shocks in Spherical Flows 47 |
| 2.6 Particle Acceleration at Shock Waves |
| 2.6.1 Basic Physical Processes 48 |
| 2.6.2 Acceleration at Spherical Shocks and AGN Spectra 50 |
| 3: Thin Accretion Disk Models 55 |
| 3.1 Standard Disk Model and Its Spectra |
| 3.1.1 Model Equations |
| 3.1.2 Structure of a Standard Disk |
| 3.1.3 Emitted radiation from a Standard Disk |
| 3.1.4 Stability of a Thin Disk |
| 3.1.5 Viscosity in a Thin Disk 64 |
| 3.2 Two Temperature Disk Models 65 |
| 3.3 Transonic Disk Models 65 |
| 3.4 Magnetized Disk Models 66 |
| 3.5 Thin Disks with Weber-Devis Magnetic Field Configuration |
| 3.5.1 Basic Equations and Magnetosonic Point Conditions |

| 3.5.2 Solution Topologies of Magnetized Accretion | 72 |
|--|-----------|
| qquad 3.6 Outflows by Extraction of Energy from Black Holes | . 73 |
| 4: Thick Accretion Disks | 75 |
| 4.1 Introduction | 75 |
| 4.2 Pseudo-Newtonian Thick Disks | |
| 4.3 General Relativistic Thick Disks | |
| 4.4 Thermodynamic Conditions inside a Thick Accretion Disk | |
| 4.5 Emitted Radiation from a Thick Accretion Disk | |
| 4.6 Ion Pressure Dominated Thick Disks | |
| 4.7 Magnetized Thick Disks | |
| 4.8 Thick Accretion Disk – To Be or Not to Be? | |
| 5: Advective Disks | |
| | |
| 5.1 Model Equations and Multiplicity of Critical Points | |
| 5.2 Adiabatic Disks With Discontinuities | |
| 5.2.1 Steady State Solutions | |
| 5.2.2 Sonic Point Conditions | |
| 5.2.3 When Does a Flow Contain Shocks? | |
| 5.2.4 Shock Conditions | |
| 5.2.5 Examples of Complete Solutions with Discontinuities | |
| 5.3 Isothermal Advective Flow with Viscosity | 95 |
| 5.4 Most General Advective Flow and Unification of Accretion Disk Models | . 96 |
| 5.5 'Advection Dominated' Disk Models | . 99 |
| 5.6 Axisymmetric Shock Waves in a Few Other Systems | 100 |
| 5.6.1 In Kerr Geometry | 100 |
| 5.6.2 In Magnetized Flows | 100 |
| 5.7 Non-Axisymmetric Spiral Shock Waves | 101 |
| 5.7.1 Introduction | 101 |
| 5.7.2 Basic Flow Equations | |
| 5.7.3 Examples of Spiral Shocks in Accretion Disks | 105 |
| 6: Numerical Simulations of Accretion Disks | 106 |
| 6.1 Introduction | . 106 |
| 6.1 Introduction 6.2 Simulation of Bondi-Hoyle-Littleton Accretion 6.3 Simulation of Bondi-Hoyle-Littleton Accretion | |
| 6.3 Simulations of Inviscid Flows | |
| 6.4 Simulations of Viscous Disks | |
| 6.5 Simulations of Flows using Radiative Transfer | |
| | |
| 7: Observational Signatures of Black Hole Accretion | 117 |
| 7.1 Introduction | |
| 7.2 Continuum Emission | |
| 7.3 Variability of AGN Spectrum | |
| 7.4 Correlated Variabilities | |
| 7.5 Variability of Disk Line Emission | |
| 7.5.1 Temporal Variation | |
| 7.5.2 Spatial Variation | 127 |
| 7.6 Quasi-Periodic Oscilaltions | 129 |

| 7.7 Our Galactic Center | | 129 |
|-------------------------|---|-------|
| 8 Concluding Remarks | | 134 |
| 9 Note Added in Proof | • | 138 |
| 10 References | | 140 |
| 11 Figure Captions | | 7-167 |

Accretion Processes On a Black Hole

Sandip K. Chakrabarti

Tata Institute Of Fundamental Research, Bombay, 400005 INDIA

Abstract

We describe astrophysical processes around a black hole keeping primarily the physics of accretion in mind. In §1, we briefly discuss the formation, evolution and detection of black holes. We also discuss the difference of flow properties around a black hole and a Newtonian star. In §2, we present past and present developments in the study of spherically accreting flows. We study the properties of Bondi flow with and without radiative transfer. In the presence of significant angular momentum, which is especially true in a binary system, matter will be accreted as a thin Keplerian disk. In §3, we discuss a large number of models of these disks including the more popular standard disk model. We present magnetized disk models as well. Since the angular momentum is high in these systems, rotational motion is the most dominant component compared to the radial or the vertical velocity components. In §4, we study thick disk models which are of low angular momentum but still have no significant radial motion. The accretion rates could be very high causing the flow to become radiation dominated and the disk to be geometrically thick. For low accretion rates, ion pressure supported disks are formed. In §5, we extensively discuss the properties of transonic flows which has with sub-Keplerian angular momentum. In the absence of shock discontinuities, these sub-Keplerian flows are basically advecting, similar to Bondi flows, close to the black holes, though far away they match Keplerian or sub-Keplerian disks. In presence of shocks, the post-shock flow becomes rotation dominated similar to thick disks. In §6, we present results of important numerical simulations of accretion flows. Significant results from the studies of evolution of viscous transonic flows are reported. In §7, we discuss some observational evidences of the black hole accretion. We also present a detailed model of a generalized accretion disk and present its spectra and compare with observations. In §8, we summarize the review and make concluding remarks.

1. Introduction

Among all the celestial objects, black holes are the simplest to describe mathematically. The simplest among the black holes, known as a Schwarzschild black hole, is characterized by its mass M alone, and has occupied a very popular place in models of active galaxies, quasars and some compact X-ray binaries. Along with the constant of gravitation, G and the velocity of light c, one can obtain a length-scale $l_{bh} = GM/c^2 = 1.5 \times 10^{14} M_9$ cm, and a time scale $t_{bh} = GM/c^3 = 5000 M_9$ s (M_9 is the mass of the central black hole in units of $10^9 M_{\odot}$). Physical quantities close to a black hole are expected to vary in these scales. The Schwarzschild radius $r_{bh} = r_g = 2l_{bh}$ of a black hole is identified as the radius of a non-rotating black hole while $r_{bh} = l_{bh}$ is the radius of a rotating black hole with maximally allowed specific angular momentum $J = GM/c = 4.5 \times 10^{24} M_9$ cm² s⁻¹ (otherwise known as the extreme Kerr black hole). Information within $r < r_{bh}$ remains inaccessible to the observers located at $r > r_{bh}$.

Since black holes are 'black', there cannot be any direct observational evidence of them. However, there are many indirect ways to 'see' if black holes are present at galactic centers or in binary systems. Most of these ways depend upon the peculiarities of the behaviour of matter close to a black hole. In the present review, we shall study these behaviours. There is a recent review on the identification of the black holes in binary systems [1], and therefore, we shall mostly concentrate on the studies around super-massive black holes, although mathematical discussions will remain valid for black holes of any mass. An earlier review on the black hole models for active galaxies [2] will be relevant for our present study and we shall refer it often. Because matter accreted on a galactic center as well as at least some matter to the compact component of a binary system may have very little angular momentum, a great deal of our investigations will be made in studying low-angular momentum accretion flows, which include spherical accretion, thick disks and the transonic accretion disks.

Nuclei of some galaxies undergo violent activity, quasars being the most extreme instances of this phenomenon. Such activity is probably short-lived compared to the galactic lifetime, and was probably most prevalent when the universe was only about one-fifth of its present age. A massive black hole is the inevitable end point of such activity [3]. Rees [2] depicted a few plausible scenarios showing that nearly all the galaxies which have undergone some 'violent' activities in the past may have black holes at their centers. In Fig. 1.1 we reproduce a figure from Rees [2] to show the possible evolutionary routes. A characteristic luminosity which may be observed from such activity is the 'Eddington limit', where the inward gravitational pull on protons balances the outward force of radiation on electrons,

$$L_{Edd} = \frac{4\pi G M m_p c}{\sigma_T} = 1.3 \times 10^{47} M_9 \text{erg s}^{-1},$$

where, m_p is the mass of the proton and σ_T is the Thomson scattering cross-section. The luminosity of the quasars and active galaxies have indeed been observed to be sometimes as high as 10^{47} erg s⁻¹ and the usual explanation for such a high energy output is that the energy is mostly coming from the gravitational binding energy of matter accreting onto a massive black hole with $M \sim 10^9 M_{\odot}$. Accretion disks very close to the black hole (which may be extending from regions just outside the horizon up to a distance of a thousand of Schwarzschild radii) have not been observed yet, but the molecular and ionized disks at distances of \sim parsec have been observed. There are several models of accretion flows which reproduce observed spectra of active galactic nuclei (AGN) and quasars very well. This may therefore indicate that accretions do take place on black holes residing in galactic centers. For instance, the characteristic black body temperature of the radiation with luminosity L_{Edd} at l_{bh} is,

$$T_E \sim 2.8 \times 10^5 M_9^{-1/4} K.$$

Indeed, radiation around this temperature is observed from accretion flows. Another way is to measure the rotational velocities around the center. The Keplerian velocity of a circular orbit of radius r (in units of l_{bh}) around a mass M is $v_{Kep} = 3 \times 10^5 r^{-1/2}$ km s⁻¹. Most recent photographs of M87 by Hubble Space Telescope indicate rotational velocities of several hundred kilometers at distances of only 60 light years from the galactic center. If the motion is truly around a black hole, the mass of it must be a few times $\sim 10^9 M_{\odot}$ at the center of M87 [4-6]. There are also indications that in the center of our own galaxy, a black hole of several thousand solar mass to several million solar mass may be present [7]. Possible presence of a massive black hole in the nucleus of the Andromeda nebula (M31) is indicated by the high-resolution measurements of the rapid rotation and large velocity dispersion of the stars [8-9]. It is estimated that a black hole of mass $10^7 M_{\odot}$ may reside at the heart of M31. From the periodic flares observed over last few decades, it is suggested that two super-massive black holes may be orbiting each other in OJ287 [10]. Such systems may be formed due to mergers of super-giant galaxies. These binaries can be long lived against gravitational radiation with life time well above the Hubble time.

The region around a massive black hole at the galactic center, with a deep gravitational potential well, is a cite of intense activity. Stars are created from the gas, and some gas is lost from the stars directly or through collisions. The gas and the stars slowly spiral their way into the center. In the following Sections, we shall present the dynamic and radiative properties of the gas flows. We shall show that depending on the boundary condition, namely the amount of matter supply, the average angular momentum of the flow, presence or absence of turbulence and viscosity in the disk, the nature of the disk as well as the radiation coming from it may be very much different. For instance, if the matter is distributed spherically symmetrically, the accretion process will be spherical Bondi accretion. If the angular momentum is quite high, very little matter may accrete unless turbulent transport of angular momentum is very efficient allowing matter to be accreted in the form of a Keplerian disk. If the angular momentum is intermediate, the the matter would accrete quasi-spherically at a large distance and would slowly take the form of a disk at a distance of tens or hundreds of Schwarzschild radius as the angular momentum becomes comparable to the local

Keplerian value. The present status of the knowledge of the accretion process indicates that disks in a binary system consisting no compact stars, may be primarily similar to the standard Keplerian type [11, 12]. However, the accretion process close to a black hole either in compact binaries or in active galaxies need not be Keplerian everywhere and the study of sub-Keplerian matter requires more attention. In some situations, discussed in §5, the viscosity and cooling parameters are such that the disk will become completely sub-Keplerian much before entering the black hole.

The physics of the accretion process on a black hole consists largely of our understanding of the accretion disks. Accordingly, we shall devote several Sections of this review on this aspect, discussing some of the major works which have provided directions in this subject. However, 'accretion' does not always mean the accretion of gas. It could be another star, or even another black hole! All these types of accretions are, in principle, verifiable observationally. Not only that, all these processes should cause the black hole and its surroundings to evolve. Thus, the question of a black hole accretion encompasses varied issues such as formation and evolution of compact binaries, quasars, evidence of the existence of black holes, the supply of fuels to the central black holes, structure and stability and radiative properties of accreting flows, merger of galaxies, merger of black holes, gravitational waves generated from black hole accretion, gravitational lensing, nucleosynthesis around black holes, formation of radio jets from the surroundings of a black hole, continuum and line emissions from an accretion disk, etc. etc. We cannot possibly cover all these issues reasonably in a single review. In the rest of this introductory Section, we shall briefly discuss the formation and evolution of central black holes in quasars, question of the supply of fuel and some other issues relevant to the accretion physics which we do not intend to discuss in detail in subsequent Sections. We then devote a few paragraphs to discuss the salient differences between the particle and fluid dynamics around a black hole and around a Newtonian star. Many of our current understanding of black hole physics is from using simple minded models of the black hole geometries, namely, using the pseudo-Newtonian potentials. These have become very useful tools in studying astrophysics around black holes in recent days and we shall be frequently using them in subsequent Sections.

1.1 Some General Issues Related to Black Hole Astrophysics

1.1.1 Formation of Black Holes

As shown in Fig. 1.1, the formation of the black holes usually involve catastrophic gravitational collapse. Stellar mass black holes form in the same way as the neutron stars, namely, by core collapse and supernovae explosion. The population of the black holes in low mass X-ray binaries could be at least as high as the population of neutron stars, or probably more. Progenitor stars more massive than $\sim 40-50M_{\odot}$ probably form black holes [13, 14]. Several numerical simulations have also been carried out to study the process of formation of black holes. Numerical simulations of head-on

collisions of relativistic clusters show that gas spheres with particles initially at rest or boosted towards each other implode towards their centers and may form black holes before colliding. When particles in a sphere are in circular orbits about their respective centers, the collisions lead to either coalescence and virialization or collapse to a black hole [15]. These examples however ignore any quantum effects such as particle creations in curves spacetime (which may have significant astrophysical implications!).

Recent discovery of large population of millisecond pulsars, and hence neutron stars, in globular clusters implies that several hundred stellar black holes (of about $10M_{\odot}$) should form within a typical cluster. In clusters of high central density, the rapid dynamical evolution will cause them to segregate to the cluster cores, where they form binary and multiple black-hole systems. During the subsequent evolution, most of the black holes are ejected on a relatively short time scale. A typical cluster may retain up to four black holes in its core, and possibly a few black holes in its halo. The presence of binary, triple and quadruple black-hole systems in cluster cores can disrupt main-sequence and giant stellar binaries which is a probable cause for the observed anomalies in the distribution of binaries in globular clusters [16].

Active galaxies refer to the galaxies which show anomalous energy output within the inner parsecs of the galactic nuclei. Occasionally, the star burst galaxies may also show activities resulting from high formation rates of stars in inner few kilo parsecs. When two gas-rich galaxies collide, huge amount of matter may fall towards the central black holes which trigger starburst activity and a quasar formation [17]. A super massive black hole may also form in multiple steps: massive black holes ($\geq 10^5 M_{\odot}$) can first form in a quasi-spherical collapse of gas clouds which came out of non-linear density perturbations above the Jeans mass after the cosmological re-combination $(200 \le (1+z) \le 1400)$. Angular momentum and energy may be extracted efficiently from the electrons through Compton friction with the cosmic background radiation. The black hole is produced, surrounded by a dark-matter halo. Later, additional mass can accrete into the system, causing activity of star formation [18]. Alternatively, dynamical evolution of compact star systems may end up in a mixture of gas and surviving stars which unavoidably collapse into a giant black hole. The subsequent evolution of the remnant star system with a massive black hole at the center can lead to the formation of a bright central source in the nuclei of active galaxies and quasars. It may also lead to the opposite case of a 'dead' frozen black hole in the nucleus of a normal galaxy [19].

Assuming a standard black hole accretion model for quasars [2], it is possible to estimate the present total mass density ρ_{BH} of quasar remnants using observations of quasar populations and of typical quasar spectra over a wide wavelength range. It is found that $\rho_{BH} \geq (1.4-2.2) \times 10^5 M_{\odot}/Mpc^{-3}$ for a quasar radiative efficiency η (= $\frac{L}{Mc^2}$, where, L is the luminosity and \dot{M} is the accretion rate) of 0.1 [20]. A typical bright galaxy is expected to contain a central black hole of mass $\geq 10^7 M_{\odot}$ and $\geq 50\%$ of ρ_{BH} may be contributed by objects of mass $\geq 10^8 M_{\odot}$ and $\geq 10\%$ by those more massive than about $6 \times 10^8 h^{-2} M_{\odot}$. During the lifetime of a galaxy, the accretion rate

itself may gradually evolve. The evolution of the accretion rate could be determined by making a very simplistic assumption that the accretion rate is either demand-limited (i.e., radiation pressure controls the accretion rate) when matter is available or supply-driven when matter is in meager amount [21]. In this scenario, a newly formed galaxy quickly grows or acquires a black hole and accretes at a rate close to the Eddington limit. The subsequent accretion takes place intermittently at an average rate that is a universal function of black hole mass and time. With these assumptions the current mass distribution of relict black holes in the nuclei of nearby galaxies can be derived [21]. Here, the accretion rate scales as $M^{-1.5}t^{-6.7}$. The number of relict black holes per decade declines only as $M^{-0.4}$ for black hole masses between $3 \times 10^7 M_{\odot}$ and $3 \times 10^9 M_{\odot}$. In order to verify such a distribution of central masses more accurate estimate of the galactic masses are to be carried out.

An understanding of the stellar rotation and velocity dispersion profiles close to a nucleus can give a hint of the nature of the central concentration. Figure 1.2 shows velocity dispersions and stellar rotations along the major axis of the Andromeda galaxy M31 and along the major axis of its bulge component [8]. The velocity dispersion is as high as 245km s⁻¹ and the mass to light ratio of 23 to 35 in this case is much higher than that in bulges and normal elliptical galaxies. Indeed, the rotational velocity fits with a Keplerian model if the mass of the central black hole is a few $\times 10^7 M_{\odot}$. Not all the luminous galaxies may have active past, however. For example, rotational velocities and velocity dispersions along the major and minor axes of the spiral galaxies NGC 2613, NGC 4699, NGC 5746, and NGC 7331 have been recently measured and the stellar kinematics were computed using maximum entropy models. It was found that for all four galaxies, models without central black holes and with constant mass to light ratio as a function of radius are able to fit the observational data. Dynamical models that include a central black hole of about $10^9 M_{\odot}$ are able to fit the observations of NGC 2613, NGC 4699, and NGC 5746 but do not fit the observations of NGC 7331. Only one out of these three candidates, namely NGC 4699, is found to be a relatively strong case to have central black hole [22].

1.1.2 Fueling Black Holes

In low mass X-ray binary systems, matter to the compact object can be supplied from the companion in two different ways. When the companion fills its Roche lobe, matter with Keplerian angular momentum is accreted through the Lagrange point (§3). If the companion has a significant wind, and the compact object moves through it, than some winds with a very little angular momentum is also accreted. Thus, fueling low mass black holes in binary systems (galactic black holes) is not a problem.

The fueling of massive black holes supposedly residing at the center of the active galaxies is an well recognized problem. This is because the most luminous of them have luminosities $L \gtrsim 10^{47}$ erg s⁻¹ requiring fuel of about a few M_{\odot} yr⁻¹. The fuel

could come from lost gases from dense star clusters or from interstellar medium or from in-falling intergalactic matter from outside the galaxy. On an average, the Population II stars lose $\sim 0.01 M_{\odot} \text{ yr}^{-1}$ per $10^9 M_{\odot}$ stellar mass which may be concentrated within a region of $r \sim 10$ pc [23]. This is clearly insufficient for AGNs. When the star density is high enough, they collide and gases are lost in the process. Star-star collision [24, 25 and winds from clusters may provide very efficient fueling. Stars can also be tidally squeezed as they approach a black hole [26-28]. Disruption of a single star may produce flares and may be indicative of the presence of a black hole [29, 30]. Detailed study of the formation of short lived flares due to the tidal disruption of stars by the massive black holes at the center of the galaxy shows that the flares may last for a few months with the peak luminosity in the extreme ultraviolet region [31]. Such flares should be detectable and would constrain the number of the remnant black holes in galactic centers. Numerical simulations have attempted to study the nature of debris formed around black holes due to tidal disruptions. The strength of the tidal encounter is related to the square root of the ratio η between surface gravity and tidal acceleration at pericenter (so that for $\eta < 1$, the star is disrupted) or the ratio between the duration of the encounter and the hydrodynamic time scale [32]. Through such encounter a flare of the order of Eddington luminosity can last for a period of about an year $(1M_{\odot})$ around $10^6 M_{\odot}$ for $\eta = 1$), after which it fades away [33]. Low luminosity Seyferts may be explained in this way. An interesting study of the fate of the bound debris is made by Rees [29]. Investigations of the tidal break-up of solar-type stars near massive black holes have shown that debris gas could be distributed throughout the galactic nucleus. Apparently, about half of the stellar debris mass remains strongly bound to the black hole. This is quickly swallowed and the rest is expelled [29]. This matter can fuel black holes in galactic nuclei during periods of enhanced tidal disruptions induced by galaxy mergers. It is also suggested that the broad line regions may be produced by debris clouds [34]. However, a detailed study of the tidal capture of stars by a massive black hole [35] shows that the maximum ratio of the cross-section for tidal capture to that for tidal disruption is ~ 3 for realistic systems. In other words, tidal captures are probably more important than tidal disruptions. Inclusion of general relativistic non-linear effects on the tidal capture of stars by a massive black hole, however, seems to show that the non-linear effects significantly re-inforce the absorption of the orbital energy by the star, and results in tidal disruptions far beyond the Roche limit [36]. Once the mass of the central body is higher than $10^{8-9}M_{\odot}$, the tidal disruption is negligible since the Schwarzschild radius of the black hole is larger compared to the tidal radius [24, 25], although the limit on the central black hole mass may be raised by a factor of 10 when fully general relativistic calculation around a Kerr black hole is considered [37]. A typical simulation sequence using Smoothed Particle Hydrodynamics (SPH) is presented in Fig. 1.3 [37] which shows how a star $(1 M_{\odot})$ is gradually deformed while passing close to the Roche radius of a black hole $(10^4 M_{\odot})$. The disk was not seen to form in these simulations, probably because a realistic steller model was not used. In a three dimensional general relativistic numerical study of tidal disruption of a main-sequence star $(M_* = 1 M_{\odot})$ by a super-massive black hole $(M_h = 10^6 M_{\odot})$, it is seen that during a close passage, as a result of relativistic effects analogous to the perihelion shift, the trajectories of the debris of the star fan out into a crescent-like shape centered on the black hole [38]. In another extensive numerical simulation [39], over 8×10^5 encounters of binary systems with black holes (having masses that range from 10 to 10^4 times that of the binary components) were considered using various collisional velocities and impact parameters. This provided estimates of the probability of the black hole tidal disruption in close encounters that produce exchange collisions. It turns out that the exchange collisions dominate over tidal dissociation if the sum of the radii of the stars is less than the binary semi-major axis. Occasionally, exchange collisions take place in encounters of black holes with soft binaries leading to black hole capture of one binary component and ejection of the other at a high speed. Observation of these high speed stars are of extreme importance in understanding the nature of the galactic nuclei. In the case of multiple mergers of galaxies, some of the black holes may escape from the galaxies with a high scattering velocity [40].

In the case of a steady gas supply, the stellar orbits diffuse to the lower angular orbits and enter a small loss cone of semi angle $\theta_{crit} \approx (t_{dyn}/t_{rlx})^{1/2}$ where, t_{dyn} and t_{rlx} are the dynamical and relaxation time scales respectively and $t_{rlx} \sim t_{dyn}N_c/lnN_c$, where N_c is the number of stars in the cluster [23]. For an almost isotropic velocity distribution of stars the tidally disrupted matter supply rate is [41, 42],

$$\dot{M}_{tid} \sim \frac{N_c M_*}{t_{rlx} ln(2/\theta_{crit})} \sim \frac{M_*}{t_{dyn}}.$$

Here, M_* is the average mass of a star in the cluster. Whereas this rate is not sufficient for fueling AGNs, the matter lost from the stellar collision can be sufficient. Indeed, the maximum rate of gas production by collision is given by [23],

$$\dot{M}_{col} \sim \frac{N_c}{t_{col}} \sim \frac{M_*}{t_{dyn}} (\frac{v_c}{v_*})^4 \sim \dot{M}_{tid} (\frac{v_c}{v_*})^4.$$

Here, v_c is the relative velocity of the colliding stars and v_* is the escape velocity from the stellar surface. The velocity v_c being comparable to the Keplerian velocity, accretion is possible when some source of viscosity is present, or when the supersonic winds formed passes through a bow shock and its velocity randomized before falling onto a black hole. In general, this seems to be more interesting possibility of supplying fuel than the other mechanisms, provided a dense star cluster is assumed a priori at the center of the galaxy.

One may imagine that matter is supplied from the extended thin accretion disk up to distances of a few (~ 10) parsec. However, at this distance the angular momentum transport by the viscous process involves a time scale of $t \sim 10^9 \alpha^{-1} T_{100}^{-1} v_{\phi,100} r_{10}$ yr, where α is the Shakura-Sunyaev viscosity parameter (usually <<1). Here, r is measured in units of 10pc, T is in units of 100K, and v_{ϕ} is in units of 100km s⁻¹. This means that the time scale is large compared to the galactic age. Also, the thin disks could be gravitationally unstable when the number density n exceeds a critical density [23], $n > n_{crit} \sim 10^6 v_{\phi,100}^2 r_{10}^{-2}$ cm⁻³. This limits the accretion rate to only $\dot{M}_{crit} \sim 3\alpha c_s^3/G \sim 5 \times 10^{-4} \alpha T_{100}^{3/2} M_{\odot} \ {\rm yr}^{-1}$. The temperature is usually below 100K, and

radiation from the inner edge cannot keep it warm enough to increase the accretion rate further. Thus, the accretion rate computed from the thin disk assumption may remain insignificant [23]. Since a self-gravitating disk would be a place where efficient star formation might occur, this gives all the more reason why fueling through the stellar winds may be taking place in active galactic nuclei [23]. This gas may remain very hot at regions far away (> 1kpc) due to heating by supernovae, or the central X-ray source [43, 44]. Cloud-cloud collision may also be a viable mechanism, though gas supplied by this process need not be very high [23].

If the gas is supplied from a number of randomly placed stars, then only those matter directed virtually towards the direction of the central black hole would be accreting on it, since otherwise it would have very high angular momentum. The escaping winds from a star may most certainly collide with winds from another star placed nearby, canceling its velocity components normal to the direction of the black hole. Thus, the actual angular momentum of matter falling onto the black hole could be very small. This situation could be very similar to the idea of Hoyle-Lyttleton [45] accretion of matter by a moving star in a gas medium. Because of low angular momentum, the flow is quasi-spherical far away from the black hole (primarily advecting, i.e., $v_r >> v_{\phi}$) and becomes 'disk'-like (primarily rotating, i.e., $v_{\phi} >> v_r$) only when the angular momentum becomes comparable to the local Keplerian angular momentum. Even in a stellar system both types of flows are possible (Section 5).

1.1.3 Evolution of Galactic Centers

Extensive numerical simulation results are present in the literature to study the dynamical and luminosity evolution of an active galaxy consisting of dense stellar system surrounding a massive black hole. A power law initial mass function, tidal disruption by central black hole, physical collisions, as well as the stellar evolutions are included in these simulations [46]. The general result is that, for low initial central stellar mass densities, stellar evolution and tidal deformations are dominant, but for high stellar densities, the physical collisions dominate. A similar study of the joint evolution of a stellar galactic nucleus and central massive black hole [47] shows that the final outcomes are differentiated by the distribution and motion of stars near the black hole which determine the rate of their penetrating into the 'loss-cone' and successive tidal disruption or swallowing by the black hole. The stellar cluster may either contract or expand by these evolution process, depending on the parameters of the total system. A massive black hole at the center of the host galaxy is found to exist either in an excited state as a powerful central source or in the ground state as a 'dead' quasar.

In our galactic nucleus, it is believed that there is a black hole not exceeding $5 \times 10^6 M_{\odot}$ [7]. If the mass were that high, the luminosity resulting from the disruption and swallowing rate would have exceeded the upper limit of the observed luminosity of 10^{40} erg s⁻¹ [24, 48]. By immersing a black hole (of mass $5 \times 10^6 M_{\odot}$) in an isothermal

extended stellar system with dispersion velocity 200 km s⁻¹, Sanders & van Oosterom [49] finds that the final black hole mass and luminosity are fairly independent of the central density. In a second simulation, a mass of $2 \times 10^7 M_{\odot}$ was used with a stellar system as that of the nucleus of M31. In both the simulations, a swallowing rate of one star per 10^4 yrs is found and the time averaged luminosity was found to be 100 times greater, i.e., about 10^{42} erg s⁻¹. Since the accretion flow time scale (of around a hundred years) is much shorter than the time scale of disruption of stars (10^4 yrs), one would expect that this energy be released in short luminous bursts on the order of 10^{44} erg s⁻¹. This is consistent with the belief that at least some of the Seyfert luminosities are generated due to the tidal disruption of stars.

Another important study has been to find out the end products of the merger of two elliptical galaxies [50]. It is observed that the central black holes sink toward the core of the merger and form a binary system. The orbital energy and the angular momentum of the binary black holes are seen to be transferred to the field stars through the dynamical friction and black hole merger can take place in a time shorter than 10^7yr . In the final phase, the orbit of the binary becomes highly eccentric as dynamical friction is most effective at the apocenter with the minimum orbital velocity. The periastron distance decreases exponentially, and eventually the black holes merge when the emission of the gravitational radiation becomes significant.

1.1.4 Black Holes in Galactic Halos?

While we are discussing the possibility of existence of black holes in general, a question arises naturally: are there black holes in the galactic halos and/or are there black holes scattered throughout the galactic disk? The composition of the dark halos and the heating of the stellar disks are still a debatable issue. There are many controversies and no firm conclusions. If, for instance, our galactic halo is composed of massive black holes with masses of the order of $10^6 M_{\odot}$, they should heat the stellar population and the dispersion velocity should steadily go up. Estimates ignoring dynamical friction suggest that the predicted velocity dispersion is in good agreement with observations [51]. However, in this case the dynamical friction would cause approximately 100 such objects to settle towards the Galactic Centre. The most likely outcome would be the accumulation of a central mass $M >> 10^6 M_{\odot}$, which is much larger than is what is predicted from the present observational constraints. This consideration argues against the hypothesis that the halo is made of $10^6 M_{\odot}$ black holes [52].

Dynamical friction may help explaining the evolution of the central massive black hole or even the formation of a dense cluster out of small black holes close to the center. When the compact remnants of massive stars are themselves significantly more massive than the normal field stars in the galactic center, they may migrate inwards as a consequence of dynamical friction [53]. The resulting mass segregation may lead to a concentration of compact objects inside the central stellar core within a Hubble time. The total mass of remnants concentrated into the inner few tenths of a parsec, $0.4 - 5 \times 10^6 M_{\odot}$, is comparable to the dynamically inferred mass in this region in our galaxy.

Could there be black holes forming all over the galaxy before the completion of the galaxy formation? Ipser & Price [54] argue that if that was the case then any such object passing through the interstellar gas of a galaxy should be highly luminous due to heating of accreted gas. It is found that both spherical and disk accretion should occur, with about 95% of the pre-galactic black holes in the Galaxy probably undergoing essentially spherical accretion. In this type of accretions, typical luminosities of the order 10³⁷ erg s⁻¹ in the far-IR are predicted which is yet to be observed making the pregalactic-black-hole hypothesis untenable.

One can put other constraints on the amount of dark matter in the form of black holes in halos. COBE results rule out hot intergalactic model for the X-ray background (XRB) and the possibility that XRB is due to discrete sources emitting at high redshifts of about 10. Indeed, there are suggestions that XRBs should be explained by the accreting massive black holes [55]. However, one may put a constraint that the X-ray emission by gas accretion onto black holes should not exceed the observed soft X-ray background. Secondly, metals produced in stellar processes that lead to black hole formation should not exceed the observed disk metal abundance. Based on these constraints, it appears unlikely that the missing disk mass could be contained in black holes [56]. Another independent constraint is that the nearest black hole in the interstellar medium should not be directly observable in optical [57]. For this, the halo black holes must be lighter than $10^3 M_{\odot}$ and the dark matter in the galactic disk cannot have black holes more massive than $10 M_{\odot}$. These black holes may be remnants of population III stars [58].

1.1.5 Some Signatures of Black Holes

Below, we present a few paragraphs describing some of the signatures of black holes about which we shall not make any further comments in the rest of this review. The observational signatures of black hole accretions will be discussed in detail in §7.

Since the ellipticals are thought to be end products of merger events, merger of binary black holes should produce intense bursts of gravitational waves detectable from earth. The mean time interval between two bursts of gravitational wave is found to be $2-5\mathrm{yr}$ [59]. These waves are detectable in proposed future space based interferometers. Numerical estimates of the frequency of mergers of binary neutron stars and black holes show that the gravitational wave detectors now under development, may be able to detect up to approximately 100 neutron star mergers per year at distances $\lesssim 200~\mathrm{Mpc}$ [60]. More conservative estimate shows that if one uses a single Laser Interferometer Gravitational-wave Observatory (LIGO)-like detector and $1.4M_{\odot}$ neutron star binaries,

rate of the coalescing binaries is $\sim 8 \times 10^{-8} \ \rm yr^{-1} \ Mpc^{-3}$. This implies that LIGO will observe approximately 50 yr⁻¹ binary in-spiral events [61]. The rate of detection of black hole mergers are supposed to be comparable to that of neutron star mergers because of the strong dependence of the power of outbursts on the masses of merging objects. Black holes in low-mass X-ray binaries (LMXBs) may be more common than neutron star binaries in LMXBs [13] and thus there may be more events with binary black hole mergers.

In case of coalescence of binary neutron stars, the duration of gravitational waves is very short and the detection of such short bursts could be difficult. In an alternative system, where a lighter black hole (say, $10M_{\odot}$) orbits around a massive black hole (say, $10^{7-8}M_{\odot}$), in the last Schwarzschild radius outside the horizon, several thousands of orbits are traversed and the detection of gravitational waves is easier. During this process the companion is bound to interact with the accretion disk (which could be sub-Keplerian or super-Keplerian in different regions) and exchange angular momentum with it. A more interesting (but probably extreme) situation may prevail, when the loss of angular momentum of the lighter companion is exactly compensated for by its gain from the disk at some radius (such gain is possible close to the black hole since the disks can have more angular momentum than Keplerian there; see §4, §6). The system becomes a steady emitter of gravitational waves [62]. Extensive numerical simulation has recently verified that such systems are stable [63]. Observation of such systems would verify the current black hole models of galactic nuclei.

Some of the cosmic radio jets are known to propagate virtually in the same direction for hundreds of millions of years. They are considered to be scaled version of the bi-polar outflows in protostars, only more powerful [64]. It is natural to assume that the source of the stability and the power of these jets are super-massive black holes at the center of active galaxies. However, except in very few cases, one cannot really obtain any constraint on the nature of the accretion disk and the black hole properties from the jet features. One suggestion is that the wiggles in jets in extragalactic radio sources could be partly due to orbital motions of two massive black holes. Supposing the wiggles in the milliarcsec radio jet of the superluminal quasar 1928+738 (4C 73.18) are due to this, the period and amplitude of the wiggles can be easily explained as due to the orbital motion of a binary black hole with mass of order $10^8 M_{\odot}$, mass ratio larger than 0.1, and orbital radius approximately 10^{16} cm. The small orbital radius suggests that the binary has been losing a significant amount of orbital energy during the last 10^7 yr, possibly by interaction with the matter which is flowing through the active galactic nucleus [62-63, 65].

For massive black holes in galactic centers, the radiation pressure dominated disks are not hot enough $(T \sim T_E)$ to produce significant nucleosynthesis. But if the flow is gas pressure dominated, the temperature of the gas would be very high $(T \sim \text{virial temperature of the protons}, T_p \sim 1.04 \times 10^{13} r^{-1} K \text{ where } r \text{ is in units of } l_{bh})$ and nucleosynthesis in the accreting gas could be important. If black holes form shortly after

decoupling, this process may even influence the element abundances in the universe [66].

In Seyfert galaxies, such as NGC 6814, Iron $K\alpha$ line is produced very close to the black hole as is evidenced by the fact that the continuum X-ray variability and the intensity of line emission are found to be well correlated by a time lag of less than 250s. Due to the variation of light travel time at various distances from the center, the changes in the double-horned line pattern would take place, first in the wings (which are formed by the innermost disk region), and then the blue and red horns. Observation of such changes may allow determination of the mass of the central black hole [67]. However, it has been recently suggested that these lines could come from outflows, rather than inflowing accretion disks [68]. Direct measurement of the disk emission lines also allows mass and inclination determination as in M87 [4-6].

One could also imagine ways to detect massive black holes $(M \sim 10^6 M_{\odot})$ in the halo. It has been suggested that radio maps from the very large baseline array (VLBA) of two milli-arcsecond jets of a gravitationally lensed quasar will show the signature of massive black holes. If there are no compact objects in this mass range along the line of sight, the two jets should be linear mappings of each other. If they are not, there must be compact objects in the halo of the galaxy that deform the images by gravitational deflection [69].

We now present a general background on some of the basics of the geometries around a Newtonian star and a black hole.

1.2 Difference Between Motions around a Newtonian Star and a Black Hole

Around a Newtonian star, the spacetime can be treated as flat and the four distance between any two points could be written as:

$$ds^{2} = -dt^{2} + dr^{2} + r^{2}(d\theta^{2} + \sin^{2}\theta d\phi^{2}).$$
(1.1)

Here we use the spherical polar coordinate. Also we adopt units where the gravitational constant G, the central mass M and the velocity of light c are all unity (G = M = c = 1). In the study around a black hole, chosen here to be rotating (Kerr solution) for generality, the distance between any two coordinate points can be obtained from [70]:

$$ds^{2} = -(1 - \frac{2r}{\Sigma})dt^{2} - \frac{4arsin^{2}\theta}{\Sigma}dtd\phi + \frac{\Sigma}{\Delta}dr^{2} + \Sigma d\theta^{2} + (r^{2} + a^{2} + \frac{2ra^{2}sin^{2}\theta}{\Sigma})sin^{2}\theta d\phi^{2}, (1.2)$$

where, a is the Kerr parameter of a black hole,

$$a = \frac{J}{M}$$
 and $\Delta = r^2 + 2r + a^2$, $\Sigma = r^2 + a^2 \cos^2 \theta$. (1.3)

The deviation from Newtonian distance becomes significant as one approaches the black hole $r \to 1$.

A second difference of importance arises out of the nature of the effective potential which the flow experiences. The gravitational potential that a test particle around a Newtonian star feels is given by,

$$\Phi_N = -\frac{1}{r}.\tag{1.4}$$

The effective potential of a rotating gas with specific angular momentum λ is obtained by the summation of the gravitational potential and the centrifugal potential.

$$V_N(r) = -\frac{1}{r} + \frac{1}{2} \frac{\lambda^2}{r^2}.$$
 (1.5)

For small r, the rotational term causes the potential to diverge to positive infinity at the origin at r = 0. Accretion onto a star of finite size r_* , requires that the barrier due to the centrifugal force is weaker compared to the gravitational term, i.e.,

$$F = \frac{dV_N(r)}{dr} = \frac{\lambda^2}{r^3} - \frac{1}{r^2} < 0.$$
 (1.6)

In other words, around a Newtonian star, only those matter with angular momentum less than the Keplerian value on the surface of the star

$$l_{Kep,N} = r_*^{1/2}. (1.7)$$

can accrete.

In the case of the black hole accretion, the situation is quite different. Here the effective potential cannot be obtained by addition of components. For simplicity, let us first consider the Schwarzschild solution (a = 0 in eq. 1.2) of the metric around a non-rotating black hole. In this case, the effective potential is given by [70, 71],

$$V_S(r) = \left[\left(1 - \frac{2}{r} \right) \left(1 + \frac{\tilde{l}^2}{r^2} \right) \right]^{1/2}. \tag{1.8}$$

 V_S becomes zero on the horizon, *independent* of the angular momentum of the flow. The conserved specific angular momentum for the particle dynamics is $\tilde{l} = u_{\phi}$. The angular momentum $l = -\frac{u_{\phi}}{u_t}$ is conserved for fluid dynamics as well as the particle dynamics. Here, $(u_t, u_r, u_{\theta}, u_{\phi})$ are the components of four velocity, u_t is the conserved specific energy. The potential experienced by the fluid is:

$$V_S(r) = \left[\frac{1 - 2/r}{1 + \frac{(1 - 2/r)l^2}{r^2}}\right]^{1/2}.$$
 (1.9)

Figure 1.4 shows the effective potential felt by a particle orbiting around a Schwarzschild black hole and around a Newtonian star for various specific angular momenta. The solid curves are for marginally stable ($l_{ms} = 3.674$, lower curve) and for marginally bound ($l_{mb} = 4$, upper curve) angular momenta respectively. The short-dashed curves are for, from bottom to top, for l = 3.51, 3.837 and 4.163 respectively and the long dashed curve is for Newtonian case with $l = l_{ms}$. If the specific angular momentum of the

flow is less than that of the marginally stable value, the flow can fall onto the black hole, without any barrier whatsoever! If the angular momentum is higher than the marginally bound value, the potential barrier is higher than 1 – the rest mass of the particle. This means that for accretion to take place, matter must have significant energy to begin with. Thus, matter must have significant radial velocity or thermal energy at a large distance. In any case, since the potential turns around and passes through zero, matter can always be made to accrete when 'pushed' sufficiently hard. Matter which has angular momentum between the marginally bound and marginally stable values would form accretion disks.

As mentioned above, unlike in Newtonian geometry, the effective potential in general relativity is not obtained by addition of its 'constituents' (the quote mark is to indicate that it may not be meaningful in general relativity to separate the constituents, such as the potential energy, rotational energy... etc.). This is because various energies in general relativity couple together to form new terms. For example, the above potential could be written as

$$V_S(r) = \left[1 - \frac{2}{r} + \frac{\tilde{l}^2}{r^2} - \frac{2\tilde{l}^2}{r^3}\right]^{1/2}.$$
 (1.10)

The presence of the $1/r^3$ term, which can be thought of as the coupling between the gravitational energy and the rotational energy or simply due to attraction of rotational 'mass' by gravity of the central object. These terms become important close to a black hole. For example, $1/r^3$ term becomes very strong near the horizon and causes the reversal of the effective potential to zero [Fig. 1.4] as one goes closer to the black hole. Thus, as the angular momentum is increased, its rotational mass and therefore the coupling term are also increased. As a result, the net radial force is always attractive at the horizon [72].

In the case of a Kerr black hole, the effective potential energy of a particle in terms of conserved particle angular momentum $\tilde{l} = u_{\phi}$ on the equatorial plane is given by,

$$V_K(r) = \omega \tilde{l} + (\alpha^2 + \tilde{l}^2 \alpha^4 / \Delta)^{1/2}.$$
 (1.11)

where,

$$\omega(r) = \frac{2a}{r^3 + a^2r^2 + 2a^2r},\tag{1.12}$$

is the rotational velocity of the zero angular momentum observer, and

$$\alpha = \frac{r^2 + a^2 - 2r}{r^2 a^2 + 2a^2/r} \tag{1.13}$$

is the red-shift factor in the Kerr geometry and

$$\Delta = r^2 + a^2 - 2r. {(1.14)}$$

This potential also goes to zero on the horizon as seen from the zero angular momentum observers. As the matter crosses the horizon, its ω becomes the same as the rotational velocity of the black hole on the horizon.

In terms of the angular momentum which is conserved both for the particles as well as for the fluids, l, this potential takes the form,

$$V_K = \frac{\alpha}{(1 - \omega l)^2 + \frac{\alpha^4 l^2}{\Delta}}.$$
(1.15)

The coupling term between the angular momentum of the black hole and the flow generates new force components [72, 73] which are responsible for various effects, such as the formation of shock waves at the outer distances in contra-rotating flows or the reversal of the trend in ellipticity of collapsing spheroids. Figure 1.5 shows the potential felt by a particle orbiting around a Kerr black hole (a = 0.95) for a range of specific angular momenta of the particle. The solid curves are for the marginally stable ($l_{ms} = 2.331$, lower curve) and marginally bound ($l_{mb} = 2.447$, upper curve) angular momenta respectively and the dashed curves are, from bottom to top, for l = 2.273, l = 2.389 and l = 2.505 respectively.

The amount of energy which the in-falling matter can dissipate during the accretion process depends upon the minimum of the effective potential. In the case of a Newtonian star, this minimum may occur close to the axis well within the star. On the surface of a star, the angular velocity coincides with the angular velocity of the star and the specific energy becomes,

$$\mathcal{E}_s = \frac{1}{2}v_{\phi,*}^2 - \frac{1}{r_*}. (1.16)$$

If the accretion disk were Keplerian, without any radial velocity, the energy of the particle just before hitting the surface would be,

$$\mathcal{E}_* = \frac{1}{2} v_{Kep,*}^2 - \frac{1}{r_*}. (1.17)$$

But,

$$v_{Kep,*} = \frac{1}{r_*^{1/2}}. (1.18)$$

Thus,

$$\mathcal{E}_* = -\frac{1}{2r_*}.\tag{1.19}$$

In other words, matter accreting through a Keplerian disk lose half of its potential energy (calculated on the star surface) in the accretion disk itself. For example, for a star of radius $r_* \sim 10^{12} {\rm cm}$, and a mass as that of our sun, energy loss would be $7.5 \times 10^{-6}\%$ which is very small indeed. Within the boundary layer which is formed on the surface of the star the amount of energy dissipated would be,

$$\mathcal{E}_s - \mathcal{E}_* = \frac{v_{Kep,*}^2 - v_{\phi,*}^2}{2}.$$
 (1.20)

On the contrary, the energy loss in accretion disks around black holes could be much higher. The lowest of the minima occurs at the marginally stable orbits. These correspond to the point of inflection of the effective potentials drawn for marginally bound angular momenta V_S and V_K (See, Figs. 1.4 and 1.5). In Schwarzschild geometry, this occurs at $r_{ms} = 6GM/c^2$ and $V_{s,ms} \sim 0.94$. This means that about 6 per cent of the rest mass can be lost from the surface of the disk. In the case of a rotating black hole, the energy release could be higher. For example, for the rotation parameter a = 0.95 (see Fig. 1.5), the marginally stable orbit is at $r_{ms} = 1.9372$, and correspondingly, $V_{K,ms} = 0.81$. Thus, about 19 percent of the energy can be released in the accretion disk! For a = 1, $V_K(r_{ms}) \sim 0.6$, i.e., about 40 percent energy could be released. Of course, the exact figure depends on the inner edge of the disk which may be located at positions other than $r = r_{ms}$ due to pressure effects (§4).

In Newtonian dynamics, various components of the energy of matter can be simply added up to obtain the total energy. Thus, for example, the conserved specific energy of a gram of in-falling rotating fluid would be given by,

$$\mathcal{E} = \frac{1}{2}v_r^2 + \frac{1}{2}v_\phi^2 - \frac{1}{r} + e + \frac{P}{\rho}$$
 (1.21)

where, P and ρ are the isotropic (total) pressure and density respectively, v_r and v_{ϕ} are the radial and azimuthal velocity components, $e = \frac{P}{(\gamma - 1)\rho}$ is the specific internal energy. This expression is obtained by integrating the radial momentum equation in the absence of any dissipative processes.

The conserved specific energy of the rotating flow in a Kerr geometry, on the other hand, is given by ([70, 71])

$$\mathcal{E} = hu_t$$

where, h is the specific enthalpy $\frac{P+\epsilon}{\rho}$ with ϵ as the internal energy density. Due to non-linearity in the expression of u_t in curved space-time, this cannot be expressed as a sum of different constituent energies.

Another important difference between the fluid dynamics around a black hole and that around a Newtonian star is that, as the flow accretes on a Newtonian star, it can directly hit the surface of the star subsonically (when the radial velocity of matter is *less* than the adiabatic sound speed) or supersonically (when the radial velocity of matter is *greater* than the adiabatic sound speed) depending on the location of the star surface. But in the case of black hole accretion, the flow is supersonic on the horizon since the velocity of sound (even for the steepest equation of state) is less than the flow velocity on the horizon, which is the velocity of light. What this implies is that a black hole accretion is necessarily transonic. This inner boundary condition has a very important implication on the properties of the accretion flows. For instance, the relativistic converging inflow passing through the inner sonic point will have sufficient radial momentum to deposite on cooler photons in an optically thick flow

[74] and produce a characteristic hard spectra which are observed from galactic black hole spectra in soft states [68]. This will not be possible for a neutron star accretion since in the latter case, although the flow would be converging, the momentum deposition would be negligible and would not be seen against the background noise. We will discuss this difference in greater detail in later Sections, particularly in §7.

1.3 Basics of Pseudo-Newtonian Geometries

In the case of most of the astrophysical systems involving a rotating compact star or a black hole, it is not essential that one solves the problem using full general relativity. Fortunately, a few tools are now available which allow one to use the Newtonian concepts (such as Equations in flat geometry, additivity of the energy components .. etc.) at the same time retaining the salient features of a black hole geometry. As long as one is not interested in astrophysical processes 'extremely' close (within $1-2r_g$) to a black hole horizon, one may safely use these tools and obtain satisfactory results. The idea here is to modify the gravitational potential in a manner that the derived force 'roughly' matches the actual force in curved spacetime in a given coordinate system. This method is significantly better than the back-of-the-envelop calculations and easily accessible by astrophysicists (who have no formal background in general relativity) without sacrificing very much of physics.

Paczyński and Wiita [75] first suggested that for many practical purposes one need not use the Schwarzschild solution and one could use a pseudo-Newtonian potential,

$$\Phi_{PN} = 1 - \frac{1}{r - 2} \tag{1.22}$$

instead of the usual -1/r potential to capture most of the physical properties of the black hole. (First term 1 denotes the rest mass of the particle, and can be dropped for Newtonian description.) Barring purists, the astrophysical community in general seems to appreciate this potential very much and a large number of recent astrophysical literature, particularly dealing with accretion disks use this potential [76-77]. The energy per unit gram of the flow can be simply expressed as:

$$\mathcal{E} = \frac{1}{2}v_r^2 + \frac{1}{2}v_\phi^2 - \frac{1}{r-2} + \frac{\gamma}{\gamma - 1}\frac{P}{\rho},\tag{1.23}$$

which is same as eq. (1.21) but the gravitational potential energy is taken from eq. (1.22). The Keplerian distribution of angular momentum obtained by equating the centrifugal force with the gravitational force,

$$l_{Kep,PN} = \frac{r^{1/2}}{(1 - 2/r)} \tag{1.24}$$

is exactly same as in Schwarzschild geometry, provided one equates $l_{Kep,PN}$ with conserved angular momentum for the flow $l_{Kep} = -u_{\phi}/u_{t}$ for the circular time-like geodesics.

Note however that this potential does not satisfy the boundary condition on the horizon, i.e., the potential does not become zero at r=2, but only at r=3. This becomes the effective horizon, as if. However, accretion flows are supposed to be so supersonic near the horizon (§5-6), and the infall time so short that they do not significantly radiate very close to the black hole, or even if they do, the radiation is mostly red-shifted away and contribute very little to the radiation that escapes the disk. Thus, these errors close to the horizon should have very little effect on the emitted spectrum from the disk, still one should be cautious against taking results close to the horizon $(r \sim 2GM/c^2)$ very seriously.

It is generally believed that the black holes in galactic centers may have some rotation. Even at the test particle level, solutions using the Kerr metric become difficult and cumbersome, particularly when the particle is not confined on the equatorial plane. Recently, an attempt has been made to simplify studies around a rotating black hole by using a pseudo-Kerr potential:

$$\Phi_k = 1 - \frac{1}{r - r_0},\tag{1.25}$$

where, r_0 is in general a function of a, the Kerr parameter, to be chosen in a manner that r_{ms} , r_{mb} roughly agree with actual Kerr results. When the test particle has a specific angular momentum \tilde{l} , the effective potential to describe it takes the form [73],

$$\Phi = 1 - \frac{1}{r - r_0} + \frac{r_1 a\tilde{l}}{r^3} + \frac{(1 - 2/r)\tilde{l}^2}{2r^2 sin^2 \theta},$$
(1.26)

where, r_1 is a suitable 'spin-orbit' coupling constant, which is in general a function of a, the rotational parameter. In eq. (1.26), the first term is clearly the rest mass of the particle. The second term describes the gravitational potential. This term is singular at $r = r_0$. When the particle has angular momentum, the energy due to coupling between the angular momentum a of the black hole and that of the particle \tilde{l} would be proportional to $a\tilde{l}/r^3$ as in the spin-orbit coupling term in a hydrogen atom. This is the third term. Similarly, the rotational energy of the particle can be described by $\frac{(1-2/r)\tilde{l}^2}{2r^2}$. (A better result for smaller Kerr parameter is obtained by choosing α^2 in stead of the factor (1-2/r); see Chakrabarti & Khanna [73].) This appears as the fourth term in eq. (1.26). This potential mimics the geometry around a rotating black hole tolerably well (provided r_0 is carefully chosen for each a so as to reproduce the marginally stable and marginally bound orbits well.).

Since there already exists an exact form of the potential in Kerr geometry, $(V_K, \text{eq. } 1.11)$ one may imagine it superfluous to 'construct' another potential which mimics the actual potential! However, if one wants to describe the flow using Newtonian concept, one needs a potential whose derivative is directly equated to the force (unlike in general relativity where the derivation of force computed from the potential is tricky). V_K does not represent such a potential. Hence a pseudo-Kerr potential is helpful.

An important usage of these potentials is that one can study more complex problems such as an ensemble of black holes, or numerical hydrodynamics, or magnetohydrodynamics around a black hole practically as simply as in Newtonian spacetime. For instance, a numerical code written for a Newtonian flat geometry, could be upgraded to study flows in a black hole geometry by just changing the potential and the force in relevant equations. One must use these potentials with some caution, however. Since they are not directly derivable from Einstein equations, they are not exact. They could be used to obtain more accurate 'correction' terms over and above the Newtonian results to study physical processes much closer to the black hole than what a usual post-Newtonian approximation would provide. Any radically new discovery using these potentials must be checked with exact theory. One of the problems, for example, which cannot be studied using the above potential is the evolution of the angular momentum of a rotating black hole in a galactic center. This is because, for a fixed function r_0 , the variation of the salient features with a, do not follow exactly as in Kerr solution [73]. So, problems which involve evolution of a should not be studied with these potentials. The choice of the potential is not unique, and different choices may yield different results depending on the application. The best way is, of course, to use the exact Kerr geometry if at all possible.

1.4 Remarks About Units and Dimensions

In a broad review such as the present one, results of different workers in the field are compiled and often the figures (with various symbols) are borrowed. It is therefore difficult to keep the choice of units same in all the Sections. We have made efforts to choose units as uniform as possible. In any case, in each Section, the units used are spelled out so as to avoid confusion.

In general, the gravitational units G = c = M = 1 would be chosen, where G is the gravitational constant, c is the velocity of light and M is the mass of the black hole. Thus the unit of velocity would be c, the unit of distance would be GM/c^2 , the unit of time would be GM/c^3 and the unit of angular momentum would be GM/c. However, sometimes, we may choose $2GM/c^2$, $2GM/c^3$ and 2GM/c as the unit of length, time and specific angular momentum. Sometimes we may find it instructive to bring back G, M, and c in the equations so as to see the explicit dependence on these quantities. So, we will mix these approaches when there is no confusion. Readers can easily check the units used as well. For instance, if the pseudo-Newtonian potential is written as $-1/2(r-1)^{-1}$ then the length unit is $2GM/c^2$, but when it is written as $-(r-2)^{-1}$ then the length unit is GM/c^2 .

Yet another cause for confusion is that we shall use M to represent the Mach number of the flow, particularly in §§2,5 & 6. However, context will be made sufficiently clear.

2 Spherical Accretion

The process of capture of matter by a gravitating object is called accretion. The rate at which matter is accreted is known as accretion rate (usually denoted by \dot{M} with units gm s⁻¹). The luminosity L emitted is given by,

$$L = \eta \dot{M}c^2 \quad \text{erg s}^{-1} \tag{2.1}$$

where, η is the efficiency of conversion of matter into energy and c is the velocity of light. For a spherically symmetric Newtonian star of $M = 1M_{\odot}$, the quantity

$$L_{Edd} = \frac{4\pi G M m_p c}{\sigma_T} = 1.3 \times 10^{38} \text{ erg s}^{-1}$$
 (2.2)

known as the Eddington luminosity, is a very useful benchmark for luminosity. It is obtained by equating the outward force exerted on electrons by radiation due to deposition of momentum through Thomson scattering with the inward gravitational force on the protons, which are coupled to these electrons via coulomb force. In the above equation, σ_T is the Thomson scattering cross-section, m_p is the mass of the proton, G and M are the gravitational constant and the mass of the central star respectively. Though it is a Newtonian concept and the computation is done using spherical geometry, the definition is generally used unchanged in measuring luminosity of accreting matter around a black hole.

In the present Section, we shall be interested in the steady behaviour of accreting matter which has no angular momentum. The flow is spherically symmetric. The importance of the study of accretion of moving gas by a compact object was realized nearly six decades ago. Imagine a compact object of mass M_* moving in a medium which has density ρ_{∞} and velocity v_{∞} at a large distance, the rate at which matter is intercepted by the star would be [45]

$$\dot{M} = \pi R_A^2 \rho_\infty v_\infty \tag{2.3}$$

where, R_A is so-called accretion radius,

$$R_A = \frac{2GM_*}{v_\infty^2}$$

where the velocity v_{∞} is roughly the escape velocity of the star. This result assumes that the gas is cold and collisionless, i.e., pressureless and therefore valid for flows which are highly supersonic $M \sim \infty$. The angular momentum of matter which could in principle be accreted onto the compact object is $\sim R_A v_{\infty} \sim G M_*/v_{\infty}$. In a medium which is homogeneous far away, most of the transverse component of the angular momentum would be canceled when gases from both sides collide in the downstream side of the star and therefore the actual angular momentum transfer could be very low [45]. In an inhomogeneous medium (with a finite density gradient), the rate of angular momentum transfer to the star is finite [78-79],

$$J \sim \dot{M} R_A^2 v_\infty / H \tag{2.4}$$

where, H is the density scale height. Clearly, $J \to 0$ as $H \to \infty$.

The effect of finite pressure (finite sound velocity a_{∞} at a large distance) was studied in more detail by Bondi [80]. As we show in the next sub-Section, the accretion rate in this case is given by,

$$\dot{M} = 4\pi\lambda R_B^2 \rho_\infty a_\infty \tag{2.5}$$

where,

$$R_B = GM_*/a_\infty^2$$

is the Bondi radius and λ is a function of the polytropic index of the gas (see §2.1). In this case, the flow must have $M \to 0$ at a large distance. For an intermediate Mach number a 'bridging' formula is suggested [80-81],

$$\dot{M} = 4\pi \lambda a_{\infty} \frac{(GM_*)^2}{(a_{\infty}^2 + v_{\infty}^2)}$$
 (2.6)

These results have become the central pieces of both analytical and numerical investigations of spherical accretion processes onto compact objects. There are many developments in the literature concerning the mathematical and the emission properties of the flow. We shall now study them in increasing order of complexity.

2.1 Bondi Accretion on a Newtonian Star

To understand the problem of the spherical accretion on a black hole better, it may be worth while to spend some time on the properties of accreting flows on a Newtonian star which is well studied and well understood. These are the so called 'Bondi solutions' [80]. We shall use G = M = c = 1 so that our use of M as the Mach number of the flow may not confuse the readers.

2.1.1 Basic Equations

Let us consider a spherical star of radius R_* surrounded by a spherically symmetric infinite cloud of gas which is rest at infinity. The equation of motion of this infalling matter is given by [80],

$$\frac{\partial u}{\partial t} + u \frac{\partial u}{\partial r} + \frac{1}{\rho} \frac{\partial P}{\partial r} + \frac{1}{r^2} = 0, \tag{2.7}$$

where u is the radial velocity, ρ is the density of the gas, P is the isotropic pressure, r and t are the radial and the time coordinate respectively. The equation is in dimensionless unit where mass, length and time are measured by M, GM/c^2 and GM/c^3 respectively. The first term is the Eulerian time derivative of the velocity at a given r, the second term is the advective term, the third term is the momentum deposition due to pressure gradient and the final term is due to the gravitational acceleration.

The continuity equation where the divergence of the mass flux is equated with the temporal variation of density at a given r, is given by,

$$\frac{\partial \rho}{\partial t} + \frac{1}{r^2} \frac{\partial}{\partial r} (\rho u r^2) = 0. \tag{2.8}$$

In the steady state solution, the terms containing $\frac{\partial}{\partial t}$ may be deleted and $\frac{\partial}{\partial r}$ may be replaced by $\frac{d}{dr}$. Assume that there is no loss of energy during the accretion and the flow is adiabatic. The flow has the equation of state: $P = K\rho^{\gamma}$, where K is a constant measuring the entropy of the flow, and γ is the adiabatic index which is the ratio of the specific heats and is assumed to be a constant throughout the flow. Using this equation of state eq. (2.7) could be integrated to obtain the conserved specific energy of the flow:

$$\mathcal{E} = \frac{1}{2}u^2 + na^2 - \frac{1}{r} = na_{\infty}^2.$$
 (2.9)

Here, n is the polytropic index, $n = \frac{1}{\gamma - 1}$. Integrating eq. (2.8) the mass flux is obtained as

$$\dot{M} = \rho u r^2. \tag{2.10}$$

apart from a geometric constant 4π . Here $a = \sqrt{\frac{\gamma P}{\rho}}$ is the adiabatic sound speed and

 a_{∞} is its value at infinity, i.e., $a_{\infty} = \sqrt{\frac{\gamma P_{\infty}}{\rho_{\infty}}}$. Using $\rho = (\frac{a^2}{\gamma K})^n$ the eq. (2.10) can be re-written as,

$$\dot{\mathcal{M}} = a^{2n} u r^2. \tag{2.11}$$

Hereafter, the quantity $\dot{\mathcal{M}} = \dot{M}\gamma^n K^n$, which is also conserved in the flow, will be called the 'accretion rate'. Equations (2.9) and (2.11) are the governing equations for two unknowns: u(r) and a(r). Differentiating these equations with respect to r and eliminating $\frac{da}{dr}$ the equation for the velocity variation is obtained as,

$$\frac{du}{dr} = \frac{\frac{1}{r^2} - \frac{2a^2}{r}}{\frac{a^2}{u} - u} = \frac{N}{D}.$$

Since the flow is assumed to be smooth everywhere, if the denominator vanishes at any radial distance r, the numerator must also vanish there. This radius is called the critical radius or the sonic radius of the flow. One therefore arrives at the so-called *sonic point conditions*:

$$u_c = a_c,$$
 i.e., $M_c = 1,$ (2.12a)

and

$$r_c = \frac{1}{2a_c^2}. (2.12b)$$

The subscript c is to denote quantities at the critical radius. The spherical surface of radius $r = r_c$ is also known as the *sound horizon* because for $r < r_c$, u > a and any

acoustic disturbances created in this region are advected towards the star. Thus, no disturbance created within this radius can cross the sound horizon and escape to larger distance. This is analogous to the event horizon of a black hole where no electromagnetic disturbance can escape outside. In terms of a_{∞} , the sound speed (or, the radial velocity) at the critical radius is obtained as,

$$a_c = \left(\frac{n}{n - 3/2}\right)^{1/2} a_{\infty}. (2.13)$$

This shows that a transonic adiabatic flow is possible only if n > 3/2, i.e., $\gamma < 5/3$. It is to be noted that a transonic flow has two extra conditions, namely, eqs. (2.12a) and (2.12b) to satisfy, whereas only one extra unknown, namely, r_c is introduced. Therefore, two conserved quantities, i.e., \mathcal{E} and $\dot{\mathcal{M}}$ cannot be independent, i.e., $\dot{\mathcal{M}} = \dot{\mathcal{M}}(\mathcal{E})$. The accretion rate $\dot{\mathcal{M}}$ for the transonic flow is easily calculated from a_{∞} as,

$$\dot{\mathcal{M}}_c = \frac{1}{4} \left(\frac{na_\infty^2}{n - 3/2} \right)^{n - 3/2}.$$

In terms of the density of the flow at infinity ρ_{∞} , the Bondi mass flux \dot{M} is written as,

$$\dot{M}_c = \frac{1}{4} \frac{\rho_{\infty}}{a_{\infty}^3} (\frac{n}{n - \frac{3}{2}})^{n - \frac{3}{2}}.$$

which is the same as eq. (2.5). Figure 2.1a shows the integral curves of the flow where the Mach number is plotted against the logarithmic radial distance [77]. The curves ABC and A'BC' are the physically significant transonic flows as they connect infinity with the surface of the star. The contours are of constant accretion rate $\dot{\mathcal{M}}$. The radial velocity u along ABC is subsonic at infinity and supersonic on the surface of the star. This is the Bondi accretion flow. The radial velocity u along A'BC' is subsonic on the surface of the star and supersonic at infinity. This is the corresponding wind flow. Other solutions such as DD' or EE' are not transonic: the former is subsonic everywhere and the latter is supersonic everywhere. In fact, in the realistic flows, EE' can also be excluded. Later, we shall show that the properties of the integral curves strongly depend upon the polytropic index n. Figure 2.1a is drawn for n=3 and Fig. 2.1b is drawn for n=3/2. Note that in Fig. 2.1b, the critical curve passes through r=0. Therefore, a neither accretion nor wind type transonic solution is possible.

The accretion rate $\dot{\mathcal{M}}_c$ associated with a transonic flow is the highest accretion rate that the star can accrete from the surrounding cloud [70, 77]. To see this, we use the independent variable M, the Mach number, instead of the velocity u. We eliminate the sound speed a from eqs. (2.9) and (2.11) to obtain,

$$f(M)\dot{\mathcal{M}}^{\frac{2}{2n+1}} = g(r),$$
 (2.14)

where,

$$f(M) = \left[\frac{1}{2}M^{\frac{4n}{2n+1}} + \frac{n}{M^{\frac{2}{2n+1}}}\right],$$

and

$$g(r) = na_{\infty}^2 r^{\frac{4}{2n+1}} + r^{\frac{3-2n}{1+2n}}.$$

f(M) and g(r) each has a minimum. f(M) is minimum at M=1, and $f_{min}=f(1)=\frac{2n+1}{2}$. g(r) is minimum at $r=r_c$ and

$$g_{min} = g(r_c) = \frac{2n+1}{4} a_{\infty}^{\frac{4n-6}{2n+1}} (\frac{2n-3}{4n})^{\frac{3-2n}{2n+1}}.$$

At r_c , we have

$$f(M) = \dot{\mathcal{M}}^{-\frac{2}{2n+1}} g_{min}. \tag{2.15}$$

Since g_{min} is already minimum, the right hand side could be further minimized by increasing $\dot{\mathcal{M}}$. But it cannot be less than f_{min} , the minimum of the left hand side. This fixes the maximum value of $\dot{\mathcal{M}} = \dot{\mathcal{M}}_{max} = (\frac{g_{min}}{f_{min}})^{\frac{2n+1}{2}}$ which turns out to be the same as $\dot{\mathcal{M}}_c$ derived above.

2.1.2 Phase Space Behaviour of the Bondi Flow

In this review we shall use the phrase 'phase space' rather loosely. In the strict sense, a phase space describes the variation of velocity with spatial coordinate. But we shall use this phrase, even when we describe Mach number variation in stead of velocity. For isothermal flows, where the sound speed is constant, these definitions are identical. In order to understand the phase space behaviour of more complex flow described in §5, we spend some time here to understand the nature of figs. 2.1ab and their variations since the Bondi flow is one of the simplest possible astrophysical flows.

Consider first the behaviour of a simple harmonic oscillator (SHO). In the case of an undamped SHO the conserved specific energy E is the sum of kinetic and potential terms:

$$E = \frac{1}{2}\dot{x}^2 + \frac{1}{2}Cx^2,\tag{2.16}$$

where C is the stiffness constant, and \dot{x} denotes the derivative with respect to time. In the phase space (x versus \dot{x} diagrams), the trajectories of constant energy are elliptical. This is because the expression for energy (written for $x \sim 0$), is the sum of two squared terms. In the neighbourhood of x = 0, the trajectories are circular in topology and x = 0 is called a 'circle' type, 'center' type or 'O'-type point. In the case of Bondi flows, the potential term is negative i.e., the 'stiffness' is negative, as if. The trajectories are hyperbolic and the critical point is 'saddle' type, or 'X'-type. In the presence of damping, the trajectories of the SHO spiral in towards x = 0. That is, the behaviour at x = 0 changes from circle type or 'O'-type to 'spiral' type. As we shall discuss in §5.3, the presence of viscosity in the flow causes the center type point to change into a spiral type point. Actually, the behaviour of the SHO at the origin could be one of the numerous kinds depending upon the relative magnitudes of the two parameters: the

damping factor b, and the stiffness constant c. Figure 2.2 schematically shows various types of critical points [77]. It is interesting to study the behaviour of the critical point in the Bondi flow which has only one parameter, namely, the polytropic index n. How does the behaviour of a critical point depend on n? To answer this, consider once again the case of a damped harmonic oscillator and classify its critical points. We start with the equation of motion:

$$\ddot{x} + b\dot{x} + cx = 0. \tag{2.17}$$

Assuming a solution of the form, $x = Ae^{\lambda t}$ with A and λ as constants, one obtains the equation for the characteristics:

$$\lambda^2 + b\lambda + c = 0. \tag{2.18}$$

Two roots of this equation,

$$\lambda_{\pm} = \frac{-b \pm (b^2 - 4c)^{1/2}}{2},\tag{2.19}$$

determine the nature of the solution. Let $D = b^2 - 4c$ denote the discriminant. The classification is done in the following manner:

D < 0: 'spiral' type if $b \neq 0$, 'O' (center)-type if b = 0;

D=0: 'Inflected nodal' type;

D>0: 'nodal' type if c>0, 'straight line' if c=0, 'X'-type c<0.

In the presence of damping in the SHO (or, viscosity in the accretion flow), the nodal type point may form. In that case both the slopes have the same sign, i.e., there are two possible solutions of accretion (or, winds). The center type point is unphysical in accretion as the flow cannot pass through this point. Figure 2.3 (adapted from [77] and [82]) shows the nature of the critical points in various regions of the parameter space. We have marked 'Gravity' and 'Viscosity' to indicate the similarity with negative stiffness and damping respectively. Viscosity would be important when angular momentum is present. In the case of accretion, viscosity should transport angular momentum outwards, and in the case of winds, the transport must be inwards. Thus, for wind solution one may think of a 'negative' viscosity as compared to the accretion. In these respects, the entire comparison with simple harmonic oscillators including the concept of negative stiffness and damping remains valid.

To determine the behaviour of Bondi solutions near the critical point, one needs to study $(\frac{dv}{dr})_c$ (note that in the SHO problem we were studying the behaviour of $\lambda = \frac{d\dot{x}}{dx}$ near x=0). Since $\frac{dv}{dr} = N/D = 0/0$ at a critical point, one must apply l'Hospital's rule. Thus,

$$\left(\frac{dv}{dr}\right)_c = \frac{\frac{dN}{dr}}{\frac{dD}{dr}}. (2.20)$$

After expanding this equation and using the critical point conditions 2.12(a-b) one obtains,

$$\left(\frac{dv}{dr}\right)_c = \frac{4a_c^3}{2n+1} \left[1 \pm \sqrt{n(n-3/2)}\right].$$
 (2.21)

In the present problem, the discriminant D = n(n-3/2) determines the nature of the critical points. For D > 0, namely, for a physical transonic solution, one must have n > 3/2. For 0 < n < 3/2, D < 0, and the critical point is of 'spiral' type. For a 'saddle' type or 'X'-type point two derivatives $(\frac{dv}{dr})_c$ must be of opposite signs, hence one must have n > 2. For 2 > n > 3/2, the critical point is 'nodal'. For n = 3/2, the critical point is 'inflected nodal' type and for n = 2, the critical point is 'straight line' type.

From the solutions just presented, one can now study the asymptotic properties of the Bondi flow. Concentrating on the supersonic branch BC, it is easy to show that the Mach number varies as,

$$M \sim r^{-\frac{2n-3}{4n}}.$$
 (2.22a)

Thus, as $r \to 0$, $M \to \infty$ only if n > 3/2. Similarly, for the branch BC', we have,

$$M \sim r^{n-3/2},$$
 (2.22b)

so that $M \to 0$ as $r \to 0$ only if n > 3/2.

At a large distance, the solution on the branch BA' behaves as

$$M \sim r^{1/n}. (2.22c)$$

Thus, $M \to \infty$ as $r \to \infty$ for any value of n.

2.2 Bondi Flow on a Black Hole

2.2.1 In Schwarzschild Geometry

In the case of a Bondi accretion on a Schwarzschild black hole, the outer boundary condition remains the same (namely, matter is at rest at infinity), but the inner boundary condition is different. Here, matter must cross the event horizon with the velocity of light c. In flows with realistic equations of state, the maximum value of a is $\frac{c}{\sqrt{3}}$. Thus a black hole accretion is transonic [77].

The stationarity condition $\frac{\partial}{\partial t} = 0$ [83] implies a conserved energy \mathcal{E} given by,

$$\mathcal{E} = hu_t = \frac{p + \epsilon}{\rho} \left(\frac{1 - 2/r}{1 - u^2} \right)^{1/2}.$$
 (2.23)

It is to be remembered that \mathcal{E} includes the rest mass of matter. Thus, the specific energy in terms of the quantities at infinity is $\mathcal{E}=1+na_{\infty}^2$. $h(=\frac{P+\epsilon}{\rho}=\frac{1}{1-na^2})$ and u_t are the specific enthalpy and the specific binding energy respectively, ϵ is the internal energy density, u is the radial velocity in the local Lorentz frame. Equation (2.23) is the relativistic generalization of Bernoulli's equation. The conservation of mass and entropy along the flow line implies that

$$\dot{\mathcal{M}} = (\frac{a^2}{1 - na^2})^n u u_t r^2. \tag{2.24}$$

(Here $\dot{\mathcal{M}}$ has the same interpretation as in the Newtonian case.) By differentiating the above two equations with respect to r and eliminating $\frac{da}{dr}$ one obtains,

$$\frac{du}{dr} = \frac{u(1-u^2)[1-a^2-2a^2(r-2)]}{r(r-2)(a^2-u^2)}.$$
(2.25)

The sonic point conditions are

$$u_c = a_c, \text{ i.e., } M_c = 1,$$
 (2.26a)

and

$$r_c = \frac{3}{2} + \frac{1}{2a_c^2}. (2.26b)$$

When a_c is as large as the velocity of light (such as when $p = \epsilon$ equation of state is chosen) the sonic point lies just on the horizon, independent of any other properties of the flow.

Although it is easy to study the adiabatic Bondi accretion with full general relativity, a rigorous study with complete radiative transfer cannot be carried out. However, for most of the astrophysical purposes this is not essential either. As a prelude to some of the study of accretion disks in the next few Sections, we shall briefly mention here the study of Bondi flow using the pseudo-Newtonian potential.

2.2.2 In pseudo-Newtonian Geometry

In the pseudo-Newtonian geometry, the conserved energy is expressed as

$$\mathcal{E} = \frac{1}{2}u^2 + na^2 - \frac{1}{r-2} = na_{\infty}^2$$
 (2.27)

and the mass flux as,

$$\dot{M} = \rho u r^2. \tag{2.28}$$

From these, the velocity gradient at any point of the flow becomes,

$$\frac{du}{dr} = \frac{\frac{1}{(r-2)^2} - \frac{2a^2}{r}}{\frac{a^2}{u} - u} = \frac{N}{D}.$$
 (2.29)

The sonic point conditions are derived as,

$$u_c = a_c, \text{ i.e., } M_c = 1,$$
 (2.30a)

and

$$r_c = 2 + \frac{1}{4a_c^2} + \sqrt{\frac{1}{a_c^2} + \frac{1}{16a_c^4}}.$$
 (2.30b)

Note that this being a Newtonian treatment, a_c is allowed to become infinity, so that the sonic point stays at the 'horizon', namely, at r=2 in the same way as in the Schwarzschild geometry. Other properties remain similar to the original Bondi solution in the Newtonian geometry.

2.3 Bondi Flow with Simple Radiative Transfer

As matter accretes onto a hole, radiations emitted would have to escape through the matter itself, and therefore will interact with the incoming matter. To see the 'zeroth' order effect of the radiation on matter, consider a spherical accretion in which the luminosity at any radial distance r is assumed to be a constant fraction of the Eddington luminosity, i.e., $L_{\gamma}(r) = CL_{Edd}$. Since the radiation force is opposite to gravity, the net force on the accreting matter due to the gravity and the radiation will be given by,

$$F_{net} = -\frac{1}{r^2} + \frac{C}{r^2} = -\frac{1-C}{r^2}. (2.31)$$

Thus the effective potential is given by,

$$\Phi_{net} = -\frac{1-C}{r}. (2.32)$$

Using this potential instead of $-\frac{1}{r}$ in equation (2.5) one can repeat the analysis. The location of the critical point is found to lie closer to the black hole, as, $r_c = \frac{1-C}{2a_c^2}$ in this case. However, the sound speed at the critical point (a_c) does not change. Clearly, a stationary transonic solution is not possible when C > 1, i.e., when the luminosity is super-Eddington [77]. The properties of the solution remain otherwise similar to what was discussed in the previous Section.

2.4 Bondi Flow with General Radiative Transfer

Observations of extremely large energy output from active galactic nuclei and quasars suggests that the radiation efficiency η has to be of the order of a few percent of the rest mass. Much of the research in accretion physics is focussed to find out this efficiency of the conversion of the rest mass to the radiated energy (eq. 2.1). The efficiency is a function of the accretion rate (opacity) and the heating and cooling mechanisms in the flow. Over the past two decades, several efforts have been made to

estimate this quantity as accurately as possible. First, we present a brief overview of the major developments in this topic. In the Bondi accretion solution presented above, the properties of a spherical adiabatic accretion is studied. In principle, energy is conserved in this case and no radiation is emitted from this flow, i.e., entropy is also advected. Several works have been reported in the literature which study spherical accretion self-consistently adding more physical processes, such as various heating and cooling mechanisms, pair productions, pre-heating of incoming gas, etc. Since the luminosity and efficiency of the emission of the gas accreted from an interstellar medium cannot be high, Shvartsman [84] suggested that the presence of magnetic field could increase the efficiency of radiation. Subsequently, magnetic field dissipation was introduced in the computation and efficiency was increased [85-86]. Earlier attempts to solve optically thick flows in general relativistic framework using radiative transfer showed divergent behaviour [87-88], till it was realized that the luminosity of the flow as seen from infinity is also an eigenvalue of the problem [89, 90]. High accretion rate solution of the general relativistic models do not seem to have significantly higher efficiency [91]. Soffel [92] found most of the the low luminosity (low temperature, effectively optically thick) solutions connecting some of the earlier solutions. In these works, Comptonization was not taken into account and the solutions were steady. Ostriker et al. [93] pointed out that the pre-heating, i.e., heating of the far away gas through Compton scattering of the radiation emitted close to the black hole could stop the flow and possibly make it unstable.

Comptonization of the flow was studied in greater detail by several authors including Maraschi, Roasio & Treves [94], Colpi, Maraschi & Treves [95] and Wandel, Yahil & Milgrom [96] (hereafter, referred to as MRT, CMT and WYM respectively). These results show that higher luminosity and higher efficiency solutions are indeed possible when accretion rate is not necessarily very high. MRT considered magnetic dissipation and therefore obtained very high luminosity. CMT studied two temperature models without the magnetic dissipation and WMY self-consistently studied the emitted radiation (by balancing Compton heating with bremsstrahlung cooling) in a non-relativistic freely falling gas. They ignored the pre-heating of the gas. WMY also found a new high luminosity solution branch in the optically thick flows.

Park [97] and Nobili, Turolla & Zampieri [98] (hereafter NTZ) studied the self-consistent solutions with pre-heating included and within a single self-consistent framework verified the presence of both the high and low luminosity branches. Park & Ostriker [99] include the effects of pair production and pre-heating and were able to locate yet another branch of solutions when the pair density is very high.

In general, the efficiencies of the spherical solutions were not found to be sufficiently high to explain the observed luminosity from active galaxies. Secondly, they cannot reproduce the observed bump in the ultraviolet in the continuum. However, it is a kind of 'paradigm' problem and should be studied in greater detail so that these may be subsequently generalized to more realistic flows, namely, flows with some angular

momentum. Below, we discuss some of the spherically symmetric models in greater detail.

2.4.1 Single Temperature Solutions

Earliest solutions of this kind which include cooling due to bremsstrahlung are due to Shapiro [85-86]. Apart from the continuity equation and the radial momentum equation (as we discussed earlier), in the presence of heating and cooling one must include the energy equation which is obtained from the thermodynamic identity,

$$v(\frac{de}{dx} - \frac{e+P}{n}[\frac{dn}{dx}]) = \Lambda - \Gamma, \qquad (2.33)$$

where, x is the non-dimensional radial coordinate, v, n, e, P are the velocity, number density of protons, proper internal energy density and isotropic pressure respectively, and Λ and Γ are the combined cooling and the heating effects respectively. Here, the decrease in entropy of the in-flowing gas is equated with the energy lost through the cooling effects (Λ) minus the energy generated (Γ). The above equation replaces the adiabatic equation of state used earlier.

As a first approximation, the electron and proton temperatures are assumed to be the same, although in reality, when cooling of electrons are efficient, the temperature of electrons would be a few orders of magnitude lower (T_p close to its virial value $m_p c^2/kr$, and $T_e \sim m_e c^2/kr$, see below). It is possible that the collective plasma processes, which can be present when magnetic field is significant, could couple electrons and protons more strongly than Coulomb coupling [100]. In this case, the electron and proton temperatures can become the same.

In the simplest of solutions one can assume no heating other than that due to compression ($\Gamma = 0$) and the cooling is only due to bremsstrahlung. Since bremsstrahlung cross-section is low, the efficiency of radiation turned out to be very small: $\eta \sim 10^{-10}$ for a $1M_{\odot}$ black hole accreting from H I region with gas number density $n_{\infty} = 1 \text{cm}^{-3}$ [85]. This situation is appropriate for a black hole immersed inside an interstellar medium. Overall efficiency η varies with number density and the mass of the black hole as: $\eta \propto n_{\infty}M$. The luminosity varies as $L \propto n_{\infty}^2M^3$. Hence, one could imagine that raising the accretion rate, luminosity and efficiency could be enhanced. However, higher density increases the optical depth and therefore the accurate inclusion of the interaction of radiation with matter becomes necessary. Furthermore, at high optical depth radiation is trapped at some distance, reducing the efficiency. This happens at the so called 'trapping radius' r_{trap} when the accretion flow advects photons inwards before they could diffuse outwards [2], i.e., $\tau_T > 1/v_r$. The radial velocity and the in-fall time scale varies as $v_r = r^{-1/2}$ and $t_{infall} = r/v_r = r^{3/2}$. From the mass conservation, the density varies as $\rho \sim \frac{\dot{M}}{r}^{-3/2}$. The optical depth due to Thomson scattering at radius r is $\tau_T \sim \dot{M} r^{-1/2}$ giving rise to $r_{trap} \sim \dot{M}$. Thus higher radiation obtained by increasing accretion rate would be advected towards the black hole.

In the presence of a radial magnetic field, cooling due to synchrotron radiation from the thermal electrons go up. Assuming that well ordered radial field should always be close to the equipartition value, $(P_{field} \sim P_{gas} \propto r^{-5/2})$ at regions close to a black hole one can obtain the variation of the magnetic field component as [84]:

$$B = \dot{M}^{1/2} G M^{1/4} r^{-5/4} \text{Gauss.}$$
 (2.34)

Inclusion of synchrotron cooling using this field variation increases the efficiency very much. Furthermore, the frequency at which the luminosity was highest in case of bremsstrahlung alone, is shifted to the thermal synchrotron frequency [86],

$$\nu_s = \frac{3}{4} \frac{eB}{\pi m_e c} (\frac{kT}{m_e c^2})^2, \tag{2.35}$$

where, m_e is the mass of the electron and k is the Boltzman constant.

The magnetic field considered so far is ordered, which is less likely. In order to keep the equipartition with the gas pressure, the fields may develop chaotic components and would render the flow turbulent in small scales. The turbulent dissipation would convert parts of the gravitational energy of the accreted matter to heat the flow at a rate [101],

$$\Gamma = \frac{1}{8\pi} \frac{GM\dot{M}}{r^4}.$$
 (2.36)

This variation is obtained by the consideration that the turbulent energy between r and r/2 be dissipated in one free fall time. Inclusion [94, 102, 103] of this heating increases the efficiency of the emission to about $\eta \sim 0.1$ when the accretion rate is high $(\dot{M} > 10^{-4} \dot{M}_{Edd})$. These latter models include Comptonization of the photons. Below, for the sake of completeness, we devote a few sentences to describe this important process.

Comptonization is the problem of energy exchange in the scattering of photons off the electrons. As the accretion rate is increased and the Thomson opacity,

$$\tau_T = \int_{r_i}^{\infty} \sigma_T n_e dr \tag{2.37}$$

approaches unity, the escaping photons gain energy due to repeated scattering with the hot electrons. For a thermal non-relativistic electron distribution with a temperature T_e , the average energy exchange per scattering is given by [104], $(h\nu, kT_e \ll m_e c^2)$,

$$\frac{\langle \Delta \nu \rangle}{\nu} = \frac{4kT_e - h\nu}{m_e c^2}.$$
 (2.38)

When $h\nu \ll kT_e$, photons gain energy due to the Doppler effect and when $h\nu \gg kT_e$, photons lose energy because of the recoil effect. As the radiation passes through the medium, the probability of repeated scattering by the same photon decreases exponentially although the corresponding gain in energy is exponentially higher. A balance of these two factors yields a power law distribution of the energy density:

$$F_{\nu} \propto \nu^{-\alpha} \tag{2.39}$$

In the limit of the high energies $(h\nu \gg kT_e)$ the exponential hard tail is formed as result of the recoil effect (the photons are unable to gain more energy than what the electrons actually have: $h\nu \propto kT_e$). The limit can also be set by ν^+ , the cyclotron self-absorption frequency [105] (the frequency at which the plasma becomes transparent to cyclo-synchrotron emission). The index α , which varies between 1 to 0.5 for an wide range of accretion rates $\dot{M}=(1 \text{ to } 10^{-2}M_{Edd})$ is obtained analytically in the non-relativistic limit [106] as,

$$\alpha = \left[\frac{9}{4} + \frac{\pi^2}{3(\tau_T + \frac{2}{3})^2\Theta}\right]^{1/2} - \frac{3}{2}$$
 (2.40a)

and numerically [107] in the relativistic limit as,

$$\alpha = -\ln A/\ln[1 + 4\Theta + 16\Theta^2] \tag{2.40b}$$

where,

$$A = \frac{3}{4}\tau_T \quad \text{for} \quad \tau_T < 1$$

and

$$A = \left(1 - \frac{3}{4\tau_T}\right) \quad \text{for} \quad \tau_T > 1.$$

and $\Theta = \frac{kT_e}{m_e c^2}$ with T_e as the electron temperature. The efficiency of radiation increases to about $\eta \sim 10^{-2}$ in this case.

It has been recently shown that the power laws are the exact solutions of the radiative transfer kinetic equations taking into account the Doppler effect only [108]. Accurate spectral indices are derived for an wide range of the optical depths and electron temperatures of the plasma cloud as follows:

$$\alpha = \frac{\beta}{\ln[1 + (\alpha + 3)\Theta/(1 + \Theta) + 4d_0^{1/\alpha}\Theta^2]}$$
 (2.40c)

where,

$$d_0(\alpha) = \frac{3[(\alpha+3)\alpha+4]\Gamma(2\alpha+2)}{(\alpha+3)(\alpha+2)^2}$$

and $\Theta = kT_e/m_ec^2$ which represents the appropriately weighted average of the electron temperature in the plasma cloud. Here, β is obtained from the eigenvalue $\zeta = exp(-\beta)$ of the corresponding eigenfunction for the appropriate radiative transfer problem. Assuming plasma geometry to be disk-like, for optical depths $\tau_0 > 0.1$,

$$\beta = \frac{\pi^2}{12(\tau_0 + 2/3)^2} (1 - e^{-1.35\tau_0}) + 0.45e^{-3.7\tau_0} \ln \frac{10}{3\tau_0}$$

and for very low optical depth ($\tau_0 < 0.1$),

$$\beta = \ln \left[\frac{1}{\tau_0 \ln(1/2\tau_0)} \right].$$

If on the other hand, the plasma has a spherical geometry, then for optical depths $(\tau_0 > 0.1)$,

$$\beta = \frac{\pi^2}{3(\tau_0 + 2/3)^2} (1 - e^{-0.7\tau_0}) + e^{-1.4\tau_0} \ln \frac{4}{3\tau_0}$$

and for very low optical depth ($\tau_0 < 0.1$)

$$\beta = \ln \frac{4}{3\tau_0}.$$

2.4.2 Two Temperature Solutions

In the case when ion-electron collision time is larger than the free-fall time, protons and electrons can be thermally decoupled and therefore one has to consider the equations for ions and electrons separately. It is important to determine the electron temperature very accurately because the emitted radiation depends on it. Protons will behave roughly adiabatically and the temperature reached by the protons (in adiabatic accretion) could reach the threshold for π^0 production so that the black hole could become a γ -ray source due to pion decay. The pion production rate and therefore the gamma ray luminosity depends strongly upon the proton temperature [95].

Since the proton temperature is higher than the electron temperature, energy can be lost by protons and gained by electrons due to the collisional energy exchange term. Electrons can lose energy due to thermal bremsstrahlung, cyclo-synchrotron radiation and Comptonization. We present here a typical analysis which includes these processes. Following CMT, we assume the length scale in the following discussion to be in units of $r_g = 2GM/c^2$. The zero energy gas, cooler at a large distance, yields a velocity (without relativistic corrections),

$$v(x) \sim x^{-1/2}$$
. (2.41)

The mass conservation law gives the number density of hydrogen as,

$$n(x) \sim x^{-3/2} \dot{M} M^{-2} \text{ cm}^{-3}.$$
 (2.42)

The optical depth for Thomson scattering,

$$\tau_T(x) \sim 1.44x^{-1/2} \dot{M}_{18} M_1^{-1}.$$
 (2.43)

The magnetic flux is assumed to be radial (monopole like). The flux conservation requires that the field varies as $B \propto x^{-2}$. With the assumption of the equipartition between the magnetic energy density and the gravitational energy density gives the field variation as:

$$B(x) = \left(\frac{8\pi m_p nGM}{3r_q}\right)^{1/2} x^{-2} \quad \text{Gauss} = 4.75 \times 10^7 \dot{M}_{18}^{1/2} M_1^{-1} x^{-2} \quad \text{Gauss}.$$
 (2.44)

Here, M_1 is the mass of the central black hole in units of $10M_{\odot}$, and \dot{M}_{18} is the mass accretion rate in units of $10^{18} \mathrm{gm \ s^{-1}}$. Maxwellian distribution is established through Coulomb collisions between electrons and protons in time [109]:

$$t_{ee} = \frac{C}{nln\Lambda_0} m_e^2 (\frac{T_e}{m_e})^{3/2}$$
 s, (2.45)

$$t_{pp} = \frac{C}{n l n \Lambda_0} m_p^2 (\frac{T_p}{m_p})^{3/2}$$
 s, (2.46)

where Λ_0 is usual Coulomb logarithm, T_e and T_p are the electron and proton temperatures and C is a constant,

$$C = \frac{3k}{4(2\pi)^{1/2}e^4}. (2.47)$$

Protons and electrons will reach the thermal equilibrium in

$$t_{ep} = \frac{C}{2nln\Lambda_0} m_e m_p (\frac{T_e}{m_e} + \frac{T_p}{m_p})^{3/2} \text{ s.}$$
 (2.48)

Close to a black hole, protons reach the virial temperature $T \sim \frac{GMm_p}{rk}$ of 10^{12}K and the electrons reach a temperature of 10^9K ($\frac{T_e}{m_e} \approx \frac{T_p}{m_p}$). With these parameters, it is interesting to compare different time scales [95],

$$t_{ee} = 2.4 \times 10^{-5} \dot{M}_{18} M_{10}^{-2} x^{3/2} (T_e/10^9)^{3/2} (ln\Lambda_0)^{-1} \text{ s},$$
 (2.49)

$$t_{ep} = \frac{m_p}{m_e} t_{ee}, \tag{2.50}$$

$$t_{pp} = \frac{m_p^2}{m_e^2} t_{ee}, (2.51)$$

with the free fall time scale

$$t_{ff} = 10^{-4} M_{10} x^{3/2} \text{s.} (2.52)$$

For optical depth near unity, a Maxwellian description is justified for the electrons, but t_{ep} and t_{pp} are both larger than t_{ff} so that for the protons, the Maxwellian distribution may break down.

The equation for energy (eq. 2.33) is written down separately for protons and electrons. Assuming v(x) and n(x) as above appropriate for a Bondi flow (thus ignoring the effect of radiation on the distribution of velocity and density) and from the definition of the internal energy $e = P/(\gamma - 1)$ it is easy to write down the equations as [84, 86, 95, 101]:

$$\frac{dT_p}{dx} + \frac{T_p}{x} + \frac{8m_p r_g^3 \pi x^2 (\Gamma_p - \Lambda_p)}{3k\dot{M}} = 0$$
 (2.53)

and

$$\frac{dT_e}{dx} + \frac{3}{2}(\gamma - 1)\frac{T_e}{x} + \frac{4m_p r_g^3 \pi (\gamma - 1)x^2 (\Gamma_e - \Lambda_e)}{k\dot{M}} = 0$$
 (2.54)

Here, $\gamma = 5/3$ is the adiabatic index for non-relativistic temperatures $(T_e \leq \frac{m_e c^2}{k})$ and $\gamma = 4/3$ for relativistic regime. The quantities $\Gamma_{p,e}$ and $\Lambda_{p,e}$ in above equations represent energy gains and energy losses due to various processes. If one neglects heating due to dissipation for protons, $\Gamma_p = 0$. The proton equation consists of two loss terms:

$$\Lambda_p = \Gamma_{ep} + \Lambda_{ib} \tag{2.55}$$

where,

$$\Gamma_{ep} = \frac{3}{2} \frac{nk(T_p - T_e)}{t_{ep}} \text{ erg cm}^{-3} \text{ s}^{-1}$$
(2.56)

is the energy transfer rate from the protons to the electrons, and

$$\Lambda_{ib} = 1.4 \times 10^{-27} n^2 \left(\frac{m_e}{m_p} T_p\right)^{1/2} \tag{2.57}$$

is the radiative energy loss for protons due to inverse bremsstrahlung.

In the electron equations $\Gamma_e = \Gamma_{ep}$ can be taken as the energy gain, and the cooling term

$$\Lambda_e = \Lambda_b + \Lambda_{cs} + \Lambda_{mc} \tag{2.58}$$

contains contribution from the the bremsstrahlung, cyclo-synchrotron and multiple-Compton scattering of the cyclo-synchrotron photons by the thermal electrons which are in units of erg cm⁻³ s⁻¹:

$$\Lambda_b = 1.4 \times 10^{-27} n^2 T^{1/2} (1 + 4.4 \times 10^{-10} T), \tag{2.59}$$

$$\Lambda_{cs} = \frac{\pi k T_e}{GM} \frac{\nu^3}{x},\tag{2.60}$$

and

$$\Lambda_{mc} = \Lambda_{cs} \left[\frac{\alpha}{\alpha - 1} \frac{(\nu_{max}/\nu^{+})^{1-\alpha} - 1}{(\nu_{max}/\nu^{+})^{-\alpha} - 1} - 1 \right], \tag{2.61}$$

where, the expression for α is as given above 2.40(a-c) and ν^+ is the synchrotron self-absorption frequency [105].

Figures 2.4(a-c) show variations of temperature of electrons and protons as functions of logarithmic radial distance from the black hole. This cases are computed for (a) $\dot{M}=10^{16}~{\rm gm~s^{-1}}$, (b-c) $\dot{M}=10^{18}~{\rm gm~s^{-1}}$ and the black hole mass is $10M_{\odot}$. The difference between (b) and (c) is that in (c), the electron-proton coupling term is artificially multiplied by a factor 20 to show the effect of strong cooling. The outer boundary is chosen at $x=10^6$, with the electron and proton temperatures same as in adiabatic ($\gamma=5/3$) Bondi solution:

$$T_e|_{out} = T_p|_{out} = T_{ad} = \frac{3}{20} \frac{m_p c^2}{k} \frac{1}{x}.$$
 (2.62)

In Fig. 2.4(a), temperatures behave as in an adiabatic solution initially, but close to the black hole, radiative losses of the electrons become so important that energy gained

through the compression of the gas as well as that obtained from protons through collisions are radiated away. Even closer to the black hole the loss is further increased due to Comptonization. In Fig. 2.4(b) the optical depth is higher and the bremsstrahlung loss reduces the overall temperature. In Fig. 2.4(c), due to the enhanced exchange of energy, protons lose more energy to electrons which lowers their temperature substantially reaching a maximum $T \ll 10^{11}$ K.

In Fig. 2.5(a-d) the spectrum of radiation emitted from electrons is shown. The spectrum has a maximum at around ν^+ , the synchrotron self-absorption frequency. At higher frequencies, the spectrum is dominated by Comptonization and is a sum of power law in frequency range from ν^+ to $3\kappa T/h$. In Figs. 2.5(a-b) the accretion rates are chosen to be 10^{16} gm s⁻¹ and 10^{18} gm s⁻¹ respectively on a black hole of mass $10 M_{\odot}$. In Figs. 2.5(c-d) the accretion rates are chosen to be 10^{23} gm s⁻¹ and 10^{25} gm s⁻¹ respectively on a black hole of mass $10^8 M_{\odot}$.

It is observed that at a fixed optical depth, the results depend very weakly on the mass of the black hole. The efficiency of the conversion of the rest mass energy to the outgoing luminosity radiated by electrons seems to be very low: $\eta \sim 0.005-0.01$. This is higher than one-temperature solutions [85-86] which neglected cooling due to Comptonization. Inclusion of dissipative heating increases the efficiency by a factor of ~ 10 [94, 101, 103], although the dissipation of fields considered is possibly an upper estimate.

The luminosity of γ rays which are produced from the pion decay is computed from [95]:

$$p + p \to p + p + \pi_0(\to 2\gamma). \tag{2.63a}$$

This pion production rate per unit volume

$$R = \frac{1}{2}n^2 \langle \sigma v_{th} \rangle \tag{2.63b}$$

(where σ is the p-p cross section for π_0 production and v_{th} is the proton thermal velocity and <> denotes average taken over the Maxwellian distribution) strongly depends on temperature [110] and therefore strongly depends on the optical depth. The inset of Figure 2.5a provides the luminosity due to gamma rays. As the accretion is increased, till the optical depth τ_T (Thomson optical depth at $r_g = 1$) reaches a value of 0.3, the luminosity due to γ rays goes as $L_{\gamma} \approx \dot{M}^2$ and with the increase of τ_T , L_{γ} decreases again. Figure 2.6 gives the the variation of L_{γ} with the accretion rate, which shows the maximum at around $\tau_T \simeq 0.3$.

2.4.3 General Relativistic Optically Thick Bondi Flow

In the adiabatic Bondi flow model (§§2.1-2.2) no outflow of energy or entropy was

allowed. The inclusion of photon diffusion effects changes the flow behaviour qualitatively. The solutions corresponding to this situation is described below [89-90].

Basic equations governing the optically thick Bondi flow are the generalization of the equations in a black hole geometry presented in §2.2. However, because of the loss of radiation, the specific energy and entropy do not remain conserved within the flow and one has to keep the momentum and the entropy equations in the differential form. The continuity equation, the radial momentum conservation equation, the Bernoulli's equation, and the diffusion equation of photons respectively take the forms:

$$r^2 \rho u u_t = \dot{M} = \text{constant},$$
 (2.64a)

$$\frac{1}{u_t}\frac{du_t}{dr} = -\frac{1}{p+\epsilon}\frac{dp}{dr},\tag{2.64b}$$

$$hu_t \dot{M} - \hat{L} = \dot{E} = \text{constant},$$
 (2.64c)

$$\hat{L} = -r^2 u_t^3 (1 + u^2) \frac{4p_r}{\rho \kappa_1} \left[\frac{1}{T} \frac{dT}{dr} + \frac{1}{u_t} \frac{du_t}{dr} \right]. \tag{2.64d}$$

Here κ_1 is the first-moment opacity [83, 89, 90]. In the case when Thomson scattering opacity is dominant, $\kappa_1 = \frac{\sigma_T}{m_p \mu_e}$; σ_T , m_p and μ_e being the Thomson scattering cross-section, the mass of a proton and the mean molecular weight per electron respectively. Also, \hat{L} is related to the diffusive luminosity L by,

$$\hat{L} = (1 + u^2)u_t^2 L. (2.65)$$

The quantity \dot{E} represents the net rate of the mass-energy accretion, allowing for the effects of the 'PdV' work and the heat transfer. Because of the presence of the 'extra' unknown over and above what was discussed in §2.2, one has to supply two unknowns, say, \dot{E} and \dot{M} to describe the flow completely.

Unlike the results for adiabatic solutions in §2.2, one now has the basic equations in differential form and the complete solution is impossible analytically. However, the trend of the solution is easily obtained by expansion of the equations around the critical point. After differentiating above equations, one can cast them in the form of eq. (2.25), and therefore similar logic holds in finding critical point conditions. Since we need to supply only two unknowns, only two of the differential equations are truly independent. Flammang chooses the velocity and the luminosity equations. The solution is a trajectory in the three-dimensional space spanned by (r, u, \hat{L}) instead of just (r, M) plane as in the adiabatic case (Fig. 2.1ab). The critical points are found to lie on the critical curve formed by the intersection of the three surfaces:

$$u = a_t, (2.66a)$$

$$\mathcal{L} = \frac{1 - a_t^2}{1 - u^2} \frac{1}{ru_t^2} - 2a_t^2, \tag{2.66b}$$

and

$$\mathcal{L} = \frac{a_s^2 - a_t^2}{a_s^2 - u^2} C. \tag{2.66c}$$

where,

$$C = \frac{1}{ru_t^2} - 2u^2, (2.67a)$$

$$\mathcal{L} \equiv \frac{b}{1 - b} \frac{\rho}{4p_r} \frac{\kappa_1}{r} \frac{\hat{L}}{u_t^3 (1 + u^2)} = -\frac{b}{1 - b} \frac{r}{Tu_t} \frac{d(Tu_t)}{dr}, \tag{2.67b}$$

$$a_t^2 = (\frac{a}{1-b}), (2.67c)$$

is the isothermal sound speed squared, and

$$a_s^2 = qb + a, (2.67d)$$

is the adiabatic sound speed squared, with

$$a \equiv \frac{\rho}{p+\epsilon} (\frac{\partial p}{\partial \rho})_T, \tag{2.67e}$$

$$b \equiv \frac{T}{p+\epsilon} (\frac{\partial p}{\partial T})_{\rho}, \tag{2.67f}$$

$$q \equiv (\frac{\partial p}{\partial \epsilon})_{\rho}, \tag{2.67g}$$

On the critical curve $\mathcal{L} = C$, there are two branches of the solution and one is good for the accretion and the other for the wind. Note that unlike the adiabatic case, the critical point occurs when the in-fall velocity equals the isothermal sound speed a_t , rather than the adiabatic sound speed a_s . The sonic point, which Flammang calls the sub-critical point lies where $u = a_s$ [77, 89, 90] and the physically significant solution must pass through this point. A simple observation from eq. (2.66c) is as follows: since in a black hole accretion, velocity runs from zero at infinity to unity at the horizon, at some point of the flow, one must have $u = a_s$. Clearly, from eq. (2.66c), at the sonic point, C must vanish to avoid any catastrophic enhancement of luminosity at that point $(\hat{L} = \hat{L}_s)$. It is easy to show that C = 0 at $u = a_s$ always.

To understand the trend of the solution, for example, the variation of the luminosity function as a function of the radial distance, one notices from the combination of eqs. 2.64(c-d) that the luminosity \hat{L} may have an exponential behaviour with the rate:

$$k = -\frac{u^2 - a_s^2}{u^2 - a_t^2} \frac{h u_t \dot{M}}{q r} \frac{\mathcal{L}}{\hat{L}}.$$
 (2.68)

In other words,

$$\frac{d\hat{L}}{dr} = k(\hat{L} - \hat{L}_s). \tag{2.69}$$

One can choose a new variable τ along the integral curve such that,

$$d\tau = k \, dr. \tag{2.70}$$

Hence eq. (2.69) becomes

$$\hat{L}(\tau) - \frac{d}{d\tau}\hat{L}(\tau) = \hat{L}_s(\tau), \tag{2.71}$$

which is integrated along the integral curve to yield:

$$\hat{L}(\tau) = \hat{L}(\tau_0) \exp(\tau - \tau_0) + \int_{\tau}^{\tau_0} \hat{L}_s(\tau') \exp(\tau - \tau') d\tau'.$$
 (2.72)

Since one is interested only in the integral curve which has finite luminosity as $\tau_0 \to \infty$, one must have for such solution,

$$\hat{L}(\tau) = \int_{\tau}^{\infty} \hat{L}_s(\tau') exp(\tau - \tau') d\tau'. \tag{2.73}$$

Expanding $\hat{L}_s(\tau')$ around τ one obtains

$$\hat{L}(\tau) = \sum_{n=0}^{\infty} \left(\frac{d}{d\tau}\right)^n \hat{L}_s(\tau), \tag{2.74}$$

or,

$$\hat{L}(r) = \sum_{n=0}^{\infty} (\frac{1}{r} \frac{d}{dr})^n \hat{L}_s(r).$$
 (2.75)

k itself could be written in a more useful form by using eqs. (2.64a), (2.67b) and (2.68):

$$k = -\frac{u}{\xi} \frac{(u^2 - a_s^2)}{(u^2 - a_t^2)} \frac{a_t^2}{a_s^2} \frac{1}{u_t (1 + u^2)}.$$
 (2.76)

where ξ is the thermal diffusivity given by,

$$\xi = \lambda_{\gamma} \frac{4p_r}{\rho} \frac{A}{b} \frac{q}{h} \frac{a_t^2}{v_s^2},\tag{2.77}$$

where

$$\lambda_{\gamma} = \frac{1}{\rho \kappa_1},\tag{2.78a}$$

is the photon diffusion length, and

$$A \equiv \frac{\rho}{p+\epsilon} (\frac{\partial \epsilon}{\partial \rho})_T. \tag{2.78b}$$

The important point to note is that k changes sign at the sonic point $u = a_s$ by passing through a zero and at the critical point $u = u_c$ by passing through a pole. The resultant solution is shown in Figure 2.7 (from [77]). The solution of \hat{L}_s obtained from eq. (2.75) blows off at $u = a_s$, as k = 0 at that point. A typical solution which satisfies the condition that it should pass through the point $u = a_s$ when C = 0, should look like the dashed curve which asymptotically merges with the \hat{L}_s curves. Figure 2.8 shows a

complete solution [89]. Cross marks are the critical points and open circle marks are the sonic points. Parameters chosen in CGS units are $M = 3M_{\odot}$, $\dot{M} = 2.954 \times 10^{-5} M_{\odot} yr^{-1}$, $\hat{L}_{\infty} = 9.795 \times 10^4 L_{\odot}$, $\hat{L}_{s,\infty} = 9.795 \times 10^4 L_{\odot}$, $\rho_{\infty} = 1.878 \times 10^{-9} g \ cm^{-3}$, $T_{\infty} = 4.313 \times 10^5 K$, $a_{s,\infty} = 8.303 \times 10^{-3} \times c$, $a_{c,\infty} = 2.814 \times 10^{-4} \times c$, $[p_{gas}/p_{rad}]_{\infty} = 1.532 \times 10^{-3}$.

2.4.4 Inclusion of Pair Production and Pre-heating

Observational results of γ -ray emission from a wide range of objects indicate that the flow reaches relativistic and semi-relativistic temperature regimes. At these temperatures, pair creation takes place via photon-photon, photon-particle and particle-particle interactions. The pairs in turn participate in other photon and pair producing processes or just annihilate into photons. Recent theoretical and observational works suggest that AGNs and quasar spectra (close to $\sim 1 MeV$) may be better explained with pair production taken into account [111]. A large number of works are present in the literature where pair production effects are considered in a flow whose dynamical and thermodynamical properties are provided a priori and are not self-consistently determined [112-114]. Detailed procedure to solve for the equilibrium pair density in thermal plasma is beyond the scope of this review and the readers are recommended to consult works referred above.

Some self-consistent models have been recently constructed where the generated radiation reacts back on the flow and controls its dynamic and thermodynamic properties. We describe below one such model, which claims to be self-consistent [99]. These solutions in spherical geometry are obtained in the range $3 \le \dot{m} \le 40 \dot{M}_{Edd}$. Pair production by all the three major processes, namely, photon-photon, photon-particle, and particle-particle interactions as well as the pair annihilation are considered. As a specific example, a flow with 90% hydrogen and 10% helium by number is considered and is assumed to be fully ionized. Electron temperatures are assumed to be different from ion temperatures ($T_i \ne T_e$).

Hydrodynamic equations which the ions and electrons satisfy are [99]:

$$\frac{de_i}{dx} - \frac{e_i + P_i}{n_i} \frac{dn_i}{dx} = \frac{3}{2} \frac{n_i k (T_i - T_e)}{t_{en} u}$$
 (2.79)

and

$$\frac{de_l}{dx} - \frac{e_l + P_l}{n_l} \frac{dn_l}{dx} = \frac{\Lambda - \Gamma}{u} + \frac{3}{2} \frac{n_i k (T_e - T_i)}{t_{ep} u} + \frac{2}{u} \frac{e_l + P_l}{n_l} (\dot{n}_C - \dot{n}_A), \tag{2.80}$$

where, n_i is the proper ion number density, n_+ is the positron density, n_e (=1.1 $n_i + n_+$) is the electron density, $n_l = n_e + n_+$, $P = P_i + P_l$, $P_i = n_i kT$, $P_l = n_l kT_e$, (the subscript l is to denote leptons), and t_{ep} is the electron-proton Coulomb time (eq. 2.50), $u \equiv cU_r$ is the radial velocity, $e_i = \frac{3}{2}n_i kT_i + 1.3n_i m_p c^2$, $e_l = \frac{3}{2}n_l x^* kT_e + n_l m_e c^2$, x^* is the coefficient to incorporate relativistic effects (x^* equals to 2 for ultra-relativistic case and 1 for non-relativistic case). Also, \dot{n}_C and \dot{n}_A denote the rate of creation and the annihilation of

pairs. These equations are generalizations of eq. (2.33) described above. The heating and cooling processes are the usual bremsstrahlung and thermal Comptonization [113, 115].

The radiation field is calculated from the radiative transfer equations [99, 116]:

$$\frac{1}{x^2} \frac{d}{dx} (x^2 F) = \frac{u}{c} \chi_{co} [F + u(E + P)] - (\Gamma - \Lambda), \tag{2.81}$$

$$\frac{dP}{dx} + \frac{3P - E}{x} = -\chi_{co}\frac{F}{c} - \frac{u}{c}\chi_{co}(E + P) + \frac{u}{c} + \frac{u}{c}\frac{\Gamma - \Lambda}{c},\tag{2.82}$$

and

$$f_E \equiv \frac{P_{co}}{E_{co}} = 1 - \frac{2}{3}e^{-1/x^2},$$
 (2.83)

where, $\chi \equiv n_l \sigma_{KN}$ is the Klein-Nishina electron scattering opacity, $\tau \equiv \int_x^\infty \chi_{co} dx$, and F, E P are radiation energy density, flux and pressure in fixed frames respectively (subscript co refers to quantities in co-moving frame). These relativistic radiation moment equations are correct up to an order of $(u/c)^1$.

The density of pairs is governed by the continuity equations which include specific pair creation rate and pair annihilation rate [99],

$$-\frac{1}{x^2}\frac{d}{dx}(x^2n_+u) = \dot{n}_C - \dot{n}_A. \tag{2.84}$$

Photons are assumed to follow Wien distribution $n_{\gamma}(\nu) \propto \nu^2 e^{-\frac{\hbar\nu}{kT_{\gamma}}}$. The radiation temperature T_{γ} is defined as,

$$T_{\gamma} = \frac{1}{4k} \frac{\int_0^{\infty} e_{\gamma}^2 n_{\gamma} de_{\gamma}}{\int_0^{\infty} e_{\gamma} n_{\gamma} de_{\gamma}},\tag{2.85}$$

where e_{γ} is the photon energy. The cross section (σ_{Th}) for photon-photon pair creation is chosen to be constant as T_{γ} is close or below the threshold temperature $m_e c^2/k$ and most of the pairs would be produced by photons which are just above this threshold. The pair creation rates from photon-photon process [111],

$$\dot{n}_{C,\gamma-\gamma} = \frac{3}{8} \ln 4 \, \sigma_{Th} c n_{\gamma,1}^2 \,, \quad n_{\gamma,1} \equiv \int \int_{h\nu_1 \ h\nu_2 > (m_e c^2)^2} n(\nu_1) n(\nu_2) d\nu_1 d\nu_2 \tag{2.86}$$

and lepton-photon process

$$\dot{n}_{C,pl-\gamma} = \frac{1}{3} \sigma_{Th} \ c \ \alpha_f n_l \ n_{\gamma,2} \ , \quad n_{\gamma,2} \equiv \int_{h\nu > (m_e c^2)^2/kT_e} n(\nu) d\nu, \tag{2.87}$$

and the pair annihilation rate [112],

$$\dot{n}_A = \frac{3}{8} \sigma_{Th} [1 + 2\theta_e^2 / \ln(1.12\theta_e + 1.3)]^{-1} cn_+ n_e$$
 (2.88)

where, $\theta_e \equiv \kappa T_e/m_e c^2$. All the other processes such as particle-particle interactions and proton-photon interactions are neglected. The radiation temperature $T_{\gamma}(x)$ depends upon the degree of Comptonization. Hence its change depends upon how far it is away from electron temperature at each x [99],

$$\frac{d \ln(T_{\gamma})}{d \ln x} = -\frac{T_e - T_{\gamma}}{T_e} Y_c, \tag{2.89}$$

where $Y_c \equiv 4\theta_e(\tau_{es} + \tau_{es}^2)$ is the Compton parameter.

Above equations are solved iteratively with an outer boundary condition close to free-fall flow. For a given \dot{m} , two self-consistent pair densities were found which give rise to two different models [99]. The higher pair density solution produces higher luminosity $(l = L/L_{Edd} \sim 10^{-2})$ and higher efficiency $(\eta \sim 10^{-4} - 10^{-2})$. This luminosity is higher by a factor as much as 10-100 than the lower pair density models.

Figure 2.9 compares the results of a collection of 'self-consistent' models computed during last two decades. The figure shows the accretion rate \dot{m} as a function of the resulting luminosity. These numbers are in units of Eddington rate and the Eddington luminosity respectively. The symbols are the following: crosses and 'circross'es ('cross' with a 'circle' at the center) represent respectively the low and high luminosity branches of the solution of Nobili, Turolla & Zampieri [98]. Open diamonds are the solutions by Blondin [91] while filled diamonds are the results of Wandel, Yahil & Milgrom [96]. Filled circles and open circles are the high and low pair density solutions of Park & Ostriker [99]. Filled squares and open squares are the one temperature optically thin and optically thick solutions of Park [97]. Shapiro [85] solution is shown in solid lines at the lower left. Dash-dotted line represents low temperature solution of Park [97]. Long dashed curves are the solutions of Soffel [92]. Time dependent solutions of Ostriker, McCray, Weaver & Yahil [93] and Cowie, Ostriker & Stark [117] fall within the regions I, II, and III bounded by short dashed lines. The dotted region in between two solid lines represents the parameter space with low or no pairs. Solutions by MRT [94], which include the magnetic dissipation, are of high luminosity and are shown with 'cirplus' ('plus' with a 'circle' at the center) and the solutions by CMT [95] (two-temperature models including Comptonization) are shown with 'plus' symbols.

A comparison of these results indicate that the self-consistent model with pair production may be relevant to the observed sub-Eddington luminosity close to the interesting accretion rate of $\dot{m} \sim 1$. Solutions without pair (e.g., NTZ high) produces luminosity $\sim 10^{-4}$. Although WYM produces much higher luminosity, it requires very high accretion rates to do so. The results of CMT shows very high luminosity ($l \sim 10^{-1}$), but they require efficient magnetic dissipation in the infall time scale. Rest of the steady solutions are likely to be unimportant because of low efficiency. The high luminosity time-dependent models could become important in explaining some long time scale AGN variability and require further investigations.

2.5 Shocks in Spherical Flows

It is clear from our discussion in §§2.1-2.2 that in a spherical accretion of adiabatic matter onto a black hole, a flow may have exactly one sonic point. The sonic surface is spherically symmetric. Such a flow has been proven to be stable by several workers. Using the most general form of the perturbation, in a complete general relativistic framework, Moncrief [118] has shown that: (a) a suitable energy norm of the perturbation outside the sonic surface remains bounded by its initial value, (b) no perturbation introduced inside the sonic surface extends to regions outside the sonic surface, (c) there is no unstable mode corresponding to a standing shock at the sonic surface, thus no unstable mode exists inside the sonic surface. The perturbations within the sonic surface are advected within the black hole through the horizon. No part of it is reflected back, hence it is never amplified. Therefore, a flow, subsonic at a large distance and becoming supersonic at the sonic point, cannot have a shock. If there were a shock, the post-shock flow would be subsonic and it would not have any other sonic point which would allow it to become supersonic again before disappearing into the black hole, thus violating the inner boundary condition at the horizon. However, when the flow is not adiabatic (or, when the spherical symmetry is broken, §5-§6), and locally there are sources of heating and cooling, the flow may pass through more than one sonic point and have shocks in between. Chang & Ostriker [119] have investigated this possibility. In this case, the polytropic index is not assumed to be strictly constant but a function of the radial distance, i.e.,

$$n = n(a). (2.90)$$

Following the same procedure used in deriving (2.13), one finds in this case that,

$$a_c^2[n(a) - \frac{3}{2}(1 + \frac{a_c}{2n_c}\frac{dn}{da}|_c)] = n_\infty a_\infty^2.$$
 (2.91)

Chang & Ostriker [119] concludes that if n is a decreasing function of a then there could be more than one sonic point. Particularly, if n oscillates around 3/2, there could be more than one sonic points in the flow and thus shock formation would be possible. Since for a perfect monatomic gas n > 3/2 corresponds to cooling of the flow and n < 3/2 corresponds to heating of the flow, a combination of bremsstrahlung cooling and Compton heating allowed them to construct quite a few self-consistent cases where spherical shocks may form.

In their quest to obtain the highest possible luminosity for a given accretion rate, Chang & Ostriker [119] concentrated their search in the region of parameter space where the previous attempts [117] did not find any stationary solutions. The reason for not obtaining stationary solution without a shock is that shortly after the flow passes through the sonic point, it is heated so rapidly that the adiabatic sound speed becomes higher compared to the infall velocity and the flow becomes subsonic. It remained so

in the post-shock region and the inner boundary condition on the black hole horizon could not be satisfied. A choice of a different cooling curve as used by Stellingwerf & Buff [120] allowed them to obtain stationary solutions which do not have standing shock waves.

Figure 2.10 shows the region of the parameter space where Chang & Ostriker [119] find solutions of stationary spherical accretion which contained shock waves (shown by open circles). In these solutions, shortly after the flow passes through the isothermal sonic point, the gas is heated and becomes subsonic. Subsequently, as the temperature approaches T_{γ} , the radiation temperature (chosen here to be 10⁸K), the Compton cooling becomes more important and the flow passes through another sonic point. Also presented in the figure are the self-consistent shock solutions of Babul, Ostriker and Mészáros [121] where the effects of pair processes are included as well. Initial conditions are chosen from the spherically symmetric solutions of Park [97]. (Kazanas and Ellison [122] also studied shocks which are supported by ion pressures.) It is observed that the luminosities of the order 10^{-1} times the Eddington luminosity could be obtained. The results seem to show very weak dependence on the exact form of the velocity profile in the shocked region of the disk. The region where high-pair density with shocks is achieved is shown in horizontal dashed lines and the region where very low or no pair density is achieved is shown in slant dashed lines. Figures 2.11(a-d), show variations of (a) velocity, (b) temperature, (c) density and (d) Mach Numbers in a specific case, clearly showing the formation of a standing shock at few $\times 10^6 r_g$. The computation is done for a $1M_{\odot}$ black hole. The luminosity (in units of Eddington luminosity) is 0.01 and the efficiency $\eta = 0.003$. The dashed curve in 2.11(a) denotes the free-fall velocity and the dashed curve in 2.11(b) denotes the virial temperature.

Results of spherical flows which include shock waves indicate that for efficient conversion of the energy, the disk accretion may not be absolutely essential. In reality, of course, the matter would always have some angular momentum, albeit very low. The angular momentum supported shocks are located much closer to the black hole (typically, at tens of Schwarzschild radius). It would therefore be useful to carry out these analysis for the more realistic cases of low-angular momentum solutions. Some of these works will be presented in §§5-7.

2.6 Particle Acceleration at Shock Waves

2.6.1 Basic Physical Processes

Highly relativistic particles are observed in cosmic rays. It is generally believed that the shock waves could be responsible to accelerate particles and to produce non-thermal radiations. To understand the basic physical mechanisms involved in the acceleration we first assume plane parallel shock waves [123, 124]. We also assume that the flow has a weak magnetic field parallel to the flow direction. We consider only those

energetic particles whose gyroradii are larger compared to the thickness of the shock waves so that they can freely pass from the pre-shock region of the flow to the post-shock region. At the shock front, the bulk velocity is randomized and the flow becomes more turbulent and heated up. Turbulent dissipation takes place in the post-shock region. In the pre-shock region, there are turbulences in the form of Alfvén waves excited by highly energized particles which diffuse through the shock and try to escape through the pre-shock region. These waves scatter the energetic particles and bring them back in the post-shock region. Thus the same particles are scattered again and again by the turbulent wakes (from post-shock region to pre-shock region) and by the Alfvén waves (from pre-shock region to post-shock region) and their energies are enhanced every time such crossing takes place [123, 124].

A cartoon picture of the shock wave is drawn in Fig. 2.12. Mean velocities of the scattering centers in the pre-shock and post-shock regions of the shock are u_- and u_+ respectively. All the energized particles in the pre-shock region return to the post-shock region due to scattering, but only some of these particles diffuse back to the pre-shock region. Let this probability be $(1 - \eta)$ with $\eta < 1$. η could be calculated from the diffusion equation:

$$\frac{\partial n}{\partial t} + u_{+} \frac{\partial n}{\partial x} = \frac{\partial}{\partial x} [D(x) \frac{\partial n}{\partial x}]$$
 (2.92)

where, n(x,t) is the particle density and D(x) is the diffusion co-efficient. Assuming that the mass flux is constant at the shock front as well as in the region far away down stream, the steady state solution takes the form:

$$n(x,t) = A + B \exp[\int_0^x \frac{u_+}{D(x')} dx']. \tag{2.93}$$

If the energetic particles have velocities $v >> u_+$, then the region of scattering in the post-shock region extends to infinity.

The flow of particles in the post shock region away from the shock is $u_+n(x,t)-D(x)\frac{\partial n}{\partial x}$ which is equal to the mass flux of the flow, $u_+n(0,t)$, x=0 being the location of the shock. Assuming isotropy in the velocity distribution, the rate at which particles cross the shock is $\frac{1}{4}vn(0,t)$ out of which $u_+n(0,t)$ escape into the post-shock region. In other words, $\frac{1}{4}v\eta n(0,t)=n(0,t)u_+$ and

$$\eta \sim \frac{4u_+}{v}.\tag{2.94}$$

During scattering, particle energy, as seen from the rest frame of the scattering centers remains intact. However, the velocities of the centers are different in the two regions. Every time a particle completes the cycle of scattering from pre- to post-shock regions and back, the energy is increased by a factor:

$$\frac{E_{k+1}}{E_k} = \frac{1 + v_{k1}(u_- - u_+)\cos\theta_{k1}/c^2}{1 + v_{k2}(u_- - u_+)\cos\theta_{k2}/c^2}.$$
 (2.95)

where, k denotes the number of times a particle has completed the cycle of crossing and re-crossing the shock front. Here, v_{k1} and v_{k2} denote the velocities of the scattered particles from pre- to post-shock region and vice versa and θ_{k1} and θ_{k2} denote the angles made by the particle path with the shock normal. Assuming $v_{k1} = v_{k2}$, and averaging over all the incident angles with the assumption of isotropic velocity distribution of particles, one obtains the differential energy distribution as,

$$N(E)dE = \frac{\mu - 1}{E_0} \left(\frac{E}{E_0}\right)^{-\mu} dE, \qquad (2.96)$$

where,

$$\mu = \frac{2u_+ + u_-}{u_- - u_+}. (2.97)$$

For non-relativistic particles of $\gamma = 5/3$, the compression ratio $\rho_+/\rho_- = u_-/u_+ \sim 4$, so that $\mu = 2$. A power law slope with the exponent $\mu \sim 2$ is close to what is observed and therefore confirms the picture of particle acceleration at the shock front. In the case of accretion onto a black hole, the velocities in the pre- and post-shock regions as functions of the shock strength (§5) are easily obtained from the solution of transonic flows, and accordingly, the exponent μ could be self-consistently determined.

In the above derivation the relativistic particles are assumed with v >> u. When protons and electrons are both injected, the protons may be non-relativistic, while the electrons may be relativistic. When the particles are non-relativistic, the probability η of the return of the particles depends upon the energy, which makes computations of μ more complex. The energy spectrum for non-relativistic particles is less steep compared with the energy spectrum for non-relativistic particles [124]. Thus, for example, for an equal number of protons and electrons injected at the shock front, the proton number density would be higher at energies in the range of $m_e c^2$ to $m_p c^2$. The density of accelerated protons may exceed that of the electrons by the factor of a few hundred.

A similar conclusion is drawn from the spectrum of accelerated particles at relativistic shock fronts by assuming that the particles undergo only the pitch angle scattering on each side of the shock so that only the first order Fermi process may take place [125, 126]. The spectral index depends sensitively on the shock velocity in the case of relativistic shocks. Non-relativistic shocks produce a spectrum with index $N(p) \propto p^{-\gamma}$, with $\gamma=2.0$ but the relativistic treatment produces γ slightly larger than 2, in agreement with observed index of 2.4. Detailed discussion on the shock acceleration processes is beyond the scope of this review and interested readers may consult Blandford & Eichler [127].

2.6.2 Acceleration at Spherical Shocks and AGN Spectra

In AGNs and quasars, emitted energy from radio to γ -ray band is found to be roughly equal in each decade of frequency range. This signifies a non-thermal origin of

most of the radiation. A plausible suggestion is that the production of the relativistic particles which emit these radiations in AGNs and quasars may be due to acceleration of protons at the accretion shocks [128]. Some self-consistent study of shock are already in the literature [129, 130] where the linear, test particle theory of first order Fermi acceleration is extended to include the energy losses by the energetic particles, the back pressure of the accelerated particles on plasma, and a self-consistent determination of the effective adiabatic index γ_{eff} . These models can be used to determine the luminosity of radiation emitted from shock accelerated particles [122].

Consider a standing shock at some radius R_1 in a spherically symmetric accretion. In-flowing thermal particles of velocity u_- may be shock accelerated via first order Fermi acceleration and relativistic protons may be produced provides the pressure to support the shock. The protons collide in the post-shock region and produce pions through $p + p \to p + p + \pi^{\pm} + \pi_0$. These pions decay to produce γ rays and relativistic electrons which subsequently produce observed radiation through synchrotron and inverse Compton emissions. Luminosity of the radiation emitted largely depends upon the ability to pressure support a shock by the relativistic protons and in the most plausible cases, it may be $\lesssim 10\%$ of the Eddington luminosity.

In the case of spherical flow geometry, the free fall velocity is given by,

$$\beta = \frac{u}{c} = \left(\frac{2GM}{c^2R}\right)^{1/2} = x^{-1/2}.$$
 (2.98)

and the number density is given by,

$$n \sim 1.15 \times 10^9 \frac{\dot{m}}{x^{3/2} M_9^2} \text{ cm}^{-3}.$$
 (2.99)

where, \dot{m} is the accretion rate in solar masses per year and $M_9 = M/(10^9 M_{\odot})$. For reference, the Eddington rate is \dot{M}_{Edd} is $\sim 2 M_{\odot} M_9 \ {\rm yr}^{-1}$ and the radius of the shock can be expressed as,

$$R \sim 3 \times 10^{14} x M_9 \text{ cm.}$$
 (2.100)

As the flow passes through a shock, the density is increased to $\langle n_i \rangle \sim 4n_-$, where n_- is the number density in the pre-shock flow. The characteristic time scale for the p-p interaction is given by,

$$\tau_{pp} \sim \frac{1}{\langle n_i \rangle \sigma c} \sim 2.4 \times 10^5 \frac{x_1^{3/2} M_9^2}{\dot{m}} \text{ s},$$
(2.101)

where, $\sigma \sim 3 \times 10^{-26} {\rm cm}^{-2}$ is the p-p cross section and x_1 is the location of the shock in units of the Schwarzschild radius.

Let Q denote the fraction of the energy flux falling onto the shock which is converted into radiation via p-p collision and pion decay. The luminosity of the radiation

will then be,

$$L_{tot} = 2\pi R_1^2 n_- m_p u_-^3 Q. (2.102)$$

Here, L_{tot} includes the loss due to neutrinos, m_p is the mass of the protons and R_1 is the shock radius.

This is same as the volume integral of the emissivity $\epsilon = \frac{\langle E_{rel} \rangle}{\tau_{pp}}$, i.e.,

$$L_{tot} \sim \frac{4\pi R_1^3 < E_{rel} >}{3\tau_{pp}},$$
 (2.103)

where, $\langle E_{rel} \rangle$ is the average energy of the relativistic particles (= $3P_{rel}$, P_{rel} being the average pressure for the relativistic particles). Equating these two expressions for the luminosities we get the radius of the shock as,

$$R_1 = \frac{Q\tau_{pp}}{P_{rel}} \frac{1}{2} n_- m_p u_-^3. \tag{2.104}$$

Elimination of R_1 and τ_{pp} using above equations yield

$$\dot{m} \sim 11QM_9/\eta,\tag{2.105}$$

where, $\eta = P_{rel}/n_-m_pu_-^3$ is the ratio of the post-shock particle pressure to the incoming ram pressure.

The quantities Q, η , and the compression ratio $r = \beta_-/\beta_+$ for high Mach number M_1 of the pre-shock flow are [122],

$$r \sim 1.4 M_1^{3/4}, \quad M_1 \ge 4,$$
 (2.106a)

$$Q \sim 1 - 3.2 M_1^{-0.62}, \quad M_1 \ge 10,$$
 (2.106b)

and

$$\eta \sim 1 - 2.4 M_1^{-0.68}, \quad M_1 \ge 10.$$
(2.106c)

Figure 2.13 shows the variation of the compression ratio r as a function of the Mach number. The solid curve is drawn when losses are included. The dotted and dashed curves are drawn when adiabatic flows with $\gamma = 4/3$ and $\gamma = 5/3$ are considered. Figure 2.14 presents the efficiencies Q and η as functions of the Mach number. Since at high Mach numbers, Q and η approach 1, one obtains in this limit,

$$\dot{m} \sim 11 M_9,$$
 (2.107)

above which no steady state solution should be possible under the physical situation described here.

Using the derived quantities above, and using definitions of L_{tot} , R, n, and the ratio \dot{m}/M_9 , the observed non-thermal luminosity becomes,

$$L \sim 1.5 \times 10^{47} \frac{Q^2 M_9}{\eta x_1}. (2.108)$$

Or, in units of Eddington luminosity, $L_E = 1.3 \times 10^{47} M_9 \text{ erg s}^{-1}$,

$$l = \frac{L}{L_E} \sim 1.2 \frac{Q^2}{\eta x_1}. (2.109)$$

Thus the luminosity is inversely proportional to the location of the shock.

The Mach number of the flow is obtained from the ratio of the gas velocity and the sound velocity,

$$M_1^2 = \frac{u_-^2}{c_{s-}^2} \sim 6.5 \times 10^4 \frac{\beta_1^2}{T_8},$$
 (2.110)

where, $c_{s-} = [\gamma(T_p + T_e)/m_p]^{1/2}$ and $\gamma = 5/3$ is assumed. Or, substituting β ,

$$x_1 = 6.5 \times 10^4 \frac{1}{T_8 M_1^2}. (2.111)$$

The pre-shock temperature is obtained from the balance of the Compton heating and cooling and is roughly constant $T_8 \sim 1$ [131]. Thus the location of the shock mostly depends on the Mach number of the flow in the pre-shock region. Non-thermal luminosity drops off rapidly as the location of the shock is increased and conversely, increases with the decrease of x_1 . For $x_1 \sim 5$, $l \sim 0.1$. In the case of extreme Kerr black hole, the minimum shock location could be much lower: $x_1 \sim 1$, raising the luminosity to a much higher value.

The total non-thermal luminosity as derived above is directly proportional to the mass of the black hole and the luminosity is expected to be much below the Eddington rate. Figure 2.15 shows the comparison between the luminosity as predicted by this model and the correlation between mass and luminosity found by Wandel & Yahil [132]. Wandel & Yahil [132] assume that the widths of H_{β} lines are due to the dynamical motions around central black holes, and show that the luminosity of a large number (~ 70) of quasars and Seyferts actually correlate with the black hole masses. Open circles and crosses are the computation results of Wandel & Yahil [132] for quasars and Seyferts respectively and the slant solid lines are from the shock acceleration model [122].

If the pairs remain coupled to the accreted matter, their contribution to the opacity is likely to reduce the effective Eddington luminosity [133]. As a result, the emitted radiation could contribute strongly to the pressure support of the shock. This effect is clearly demonstrated by using a simple model of a shock that is mediated by Fermi-accelerated relativistic protons and radiation and in which e^+-e^- pair are produced through photon-photon collisions. When pair dominates, the maximum mass accretion rate for the steady state solutions are found to be significantly lower than the value predicted from the model of Kazanas & Ellision [122].

It is possible that these models are probably irrelevant for mass ranges other than $2 < \frac{\dot{m}}{M_9} < 10$, since the steady spherical shock solutions ceases to exist in this scheme.

However, in more realistic accretion flows, other effects such as the presence of angular momentum (§§5-7) and magnetic field are important. Here, the region of parameter space where shocks can exist is increased, and therefore a similar mechanism for the production of non-thermal radiation may work for a wider range of accretion rates as well.

3 Thin Accretion Disk Models

In the last Section, we discussed the properties of spherically symmetric accretion The infall velocity was very high and hence for a given accretion rate, the density was very low. Therefore, these flows were found to be inefficient in converting the rest mass energy of inflowing matter into radiation. When a flow has some angular momentum, the inflow velocity becomes much smaller and the density much higher. The infall time being higher, viscosity has time to dissipate angular momentum (except in regions very close to the black hole) and energy. As matter loses angular momentum, it sinks deeper into the potential well and radiates more efficiently. In the case of an accretion disk around a Schwarzschild black hole, the disk can radiate up to six percent of the rest mass of the infalling matter and the case of an accretion on a Kerr black hole, the efficiency could be up to forty percent depending upon the rotation parameter (§1). However, the actual efficiency depends on quantities such as viscosity parameter and the cooling processes inside the disk. This energy is released in the entire electromagnetic spectrum and the success of a disk model depends on its ability to describe the way this energy is distributed in various frequency bands. The temperature and density distributions as well as the geometrical shape of the disk dictates the nature of the emerging radiation spectrum. These, in turn, depend on the outer boundary condition, namely, the rate of matter supply, the specific angular momentum, as well as the energy content of the matter.

In the case of a binary system, where one of the components is compact, i.e., a white dwarf, neutron star or a black hole, the companion is stripped of its matter due to the tidal effects. The matter, with a specific angular momentum equal to that of the companion gradually falls towards the central body as the angular momentum is removed by viscosity. The flow encircles the compact primary and forms a quasi-stationary structure around it, preferably in the orbital plane. This quasi-stationary structure, commonly known as an accretion disk, may contain very little matter compared to the binary components, but it is the most important ingredient of an accreting binary system from the observational point of view.

To understand the circumstance in which an accretion disk may form around a black hole, we consider a binary system with component masses M_1 and M_2 having angular velocity Ω . The effective potential of the corresponding Newtonian system is given by,

$$\Phi_{eff} = -\frac{M_1}{|\vec{r} - \vec{r_1}|} - \frac{M_2}{|\vec{r} - \vec{r_2}|} - \frac{1}{2}(\vec{\Omega} \times \vec{r}). \tag{3.1}$$

Fig. 3.1 shows the equipotential surfaces (surfaces of constant Φ_{eff}) of a typical binary system with mass ratio $M_1/M_2 = 1/3$ drawn with the center of mass as the origin. The distance is measured in units of GM_1/c^2 and the separation of the stars is chosen to be $6GM_1/c^2$ for illustration. Five points of four distinct types marked as L_1 , L_2 , L_3 and L_4 are the so-called Lagrange points where Φ_{eff} is locally or globally an extremum. The value of Φ_{eff} passing through these points are -1.290, -1.187, -1.082 and -0.9376

respectively. The innermost self-intersecting contour marks the Roche lobes of two stars. The lobes meet at L_1 , the inner Lagrange point. Matter from the normal star M_2 overflows its Roche lobe and enters within the Roche lobe of the compact star M_1 through L_1 while remaining in the same plane as that of the binary orbit and eventually forming an accretion disk. Since the flow has a considerable angular momentum to begin with, it is reasonable to assume that the disk will form and the viscosity would transport angular momentum from the inner part to the outer part to allow matter to accrete onto the primary. The standard accretion disks, which are Keplerian in nature, describes the behaviour of the disks of this type. Of course, some matter from the winds of the companion will also be accreted by the primary, and the Keplerian flow could become sub- or super-Keplerian close to the black hole due to the terms (such as advection, pressure and cooling efficiency) neglected in standard disks. Therefore, flows close to the compact object will be an admixture of Keplerian and sub-Keplerian matter. Behaviour of such disks will be discussed in SS5-7.

In the case of active galaxies and quasars, the situation could be somewhat different. Matter may be supplied to the central black hole very intermittently, and the angular momentum of the supplied matter at the outer edge is not necessarily as high as Keplerian. This is because the matter may originate from winds of star clusters and the supersonic winds may pass through shock waves which randomize some of their velocity components. They may also lose much of the angular momenta through collision with other winds. Thus the flow is expected to be of low angular momentum, quasi-spherical and mostly advecting $(v_r >> v_\phi)$. Matter tend to be almost freely falling till it 'hits' the centrifugal barrier, which brakes the flow and causes a strong shock formation in the disk. The post-shock flow has initially very little infall velocity dominated by circular motion, and can be described by the so-called 'thick' accretion disk models. These disks have very little viscosity and therefore radiation efficiency could be somewhat intermediate between a spherical flow and a thin Keplerian disk. As the viscosity of these disks are increased, the shock wave becomes weaker, the efficiency of radiation becomes higher, and the disks become quasi-Keplerian. These disks will be discussed in subsequent Sections. In this Section, we shall deal with the standard Keplerian disk models and its variations.

3.1 Standard Thin Disk Model And Its Spectra

The standard disk model, which was originally conceived to describe Roche lobe accretion in a binary system is discussed extensively in the literature [11-12, 70, 134], and so we shall discuss this model only briefly.

3.1.1 Model Equations

In this model, the disk is assumed to be thin, i.e, $H(r) \ll r$. The heat generated by the viscous stress is radiated away efficiently in the vertical direction and the disk

becomes cool $kT \ll GMm_p/r$, contrary to what we have seen in the spherical accretion where the temperature is virial $kT \sim GMm_p/r$. Thus, the thin disks are highly non-adiabatic. In the thin disk limit, vertical velocity could be neglected compared to the radial velocity or azimuthal velocity. The vertical equation is solved independent of the radial equations. Equations in two directions are therefore decoupled. The accretion rate is assumed to be much lower compared to the Eddington rate and the pressure is negligible so that the radial force balance equation dictates the specific angular momentum distribution to become Keplerian. A Keplerian circular orbit of radius r around a Newtonian star has an angular momentum,

$$\tilde{l} = (GMr)^{1/2}.$$
 (3.2)

Let 2H be the vertical height of the disk and Σ be the surface density of the disk at radius r. Therefore,

$$\Sigma \equiv \int_{-H}^{H} \rho dz. \tag{3.3}$$

 ρ is computed on the mid plane of the disk. Replacing the integral of products by the product of the averages, the above integral becomes,

$$\Sigma \approx 2H\rho. \tag{3.4}$$

For a Keplerian disk, the stress tensor is

$$t_{r\phi} = \eta r \frac{d\Omega}{dr} = -\frac{3}{2}\eta\Omega, \tag{3.5}$$

where,

$$\Omega^2 = GM/r^3 \tag{3.6}$$

is the Keplerian angular velocity. Let f_{ϕ} denote the viscous stress exerted in the ϕ direction by the fluid element at r on neighbouring element at r + dr (Fig. 3.2). The viscous stress is related to the stress tensor according to $f_{\phi} = -t_{r\phi}$ and therefore,

$$f_{\phi} = -t_{r\phi} = \frac{3}{2}\eta\Omega = \frac{3}{2}\eta(GM/r^3)^{1/2}.$$
 (3.7a)

Here η is the dynamic viscosity coefficient.

To obtain a steady state disk structure, one has to solve four equations simultaneously which describe the conservations of the rest mass, the specific angular momentum, the specific energy and the vertical momentum balance condition. In addition, a viscosity law must be specified which should transport angular momentum outwards allowing matter to fall in.

(a) Equation describing the rest mass conservation:

As the flow approaches the compact star, it is compressed due to geometry and the density is increased. Assuming baryons are conserved the variation of density is obtained from the integral of the continuity equation which defines the accretion rate \dot{M} as,

$$\dot{M} = 2\pi r \Sigma v_r = \text{constant.}$$
 (3.7b)

(b) Equation describing angular momentum conservation:

As the flow approaches the compact star, its angular momentum must be transported outwards, since the angular momentum distribution is supposed to be maintained at the Keplerian value. This requires the presence of significant viscosity in the disk. The necessary viscous stress is obtained by forcing the flow to have Keplerian angular momentum everywhere. The torque applied by the stress is given by (see, Fig. 3.2),

$$\mathcal{G} = f_{\phi}(2\pi r.2H)r = \dot{M}(GM)^{1/2}(r^{1/2} - r_I^{1/2}), \tag{3.7c}$$

where, r_I is the inner edge of the disk which is usually assumed at the marginally stable orbit at $6GM/c^2$ in the Schwarzschild geometry.

(c) Equation governing the energy conservation:

Energy generated by viscous dissipation at each radial distance must be radiated away. The heat is generated by the viscosity at the rate,

$$Q_{+} \sim (t_{r\phi})^{2}/\eta = -\frac{f_{\phi}t_{r\phi}}{\eta}.$$
 (3.7d)

Using eqs. (3.7a) and (3.7c), the flux (half \times vertical height \times heat per unit volume per unit time) is obtained as,

$$F(r) = HQ_{+} = \frac{3\dot{M}GM}{4\pi r^{3}} \left[1 - \left(\frac{r_{I}}{r}\right)^{1/2}\right]. \tag{3.7e}$$

Emitted energy does not depend upon the exact viscosity law because whatever be the law, viscosity has to work in a manner that the disk remains Keplerian. The luminosity of the disk is obtained by integrating over the radial extent of the disk,

$$L = \int_{r_I}^{\infty} 2F \times 2\pi r dr = \frac{1}{2} \frac{GM\dot{M}}{r_I}.$$
 (3.7f)

Note that this luminosity is exactly half the potential energy of the matter at the inner edge of the disk. This magical factor is due to the fact the Keplerian distribution is assumed. If there were no loss of energy, the rotational velocity at the inner edge should have been obtained from,

$$\frac{1}{2}v_{\phi}^2 = \frac{GM}{r}.$$

But instead it is,

$$\frac{1}{2}v_{\phi K}^2 = \frac{GM}{2r},$$

because of the choice of angular momentum distribution at the inner edge. So, half of the energy must come out of the disk whatever be the physical viscosity, in order to maintain a Keplerian disk.

(d) Equation governing the vertical momentum balance:

Since the disk is thin, the vertical velocity component must be much smaller compared to other velocity components. In this case, one can ignore the advection term (containing v_z) in the vertical (z) component of the Euler equation:

$$\frac{1}{\rho} \frac{dP}{dz} = -\frac{GM}{r^2} \frac{z}{r}.$$
(3.7g)

Setting $\Delta P \sim P$ and $\Delta z \sim H$, we obtain,

$$H \sim \frac{a_s}{\Omega}.$$
 (3.7h)

Thus,

$$\frac{H}{r} \sim \frac{a_s}{v_\phi}$$
.

Hence, the thin disk condition $H(r) \ll r$ boils down to assuming that the flow is subsonic with respect to the azimuthal velocity.

It is generally agreed that the exact nature of the physical viscous mechanisms which may be working in an accretion disk is very poorly understood. Molecular and radiative viscosities are usually too low for a cool Keplerian disk. One of the possibilities is to consider small scale turbulent dissipation. In this case, the coefficient of viscosity is given by:

$$\eta \sim \rho \ v_{turb} \ l_{turb},$$
(3.7*i*)

where, v_{turb} is the velocity of turbulent cells relative to the mean gas motion and l_{turb} is the size of the largest turbulent cells. Shocks dissipate energy into heat for supersonic turbulence to enforce $v_{turb} \leq c_s$. The largest cell sizes are bounded by the disk thickness, so $l_{turb} \leq H$, thus the viscous stress is bounded by,

$$f_{\phi} = -t_{r\phi} \le \rho v_s H\Omega \sim \rho c_s^2 \sim P. \tag{3.7j}$$

Therefore, in general,

$$f_{\phi} = \alpha P, \tag{3.7k}$$

with $\alpha < 1$. This is the α disk prescription of Shakura and Sunyaev [11]. Some attempts have been made to obtain α using actual physical processes involved in the disk. We shall discuss this towards the end of this Section.

This generally used prescription is inadequate in describing flows which include discontinuity such as shock waves. We shall discuss this in §5.

(e) Opacity of the disk:

In the standard accretion disk model, first presented in the context of binary systems, the mass of the black hole may be small – a few times M_{\odot} . The temperature of the flow at the inner part of the disk is hot enough to have the whole disk fully ionized and the opacity may be assumed to be dominated by the Thomson electron scattering with the coefficient,

$$\kappa_{es} = 0.40 \text{ cm}^2 \text{ gm}^{-1}.$$
(3.7*l*)

In the cooler part of the disk (far from the black hole), absorption dominates over scattering and in the inner part of the disk, scattering dominates over absorption. The frequency averaged Rossland mean absorption opacity is:

$$\kappa_{abs} \sim \kappa_{ff} \sim 0.64 \times 10^{23} \rho T^{-7/2}$$
.

The mean opacity which can be used throughout the disk is then,

$$\frac{1}{\kappa_{mean}} = \frac{1}{\kappa_{scat}} + \frac{1}{\kappa_{abs}}. (3.7m)$$

(f) Total pressure inside the disk:

Total pressure of the disk is the sum of the gas pressure and the radiation pressure. For pure ionized hydrogen,

$$P(\rho, T) = \frac{2\rho kT}{m_p} + P_{rad}.$$
(3.7n)

If the radiation is in local thermodynamic equilibrium, its pressure is obtained using Planck distribution: $P_{rad} = \frac{1}{3}aT^4$.

(g) Radiative Transport Equation:

The heat flux goes out of the disk, mostly by radiation, rather than convection or conduction. In the optically thick regime, $\tau >> 1$, and the radiation is transported via diffusion,

$$F = -\frac{c}{3} \frac{d(aT^4)}{d\tau}.$$

Here, $\tau = \int_0^H \kappa_{mean} \rho dz \sim K\Sigma$ is the optical depth computed from the Rossland-mean opacity (K is a suitable vertical average of opacity). Replacing differentials by finite differences, we obtain,

$$F \approx \frac{acT^4}{\tau} = \frac{acT^4}{K\Sigma}.$$
 (3.70)

This regime applies to the outer part of the disk, where the thickness is high, and the innermost part where the temperature is high.

3.1.2 Structure of a Standard Disk

The eqs. 3.7(a-c), 3.7(e), 3.7(h), 3.7(k), 3.7(m-o) can be solved for nine unknowns $\rho(r)$, H(r), $\Sigma(r)$, $v_r(r)$, P(r), T(r), $f_{\phi}(r)$, $\kappa_{mean}(r)$, F(r) as functions of r, \dot{M} , M. The solutions are obtained by Shakura & Sunyaev [11] and Novikov & Thorne [12]. The general result is that for a given M and \dot{M} , there are three regimes depending upon r [11-12, 70]. The outer region (large r) is dominated by the gas pressure and free-free absorption is the major contribution to opacity. The middle region (at an intermediate r) gas pressure may still dominate the radiation pressure but the opacity is due to electron scattering. The transition radius between these two regions is obtained by the condition $\kappa_{ff} \sim \kappa_{es}$. At the innermost region (very small r) the radiation pressure dominates and the scattering is the main cause of opacity. The transition from the middle region to the inner region is obtained by the condition $P_{gas} \sim P_{rad}$.

The expression for the thermodynamic quantities are [11, 70]:

$$F(r) = 5 \times 10^{26} M^{-2} \dot{M}_{17} r^{-3} [1 - \sqrt{\frac{6}{r}}] \quad \text{erg cm}^{-2} s^{-1},$$

$$\Sigma(r) = 7\alpha^{-1} M \dot{M}_{17}^{-1} r^{3/2} [1 - \sqrt{\frac{6}{r}}]^{-1} \quad \text{gm cm}^{-2},$$

$$H(r) = 10^{5} \dot{M}_{17} [1 - \sqrt{\frac{6}{r}}] \quad \text{em},$$

$$\rho(r) = 3 \times 10^{-5} \alpha^{-1} M \dot{M}_{17}^{-2} r^{3/2} [1 - \sqrt{\frac{6}{r}}]^{-2} \quad \text{gm cm}^{-3},$$

$$T(r) = 5 \times 10^{7} (\alpha M)^{-1/4} r^{-3/4} \text{ K},$$

$$\tau_{es}(r) = 3\alpha^{-1} M \dot{M}_{17}^{-1} r^{3/2} [1 - \sqrt{\frac{6}{r}}]^{-1},$$
(3.8)

In these expressions, M is measured in units of the mass of the Sun, \dot{M}_{17} is in units of 10^{17} gm s⁻¹ and the r is measured in units of GMM_{\odot}/c^2 .

3.1.3 Emitted Radiation from a Standard Disk

In case the disk is optically thick and the opacity due to free-free absorption is more important than the opacity due to scattering, then the emission is black body with the surface temperature computed from the local effective temperature, i.e. [11, 70],

$$T_s(r) = \left[\frac{F(r)}{\sigma}\right]^{1/4} \approx 5 \times 10^7 \left(\frac{M}{M_{\odot}}\right)^{-1/2} \dot{M}_{17}^{1/4} r^{-3/4} \left(1 - \sqrt{\frac{6}{r}}\right)^{1/4} \text{ K.}$$
 (3.9)

where $\sigma = ac/4$, and a is the radiation density constant. The intensity of the emerging radiation is

$$I_{\nu} = B_{\nu}(T_s) = \frac{2h\nu^3}{c^2} \frac{1}{e^{\frac{h\nu}{kT_s}} - 1}.$$
 (3.10)

The flux of radiation crossing outwards through the surface is then related to the intensity I_{ν} by,

$$F_{\nu} \sim \int_{0}^{\pi/2} I_{\nu} cos\theta d\Omega \sim 2\pi B_{\nu}(T_s). \tag{3.11}$$

To obtain the intensity distribution, one computes T_s at each radius using eq. (3.9). At each frequency, the intensity due to black body emission at each radius is then calculated from eq. (3.10). It is then multiplied by the surface area of each annulus at radius r. The contributions are then summed over. However, the above assumption of black body radiation is satisfied only in the outer parts of the disk. In the inner region, where the scattering opacity dominates over free-free absorption, the temperature is somewhat higher than the black body temperature and the intensity of emerging radiation is expressible as,

$$I_{\nu} \sim B_{\nu}(T_s)(\kappa_{\nu}^{ff}/\kappa_{es})^{1/2},$$
 (3.12)

where, κ_{ν}^{ff} is the opacity coefficients for free-free absorption which for ionized hydrogen is given by,

$$\kappa_{\nu}^{ff} \sim 1.5 \times 10^{25} \rho T_s^{-3.5} \frac{1 - e^{-x}}{r^3} \text{ cm}^2 \text{ gm}^{-1}.$$
(3.13)

Here, $x = h\nu/kT_s$, k being the Boltzman constant. In this regime one obtains,

$$F_{\nu} \propto \frac{x^{3/2} exp(-x/2)}{(e^x - 1)^{1/2}}.$$
 (3.14)

This is the modified black body spectrum. Integrating over all range of ν ,

$$F \sim 6.2 \times 10^{19} \rho^{1/2} T_s^{9/4} \text{ erg cm}^{-2} \text{ s}^{-1}.$$
 (3.15)

Using this expression for flux along with eqs. 3.7(e) and 3.8, the temperature is obtained as,

$$T_s = 2 \times 10^9 \alpha^{2/9} (M/M_{\odot})^{-10/9} \dot{M}_{17}^{8/9} r^{-17/9} [1 - \sqrt{\frac{6}{r}}]^{8/9} \text{ K.}$$
 (3.16)

This is much hotter than the corresponding black body temperature at the same radial distance r. This is because black body emission is the most efficient mechanism of radiation. Any other mechanism must be much hotter in order to emit the same amount of flux.

The integral radiation spectrum of the disk computed for different accretion rate \dot{M} and viscosity parameter α is shown in Fig. 3.3. The upper curves are drawn for accretion rate comparable to the critical rate $\dot{M}_{crit} = 3 \times 10^{-8} \frac{0.06}{\eta} M_{\odot} \text{ yr}^{-1}$ with $\eta = 0.06$ for Schwarzschild black holes. The spectrum depends on α : higher α causes the spectrum to be flatter. The lower set of curves are drawn for accretion rate a

hundred times smaller where the outcome is basically insensitive to α parameter as well. The region 'BB' is contributed by the outer region of the disk which emits black body spectrum: $L_{\nu} \sim \nu^{1/3}$. The region marked 'Modified BB' is contributed by the inner and the central regions of the disk where electron scattering opacity is dominant over the free-free absorption and the resultant spectrum is flat: $L_{\nu} \sim \nu^{0}$. The exponential tail $\sim exp(-h\nu/kT)$ is from the very hot innermost part of the disk.

3.1.4 Stability of a Thin Disk

Inner region of the thin accretion disks is found to be notoriously unstable [134] due to thermal and viscous instabilities:

(a) Thermal instability: Consider first the radiation pressure and Thomson scattering-dominated inner disk. In the time scale we are interested, the mass transfer is not significant, so that the surface density Σ could be treated as constant. The internal pressure of the gas P varies as $P \sim \Sigma \Omega^2 H \propto H$. Hence, the rate of viscous heating per unit area of disk is given by,

$$Q^{+} = \frac{3\mathcal{G}\Omega}{4\pi r^{2}} = 3\alpha P\Omega H \propto \alpha H^{2}.$$
 (3.17)

Here, $\mathcal{G} \sim \dot{M}(GMr^{1/2})$ is the viscous torque (eq. 3.7c) assumed to be αP . Now, the radiative cooling rate is

$$Q^- = P/\tau_T \propto H. \tag{3.18}$$

When a disk is in thermal equilibrium, $Q^+ = Q^-$. As the thickness is slightly increased, the rate of energy production will be faster than the rate of radiative cooling, thereby heating the disk and increasing the disk height even further. When the disk thickness is slightly reduced, the heating would be reduced much faster than the rate at which cooling would take place. This will cause the disk to become thinner still. This behaviour shows that the disk is thermally unstable. The instability depends strongly upon the assumption of viscosity prescription with constant α . In a realistic accretion disk, which will advect away energy and entropy, such instability may not exist.

The general criterion for thermal instability is [11, 134]:

$$\left[\frac{\partial(Q^+ - Q^-)}{\partial H}\right]_{\Sigma} > 0. \tag{3.19}$$

Such an instability produces corrugated disk surface. The amplitude of the corrugation may be limited by non-linear effects. The growth time scale is given by,

$$t_{th} \sim \frac{2\pi}{\Omega \alpha}.\tag{3.20}$$

(b) Viscous Instability: This instability develops in a much shorter, accretion time scale. In this case, as the accretion rate of the disk is suddenly changed, the density should

also change in a manner that,

$$\frac{d(\nu\Sigma)}{d\Sigma} > 0, \tag{3.21}$$

in order to remain stable. If the density cannot increase, for example, with the increase of the accretion rate, then the disk will have viscous instability. A time dependent behaviour of a thin disk resulting out of this which has been found to be of particular importance in explaining the dwarf novae outbursts is called a limit cycle behaviour. In this case, the mass accretion rate varies with the variation of density (at a given radius of the disk) as in Figure 3.4. As discussed above, the region of the curve BD having negative slope would be viscous unstable and the disk density would oscillate between the two branches AB and CD which have positive slopes [135]. Such behaviour is found to be present even when one considers accretion disks around super-massive black holes [136]. In this case, the oscillatory behaviour is seen with period 10^{4-7} yr operating at distances of 10^{15-16} cm. Of course, self-gravity of the disk might play an important role in active galaxies so that the simple dwarf-novae type computation need not hold.

3.1.5 Viscosity in a Thin Disk

There is a big uncertainly in the nature of the viscosity inside a thin accretion disk. One of the major problems is to explain the origin of sufficiently large viscosity that seems to be present inside accretion disks in the binary systems. The generally accepted view is that the viscosity may be due to magnetic transport of angular momentum [137-139] or due to turbulent transport [140] which can operate inside the disk. If magnetic field is coherent and threads the disk as in proto-stellar disks, the transport through the wind is efficient [137]. If the accretion flow contains stochastic flux tubes, they would be repeatedly sheared and re-connected. Some blobs with larger angular momentum would diffuse radially outwards and some other would be advected inwards. The net effect causes the transport with an effective $\alpha \sim 0.01$. Other methods of magnetic transport include the production of violently turbulent disk due to rapid growth of weak magnetic fields by an instability in presence of differentially rotating Keplerian disks [139]. This so-called Balbus-Hawley instability works in the following way: Imagine two blobs of matter attached to a vertical magnetic flux tube (at $R = R_0$) inside the differentially rotating disk which rotates faster at smaller radius (Fig. 3.5). Let the blob positions be displaced radially, in a way that one blob is inside the other (radially). Magnetic flux tube will force them to rotate with the angular velocity $\Omega(R_0)$ of the average position R_0 of the fields. Thus, the blob inside (at $R_0 - dR$) will be forced to rotate slower than its ambience. This will reduce its centrifugal force and it will sink further. The outer blob (at $R_0 + dR$) will rotate faster than its ambience. This blob will have more centrifugal force than the average value and will move further outwards. This instability causes net transport of angular momentum outwards and would be a source of viscosity. The calculated α is about ~ 0.01 . In presence of toroidal magnetic field, such argument may be applicable provided magnetic tension is not important (Fig. 3.5). Close to a black hole, where the tension may be the dominent force (if the temperature is high enough: $T \gtrsim 10^{10} \text{K}$) [141] the whole flux tube would be advected towards the black hole in a much shorter time than the growth time scale of this perturbation. Another detailed model which attempts to compute α parameter assumes that the angular momentum is transported by internal waves inside an unmagnetized disk. Vishniac & Diamond [140] use perturbation analysis of a thin, inviscid accretion disk with adiabatic vertical structure, including the effects of shearing, but ignoring radial structure to calculate the so called α parameter in a quantitative manner. They classify the waves into two classes: sound waves and internal waves. The non-axisymmetric mode $m = \pm 1$ inward traveling internal waves deposit negative angular momentum in the disk. These are excited at the outer rim of the disk at the location of the accretion stream hitting the disk. An estimate of the effective viscosity is $\nu = (H/r)^2(H/c_s)$ where H is the disk scale height and c_s is the velocity of sound. These internal waves are similar to the spiral shock waves generated in simulations of Sawada, Matsuda and Hachisu [142] in the context of a two dimensional thin disk. The internal waves are incoherent as opposed to the spiral shock simulations [142] where a coherent shock pattern forms.

3.2 Two Temperature Disk Models

Thermal, geometrically thin and optically thick disks which have been discussed so far, can be unstable at the inner edge and are too cool to produce X-rays observed in binaries and active galaxies and quasars. There are some models where the disks are much hotter. These are optically thin, two temperature Comptonized soft photon disks and pure bremsstrahlung disks [143]. As before, there are two parameters in these models, viscosity parameter α and accretion rate M. For physically reasonable values of these parameters, the temperature could become very high since the potential energy is virialized, particularly when the accretion rate is low ($\S4.6$). Soft photons from the outer disk is intercepted by the inner region and are Comptonized. An interesting variation of these models is discussed by White & Lightman [144] who consider two temperature Comptonized bremsstrahlung disks. In these disks, there is a critical accretion rate $\dot{M}(\alpha)_{crit}$ above which there is no steady state solution for $r \leq 10GM/c^2$ (runaway pair production). Depending on α , \dot{M}_{crit} corresponds to a rate ranging from 0.03 to 0.1. For $M < M_{crit}$, there are two solutions, one with a high density and the other with a low density of pairs. Another important result from these studies is that for Comptonized soft photon disks, steady solutions are possible for all M and α . Reasonable amount of X-rays could be produced by this mechanism though the details of the observations required further refinement which we discuss on $\S7.2$. These results hold for two temperature disks. If electron and protons couple more strongly than the Coulomb coupling, the temperatures become equal. In this case, there is also a critical accretion rate, and depending upon α , the luminosity varies from 6×10^{-5} to $0.03L_{edd}$. Single temperature disks are very hot and might be ruled out by the constraints from γ -ray background and therefore no efficient coupling between protons and electrons may be allowed in these disks.

3.3 Transonic Disk Models

The standard Shakura-Sunyaev thin accretion disk models [11-12] do not accurately describe the flow close to the black hole as the solution is terminated at the marginally stable orbit r_{ms} . Since the black hole accretion is necessarily transonic, it may be important to know how a Keplerian flow behaves when it passes between the marginally stable orbit and the horizon of the black hole. A number of efforts have been made to study the so-called 'transonic' solution [145-146]. A general feature of these solutions is that, unlike Shakura-Sunyaev disks, these disks pass through the inner sonic point close to the horizon. They are otherwise Keplerian at larger distances. Though the first goal, i.e, to have a solution which passes through the inner sonic point is achieved with success, smoothly matching of Keplerian solutions has been a major problem and this usually introduces some arbitrary parameters, such as the matching radius, matching radial and angular velocities etc. Figure 3.6, taken from Abramowicz et al. [146] shows a few self-consistent angular momentum distribution inside disks which are Keplerian at large distances. The distribution seems to depend strongly upon the radial distance where Keplerian distribution is matched. The important feature is that the angular momentum remains almost constant close the black hole as the flow becomes supersonic. Another important aspect of this work is that it attempts to 'stabilize' thin accretion disks against viscous and thermal instability [134] by advecting the perturbations away as quickly as they develop. Such features are present also in globally complete advective disks discussed in §5. This supersonic inner region is probably less relevant for the observational point of view as the infall time in this region is much smaller compared to the viscous time scale, and therefore this region does not radiate efficiently. The spectrum and other properties of these smooth transonic solutions are expected to be similar to the standard thin accretion disks and therefore we shall not discuss them any further. Recently, this model is generalized by removing the assumption of vertical integration and solving the equations self-similarly. We shall discuss them in $\S 5.5$.

3.4 Magnetized Disk Models

It is usually believed that the origin of the bipolar outflows and jets are related to the properties of accretion disks. Outflows and jets can extract angular momentum from disks very efficiently (especially when there is no binary companion), and thereby aid accretion process. Since various properties (such as velocity, kinematic luminosity, etc.) of an outflow must be directly related to the properties of the underlying disk, theoretical disk models as well as numerical simulations must produce both the disk and the jet simultaneously. There are a few theoretical models which achieve this in the context of bi-polar outflows [137] and in the context of radio jets [147-150]. Pudritz & Norman [137] show that angular momentum transport in a bipolar outflow is consistent with its loss from the proto-stellar disk. In the latter case [147-150], magnetohydrodynamic equations are solved inside as well as outside of the disk and the solutions are matched on the disk boundary. So far, no satisfactory numerical work is present which successfully produce collimated and accelerated outflows/jets which are originated from magnetized disks, even though separate simulations of magnetized

disks and jets are present in the literature. Some of the simulations have obtained new insights into old problems – examples being the Balbus & Hawley instability [139] and the detailed instabilities at the working surface of a radio jet. Below, we present a comparative study of the typical self-consistent solutions of the magnetized accretion disk which also produces collimated radio jets.

Blandford & Payne [147] consider centrifugally driven self-similar MHD winds originating from infinitesimally thin, Keplerian disks. In this model, matter is ejected using a 'sling-shot' mechanism if the field line is sufficiently bent outwards, much like the outward motion of a 'bead' on an inclined and rigidly rotating wire. The effective potential for the bead on a wire attached at $r = r_0$ on a Keplerian disk is [147],

$$\Phi = -\frac{GM}{r_0} \left[\frac{1}{2} \left(\frac{r}{r_0} \right)^2 + \frac{r_0}{(r^2 + z^2)^{1/2}} \right]$$
 (3.22)

The 'bead' will be unbound if the wire makes an angle $\theta > 60^{\circ}$ with the vertical axis. In a magnetized disk, the wire is likened to be the magnetic field lines which may be thought to rotate rigidly till the Alfvén point and the bead is likened to be lumps of matter ejected from the disk. This work shows that collimated bipolar jets may be formed from a Keplerian disk. In reality disks need not be Keplerian and in presence of a black hole geometry the potential would be modified, particularly close to the black hole. Close to a black hole, one would require a much higher inclination (than 60°) in order that matter may come out of the strong gravitational field.

Contopoulos & Lovelace [151] assume a power law distribution of the magnetic field, $B(r,z) \propto r^q B(z)$ and a self-similar flow out of an infinitesimally thin Keplerian disk. They find that asymptotically collimated jets are obtained when q < -1. Königl [149] numerically determines the self-similar magnetic field structure inside a cold, partially ionized Keplerian disk. He also shows that there exists disk parameters which can, in principle, produce Blandford-Payne [147] type winds that attain super-Alfvénic velocity at a finite distance from the disk surface.

A more general solution of the field where the field inside the disk, as well as outside the disk are solved simultaneously, are presented in Chakrabarti and Bhaskaran [150]. Similar to Blandford & Payne [147] and Königl [149] solutions, this work also assumes that the field is self-similar in radial direction, but the functional relationship inside the disk is different from that of the outside. The solutions are obtained analytically by Taylor series expansion of the field variables inside and outside the disk and matching the solutions at the disk boundary, the location of which is obtained self-consistently. The important result which emerges from this exercise is that it proves analytically the existence of a complete outflow solutions from a magnetized disk which pass through the Alfvén surface at a finite distance. Solutions are obtained using a non-Keplerian angular momentum distribution $l = C_1 r^n$, where n need not be 0.5 and C_1 need not be $\sqrt{(GM)}$. Indeed, more promising solutions are obtained only for sub-Keplerian disks.

A typical solution of magnetized accretion disk is shown in Fig. 3.7 which contains all the generic features found in these solutions. The solution is drawn in R-Z plane. The solid curves are the resultant field lines. The long-dashed line indicates the disk boundary where two solutions are matched and the inclined short-dashed line indicates the Alfvén surface. One notices that inside the disk the magnetic field lines are bent as if advected by the inflow. Outside of the disk, the field lines seem to diverge due to centrifugal acceleration. But this is soon overcome by the tension of the azimuthal field [which ($\sim 1/r$) dominates over poloidal component ($\sim 1/r^2$) as the flow propagates outwards], because of which the field lines bend back towards the axis. It is expected that after the initial collimation, the field lines should become parallel to the Z-axis, the axis of the outflow, as the magnetic pressure is likely to rise near the axis. The inclusion of higher order expansion in Taylor series would be needed to show such effects. According to the criterion of Contopoulos & Lovelace [151], q = -0.5 in these solutions (flux is assumed constant with radial distance [150]) and therefore these represent well behaved collimated asymptotic solution.

The jet solution presented above has all the necessary ingredients to be a 'good' solution. They are bent along the flow inside the disk, diverge outside the disk due to centrifugal force and then collimate back towards the axis to form the jet. A large number of other recent works have been able to reproduce some of these aspects [152-154]. Particularly interesting is the time evolution of the advected magnetic field which vertically threads an accretion disk [154]. This work shows that field lines, initially uniform in the vertical direction are carried with the flow towards the center inside the disk and form an hour-glass pattern. Some other studies also [148, 155] show that azimuthal component of the magnetic field does contribute to collimate jets.

Another class of magnetized disk solutions are present in the literature in which the background flow is assumed to be the same as the standard Keplerian disks and the magnetic field is assumed to be sheared and advected by the flow [156-157]. These works show that magnetic dynamo is not essential in disk models if sufficient magnetic flux is steadily fed into the disk. The field configurations close to the disk surface become Blandford-Payne [147] type and can, in principle, launch cosmic jets. In Figures 3.8(a-b), the field topologies (with even and odd symmetries) inside a disk are shown which can probably be matched with jet solutions. Apart from these disk models showing generic effects, some completely new physical results have been discovered in Keplerian disks around a Kerr black hole. The gravitomagnetic potential of a rotating black hole in the presence of a differentially rotating disk is seen to drive a self-excited dynamo and amplify weak (even axisymmetric) magnetic field to a higher field strength [158]. The source term for the dynamo effect is present in the Maxwell's equation in Kerr metric [159] and therefore does not violate Cowling's theorem. Figure 3.9 shows the poloidal flux Ψ at t=4.6 times the diffusion time scale

$$t_{diff} = \frac{r_g^2}{\eta_0} \sim 4 \times 10^5 M_9 (0.1/\alpha_T) (r_g/2H_{in})^2 (c/2r_g\Omega_H) \quad \text{s}, \tag{3.23}$$

where, η_0 is the turbulent diffusivity at the horizon for extremely rotating black hole, M_9 is the mass of the black hole in units of $10^9 M_{\odot}$, α_T is the α parameter due to the turbulent viscosity, r_g is the Schwarzschild radius, H_{in} is the height of the disk at the inner edge and Ω_H is the rotational velocity of the black hole on the horizon. The Figure is drawn for the Kerr parameter a = 0.98.

The jet solutions presented above have been constructed in a manner that the angular momentum transport by the jet is such that the disk is maintained Keplerian or quasi-Keplerian. In reality, disks in active galaxies need not have so much angular momentum in the first place and therefore, so-called 'angular momentum' problem does not apply. In §4.6 we shall discuss magnetic thick disks where the toroidal fields are ejected from the disks due to combined effects of magnetic tension and buoyancy and the jets may be produced without significant poloidal component.

3.5 Thin Disks with Weber-Devis Magnetic Field Configuration

One of the simplest magnetized disk models could be a conical flow which has ordered radial and azimuthal magnetic field components. Such a flow passes through the magnetosonic points and can also have shock waves in them. In the context of solar winds, such field configurations were first studied by Weber & Devis [160]. Although these studies were originally made for wind type flows, recent studies of accretion and wind flows with these field configurations show very rich topologies in the phase space and they have now been extensively studied [77, 161]. We present below the general procedure of studying these solutions using a pseudo-Newtonian potential. These solutions (which are not self-similar) have completely new topologies with fast-magnetosonic points forming at finite distance. They have since been generalized in the external Kerr black hole geometry and are seen to have the same features [161].

Let us start with a conical wedge shaped flow which is assumed to have an adiabatic equation of state $P = K \rho^{\gamma}$, where P and ρ denote the isotropic gas plus radiation pressure and the matter density respectively, K is the adiabatic constant which measures the entropy of the flow and γ is the adiabatic index given by the ratio of specific heats. We use $\gamma = 4/3$ for the relativistic flows. K remains constant throughout the flow if it is shock-free, otherwise it changes at the shock. The solution with shock waves will be discussed in §5.

3.5.1 Basic Equations and Magnetosonic Point Conditions

The basic equations are [cf. $\S 2$]:

(a) the energy conservation,

$$E = \frac{1}{2}u^2 + \frac{1}{2}\vartheta_{\phi}^2 + \frac{\gamma}{\gamma - 1}\frac{p}{\rho} + \Phi(r) - \frac{B_{\phi}B_r\Omega r}{4\pi\rho u},$$
 (3.24a)

(b) the angular momentum conservation,

$$L = r\vartheta_{\phi} - \frac{B_r B_{\phi} r}{4\pi \rho u},\tag{3.24b}$$

(c) the mass flux conservation,

$$\dot{M} = \rho u r^2, \tag{3.24c}$$

(d) the radial magnetic flux conservation,

$$C_1 = B_r r^2, (3.24d)$$

and finally,

(e) the Maxwell's equation for a perfectly conducting fluid, $\vec{e} = -\vec{v} \times \vec{B} = 0$,

$$r(uB_{\phi} - \vartheta_{\phi}B_r) = -\Omega C_1. \tag{3.24e}$$

Here u is the radial component of the velocity, ϑ_{ϕ} is the azimuthal component of velocity, B_r is the radial component of magnetic field, B_{ϕ} is the azimuthal component of the magnetic field, $\Phi(r)$ is the gravitational potential due to the central star, and Ω is the constant angular velocity of the surface of the star. In the energy conservation eq. (3.24a), the final term represents energy transported out by magnetic fields and is equal to the Poynting energy flux. The specific angular momentum L in (3.24b) consists of two terms: the first term is the ordinary angular momentum and the second term is due to the torque associated with magnetic stresses. For the present purpose we rewrite eqs. 3.24(a-c) as follows [162]:

$$\mathcal{E} = E - L\Omega = \frac{1}{2}u^2 + \frac{1}{2}\vartheta_{\phi}^2 + na^2 + \Phi(r) - \vartheta_{\phi}\Omega r, \qquad (3.25a)$$

$$L = r\theta_{\phi} - C_2 r B_{\phi}, \tag{3.25b}$$

$$\dot{\mathcal{M}} = a^{2n} u r^2, \tag{3.25c}$$

where $a = (\gamma p/\rho)^{1/2}$, the adiabatic sound speed and

$$C_2 = \frac{B_r}{4\pi\rho u} = \frac{C_1}{4\pi\dot{M}}. (3.26)$$

 $\Phi(r)$ is given by $\Phi_N = -GM/r$, or $\Phi_S = -GM/(r - 2GM/c^2)$ depending upon whether the flow is around a Newtonian star or a compact, general relativistic non-rotating star

or a black hole. $n=1/(\gamma-1)$ is the polytropic index. The specific energy E has been re-defined after incorporating the constant rotational contribution. Thus, \mathcal{E} is allowed to be negative even for an unbound flow. $\dot{\mathcal{M}} \sim K^n \dot{M}$ measures the entropy of the flow and usually changes at the shock waves. As in §2, we shall use the phrases 'accretion rate' for $\dot{\mathcal{M}}$ and 'mass flux' for \dot{M} .

First, we eliminate B_{ϕ} from eqs. (3.24e) and (3.25b) to obtain

$$\vartheta_{\phi} = \frac{uL - \Omega C_1 C_2}{ru - \frac{C_1 C_2}{r}}.$$
(3.27)

Since ϑ_{ϕ} is expected to be smooth everywhere one obtains the condition that wherever denominator vanishes, numerator must also vanish there. This condition is satisfied at the Alfvén radius, $r = r_a$, where $u = u_a = C_1 C_2 / r_a^2 = \Omega C_1 C_2 / L$. The total angular momentum L and the angular velocity of the star Ω are related: $L = \Omega r_a^2$. Because the flow has to pass through the Alfvén radius r_a with Alfvén velocity u_a , we use below these as the units of distance and velocity. Time is measured in units of $\frac{r_a}{u_a}$. Thus, in these units $L = \Omega$, $B_{ra} = C_1$ and the product of the constants $C_1 C_2 = 1$. Equation (3.49) reduces to

$$\vartheta_{\phi} = \frac{(u-1)\Omega r}{ur^2 - 1}.\tag{3.28}$$

We continue to use the same notations for the dimensionless quantities since there arises no confusion. To simplify the expressions, we specify the field B_r at the Alfvén point to be unity prior to any calculations so that $C_1 = C_2 = 1$, $4\pi \dot{M} = 1$. Also, $g_0 = GM/(u_a^2 r_a)$ is a constant which measures the mass of the central body and $\bar{c} = c/u_a$ is the velocity of light in units of the Alfvén speed. Differentiating eqs. (3.24a) and (3.24b) with respect to r, and eliminating da/dr, we get

$$\frac{du}{dr} = \frac{N}{D},\tag{3.29}$$

where

$$N = ur[(ur^2 - 1)^2(u - 1)\Omega^2 + (\frac{2a^2}{r^2} - \frac{\Phi'}{r})(ur^2 - 1)^3 + u\Omega^2(1 - r^2)(u - 1)(ur^2 + 1)], (3.30a)$$

and

$$D = (u^2 - a^2)(ur^2 - 1)^3 - u^2r^2\Omega^2(r^2 - 1)^2.$$
(3.30b)

Here

$$\Phi' = \Phi'_N = g_0/r^2,$$

for a Newtonian star, or,

$$\Phi' = \Phi_S = g_0/(r - 2g_0/\bar{c}^2)^2,$$

for a Schwarzschild black hole or a compact nonrotating star. Prime indicates derivative with respect to r. It is clear that both numerator and denominator vanish identically

at the Alfvén point. However, there are other points in the phase space [spanned by the pair (r, u)] where they vanish also. These points (r_c, u_c) are the slow and the fast magnetosonic points. These locations are obtained by eliminating sound speed a from the numerator and the denominator for a given \mathcal{E} and L. In Fig. 3.10, the contours of constant \mathcal{E} and L in the (r_c, u_c) plane are shown. Solid contours are drawn for L=1.2, 1.8, 2.2345, 3.0, and the dashed contours are drawn for $\mathcal{E}=1.2, 1.8, 2.355, 2.8$ respectively. A non-dissipative flow preserves energy and angular momentum. Therefore, the intersections of given \mathcal{E} and L curves give the locations of all critical points corresponding to these conserved quantities. The points where $\frac{du_c}{dr_c}|_{\mathcal{E}} < 0$ are the 'X'-

type critical points and the points where $\frac{du_c}{dr_c}|_{\mathcal{E}} > 0$ are the 'O'-type critical points. For example, five critical points formed at the intersections of $\mathcal{E} = 1.8$ and L = 1.8 curves are marked by 'X' and 'O'. The points where $u_c r_c^2 < 1$ are the slow magnetosonic, and the points where $u_c r_c^2 > 1$ are the fast magnetosonic.

3.5.2 Solution Topologies of Magnetized Accretion

For a given set of parameters a flow can have five critical points other than regular Alfvén point at u=r=1. Figures 3.11(a-f) show distinctly different topologies of the solution. Here the radial velocity u is plotted against r. Contours are of different 'accretion rates' $\dot{\mathcal{M}}$. Each diagram is drawn for a different energy. In (a) $L=10^{-4}$, $\mathcal{E}=2.0$, Bondi-like slow point is present. In (b) L=1.0, $\mathcal{E}=-0.5$, the rotational slow and the fast 'O'-type points are present, in (c) L=1.0, $\mathcal{E}=1.8871$, all the five sonic points are present. Notice that the lower left branch of Bondi-like point is not connected to infinity. This branch opens up as L is increased as in (d-f). In (d) L=1.7, $\mathcal{E}=-2.0$, the Bondi-like slow and the fast 'O'-type points are present. In (e) L=1.7, $\mathcal{E}=0.0$, the Bondi-like and the rotational slow points, and slow as well as the fast 'O'-type points are present. In (f), L=1.7, $\mathcal{E}=4.0$, all the fast points are absent. The critical wind solutions are marked by $u_{\alpha 1}$, $u_{\alpha 2}$, $u_{\beta 1}$, and $u_{\beta 2}$.

In the case of accretion flows, any of the topologies in Fig. 3.11(a), 3.11(c-f) could be used as the flow passes through the magnetosonic point close to the black hole. The choice depends upon the accretion rate. The topology 3.11(c) is important for shock transitions, which we shall discuss in §5.

3.6 Outflows by Extraction of Energy from Black Holes

So far, we discussed the formation of winds using thermal, kinetic, and/or magnetic energies close to the origin of the outflows on the accretion disks. It is well known that within the ergosphere [defined by $r = M + (M^2 - a^2 \cos^2 \theta^2)^{1/2}$] where any flow is forced to co-rotate with the black hole, energy of test bodies could be negative. This property can be exploited to extract energy directly from the black holes, as was con-

ceived by Penrose [163]. In this case, matter with positive energy could accrete from infinity and 'somehow' split into two components with one component having negative specific energy and the other component having specific energy more than that at the initial flow. If this latter component could be expelled from the ergosphere, then an energized outflow could be created. The energy extraction can continue until the black hole attains the so called irreducible mass [164] M_{ir} defined by

$$M^2 = M_{ir}^2 + a^2 M^2 / 4 M_{ir}^2.$$

Thus, $M_{ir} = (r_+ M/2)^{1/2}$ (r_+ being the horizon). It is clear from the definition that only the rotational energy could be extracted. For an extremely rotating Kerr black hole a = 1 and the corresponding 'reducible' energy is $\Delta M = M - M_{ir} \sim 29\%$.

Several works are devoted to device models to extract this energy in astrophysically feasible way and in most of the cases the process involves magnetic fields. Similar to Blandford-Payne process described in §3.4, where the disk is slowed down by the magnetic fields passing through it, one could imagine slowing down the black hole itself by threaded magnetic fields. Magnetic flux tubes advected by the accretion disk may be collected close to the black hole which eventually threads the hole. This is possible because a black hole has a finite resistance [165] as the field decay time of a conducting sphere of radius R cannot be shorter than the light crossing time $R^2/4\pi\sigma \sim GM/c^3$.

An important participant to the energy extraction process is a new force close to a rotating black hole, known as the gravitomagnetic force. This is derived from the so-called gravitomagnetic potential [166] β^{j} . This is also called the 'shift function' since this is the rate at which the grid coordinates shift with respect to zero angular momentum observers, i.e., observers moving with angular velocity,

$$\omega \sim \frac{2aMr}{\Sigma^2}$$

as seen from infinity, where $\Sigma = r^2 + a^2 cos^2 \theta$. The gravitomagnetic force interacts with the external magnetic field \vec{B} to produce a magnetic-gravitomagnetic battery effect with EMF [166],

$$EMF = \int_{\mathcal{C}} -\vec{\beta} \times \vec{B}.\vec{dl}$$

the integral is taken along a closed curve suitably chosen to include regions along and across the threaded field lines. In a special case, when the external field is uniform at infinity, an exact solution of the electric and magnetic fields could be obtained [167]. The battery is very powerful, producing an electric field of about $E \sim Ba/M \sim 3 \times 10^6$ volts/cm (a/M). Thus the voltage drop between the horizon and a few Schwarzschild radii would be tremendous: $V \sim Er_+ \sim Ba \sim 10^{20}$ volts for a $M=10^9 M_{\odot}$ black hole [166]. Particularly interesting is the region where the electric field is parallel to the magnetic field lines. Here, similar to the pulsar model which produces a spark gap on the neutron star surface, the charged particles from the accreting disk could be accelerated along the field lines rapidly, causing them to radiate high energy γ -ray

photons tangential to the field lines. Charges may also be formed by vacuum breakdown due to high voltage and hard γ rays may also be supplied by hard bremsstrahlung radiation from accretion disks with a very small accretion rate (which keeps the disks hotter). As the field lines bend, these photons scatter off these fields producing electron-positron pairs which are again accelerated and the same process continues creating a magnetosphere around a rotating black hole [168]. The field required for this process is around $10^4\mathrm{G}$ which is roughly the equipartition field of the plasma. The Poynting flux transports power from the black hole and the accretion disk along the flux tubes rotating roughly at an angular velocity half of that of the horizon [169]. This power could be sufficient to drive the outflows observed in active galaxies.

An insight into the energy extraction process through Blandford- Znajek mechanism could be obtained in the following way [168]. Consider a thermally conducting disk rotating with an angular velocity $\Omega_H > 0$ is surrounded by a thermally insulated annual ring which rotates with an angular velocity ω . Suppose these two systems are coupled by friction which is proportional to the difference between these two angular velocities: $K(\Omega_H - \omega)$. This frictional couple will increase the rotational energy of the ring at a rate $K\omega(\Omega_H - \omega)$ and decrease the rotational energy of the disk at a rate $K\Omega_H(\Omega_H - \omega)$. The rest will be spent in heat generation $K(\Omega_H - \omega)^2$. When $\Omega_H > \omega$, the efficiency of mechanical energy transfer to the ring is ω/Ω_H .

In the present situation, similar transfer takes place between the rotating hole (with angular velocity Ω_H) and the surroundings magnetosphere. The frictional coupling is thought to reside inside the event horizon where the electrical circuit is presumably complete. In Fig. 3.12, we show schematically these processes. The dashed circle is the event horizon $r=r_+$. The solid curves are the surfaces of constant poloidal field lines $A_\phi=$ const. Some of them pass along the polar region (A_p) and some other pass through the equatorial plane of the disk (A_e) . A current flows down the magnetosphere into the hole and comes out into the disk on the equatorial plane. In the magnetosphere, SG is the spark gap where positrons and electrons are created. Positrons flow into the hole along the poloidal field and electrons fly away from the hole carrying energy and angular momentum. The short-dashed surfaces denoted by L are the locations where the particles slip out of the A_ϕ surfaces as otherwise they would be rotating faster than the speed of light.

4 Thick Accretion Disks

4.1 Introduction

When the accretion rate is high $(\dot{M} >> \dot{M}_{Edd})$, radiation emitted by the in-falling matter exerts a significant pressure on the gas. This pressure must be incorporated to find the dynamical structure of the disk and in determining the thermodynamical quantities inside the disk. The radiation pressure inflates the disk, and makes it geometrically 'thick' $[H(r) \sim r]$. Incorporation of the radiation pressure term in Euler equation modifies the angular momentum distribution from that of the Keplerian disk. To see this, let us consider the radial component of the Euler equation,

$$v_r \frac{dv_r}{dr} + \frac{1}{\rho} \frac{dP}{dr} - \frac{l^2(r)}{r^3} + F(r) = 0$$

where F(r) is the force due to gravity and l(r) is the specific angular momentum distribution. Ignoring the advection term for the moment, one finds the distribution of angular momentum as [170],

$$l(r) \propto [r^3 F(r) + \frac{r^3}{\rho} \frac{dP}{dr}]^{1/2}.$$
 (4.1)

Clearly, wherever the pressure gradient term is positive(negative), the angular momentum is higher(lower) than Keplerian. This term is significant when $GM/r \sim P/\rho \sim a_s^2$, where a_s is the sound speed. This is the essence of thick accretion disk models. This is a general result and is valid even when a Newtonian treatment is made.

First quantitative study of the effect of radiation pressure on the angular momentum distribution was carried out almost two decades ago [171]. Figures 4.1(a-b) show the variation of the angular velocity ω and radial velocity $v = v_r$ in units of the Keplerian angular velocity $[\omega_K = (GM/r_0^3)^{1/2}]$ the free-fall velocity $v_K = (GM/r_0)^{1/2}$ at the inner edge of the disk r_0 where the shear stress is assumed to vanish $(r_0 = 3r_g = 6GM/c^2)$ in the Shakura-Sunyaev disks [11]). In Fig. 4.1(a), the accretion rate is chosen to be the same as the critical rate, $\dot{M}_c = L_{Edd}/(c^2\eta)$ with $\eta \approx GM/2r_0$, the efficiency factor. The dashed curve shows the Keplerian distribution. The important conclusion drawn here is that close to $r \sim (2-5)r_0$, the angular momentum is higher than Keplerian and at distances farther away, it becomes sub-Keplerian. The effect becomes stronger when the accretion rate goes up. Figure 4.1(b) shows the result for accretion rate 25 times higher than the critical rate and the deviation from the Keplerian curve is also seen to be higher. The velocity of the flow becomes smaller than Keplerian at $r \sim r_0$ as well.

In the case of critical or super-critical accretion around a black hole, the effects of radiation are expected to be the same as that described above. One can study the subject in a reverse order. One can assume an ad-hoc angular momentum distribution which deviates from the Keplerian distribution as above, and find the radiation field

required to produce such a distribution. In Fig. 4.2, a typical angular momentum distribution inside a thick accretion disk (short dashed curve) around a black hole is shown. Typically, the angular momentum of the bulk of the disk is below Keplerian (solid curve) value. Only within a region close to the marginally stable orbit (minimum of the Keplerian distribution), the angular momentum is above Keplerian, or super-Keplerian. The pressure of the radiation pushes the inner edge of the disk much closer to the black hole, i.e., the inner radius of the disk around a Schwarzschild black hole is situated at $2r_g < r < 3r_g$. Since the potential (Fig. 1.4) is less deeper at this range than at $r = 3r_g$, these disks are less efficient than a Keplerian disk. Secondly, matter is accreted by the strong pressure gradient term in the Euler equation, hence viscosity is unimportant.

The thick disk angular momentum distribution intersects with the Keplerian distribution (solid curve) at two locations, r_i and r_c , the inner edge and the center of the disk respectively. At r_c , the pressure not only does not vanish but it is maximum. However, still the flow is Keplerian, because the pressure gradient term vanishes. At $r < r_c$, the pressure gradient term is directed towards the black hole and the flow requires more angular momentum to fight against the combined gravity and pressure gradient term. At $r > r_c$, the pressure gradient term is directed away from the center and the flow requires an angular momentum less compared to the Keplerian value since a part of the pressure gradient term fights against gravity. One of the important characteristics of the equipotential surfaces of a thick accretion disk around a black hole is the presence of a cusp very similar to the Lagrange point in a Roche lobe overflow (cf. Fig. 3.1). In this case, matter fills the closed potential and forms the thick accretion disk, and the excess matter is accreted to the black hole through the cusp. The cusp is formed at r_i between the marginally bound $(2r_q)$ and marginally stable $(3r_q)$ orbits. For comparison, the Keplerian distribution in a Newtonian geometry is also presented in the Figure. The angular momentum in a thick disk is monotonic and intersects this distribution only once, and therefore, no cusp is expected to form in a thick disk in Newtonian geometry.

Before we go about discussing the model in detail, we draw a cartoon figure to indicate forces acting on a blob of matter inside a thick accretion disk. Figure 4.3 shows schematically an equipotential surface. The gravitational force acts radially inwards and the centrifugal force acts in a direction normal to the angular momentum vector. Addition of these two vectors produces a net force along the effective gravity. In order to remain in hydrostatic equilibrium, a force of equal magnitude due to the pressure gradient must act opposite to this direction. The tangents drawn normal to the pressure balance produce the equipotential surface.

Earlier attempts to mimic the super-Keplerian behaviour of the angular momentum distribution were made by choosing the specific angular momentum to be constant inside the disk. Lynden-Bell [172] showed that a flow with a constant angular momentum would avoid the region inside two symmetric vortices (funnels or chimneys) along the axis of the black hole, thought to be located at the center of quasars from very

early days [173]. These funnel-like regions, like two giant vortices along the axis are devoid of matter and filled up with hot and anisotropic radiation field due to leakage of radiation from the disk interior. These regions were considered to be suitable places to accelerate matter to form radio jets. Intensive works followed [75, 174-180] to study the properties of the thick accretion disks. Most of these fully general relativistic models study the properties of the barotropic fluid of constant angular momentum neglecting the self-gravity of the flow, though in more recent works self-gravity has been included. Below, we present a simple model of the thick accretion disk.

4.2 Pseudo-Newtonian Thick Disks

Paczyński & Wiita [75] using a pseudo-Newtonian potential to mimic the Schwarzschild black hole geometry studies the thick accretion disk models assuming that the angular momentum is distributed as a power law of the axial distance. The force balance condition which determines the structure of a thick accretion disk is given by,

$$\frac{\nabla P}{\rho} = -\nabla \phi + \frac{l^2}{(r\sin\theta)^3} \nabla R,\tag{4.2}$$

where, P and ρ are isotropic pressure and density respectively, l is the specific angular momentum inside the disk, ϕ is the gravitational potential, and $R = r \sin \theta$ is the axial distance. In the absence of a complete theory of viscous flow around a black hole, the angular momentum distribution is chosen to be a power law $l(r,\theta) = l_0(r \sin \theta)^n$ inside the disk (θ is the angle measured from the z axis). Here, l_0 and n are positive constants, with $0.5 \ge n \ge 0$. The positivity of n is required by the Höland stability criterion [181] under axisymmetric perturbation: $dl/dr \ge 0$. For simplicity, assume that the equation of state is barotropic, i.e., $P = P(\rho)$. In this case, the left hand side of the equation becomes integrable. $W = W(P) = -\int \frac{dP}{\rho}$ surfaces are equipotential surfaces, which are also surfaces of constant pressure, density and temperature. These surfaces are obtained by integrating above equation as,

$$W(P) - W(P_{out}) = -\frac{1}{2(r-1)} - \frac{l_{out}^2}{2n-2} (r\sin\theta)^{2n-2},$$
(4.3)

where $W(P_{out})$ is the integration constant signifying the potential at the outermost surface with pressure P_{out} . For a given pair (l_0, n) there exists a point inside the disk where the potential is minimum which corresponds to the center of the disk. As in the case of stars, the potential gradually rises outwards till it reaches $W(P_{out})$.

Using above equation of state, one obtains the expression for temperature (in ${}^{o}K$) to be,

$$T_e(r) = T_e(R_{out}) - \left(\frac{\mu\beta c^2}{4R_G}\right) \left\{ \frac{1}{2} \left[\frac{1}{r_{out} - 1} - \frac{1}{r - 1} \right] + \frac{l_0^2}{2n - 2} \left[r_{out}^{2n - 2} - (r\sin\theta)^{2n - 2} \right] \right\}, (4.4)$$

where $R_{out} = r_{out}r_g$ is the distance of the outer edge of the disk on the equatorial plane and R_G , the gas constant, β is the ratio of gas pressure to total pressure and μ is the

mean electron number per baryon. Temperature is maximum at the center of the disk and gradually falls off as one moves away from it.

The equipotential surfaces are shown in Fig. 4.4a. I and C denote the inner edge (cusp) and the center of the disk respectively. Here, the angular momentum is chosen to be higher than marginally stable value and the cusp is present. When angular momentum is farther reduced so that it is everywhere below marginally bound value, the cusp is absent and the equipotentials are quasi-spherical, open and matter cannot stay in to form a disk. In Fig. 4.4b, the equipotentials in the Newtonian geometry are shown to compare the topological properties. As discussed before (cf. Fig. 4.2) no cusp is formed in this case, independent of angular momentum.

When the barotropic equation of state is chosen, surfaces of constant pressure, density and temperature coincide. These quantities are maximum at the center of the disk. Alternative disk models have also been proposed where the accretion is in the equatorial plane [177]. These models are found to be very sensitive to the external boundary condition and could be globally unstable with non-axisymmetric instabilities [182]. In some astrophysical models accretion disks are equipped with corona similar to solar surface [141]. Here, magnetic flux tubes need to be anchored deep inside the disk. This is possible in the isothermal thick disks, or disks in which entropy rises outwards are also considered. These magnetized disks will be studied in §4.7.

4.3 General Relativistic Thick Disks

First few attempts to determine the structure of a thick accretion disk were made using general relativistic equations [174-176]. The equations governing the rotational motion of the flow are:

$$\frac{\nabla_i P}{P + \epsilon} = -\nabla_i (\ln u_t) + \frac{\omega \nabla_i l}{(1 - \omega l)},\tag{4.5}$$

where P and ϵ denote the isotropic pressure and the internal energy density respectively, u_{μ} (with $\mu = t, 0, 0, \phi$) are the four velocity components and $\omega = \frac{u^{\phi}}{u_t}$ and $l = -\frac{u_{\phi}}{u_t}$ denote the angular velocity and specific angular momentum respectively.

When the equation of state is chosen to be barotropic, $P = P(\epsilon)$. In this case, the left hand can be written as the gradient of a potential. The first term on the right hand side is already written in this manner. Hence the remaining term on the right hand side also has to be the gradient of a scaler, i.e., $\omega = \omega(l)$. This is so called von Zeipel theorem. The surfaces of constant ω/l are of great importance as they are the surfaces where angular momentum of the disk must remain constant [174-176, 178-179, 183-184]. In the Schwarzschild geometry, λ is obtained from:

$$\lambda^2 = -\frac{g_{\phi\phi}}{q_{tt}},\tag{4.6a}$$

and in Kerr geometry, it is obtained from,

$$\lambda^2 = -\frac{lg_{\phi\phi} + l^2 g_{t\phi}}{g_{t\phi} + lg_{tt}}.\tag{4.6b}$$

Earlier attempts to study specific cases of these surfaces show cylindrical surfaces which are asymptotically flat cylinders [174], though in general they can be of remarkable complexity. A catalogue of these surfaces [183] show that these surfaces could have toroidal topology as well. A knowledge of these surfaces finds a major application in studying thick accretion disks [178, 179] as well as the study of structure and stability of relativistic rotating stars [184]. The Euler equations could be integrated if angular momentum is chosen to be constant over these surfaces: $l = l(\lambda)$. This prescription allows a generalized study of thick accretion disks for any axisymmetric spacetime. The important point is to realize that a parameter $\lambda = \sqrt{(l/\omega)}$ could be defined which is roughly the Newtonian equivalent of the axial distance. Similar to the power-law distribution of angular momentum by Paczyński-Wiita [75], one could assume the angular momentum distribution to be,

$$l(\lambda) = c\lambda^n, \tag{4.7}$$

with c and n as two positive constants. Vorticity free (l = constant) disks are obtained by putting n = 0 and the rigid body ($\omega = constant$) disks are obtained by putting n = 2. In general, in it observed that for thick accretion disks, $0 \le n < 0.5$. The Rayleigh criteria of stability implies that the angular momentum increases outwards. This is possible with $n \ge 0$ provided $r > 3GM/c^2$, the circular photon orbit in the Schwarzschild geometry. In the Kerr geometry also the function λ behaves in a way that it is monotonically rising outwards outside the photon orbit [179, 184].

4.4 Thermodynamic Condition inside a Thick Accretion Disk

The angular momentum of a thick accretion disk intersects with the Keplerian distribution at two different points (Fig. 4.2). The innermost one of these two is at the inner edge (r_i) of the disk, where the disk is pressure free. At the other intersection (r_c) , the pressure gradient is zero and the pressure of the disk is maximum. Density and temperature are also maximum (for barotropic disks) at this point. In this respect the disk behaves as a toroidal star. Figure 4.5 gives the thermodynamic condition inside a thick accretion disk [2, 185-187]. The variation of central temperature and density in the disk are shown as a function of the ratio of the gas pressure to the total pressure β . Also shown are the optical depth τ (due to Thomson scattering) and entropy density s. Two regions are separated: in region $\tau < 1$, the disk is optically thin and the radiation leaks out, so that thick disks do not form. In the region marked as 'self-gravity', the mass of the disk becomes comparable or more than the central black hole and the self-gravity of the disk cannot be ignored. This happens when $\rho(r_c) \geq M/r_c^3$.

When the self-gravity becomes important, the Keplerian distribution of angular momentum is qualitatively changed [188-190]. Assuming that most of the matter is

concentrated at the center of the disk where the density is maximum, and assuming that the rotational energy of the disk can be ignored compared to the rest mass energy, it is possible to compute the Keplerian distribution of angular momentum fully general relativistically [188]. Figure 4.6 shows the distribution when the mass of the disk is three (short dashed), five (medium dashed) and ten (long dashed) percent as heavy as the central compact object [188]. For comparison, the Keplerian distribution in the absence of the disk is also shown by the solid curve. The presence of the annular ring at $r_c = 9.0$ increases the outward force on the particles for $2 < r < r_c$. Hence the angular momentum required is lower. Similarly, in the presence of the ring, the inward force on particles orbiting at $r_c < r < \infty$ is higher so that the angular momentum needed to stay at a given orbit is higher. These are reflected in this Figure. A thick accretion disk, if stable, is expected to be much hotter when self gravity is important, since the deviation from Keplerian is going to be higher. More realistic models of self-gravitating thick accretion disks have recently been computed, with similar conclusions [189-190].

It is clear that for low mass black holes, the temperature of a radiation pressure dominated disks is very high for a given $\dot{m} = \frac{\dot{M}}{\dot{M}_{Edd}}$. This gives rise to the possibility of significant nuclear reactions in the disk. In general, it is observed [185-187] that unless viscosity is negligible, nucleosynthesis is unimportant in radiation pressure supported accretion disks around super-massive black holes. When a stellar mass black hole is considered, significant nuclear reaction may take place inside the disk [187, 191] and the composition of the gas and the outgoing jet may change [187]. A number of such stellar mass holes in a galaxy would be sufficient to produce the observed metalicity of the galaxy.

4.5 Emitted Radiation from a Thick Accretion Disk

One of the attractive features of a thick accretion disk is that it produces super-Eddington luminosity in the funnel [75]. On the surface of a funnel, the pressure gradient is balanced by the combined effects of the gravity and the centrifugal force. The effective gravity is vary strong close to the axis, and therefore the luminosity exceeds several times the Eddington luminosity. This is a useful feature in the context of cosmic jet acceleration by radiation pressure in the funnel itself [192]. However, excess directionality may also be a negative aspect of this model. The emergent radiation may be highly anisotropic and is emitted mostly along the vertical z-direction. The torus viewed pole-on may show very large soft X-ray/UV excess but the one viewed edge-on may be cooler.

Knowledge of radiation pressure support and the electron scattering opacity allows one to compute the flux radiated from the surface of the torus. The critical flux emitted from the disk surface (assuming it is in radiative and hydrostatic equilibrium), is given by [193]:

$$F_r = \frac{c}{\kappa_T g_{eff}} = -\frac{c}{\kappa_T} (-\nabla \phi + \omega^2 r), \tag{4.8}$$

where g_{eff} is the effective gravity which is perpendicular to the disk surface (Fig. 4.3), $\phi = \phi_s$ the pseudo-Newtonian potential for the Schwarzschild geometry and $\omega = l/r^2$ is the rotational velocity of the flow. The radial dependence of the effective temperature is calculated by equating the flux above with σT_{eff}^4 .

The luminosity of the disk, for the ratio $Q = r_{out}/r_{in} > 50$ is found out to be,

$$L/L_E \sim 3.8 \log Q - 2.43.$$
 (4.9)

(Here the subscripts 'out' and 'in' refer to quantities at the outer and inner edges respectively.) Inside the torus, no local balance of energy is possible, as the radiation transports energy in both the radial and the vertical direction. The total energy liberated is given by,

$$L_q = \dot{M}[e_{in} - e_{out} - \omega_{out}(l_{out} - l_{in})]. \tag{4.10}$$

As the inner edge goes to r_{mb} , the $e_{in} \to 0$, so an extremely large disk is needed to supply the same luminosity.

Characteristics of the spectrum resulting from a typical model [193] is discussed below. Figures 4.7-4.10 show the temperature variation on a thick disk surface, disk spectrum at various inclination angles, specific luminosity at various viewing angles and a comparison of a few model dependent spectra. In Fig. 4.7, temperature distributions in a thin disk (dotted curve) and in a thick disk (dashed curve) are compared for the same central mass and the accretion rate. In Fig. 4.8, the disk spectra at inclination angles (a) $i = 90^{\circ}$, (b) $i = 50^{\circ}$, (c) $i = 25^{\circ}$ and (d) $i = 0^{\circ}$ are compared. Due to the presence of the funnel, the spectrum depends very strongly on the inclination angle. Another way of seeing this is to plot the specific luminosity at a few (observed) frequencies (ν) as a function of inclination angle. In Fig. 4.9, this is shown for $\log(\nu)$ equal to (a) 15.5, (b) 16.0, (c) 16.5 and (d) 17 respectively. In optical and ultraviolet regions, specific luminosity is almost independent of the angle, but at higher frequencies the dependence is very strong and may present some problem in modeling active galaxies. In Fig. 4.10, a comparison of the thin disk spectrum (dashed curve) is made with the spectra of a thick disk with various effects. The solid line represents the spectrum without the reflection effects from the funnel whereas the dotted line includes the reflection effects. The dash-dotted curve is obtained by assuming a sum of black body spectrum from each annulus of the disk. Compared to a thin disk, the thick disk (with reflection effects) produces more emission at higher frequencies.

4.6 Ion Pressure Dominated Thick Disks

When the cooling time scale is longer compared with the in-fall time the protons remain very hot — close to the virial temperature and the electrons cool through

synchrotron or Compton processes. The excess ion pressure can puff-up the disk and can produce a different kind of thick disk, the so called ion pressure supported disk [194]. If Coulomb coupling is the only ion-electron coupling, then the condition of longer cooling time scale is satisfied if [2],

$$\dot{M}\alpha^{-2} < 50\dot{M}_{Edd} \tag{4.11}$$

For any $\alpha \sim v_{infall}/v_{freefall}$ there is always some smaller \dot{M} for which above condition may be satisfied and ion pressure disk could be formed. This condition may, in particular be true, if in some AGNs the matter supply is scanty.

The above condition assumes the absence of pair-productions or collective plasma processes which may strengthen ion-electron coupling and cause rapid cooling of protons [195-196]. In the presence of these collective processes (in presence of strong magnetic field, for example) an ion torus may be rapidly cooled and deflated. The restoring effects can bring the cool disk back to the hot torus configuration. Such instability may also cause AGN variabilities [196].

In a gas pressure dominated thick disk the gas may be completely photo-dissociated and the protons would accrete onto a black hole (as they 'feel' the magnetic viscosity), while neutrons would orbit till they decay. As a result, neutron torus may form which combines with the incoming fresh matter and produce neutron-rich elements in the galaxy [197].

4.7 Magnetized Thick Disks

We have already discussed a few models of magnetized thin accretion disks (§3.4). No similar detailed study has been made of magnetized thick accretion disks and the associated jet production. A partial reason is that the thick accretion disks (both the rotation dominated radiation tori and the advection dominated ion tori) may have very little angular momentum and matter may fall into the hole without any need for a viscosity. Furthermore, the thick accretion disks have funnels or chimneys where the anisotropic radiation field could be sufficiently strong to accelerate radio jets. Thus there was no immediate need to construct detailed magnetized thick disk models. Nevertheless, magnetic fields are observed in jets and magnetic activity in the funnel regions are thought to be responsible for the rapid variation of polarization in BL-Lacs. Therefore, this requires some attention.

Recently, a thorough analytical study has been made of the behaviour of the axisymmetric flux tubes inside a thick accretion disk [141]. Magnetic field is expected to be brought along with the in-falling matter and are expected to be sheared to form mainly toroidal flux tubes in the disk. Due to the joint effects of drag, Coriolis force, magnetic tensions, buoyancy force a significant fraction of these fields are found to be emerging in the funnel whereas the remaining fraction would be expelled from the outer

parts of the disk. A few important observations of this study is that (a) if the disk is sufficiently hot $(T_p > 4 \times 10^{10} K)$, the magnetic tension dominates all other effects and the tube collapses catastrophically on the axis (rapid pinch), possibly squeezing out plasma in the disk along the axis of the black hole in the process to form radio jets. (b) Formation of coronae in an accretion disk is not *automatic*, namely, presence of magnetic field inside a disk does not automatically imply that a hot magnetic coronae would form. The formation requires the ability of the accretion disks to anchor flux tubes inside the disk. This means that the disk should have an internal structure akin to the solar interior and the entropy must increase outwards. If the entropy condition is proper, the coronae would form, otherwise it would come out of the disk as a whole without causing any flare. In former case there would be sporadic flaring events on the disk surface, whereas in the latter case, the collapse of fields in the funnel would cause destruction of the inner part of the disk and formation of blobby radio jets. Detailed observation of GRS1915+105 shows these features [198]. Since the inner part of the accretion disk could literally disappear by this magnetic process, radio flares should accompany reduction of X-ray flux in this objects. Since the physical process is generic, such processes could also be responsible for the formation of jets in active galaxies and similar anti-correlation may be expected, though time delay effects are to be incorporated for a detailed modeling.

4.8 Thick Accretion Disk – To Be or Not To Be?

Thick accretion disks have many 'pleasant' features such as the production of supercritical luminosity, possible ability to collimate jets, magnetic activity in the funnel as the explanation of the rapid variability in BL-Lacs, production of metalicity in the galaxy by nucleosynthesis, etc. [180]. However, as mentioned above, the strong anisotropic nature of the emission properties of a thick accretion disk is a major disadvantage. Another problem is that a non-accreting thick disk is found to be dynamically and globally unstable due to non-axisymmetric instability [199-201]. In this type of instability, disks with a large shear were found to be unstable due to non-axisymmetric perturbations. A necessary condition in this instability is that the co-rotation radius (the radius where the mode rotates with the disk fluid) of the corresponding normal mode must be within the disk. Since usually the angular velocity of the flow decreases outwards, the mode rotates slower or faster compared to the flow depending on whether it is inside or outside the corotation resonance. Angular momentum is transported from regions inside the resonance radius to the region outside which leads to amplification of the perturbation and therefore the growth of instability. The instability grows faster if the angular momentum distribution is closer to a constant. It is shown in particular, that if the angular momentum distribution were represented as a power law $l(r) \propto r^n$. then, for n < 0.27, the perturbation is found to grow. The analytical work are carried out using non-accreting slender torus approximation and the perturbation is found to grow fastest for $n \sim 0$. Numerical simulations of slender tori verify the presence of this instability [202-203] though for very thick accretion disks the instability grows much more slowly [204]. The presence of accretion processes is found to remove the instability as well [205-206].

An ideal thick accretion disk requires the flow to have a very low angular momentum and a very small radial velocity. Typically, the angular momentum required is a little above the marginally stable value close to a black hole. Also, a radiation pressure supported thick accretion disk ideally has negligible radial velocity. It is unclear how such a structure can be formed with matter supply from stars and wind, given that either the incoming matter has Keplerian angular momentum with a little radial motion, or with low angular momentum but significant radial motion. Thus matching this structure with outer boundary cannot be smooth. What in reality may be happening is that in the presence of small angular momentum matter first 'hits' the centrifugal barrier and forms a strong shock (§5) where the flow thickens to form a torus and subsequently falls on a black hole after passing through the inner sonic point. High accretion rate would cause radiation pressure dominated tori, whereas low accretion rates would produce ion pressure supported tori. The low angular momentum pre-shock flow is almost freely falling. The flow in the immediate post-shock region has a very little radial velocity and therefore it is rotation dominated. This region resembles a thick accretion disk with an atmosphere and outgoing winds ($\S6$). Thus, it is possible that in reality, thick disks, formed by strong shock waves or by sudden deviation of the disk from Keplerian distribution, might be formed which becomes transonic at the inner edge and therefore stable under non-axisymmetric instability. It is also possible that since a well defined funnel with a geometrically sharp boundary need not exist, the anisotropy of the emission might be reduced, particularly because the disk is of much smaller in size $(r_{out} \sim r_{shock} \sim 10-20r_q)$. The collimating property of jets may suffer at the same time, but this is not crucial since toroidal fields produced by the strong shear in the post-shock region can collimate the jet as well. The variation of the accretion rate changes the shock location and the shape and size of the thick accretion disk. This might cause variabilities observed in many active galaxies (§7).

5 Advective Disks

We discussed in the previous Sections that in the case of accretion on central black holes in binary systems and in active galaxies and quasars, the angular momentum of the flow need not be Keplerian everywhere. In a binary system, matter could be accreted both through the winds (sub-Keplerian flow) and through the Lagrange point (Keplerian flow). In the absence of winds, specially in low mass X-ray binary (LMXB) systems where winds may be absent, the sub-Keplerian matter could still be produced from the Keplerian flow close to the black hole. In an active galaxy, the same situation may prevail although it is likely that matter is accreted solely from the winds of stars very far away which has very little angular momentum. The sub-Keplerian flow, whether it originates from Keplerian disk or not, will have a significant velocity, since the centrifugal force is not sufficient to overcome gravity. In either of the above cases, the sub-Keplerian flow should behave in the following way: at first, it accretes quasispherically with an infall time similar to the free-fall time $t_{infall} \sim r/v_{ff} \sim r^{3/2}$ until the specific angular momentum of the flow becomes comparable to the local Keplerian angular momentum $l^2(r) \sim l_{Kep}^2(r_s)$. At this point, $r_s \sim l^2(r)$ ($\sim 8r_g$ for marginally bound angular momentum) the flow may be virtually stopped by the centrifugal barrier, and a standing shock will form. Subsequently, the flow continues its journey to the black hole and accretes on it supersonically. Due to pressure effects, the shock actually forms farther away and also when the angular momentum is less that marginally stable value. The shock can form anywhere between 10 to $10^4 r_g$ depending on the specific energy and angular momentum of the flow and the heating and cooling mechanisms. The kinetic energy of the almost freely falling advecting flow is thermalized rather abruptly at the shock which heats up the flow to about the virial temperature. The shock heated region occupies a very large area of the disk since it forms far away from the inner edge, and therefore it influences the spectrum of the disk significantly. In fact, this region can be compared with the boundary layer of a star where the soft radiations are hardened through Comptonization and other effects. If the viscosity of the flow is small enough so that the shock is strong and thin, the hot and the cold phases of the flow co-habit side by side. The shock re-processes soft photons (either from synchrotron photons from the preshock flow, or from soft photon from Keplerian disk on the equatorial plane) and emit observed gamma rays. The location and the strength of the shocks are very sensitive to the flow parameters, such as the energy and the angular momentum, and therefore, such discontinuous flows may explain correlated variabilities in UV/X-ray and optical frequency bands observed in many active galaxies and quasars. Shock acceleration of particles and photons can explain the origin of the high energy γ -rays and cosmic rays [122-130]. In recent years, observations of the continuum as well as line emission properties indicate that many of the disks in active galaxies and quasars are non-Keplerian [207-212]. Black hole candidate spectra also show transition from soft to hard states which are described by varying degree of combination of the power law spectra with soft 'black-body' type spectra. We shall briefly discuss the structure of these sub-Keplerian disks in the present Section and differ the discussion on the observational properties till §7.

Although we have emphasized on shock formation by sub-Keplerian flows, it is not the 'only' choice. In a large range of parameter space, spanned by angular momentum, entropy and the polytropic index, the shocks are not formed at all. The flow passes either through the outer sonic point, or through the sonic point. Sometimes, for higher viscosity, the flow with have both the choices simultaneously, though, in such cases, it chooses only the one passing through the inner sonic point because of higher entropy at the inner sonic point of the flow. An important reason why these shock solutions could be relevant is that even when the steady shocks are not predicted by theoretical analysis, they form but travel backwards to infinity while making the disk subsonic and possibly Keplerian. Thus shocks are important ingradients in undertanding a disk formation, specially when matter supply is time dependent. When the flow only has the outer sonic point, it forms ion supported advective flows as in [194].

We have already shown in §2 that a pure adiabatic spherical flow cannot have a shock as the flow has only one sonic horizon. In the presence of heating and cooling and other geometrical effects, shocks can form in a spherical flow, but the efficiency of emission was not seen to be very high as the shock forms very far away from the black hole: $r \sim 10^6 r_q$. In the context of the study of the solar and stellar wind, where the variation of geometrical shape of the wind and deposition of radiation momentum can introduce more than one sonic point, shock waves are found to be common. Indeed, they are studied for quite some time [213]. In the context of the accretion flows, the presence of a significant angular momentum is found to increase the number of saddle type sonic points from one to two [214]. Early numerical simulations reveal the presence of traveling shock waves in low angular momentum accretion flows [215-216] (possibly due to the inherent viscosity, and the choice of input parameters). Subsequently, using a simple model of adiabatic flows, it was pointed out that similar to the solar wind case, multiple sonic points may lead to the formation of shock waves in the disks as well [217]. Currently, shock waves in accretion disks (whether steady or non-steady) are considered to be indispensable parts of accretion of low angular momentum region of a disk [68, 77, 218]. In this Section, we present the theory of these discontinuous accretion flows very briefly.

In the next subsection, we present model equations and provide physical arguments as to why there are multiple critical points in sub-Keplerian accretion flows around black holes. In §5.2, we present solutions of adiabatic flows with discontinuities. In §5.3, we present an example of the isothermal solution which includes viscosity. In §5.4, we use most general heating and cooling processes in shock study and discuss about the unification of disk models around black holes. In §5.5, we discuss self-similar solutions of the model equations in Newtonian geometry. In §5.6, we discuss the nature of shock solutions in Kerr geometry and in magnetized disks. In §5.7, we deviate from axisymmetric situation considered so far, and discuss self-similar non-axisymmetric spiral shock waves. In this case, a density perturbation (induced by a passing companion, globular cluster, or tidal capture of molecular clouds) can become steeper as it propagates towards the black hole and produce spiral shock waves in the disk. These disks

are sufficiently non-axisymmetric so as to influence the observational results.

5.1 Model Equations and Multiplicity of Critical Points

The models discussed in §2 - §4 are somewhat limited in the sense that either the angular momentum (§2), or the advective effects (§3 - §4) or the pressure effects (§3) are not fully taken into account. A 'grand unified' disk model, must not only include all these effects self-consistently, but also reproduce the earlier disk models as special cases, and at the same time produce new solutions (if possible) such as the solution with discontinuities (shock waves). Above all, it should produce the steady and time-dependent spectra compatible with observations. We shall present solutions of this model in this Section. To avoid complexity of the most general equations, one usually solves vertically integrated equations which reduces the dimension of the problem from three to two and are therefore easily solvable.

The steady state model equations which one has to use are [68, 76-77, 219]:

(a) The radial momentum equation:

$$\vartheta \frac{d\vartheta}{dx} + \frac{1}{\rho} \frac{dP}{d\rho} + \frac{\lambda_{Kep}^2 - \lambda^2}{x^3} = 0, \tag{5.1a}$$

(b) The continuity equation:

$$\frac{d}{dx}(\rho x h \vartheta) = 0, (5.1b)$$

(c) The azimuthal momentum equation:

$$\vartheta \frac{d\lambda(x)}{dx} - \frac{1}{\rho x h} \frac{d}{dx} \left(\frac{\alpha P x^3 h}{\Omega_{Kep}} \frac{d\Omega}{dx} \right) = 0$$
 (5.1c)

(d) The entropy equation:

$$\Sigma \vartheta T \frac{ds}{dx} = Q^{+} - Q^{-} \tag{5.1d}$$

Here λ_{Kep} and Ω_{Kep} are the Keplerian angular momentum and Keplerian angular velocity respectively, Σ is the density ρ vertically integrated, h = h(x) is the half-thickness of the disk at radial distance x, ϑ is the radial velocity, s is the entropy density of the flow, Q^+ and Q^- are the heat gained and lost by the flow. $\lambda(x)$ is the angular momentum distribution.

First we argue in general terms that the flow satisfying the above set of equations has multiple critical points.

In the case of a black hole accretion, matter which is at rest at infinity can fall onto a black hole even when the specific angular momentum is as high as marginally stable value $\lambda < \lambda_{ms}$ (§1). When $\lambda_{ms}(x_{ms}) < \lambda < \lambda_{mb}(x_{mb})$, matter will form a disk which may accrete and lose binding energy $1 - \phi(x_{in})$ where, $\phi(x_{in})$ is the potential energy at the inner edge x_{in} of the disk. When $\lambda > \lambda_{mb}(x_{mb})$, matter at rest at infinity will be bounced back by the potential barrier (Fig. 1.4). Matter with energy higher than $\phi = \phi_{max}(\lambda)$ can overcome the barrier and fall into a black hole.

The above picture is valid for particle dynamics. When one considers a fluid motion, the picture is somewhat different due to the presence of flow pressure. Here, matter starts 'feeling' the centrifugal barrier even before actually reaching it, and starts piling up before falling onto a black hole. Here, the ram pressure of the advective, low angular momentum, pre-shock flow roughly matches with the thermal pressure of the rotation dominated post-shock flow and a standing shock wave is formed. In order to have a shock, however, the flow, subsonic at a large distance, must first pass through a sonic point far away from the black hole (the so-called outer sonic point similar to what is seen in a Bondi flow) and becomes supersonic. After this, the flow passes through a shock transition and becomes subsonic. In order to satisfy the inner boundary condition, i.e., supersonicity on the horizon, the flow has to pass through another sonic point close to the horizon (inner sonic point). Thus, to have a shock solution on an accretion flow, there should be at least two saddle type $(\S 1)$ critical points. If the gas has polytropic index closer to 5/3 (actually, $\gamma \gtrsim 1.5$ in the above model), the outer sonic point does not exist, and shocks can form only if the flow is already supersonic (such as from winds of another star).

To understand the origin of the multiple critical points in a rotating accretion flow, we write the specific energy of an inviscid, thin, isothermal flow (obtained by integrating eq. 5.1a with $P/\rho = constant$),

$$\mathcal{E} = \frac{1}{2}\vartheta^2 + a_0^2 log(\Sigma) + \frac{1}{2}\frac{\lambda^2}{x^2} - \frac{1}{2(x-1)}$$
 (5.2)

Here, the first term is the radial kinetic energy (ϑ = radial velocity), second term is the thermal energy (a_0 =constant sound speed; Σ = surface density), third term is due to the rotational kinetic energy (λ = constant specific angular momentum) and the final

term is due to the gravitational potential energy, as described by the Paczyński-Wiita [75] pseudo-potential (§1). Ignoring the slowly varying logarithmic term, we note that the constant energy surfaces behave differently in three different regimes:

(a) Close to the black hole $(x \sim 1)$:

When the flow is close to the horizon, the potential energy term is dominant compared to the rotational kinetic energy term and the energy behaves as,

$$\mathcal{E} \sim \frac{1}{2}\vartheta^2 - \frac{1}{2(x-1)}.\tag{5.3a}$$

The negative sign signifies that the contours of constant energy in the v vs. x space have hyperbolic character. The asymptotes cross to form a saddle type (inner) sonic point [Fig. 2.2], very similar to a Bondi flow.

(b) Far away from the black hole $(x \sim \infty)$:

At distances very far away from the horizon, the potential term is again dominant over the rotational energy term, which falls off as $1/x^2$. As a result, the energy varies with x exactly same way as in eq. 5.3(a):

$$\mathcal{E} \sim \frac{1}{2}\vartheta^2 - \frac{1}{2(x-1)}.\tag{5.3b}$$

In this case also, the contours of constant energy are of hyperbolic type and the asymptotes cross to produce the outer saddle type sonic point [Fig. 2.2].

(c) Intermediate distances $(x \sim \lambda)$:

At intermediate distances, the rotational energy term dominates over the gravitational potential energy and energy equation becomes:

$$\mathcal{E} \sim \frac{1}{2}\vartheta^2 + \frac{\lambda^2}{2x^2}.\tag{5.3c}$$

In this case, the positive sign indicates that the contours of constant energy would be elliptical in shape, similar to the energy contours in simple harmonic oscillators. An 'O' type or center type sonic point [Fig. 2.2] is formed at the center of the ellipse.

Thus the flow may have three sonic points, two saddle type and one center type. Of course, whether or not all these three points would actually exist will depend on the angular momentum of the flow and the heating and cooling processes determining the polytropic index of the flow (determining the thermal energy term, ignored in above arguments). If the angular momentum is significant (and $\gamma \leq 1.5$), all these three

points would be present. In the absence of angular momentum, three critical points would merge into a single one as in the Bondi flow (§2). Another point of importance is that the inner sonic point exists only in the case of black hole accretion [77, 218]. A sufficiently compact neutron star with a radius less than ~ 2.5 , may also have the inner sonic point, tough such compactness may be unlikely. The two outer sonic points may exist in the case of stellar accretion as well. This can give rise to significant differences in observational results between disks around a black hole and a neutron star, for instance [68, 77, 218]. The inner edge of a flow enters the black hole supersonically whereas it must be subsonic on a neutron star. Thus, the flow will Comptonize soft photons in an optically thick, cool disk and produce a spectrum characteristics of a convergent flow [74] with a spectral index $\alpha \sim 2-1.5$ (§7). However, for a neutron star, the flow is highly subsonic at the surface, and such a component should not be present. This is indeed what is observed.

Although the pseudo-Newtonian potential has been used in the above argument, it is easy to verify that a full general relativistic treatment [77] also produces the same number of sonic points and display the same behaviour. Similarly, arguments about the number of critical points remain valid even when the more general flows are considered. In the case of viscous flows, the 'O' type sonic point is changed to a spiral type (Fig. 2.2) as in the case of a damped simple harmonic oscillator. In the case of magnetized flows, the number of sonic points could be five (Fig. 3.11).

5.2 Adiabatic Disks with Discontinuities

5.2.1 Steady State Solutions

We assume a thin, rotating, adiabatic accretion flow. In this model, the complete radial momentum equation and the accretion rate equation are written on the equatorial plane, while in the vertical direction only hydrostatic balance condition is used $h(x) \sim ax^{3/2}$. The momentum balance equation which must be satisfied at the shock is vertically integrated. This model is known as one-and-a-half dimensional flow or hybrid flow [77, 218]. For simplicity, the pseudo-Newtonian potential [75] (§1) is used in place of full general relativity. Flow is assumed to be inviscid, and therefore the specific angular momentum is constant everywhere. Matter is accreted only due to pressure gradient force. If a shock wave exists, the entropy remains separately constant, before and after the flow. The entropy generated at the shock as well as the entire energy is completely advected towards the black hole. These flows are thus raditively inefficient.

The dimensionless energy conservation equation can be written as (cf. eq.5.1a):

$$\mathcal{E} = \frac{\vartheta_e^2}{2} + \frac{a_e^2}{\gamma - 1} + \frac{\lambda^2}{2x^2} - \frac{1}{2(x - 1)}.$$
 (5.4)

Here ϑ_e and a_e are the non-dimensional radial and the sound velocities on the equatorial

plane measured in units of velocity of light c, x is the non-dimensional radial distance measured in units of the Schwarzschild radius $r_g = 2GM/c^2$, and λ is the constant specific angular momentum in units of 2GM/c. Subscripts e refer to the quantities measured on the equatorial plane. Apart from a geometric factor, the mass flux conservation equation is given by

$$\dot{M} = \vartheta_e \rho_e x h(x), \tag{5.5}$$

If the flow is in hydrostatic equilibrium in the transverse direction, the height of the disk h(x) is given by,

$$h(x) = a_e x^{1/2} (x - 1). (5.6)$$

We write the mass conservation equation in terms of ϑ_e and a_e in the following way:

$$\dot{\mathcal{M}} = \vartheta_e a_e^q x^{3/2} (x - 1), \tag{5.7}$$

where q = 2n + 1, n being the polytropic index of the flow. q takes the value 2n if the flow boundary is fixed. $\dot{\mathcal{M}} \sim \dot{M} K^n$ would be called 'accretion rate' here, though it changes at the shock due the generation of entropy (i.e., variation of K). In a radiation dominated flow, the total pressure of written as the sum of gas pressure and the radiation pressure. Defining β to be the ratio of the gas pressure to total pressure we obtain [211]:

$$\dot{\mathcal{M}} = 1.26 \times 10^{-21} \frac{M_{\odot}}{M} \frac{1 - \beta}{\beta^4} \frac{\dot{M}}{\dot{M}_{Edd}},$$
 (5.8)

in c.g.s. units. Here, n=3 is used for the illustration purpose and pure hydrogen is used as the chemical composition of the gas. \dot{M}_{Edd} is the Eddington accretion rate given by, $\dot{M}_{Edd} = L_{Edd}/c^2$. For $n \leq 2$, the shock solutions do not exist in this model.

5.2.2 Sonic Point Conditions

The sonic point conditions as obtained following the procedure in §2,

$$\vartheta_c^2 = \nu a_c^2, \tag{5.9a}$$

and

$$a_c^2 = \frac{2(x_c - 1)}{\nu x_c^2} \frac{(\lambda^2 K(x_c) - \lambda^2)}{(5x_c - 3)}.$$
 (5.9b)

where $\nu = \frac{2n}{2n+1}$. The energy of the flow \mathcal{E} with angular momentum λ passing through a critical point at x_c is given by,

$$\mathcal{E} = \frac{\lambda^2}{2x_c^2} \left[1 - \frac{(4n+4)(x_c-1)}{5x_c-3} \right] + \frac{(n+1)x_c}{(x_c-1)(5x_c-3)} - \frac{1}{2(x_c-1)},\tag{5.10}$$

or, conversely,

$$\lambda^2 = \frac{[\mathcal{E}(x_c - 1) - 2(n+1)x_c + 1](5x_c - 3)x_c^2}{[(4n+1) - (4n-1)x_c](x_c - 1)}.$$
 (5.11)

Although we started with three conserved quantities, namely, \mathcal{E} , $\dot{\mathcal{M}}$ and λ , not all of them can be specified independently if the flow is transonic. This is because we have three unknowns $\vartheta_e(x)$, $a_e(x)$ and x_c , and we need three equations to solve them uniquely. Together with the two transonic conditions 5.9(a-b), we need only one more quantity: either the energy or the accretion rate. Thus, exactly as in the Bondi flow, $\dot{\mathcal{M}} = \dot{\mathcal{M}}(\mathcal{E}, \lambda)$. In other words, the parameters for a stationary transonic solution lie on a hypersurface:

$$\mathcal{F}(\mathcal{E}, \dot{\mathcal{M}}, \lambda) = 0. \tag{5.12}$$

Of course, if one is interested in the actual entropy density, or mass flux \dot{M} (and not the combined form $\dot{\mathcal{M}}$), one has to supply another quantity, such as $\rho = \rho_{\infty}$ at the outer boundary as in the Bondi flow.

5.2.3 When does a Flow Contain Shocks?

When there are two 'X'-type critical points, \mathcal{M} (i.e., entropy) calculated at these two points are not usually equal [77, 218]. That is, if we denote the outer and the inner critical point locations as x_o and x_i respectively, then, $\mathcal{M}(\mathcal{E}, \lambda, x_o) \neq \mathcal{M}(\mathcal{E}, \lambda, x_i)$. However, for a given λ , there exists one and only one energy \mathcal{E}_m such that $\mathcal{M}_m(\mathcal{E}_m, \lambda, x_o) = \dot{\mathcal{M}}_m(\mathcal{E}_m, \lambda, x_i)$. In Fig. 5.1, we plot \mathcal{E} against $\dot{\mathcal{M}}$ for a given angular momentum $\lambda = 1.675$. This so-called "swallow-tail" singularity is produced by the projection of an otherwise smooth curve, drawn for a constant angular momentum on the surface:

$$x_c = x_c(\dot{\mathcal{M}}, \mathcal{E}). \tag{5.13}$$

A flow with parameters from the branch AB passes through the inner 'X'-type critical point, and with parameters from the branch CD passes through the outer 'X'-type critical point. The parameters on the branch BC are calculated at the 'O'-type critical points and are unphysical since a flow cannot pass through these points. The crossing point M represents the case when $\dot{\mathcal{M}}$ at both the critical points are identical. The parameter space division in terms of the energy of the flow is also shown in this Figure. For $\mathcal{E} \geq \mathcal{E}_i$ there is only one critical point. For $\mathcal{E}_m \leq \mathcal{E} \leq \mathcal{E}_i$, the accretion rate $\dot{\mathcal{M}}_o \geq \dot{\mathcal{M}}_i$. For $\mathcal{E}_s \leq \mathcal{E} \leq \mathcal{E}_m$, $\dot{\mathcal{M}}_o \leq \dot{\mathcal{M}}_i$. For $\mathcal{E} < \mathcal{E}_s$, the flow passes through only the outer critical point. Similar division can be made in terms of the accretion rate. Referring to Figure 5.1, a shock therefore connects flows with two sets of parameters $(\lambda, \mathcal{M}, \mathcal{E})$, one from the branch AB and the other from the branch CD. The basic stationary equations above contain no dissipative terms and therefore can be consistent only with the Rankine-Hugoniot shock solutions which conserves energy. Schematic shock transitions in typical cases are shown in Figure 5.1 by horizontal lines s_1s_2 and w_1w_2 . The former one is in accretion and the latter one is in wind. However, the shocks in thin, otherwise dissipation-free astrophysical flows may radiate away energy through the upper and the lower boundaries simply because of the presence of the relatively strong temperature gradient. If the length scale in which such radiations occur is small compared to the other (such as the diffusion and cooling) length scales of the flow, one can include such radiative effects by suitable choices of the shock conditions.

5.2.4 Shock Conditions

A shock is characterized by four a priori unknown quantities: the shock location x_s , and the possible jumps in the two independent velocities u, a and in the polytropic constant K (entropy, or \mathcal{M}) i.e.,

$$x = x_s, (5.14a)$$

$$\Delta a = a_{+}(x_s) - a_{-}(x_s), \tag{5.14b}$$

$$\Delta u = u_{+}(x_s) - u_{-}(x_s), \tag{5.14c}$$

and finally,

$$\Delta K = K_{+} - K_{-}. \tag{5.14d}$$

Subscripts minus (-) and plus (+) denote quantities before and after the shock. Independent of the nature of a shock, the conservation of the fluxes of mass and momentum,

$$\dot{M}_{+} = \dot{M}_{-},$$
 (5.15a)

$$W_{+} + \Sigma_{+} u_{+}^{2} = W_{-} + \Sigma_{-} u_{-}^{2}, \tag{5.15b}$$

provide two constraints on these four quantities. W and Σ denote the pressure and density integrated over the vertical direction. Since we are dealing with inviscid flows and axisymmetric shocks, $\lambda_+ = \lambda_-$ is always fulfilled and gives no extra constraint. The pre-shock quantities are determined by the outside boundary conditions in the case of accretion flows or by the inner boundary conditions in the case of winds. The post-shock quantities, which are given by $(\lambda_+, \dot{\mathcal{M}}_+, \mathcal{E}_+)$, must obey the sonic point conditions 5.9(a-b) at the critical point after the shock. This provides the third condition. The fourth and the final condition models the nature of the dissipative processes (cf. eq. 5.1d) at the shock and uniquely characterizes the shock as well as the post-shock flow properties. A single parameter [219],

$$f(x_s) = \frac{(Q_+ - Q_-)_+}{(Q_+ - Q_-)_-} \tag{5.16}$$

determines the nature of the energy dissipation and/or the entropy generation at the shock (eq. 5.1d). Therefore, these shocks may differ qualitatively from the "Rankine-Hugoniot" shocks discussed in the standard text books in the way the fourth condition, connected with dissipation, is formulated. This freedom is not surprising, as the astrophysical flow is in direct contact with the surroundings, as opposed to shock waves in a standard shock tube problem where the flow is confined in a tube and preserves energy. Secondly, the entropy generated at the shock need not be advected completely. A part of it could be radiated away as well.

In a general case, the fourth shock condition can be formally written as [77, 219],

$$(\mathcal{E}_{+} - \mathcal{E}_{-}) - A(\dot{\mathcal{M}}_{+} - \dot{\mathcal{M}}_{-}) = 0.$$
 (5.17)

This can be considered as the most general shock condition. For a given set of initial parameters, choosing the ratio A from 0 to $+\infty$, one obtains all the possible shock solutions. This parameter basically describes the behaviour of the entropy generated at the shock. Three special cases of eq. (5.17) are of significance. They are: (a) A = 0. In this case the energy is conserved at the discontinuity and Rankine-Hugoniot shocks $(\mathcal{E}_+ = \mathcal{E}_-)$ are formed. The entropy generated at the shock is entirely advected by the flow inwards of the shock for the disks (and outwards of the shock for the winds) and the raditive efficiency is completely negligible. (b) $A = \infty$. Here the entropy generated at the shock is totally radiated away, and the isentropic compression waves $(\dot{\mathcal{M}}_+ = \dot{\mathcal{M}}_-)$ are formed. (c) At some intermediate A an isothermal shock wave $(a_+ = a_-)$ may form where the energy and entropy change in a manner that the temperature of the flow at the shock remains constant [219, 77].

Assuming the Rankine-Hugoniot shock conditions, the location of the shock is easily determined, by rewriting shock conditions in terms of the Mach numbers before and after the flow. This gives the following conditions [77, 218]:

$$C = \frac{\left[M_{+}(3\gamma - 1) + \frac{2}{M_{+}}\right]^{2}}{2 + (\gamma - 1)M_{+}^{2}} = \frac{\left[M_{-}(3\gamma - 1) + \frac{2}{M_{-}}\right]^{2}}{2 + (\gamma - 1)M_{-}^{2}}.$$
 (5.18)

The constant C as defined above is invariant across the shock. Mach numbers of the flow just before and after the shock can be written down in terms of C as,

$$M_{\pm}^{2} = \frac{2(3\gamma - 1) - C \pm \sqrt{C^{2} - 8C\gamma}}{(\gamma - 1)C - (3\gamma - 1)^{2}}.$$
 (5.19a)

The product of the Mach numbers is given by,

$$M_{+}M_{-} = \frac{2}{[(3\gamma - 1)^{2} - (\gamma - 1)C]^{1/2}}.$$
 (5.19b)

The weakest shock which may form in a transonic flow in vertical equilibrium has the pre-shock Mach number $M_{-} = \sqrt{2/(\gamma + 1)}$. The corresponding location of the shock coincides with the sonic point. It is easy to verify that the post-shock Mach number is also the same. Thus, the minimum shock strength is unity, which is expected from a self-consistent model of this type.

5.2.5 Examples of Complete Solutions with Discontinuities

Returning to Fig. 5.1, we note that for $\mathcal{E} \geq \mathcal{E}_i$, there is only one critical point and no shock is possible. For $\mathcal{E}_m \leq \mathcal{E} \leq \mathcal{E}_i$, $\dot{\mathcal{M}}_o \geq \dot{\mathcal{M}}_i$ and a shock in an accreting flow is not possible either, since the entropy will decrease in the process. However, shocks can form in winds with the change of entropy corresponding to $\dot{\mathcal{M}}(w_1) - \dot{\mathcal{M}}(w_2)$. For $\mathcal{E}_s \leq \mathcal{E} \leq \mathcal{E}_m$, shocks form in accretion (but not in winds) with the change of entropy calculated from the two intersection points s_1 and s_2 . For $\mathcal{E} < \mathcal{E}_s$, a flow passes only through the outer critical point and the shocks are not possible. This figure was drawn

for a given angular momentum of the flow. For other angular momentum the region of interest will be different [77, 218]. A general procedure to obtain the shock locations must involve verifying if the Mach number relation (eq. 5.18a) is satisfied at any point in the flow. This is done by plotting the contours of constant \mathcal{M}_{-} and constant \mathcal{M}_{+} (i.e., contours of pre-shock and post-shock entropies) for a given set of energy \mathcal{E} and angular momentum λ and see whether/where they intersect. An example of a selfconsistent shock solution (in the limit of zero viscosity) is shown in Fig. 5.2 for the flow parameters $\mathcal{E} = 0.689 \times 10^{-2}$, $\dot{\mathcal{M}}_- = 0.831 \times 10^{-5}$, $\lambda = 1.65$. The four possible shock locations denoted by X_{s1} , X_{s2} , X_{s3} , and X_{s4} are shown where all the shock conditions are simultaneously satisfied. In the case of black hole accretion flows, which are subsonic at a large distance and supersonic on the horizon, X_{s2} and X_{s3} are the only two possibilities for shock locations. However, for accretion onto the neutron stars, X_{s1} is also a formal possibility provided the inner sonic point actually forms. In reality, in a neutron star accretion, the inner sonic point may not exist, and the shock transition jumps to a branch which will remain subsonic till it hits the surface. The contours are of constant 'accretion rate' $\dot{\mathcal{M}}$. Only the solution with arrows is the allowed stationary solution, the others are just the integral curves.

In Fig. 5.2 one notices that there are four locations, X_{s1} , X_{s2} , X_{s3} and X_{s3} , where all the shock conditions are satisfied and both the shocks are of same strength with the same amount of entropy generated. However, since the flow cannot pass through all the shocks, only one of them can be stable at the most. Which one of these two shocks is stable? A local stability analysis does not seem to be able to answer this question uniquely [77, 218]. However the riddle is easily resolved by using a simple consideration of varying the (total) pressure at the post-shock flow. If a shock is perturbed on either way from its equilibrium location, (where pressure balance is maintained), and the excess pressure is directed in such a way that the shock returns to its stationary location, then that shock must be stable [220]. Indeed through extensive numerical simulations (§6), as well as analytical works [220-223] it has been established beyond doubt that in accretion, the shock located at X_{s3} is stable, while solutions at other locations are unstable. The stable shock generates exactly the right amount of entropy which is advected with the flow to enable it to pass through the inner sonic point. Since the flow is chosen to be adiabatic, entropy is separately constant before and after the shock. Another important feature of these solutions is that, the flow is radiatively inefficient (in fact, energy and entropy are completely advected with the flow towards the black hole). In the case of the winds, the situation is completely opposite. Here, the entropy at the outer sonic point is higher than the entropy at the inner sonic point. The shock located at X_{s2} is found to be stable [220]. Details are already in the literature [77, 218] and we do not discuss them here.

5.3 Isothermal Advective Flow with Viscosity

Important properties of viscous transonic flows emerge only when global solutions of eqs. 5.1(a-d) are obtained. Most complete global solution was first found in the

context of viscous, isothermal flows [77, 224-225]. The inviscid isothermal flow has two possible locations where shocks may form, exactly as in the adiabatic case. However, when the viscosity is added, the most important change that occurs is the change of the 'O' type sonic points to the spiral type sonic point (Fig. 2.2). At the same time, the stable shock at X_{s3} (away from the black hole) becomes weaker, breaking the ambiguity. At a critical viscosity parameter (in this case, $\alpha_c \sim 0.015$, which depends upon the disk temperature, sonic point location x_{in} and $\lambda(x_{in})$, the shock at X_{s3} disappears altogether. At the same time, the topology of the solution changes so as to allow two smooth solutions, one with a higher dissipation passes through the inner sonic point and the other with a lower dissipation passes through the outer sonic point. Figures 5.3(a-d) show this transition of topologies. In Figs. 5.3a and 5.3c, low viscosity parameter ($\alpha = 0.01$) is used. The shock at X_{s3} (which is stable) is weaker but it is still present. The shock-free solution can pass only through the outer sonic point, exactly as in the inviscid case, but in reality it does not since it has a choice to pass through the shock. In Fig. 5.3(b) and Fig. 5.3(d) drawn for $\alpha = 0.02$, the flow becomes shock-free, and passes through the inner sonic point. In both the cases, the flow becomes Keplerian at a large distance. The flow also has a solution to pass through the outer sonic point, but the energy required is higher. The critical α parameter above which the shock disappears and the flow becomes Keplerian depends upon other assumptions, such as the viscosity prescriptions and the accretion rate and angular momentum at the inner sonic point as we discuss below. The numerical simulation results of this case will be discussed in the next Section §6 [225].

5.4 Most General Advective Flow and Unification of Accretion Disk Models

Fig. 5.4(a-b) show the first attempt to unify different sub-Keplerian disk models in the limit of very small viscosity [77, 218]. In 5.4a, the 'accretion rate' (which is a combination of true accretion rate and entropy, see Eq. 5.7) is plotted against angular momentum. The zone marked by I, represents the region where the flow has only the inner sonic point. The zone marked by W, has two sonic points but, $\dot{\mathcal{M}}(\mathcal{E}, \lambda, x_o) \geq \dot{\mathcal{M}}(\mathcal{E}, \lambda, x_i)$, so that shocks are possible in winds but accretion can also occur through the inner sonic point. The zone markes by A has two sonic points but, $\dot{\mathcal{M}}(\mathcal{E}, \lambda, x_o) \leq \dot{\mathcal{M}}(\mathcal{E}, \lambda, x_i)$ so that shocks are possible in accretion if shock conditions are satisfied. The zone marked by O has only outer sonic point respectively. Fig 5.4b is further divided to show whether or not shocks actually form. If viscosity is higher than α_c shocks disappear altogether since the topology changes, and this particular sub-division is modified on a case by case basis.

Referring to Eqn. 5.1(a-d), one notes that typically, for optically thick flow, one has, in the limit of diffusion approximation, $Q_- = 4acT^4/3k\Sigma$, and for optically thin flows, Q_- is given by bremmstrahlung, Comptonization and other processes (such as synchrotron processes if magnetic field is present). The heat generation with α viscosity is simply, $Q_+ \propto \alpha P x \frac{d\Omega}{dx}$. The result is however same as above. The critical viscosity

 $0 < \alpha_c < 1.0$ becomes a function of the relative importance of Q_- vis-a-vis Q_+ , the viscosity parameter, location of inner sonic point and the angular momentum at the inner edge of the disk. For $\alpha < \alpha_c$, the flow may have a shock but for $\alpha > \alpha_c$ the flow simply passes through the inner sonic point similar to what was discussed §5.3. Thus, the most general transonic flow shows no new topology other than what was seen in the context of isothermal flows.

To understand the shock formation properties, one needs to know how entropy and energies behave at the sonic points ([226], Fig. 5.1). Fig. 5.5 shows entropy s vsenergy $E(x) = 0.5\vartheta^2 + (\gamma - 1)^{-1}a^2 + 0.5 \lambda^2/x^2 - 0.5 (x - 1)^{-1}$ plots at the sonic points for $\gamma = 4/3$ (left) and $\gamma = 5/3$ (right) for $\alpha = 0$, 0.4 0.8 and $f = (Q_+ - Q_-)/Q_+ = 0$ (cooling dominated) and f = 1 (heating dominated) respectively (as marked on the curves). Angular momentum at the inner edge $\lambda_{in} = 1.6$ is chosen. Solid, dashed and dotted regions of the curves are the saddle, nodal and spiral (circle type for $\alpha = 0$) type sonic points respectively (§2). For $\gamma = 4/3$, the branches AMB and CMD (or the like in other curves in this figure) are the loci for inner (x_{in}) and outer (x_{out}) sonic points (77, 218) similar to what was discussed about Fig. 5.1. For a shock in accretion to be possible, pre-shock flow parameter must lie somewhere on the branch MD and the post-shock flow parameter must lie somewhere on MB as long as the energy and entropy conditions: $E(x_{in}) \leq E(x_{out})$ and $s(x_{in}) \geq s(x_{out})$ are satisfied. A typical shock transition \vec{ss} is shown (cf. Fig. 5.1). For $\gamma = 5/3$, the outer sonic point does not exist in this model as discussed above (but can exist in a thin disk with a constant height, for example). Thus shocks can form only if the flow is already supersonic (such as, when originates from winds of a companion). For both γ s, one notices that as the viscosity is increased, the outer sonic point no longer remains saddle type and only the inner sonic point exists. Thus, shock transitions are no longer possible. Flow parameters (e.g., the inner sonic point) originally on the branch of type AM, enters in the branch of type MB(i.e., below M) as α is increased from 0 to α_{c1} and shocks become possible. However, it escapes the shock region for $\alpha > \alpha_c$. Thus, for $\alpha > \alpha_c$, only allowed solutions are those which pass through the inner sonic point and therefore no shock solution in accretion is possible.

Fig. 5.6 shows an example of a most general solution with a shock wave, where $Q_-/Q_+=0.5$ is chosen everywhere and $\alpha=0.05$ (here, $\alpha_c\sim0.1$). The stable shock transition is shown by the vertical dashed curve. For $\alpha>\alpha_c$, the faster rate of angular momentum transport in the post-shock region eventually drives the shock wave to a large distance making the flow subsonic and Keplerian. Secondly, if $\alpha>\alpha_c$ in the equatorial plane and $\alpha<\alpha_c$ above, then the pre-shock and post-shock solutions are described by optically thick Keplerian disk and optically thin transonic disk respectively. This property is used in §7 where the most general disk model and its observational properties will be discussed.

One important aspect of viscous, transonic flow which was not adequately stressed so far, is that an originally Keplerian disk could become sub-Keplerian very close to

the black hole. This could be seen easily from the angular momentum distribution of the viscous flow (from eq. 5.1c) ([224-226]):

$$\lambda(x) - \lambda(x_{in}) = \frac{\alpha a^2 x}{v}$$

Fig. 5.7 shows examples of the ratio of the disk angular momentum distribution to the Keplerian distribution (for $x < 3r_g$, $\lambda_{Kep}(x) = \lambda_{3r_g}$ is kept for stability reasons) as a function of distance from the black hole [68]. The ratios show deviation from Keplerian due to advection, pressure and viscous effects. Three diverse cases have been chosen to illustrate how non-Keplerian the flow can get. In Case A (marked 'A'), $\lambda(x_{in}) = 1.88$, $x_c = 2.2$, $\alpha = 0.005$, $\gamma = 4/3$ (radiation pressure dominated) and $Q_- = Q_+$. The flow deviated from Keplerian disk at $x_{Kep} = 7.5r_g$ and even becomes super-Keplerian (ratio > 1) close to the black hole. In Case B (marked 'B'), $x_c = 2.3$, $\lambda(x_{in}) = 1.7$, $\gamma = 5/3$ (gas pressure dominated), $\alpha = 0.02$ and $Q_- = Q_+$. Here the flow deviates from Keplerian at $90r_g$ and always remained sub-Keplerian. In both the cases above, there is no shock formation. In Case C (marked 'C'), the flow passes through a shock at $x = 13.9r_g$ (angular momentum distribution remained continuous) and remains completely sub-Keplerian after deviating from the Keplerian disk at $x = 480r_g$. The parameters chosen are $\lambda(x_{in}) = 1.6$, $x_c = 2.87$, $\gamma = 4/3$, $\alpha = 0.05$ and $Q_- = 0.5Q_+$. This important result enables one to construct a general accretion disk model as discussed in §7.

To be concrete about heating and cooling processes, we present a simpler example here with a power-law cooling $\Lambda \propto \rho^2 (T/T_0)^{\alpha_b}$ in the flow and the polytropic index $\gamma = 5/3$. For $\alpha_b = 0.5$, this represents bremmstrahlung cooling. Assume that $\alpha = 0$, so that $\lambda = \text{const.}$ The governing equations could be written as:

(a) The entropy equation:

$$\frac{\partial(e + \frac{P}{\rho})}{\partial x} - \zeta_{\alpha} \frac{a^{2\alpha_b} \rho}{\vartheta} = 0 \tag{5.20a}$$

(b) The radial momentum equation:

$$v\frac{\partial \vartheta}{\partial x} + \frac{1}{\rho} \frac{\partial P}{\partial x} + \psi'(x) = 0, \tag{5.20b}$$

(c) The continuity equation:

$$\frac{1}{x}\frac{\partial}{\partial x}(\rho \vartheta x) = 0. \tag{5.20c}$$

Here, x is the radial coordinate, $\psi(x)$ is the effective potential energy $\psi(x) = g(x) + \lambda^2/2x^2$ with g(x) as the radial force potential, which in the pseudo-Newtonian model takes the form: $g(x) = -\frac{1}{2}(x-1)^{-1}$, e is the internal energy $e = \frac{P}{(\gamma-1)\rho}$, ϑ is the radial component of velocity and a is the adiabatic sound velocity: $a^2 = \frac{\gamma P}{\rho}$. Prime denotes derivative with respect to x. ζ_{α} is the non-dimensional bremsstrahlung loss coefficient,

$$\zeta_{\alpha} = \frac{j\rho_{ref}x_{ref}\mu^{\alpha}}{(m_{p})^{2-\alpha}\gamma^{\alpha}\kappa^{\alpha}v_{ref}^{2}}$$
(5.21)

where, $\mu=0.5$ and $j=1.4\times 10^{-27}$ c.g.s. unit for ionized hydrogen, m_p is the mass of the proton, and κ is the Boltzman constant. The cooling law to be used is $\Lambda=\zeta_{1/2}\rho^2(T/T_0)^{\alpha}$. In this case, the coefficient is constant and only the cooling exponent α varies. ρ_{ref} is the reference density at the outer edge, $v_{ref}=c$, $x_{ref}=2GM/c^2$, and T_0 is the reference temperature.

Figure 5.8 shows the example of the shock solution with $\alpha_b = 0.5$ (solid) and $\alpha_b = 0.6$ (long-dashed). The short-dashed curve is without cooling for comparison. Due to cooling, the shock becomes weaker and comes closer to the black hole. A thorough understanding requires a fully time dependent solution [227], because the flow is expected to show interesting behaviour. As the shock is perturbed and propagates outwards, the post-shock region becomes hotter since the relative velocity between the shock and the incoming flow is higher. The cooling rate goes up eventually stopping the outward motion of the shock when the flow has a sufficient time to cool. As the shock returns towards the black hole, lower temperature and therefore lower pressure in the post-shock region is unable to balance the pre-shock ram pressure and the shock collapse continues till the higher temperature closer to the black hole is reached. The shock then overshoots this region and bounces from from higher pressure region and the cycle continues. Thus the shock may show oscillations whenever the cooling time scale roughly agrees with the infall time scale: $t_{cool} \approx t_{infall}$. In the next section (§6) we show some results of time dependent simulations which show these oscillations [227]. Similar oscillatory behaviour has also been seen in shocks in accretion columns of white dwarfs [228].

5.5 'Advection Dominated' Disk Models

Recently, it has been stressed that a particular aspect of the above solutions, namely, the advection of energy and entropy of the transonic equations may be more important than realized before. A sub-class of the general solution is thus termed 'advection dominated disks'. As we stressed before, because of advection, the energy release is very inefficient as it is advected towards the black hole. However, the assumption of the vertical integration of the above model was removed by Narayan and his collaborators [229]. This latter study shows that the disks may or may not be advection dominated depending on the cooling processes operating inside the disk. The importance of these works lies in their ability to provide a global solution of quasi-spherical viscous flows (albeit using very restricted assumptions, such as self-similarity) and to establish that the quasi-spherical solutions obtained by these models are similar in every respect to the vertically averaged viscous transonic models. This confirms earlier numerical simulation works [259] as discussed in the next Section.

A global solution is obtained where a number of physical processes are included. (a) The assumption of self-similarity is made with a constant ratio of heating and cooling [229] Q_+/Q_- , (b) wherever this assumption is dropped, solution is obtained at a given

radial distance R of a Keplerian disk [230] and was shown that advection will stabilize the flow (an attempt to show this earlier was made in [146]), (c) bremsstrahlung, is added self-consistently, (d)the 'bridging formula' of Wandel and Liang [231] is used to take into account $\tau \sim 1$ regions. The basic conclusions of these models are the followings: (1) that the advection of entropy is very important in establishing a stable solution of accretion disk, (2) the winds may be formed if the flows have positive specific energies, (3) the angular velocity Ω is far less than the Keplerian velocity Ω_K , (4) the efficiency of radiation is found to be very small, since most of the energy is advected away.

These newly discovered results completely confirms fully consistent transonic advective flows solutions discussed earlier (§5.2-5.4) and therefore do not represent any fundamentally new solution. Importance, however, lies in their ability to separate out the effects of advection. An artifact of the self-similar transonic flow model is that it has constant Mach number throughout. This sharply contrasts with the exact nature of Mach number variation shown in Figs. 5.3(a-b) and 5.6, where the flow Mach number varies considerably while passing through the sonic points and shock waves. In an exact solution [226], even around $r \sim 10r_g$, generally $v_r << v_\phi$ and so advection is not dominated.

5.6 Axisymmetric Shock Waves in a Few Other Systems

5.6.1 In Kerr Geometry

Solution including shock waves using fully general relativistic equations in Kerr geometry produce very similar results as in Schwarzschild geometry. However, the sonic points and the location of the shock waves are found to be very sensitive to the Kerr parameter a. In particular, in the contra-rotating flows, the shocks were seen to be formed farther away from the black hole [77, 232]. Numerical simulations by smoothed particle hydrodynamics show that these shocks are stable [233] as well.

5.6.2 In Magnetized Flows

In the case of a magnetized accretion, other than regular Alfvén point at u=r=1, five critical points may be present in the flow (§3). Accordingly, a large number of new topologies emerge (Fig. 3.11a-f). These new topologies allow the formation of shock waves in accretion as well as in winds. In a complete solution of accretion disk which includes a standing shock wave, the flow must satisfy a set of conditions on either side of the discontinuity. These are [77, 161]:

(a) the total energy flux is conserved:

$$\frac{1}{2}\vartheta_{r+}^2 + \frac{1}{2}\vartheta_{\phi+}^2 + na_+^2 - \vartheta_{\phi_+}\Omega r_+ = \frac{1}{2}\vartheta_{r-}^2 + \frac{1}{2}\vartheta_{\phi-}^2 + na_-^2 - \vartheta_{\phi_-}\Omega r_-, \tag{5.22a}$$

(b) the total mass flux is conserved:

$$\rho_+ \vartheta_{r+} = \rho_- \vartheta_{r-}, \tag{5.22b}$$

(c) the radial momentum is balanced:

$$p_{+} + \rho_{+} \vartheta_{r+}^{2} + \frac{B_{\phi+}^{2}}{8\pi} = p_{-} + \rho_{-} \vartheta_{r-}^{2} + \frac{B_{\phi-}^{2}}{8\pi}, \tag{5.22c}$$

(d) the transverse momentum is balanced:

$$\rho_{+}\vartheta_{r+}\vartheta_{\phi+} - \frac{B_{r+}B_{\phi+}}{4\pi} = \rho_{-}\vartheta_{r-}\vartheta_{\phi-} - \frac{B_{r-}B_{\phi-}}{4\pi}, \tag{5.22d}$$

(e) the radial magnetic flux is conserved:

$$B_{r+} = B_{r-}, (5.22e)$$

and finally,

(f) the field equation is independently satisfied on either side of the shock:

$$\vartheta_{\phi+}B_{r+} - \vartheta_{r+}B_{\phi+} = \vartheta_{\phi-}B_{r-} - \vartheta_{r-}B_{\phi-}. \tag{5.22}$$

Six conditions 5.22(a-f), together with the transmagnetosonicity of the post-shock and the pre-shock flows are enough to calculate all the variables uniquely including the location of the shock [77, 161].

In Figure 5.9, an example of the shock formation in an accretion flow is presented [77, 161]. Here, two critical solutions passing through rotational and Bondi-like slow magnetosonic points are connected by a shock transition. Paczyński-Wiita potential [75] is chosen for computational purpose. The parameters are: $L = \Omega = 1.45$ and $g_0 = 1.334$. The solution is shown in arrows and the shock transition is shown by a vertical dashed line. Other parameters are: $\mathcal{E} = 0.2$, $\dot{\mathcal{M}}_- = 0.4857$, $\dot{\mathcal{M}}_+ = 0.5074$, $B_{\phi+} = 0.556$, $B_{\phi-} = 1.106$, $\theta_{\phi+} = 1.875$, $\theta_{\phi-} = 2.424$, $u_+ = 0.417$, $u_- = 0.621$, $r_s = 1.0995$, r_s being the location of the shock. Dashed curves are the contours of constant slow magnetosonic wave velocities. The pre-shock flow is super(slow)magnetosonic and the post-shock flow is sub(slow)magnetosonic and both are sub-Alfvénic, thus satisfying the condition of the formation of the slow shocks [77]. Shock location is found to be unique. These works are carried out with pseudo-Newtonian potentials. However, no new solution topologies appear when the exact Kerr geometry is used [162] and therefore, possibly no new types of shock solutions are expected.

5.7 Non-Axisymmetric Spiral Shock Waves

5.7.1 Introduction

So far, we have concentrated on specific model flows which are axisymmetric. However, in a binary system with one component a compact star, the disk moves in a non-axisymmetric potential because the secondary normal star exerts non-axisymmetric tidal force on the accretion disk around the compact primary. Numerical simulations have shown formation of spiral density waves eventually steepening to produce spiral shocks [142, 234-236] In the case of active galaxies, spiral shocks could be induced due to the passage of a massive object, such as a globular cluster, molecular cloud, dwarf galaxy or another black hole [6, 237]. These shocks may also be induced by non-axisymmetric instabilities inside the disk or due to tidal capture of a molecular cloud.

Study of spiral shocks are important because they allow accretion to take place in the absence of any explicit viscosity in the flow. Furthermore, recent observations of the temporal [239-247] and spatial variability [4-5] of line emissions from ionized disks around black holes indicate that the disks around super-massive black holes may have spiral shock waves [6, 212]. We shall discuss it here very briefly for the sake of completion of the review on accretion disks which include shock waves.

5.7.2 Basic Flow Equations

Consider some matter which is accreting on a Newtonian star non-axisymmetrically. Assume that the flow equations are two-and-a-half (2.5) dimensionally correct in the sense that whereas radial and azimuthal components of the momentum equations are kept exactly, momentum of the flow in the vertical direction (direction off the equatorial plane of the disk) is neglected. Assume that the flow is in hydrostatic equilibrium at each point in this direction, i.e., vertical pressure balance is maintained throughout. Assume that the shocks are self-similar [248].

In this sub-section, the radial distance r is measured in units of $\frac{GM}{c^2}$, the velocity components are measured in units of c, time is measured in units of $\frac{GM}{c^3}$. The equations of motion in cylindrical polar (r, ϕ, z) coordinate are first written in the spiral coordinate $(x = r \text{ and } \psi = \phi + \beta(r))$ and the solutions are assumed of the form [77, 248]:

$$u = x^{-n_u} q_1(\psi), (5.23a)$$

$$v = x^{-n_v} q_2(\psi), (5.23b)$$

$$\rho = x^{-n_{\rho}} q_{\rho}(\psi), \tag{5.23c}$$

$$p = x^{-n_p} q_p(\psi), \tag{5.23d}$$

$$\frac{d\beta}{dx} = x^{-n_{\beta}}B. \tag{5.23e}$$

Here u and v are the radial and the azimuthal velocity components, ρ and p are the density and the pressure of the flow, 2h is the local vertical thickness of the flow. n_u , n_v , n_ρ , n_P , n_β and B are constants. Gravitational potential is that of a point Newtonian body. Pseudo-Newtonian potential used in the previous Sections cannot be used here, because that would introduce a preferred length scale in the system, breaking self-similarity. Let the equation of state be: $P = K \rho^{\gamma}$, where K is the adiabatic constant, a measure of entropy of the flow and γ is the adiabatic index. In terms of the polytropic index n, $\gamma = 1 + 1/n$. The quantity K remains constant in the azimuthal direction in between the two shocks. It can change only at a shock. In the absence of the radiative loss, the generated entropy is advected by the flow.

Using above form of the solutions in the respective hydrodynamic equations one obtains [77, 248],

$$n_u = n_v = \frac{1}{2}, n_\beta = 1, n_\rho - n_p = -1.$$
 (5.24)

The adiabatic sound speed $a = (\partial p/\partial \rho)^{1/2}$ varies as

$$a = (\gamma p/\rho)^{1/2} = x^{-1/2} q_3^{1/2}(\psi). \tag{5.25}$$

Accordingly, from the consideration of the hydrostatic balance, the thickness of the disk is obtained as

$$h = ax^{3/2} = xq_3^{1/2}(\psi), (5.26)$$

apart from a geometrical constant. Using such variations, the continuity equation takes the form:

$$q_1 q_\rho q_3^{1/2} (3/2 - n_\rho) + \frac{\partial}{\partial \psi} [q_\rho (q_2 + Bq_1) q_3^{1/2}] = 0.$$
 (5.27)

Integrating the above equation, one obtains

$$(3/2 - n_{\rho}) \int_{0}^{2\pi} q_{1}q_{\rho}q_{3}^{1/2} d\psi + [q_{\rho}(q_{2} + Bq_{1})q_{3}^{1/2}]_{0}^{2\pi} = 0.$$
 (5.28)

The bracketed term must be equal at both the limits since it is the mass flux in the azimuthal direction. The first term, i.e.,

$$\dot{M}_{\parallel} = \int_0^{2\pi} q_1 q_{\rho} q_3^{1/2} d\psi, \qquad (5.29)$$

represents the net mass flux in the radial direction, which is non-zero only if $n_{\rho} = 3/2$. We choose this value of n_{ρ} . However, $n_{\rho} \neq 3/2$ (where the net flux is zero) case may also be important in certain circumstances where both the wind and the accretion take place simultaneously. If instead of the assumption of vertical equilibrium, the flow is chosen to be conical or of constant thickness [236], the value of n_{ρ} would be 3/2 and 1/2 respectively and h would be independent of ψ .

A simple solution is obtained by choosing the 'spirality' B to be given by $B = \tan \theta$, where θ is the constant winding angle (angle between the radial direction and the

outward tangent of $\psi = \text{constant curve}$). With this choice, flow variables take the forms:

$$u = x^{-1/2}q_1(\psi), (5.30a)$$

$$v = x^{-1/2}q_2(\psi), \tag{5.30b}$$

$$a = x^{-1/2}q_3^{1/2}(\psi), (5.30c)$$

$$\rho = x^{-3/2} q_o(\psi), \tag{5.30d}$$

$$p = x^{-5/2}q_p(\psi), (5.30e)$$

and

$$\frac{d\beta}{dx} = x^{-1}B. ag{5.30}f$$

The adiabatic constant K, which is a measure of entropy, remain constant on a flow line in between two shocks, but changes at the shock itself. The variation of K with the radial distance can be calculated using the definition of the sound speed and is given by,

$$K(x) = x^{3\gamma/2 - 5/2} K_o(\psi), \tag{5.30g}$$

where $K_o = q_p/q_\rho^{\gamma}$ is constant on a given spiral coordinate ψ . Since entropy must increase inwards in accretion and outwards in winds, one must have

$$\gamma \le 5/3$$
, or equivalently, $n > 3/2$, (5.31a)

for accretion, and,

$$\gamma \ge 5/3$$
, or equivalently, $n < 3/2$, (5.31b)

for winds.

The location of the sonic surface could be studied following procedures as described in earlier Sections. The nature of sonic points depends strongly upon the conserved quantities of the flow. The usual practice is to supply two parameters, B—measuring the spirality of the shock surface and q_{2c} —the azimuthal velocity coefficient on the sonic surface. Other quantities, such as q_1 , q_3 , γ are determined self-consistently. One also assumes that when shocks are present they are equidistant in the angular scale ψ . Sonic surfaces which lie in between the shocks are also equidistant. Thus, if there are n_s number of shocks, the angular distance in between two successive shocks as well as sonic surfaces is given by $\delta\psi = 2\pi/n_s$. Figure 5.10 shows schematically an accretion disk which includes two shocks at $\psi = \psi_{s1}$ and $\psi = \psi_{s2}$ and two sonic surfaces at $\psi = \psi_{c1}$ and $\psi = \psi_{c2}$. One can write down the location of a shock formed just prior to a sonic surface as $\psi_{s1} = \psi_{c1} - \epsilon \delta \psi$, and the location of a shock formed just after the sonic surface as $\psi_{s2} = \psi_{c1} + (1 - \epsilon)\delta\psi$, where $0 \le \epsilon \le 1$ is to be determined for the given conserved quantities of the flow.

Some of the important properties of the self-similar shock solutions are: whereas the velocity components individually depend upon the radial distance, Mach numbers of pre-shock and post-shock flows as well as the strength of the shock do not. Since the disk is self-similar, the height of the disk is directly proportional to the distance on the surfaces of constant ψ . The height varies in the azimuthal direction as ψ changes. Angular momentum per unit mass λ dissipated at the shock is given by,

$$\frac{\lambda_{+}}{\lambda_{-}} = \frac{q_{2+}}{q_{2-}}.\tag{5.32}$$

Recently, this self-similar procedure to solve vertically averaged flow has been adopted to solve axisymmetric flows as well [229]. This self-similar vertically averaged flow is found to be very useful to study quasi-spherical flows [229].

5.7.3 Examples of Spiral Shocks in Accretion Disks

To obtain a solution which includes spiral shock waves, one supplies the number of spiral shocks n_s , the spiral angle parameter $B = \tan \theta$, and the azimuthal velocity coefficient q_{2c} . The polytropic index n, the shock location ϵ and the entire velocity field, namely, $q_i(\psi)$ becomes known.

Figures 5.11(a-b) show an example of solution with a two-armed spiral shock. In Fig. 5.11(a), a 2-shock solution in accretion is shown with dashed vertical lines (ψ_{s1} and ψ_{s2}) [77]. Crosses represent locations of the sonic surfaces (ψ_{c1} and ψ_{c2}). Figure 5.11(b) shows the variation of velocity components in between two shocks. The input parameters are: B=-1.0, $q_{2c}=0.02$, and the results are n=6.1842, $\epsilon=0.7274$, $M_-=1.0394$, $M_+=0.8909$. The strength of the shock M_-/M_+ is 1.17. The shock is therefore reasonably weak.

One intriguing conclusion in the study of non-axisymmetric shocks is that there are two distinctly separate regions in the parameter space, one marked by a large rotational velocity and a small radial velocity $(v_r << v_\phi)$ and the other by a large radial velocity and a small rotational velocity $(v_r >> v_\phi)$, for which shock solutions exist in accretions and winds [77, 248]. These are the 'high' and the 'low' states respectively. Furthermore, it is observed that in the 'high' state, shocks are substantially weak for small B, and very strong for large B. The existence of these bifurcations in states may be significant in the astrophysical context. The accretion rate is found to be lower in the 'high' state and higher in the 'low' state. Many of the variabilities observed in the disk spectra could be due to such switching. In numerical simulations of accretion disks, (§6), spiral shocks are found to be unstable under various circumstances and it is possible that these are the manifestations of the instabilities discussed in this Section.

6 Numerical Simulation of Accretion Processes

6.1 Introduction

In the last few sections we have concentrated on the theoretical models of the accretion flows. Though analytical models are always welcome, they basically describe the stationary properties of an accretion disk. There are increasing evidence that most of the astrophysical systems which are believed to harbour accretion disks and black holes are also variable in some time scales or the other. Occasionally, the same system shows variabilities in completely different time scales (an example being the X-Ray flickering and optical micro-variabilities in Blazers, see §7). Sometimes, analytical stability analysis helps to sort out which of the models might be applicable, but such a procedure is often very difficult and scopes are limited. Theoretical models investigate various types of different detailed *physical* processes (e.g., radiative transfer) in an accretion disk (which is why there are so many models in the literature), but fail to study detailed dynamical behaviour. The numerical simulations, on the other hand, have been very successful in obtaining the dynamical behaviour (e.g., presence of various instabilities, shock waves, etc.), though many of the important physical ingredients are missing (which is why there are only a few disk simulation results available). In fact, the goal of these two directions so far have been complementary and it is possible that neither of them can ever be totally independent. Though it might seem obvious that the results from numerical models should correspond more closely to the observations and therefore they must play a major role, so far, the aim and scope of this approach have been found to be limited as well. In future, one has to include more physical processes in the code so that both the physics and the dynamics emerge from the same simulation. In certain situations, the exact nature of physical processes (such as, viscous process which is essential for transporting angular momentum) may be illusive and the theoretical input to numerical works has been very little. This has resulted in the fact that many of the disk simulations have no 'physical' dissipation. They are energy and angular momentum conserving, and show violent behaviour such as strong shock waves, contrary to some of the more popular theoretical disk models which do not have these discontinuities.

Some of the theoretical models of accretion disks which we discussed in the past have been put to rigorous tests of numerical simulation. Below, we present some important developments in this direction in recent years.

6.2 Simulation of Bondi-Hoyle-Lyttleton Accretion

In §2, we discussed steady state accretion on a compact star immersed inside an infinite medium. In a variety of astrophysical situations, such as (a) in massive X-ray binaries containing neutron stars and black holes which have wind producing OB companion, (b) in symbiotic binaries where white dwarfs accrete from the winds of

cool giants, etc. such accretion processes have been found to take place. Since these are typically time dependent situations, a number of recent works carry out numerical simulations of these systems. From these results we have learned the dependence of mass and angular momentum accretion rates on various physical parameters [249-257]. We present here a summary of our present understanding of the numerical results.

In case of the flow with a finite density and velocity gradients, Matsuda et al. [250] and Taam & Fryxall [251] show that a steady state is not achieved. Blondin et al. [252] performed a two dimensional simulation of gas flow in the orbital plane of a massive X-ray binary system. The mass accretion is primarily fueled by the radiation driven wind from an early-type companion. In these simulations a new phenomenon was discovered. It was noticed that instead of a disk-like accretion, the flow makes an unstable channel to accrete onto the compact object. The channel itself switches sides or 'flip-flops' episodically. In between two states, a transient disk structure is formed which is found to change its sense of rotation. These simulations were further repeated with higher resolutions with adiabatic or nearly isothermal [254-255] and isothermal gas [255] and the same unstable behaviour was verified. In these mostly two dimensional simulations, matter accretion rate is found to be similar to the Bondi rate (eq. 2.6), but the angular momentum transfer rate is only about thirty percent of the angular momentum deposited on the accretion cylinder $\sim 0.3 GM/v_{\infty}$.

Fig. 6.1 presents a typical simulation result of the two dimensional wind accretion. Here the medium at infinity is chosen to be homogeneous. The density contours at times (a) 28.35, (b) 30.00, (c) 35.10 and (d) 37.50 are shown. Here the distances and times are measured in units of R_A and R_A/a_{∞} , respectively. The sound crossing time through the whole grid is 8 in this unit. The flow is chosen nearly isothermal: $\gamma = 1.005$. The flip-flop occurs in a time scale of the sound crossing time of the flow close to the compact object, and possibly directly proportional to the sound crossing time of the central object itself, as a large object is found to develop instability only very slowly.

The growth of this instability in two-dimensional accretion always follow this sequence [254]: radial modes are first excited which generates 'pumping' type accretion where sometimes more matter is dumped than the compact object can accrete. This leads to the formation of a dome-shaped shock on the upstream side of the object. The entire shock cone moves entirely on one side or the other while forming small accretion disks which switches its sense of rotation. Eventually, however, the shock cone settles down to the symmetric position and the accretion is less violent.

In the more realistic case of simulations in a three-dimensional flow, the flipflop instability was not found to be very strong, or perhaps negligible [254, 257]. The angular momentum transfer is also found to be smaller than what is observed in the two dimensional simulations. This behaviour has an important bearing on the study of the quasi-spherical accretion flows with some angular momentum as well as to construct a generalized accretion disk model around black hole as we shall see below.

6.3 Simulation of Inviscid Flows

The first significant attempt to study the behaviour of matter around black holes was made by Wilson [258]. An Eulerian, fully general relativistic, first-order backward space difference technique was used. The spatial resolution was low and the system was evolved till $\sim 100GM/c^3$. It was shown that the large angular momentum accretion is accompanied by shock waves which travel outwards. This code was later improved upon, with the number of grid points as well as the evolution time higher by several orders of magnitude. A series of very important simulations were made with this code to show that thick accretion disks can indeed form in inviscid flows [215-216]. These simulations also confirm the results of Wilson [258] that non-steady shock waves are formed which travel outwards. From the post-shock flow, a very strong wind is generated which is hollow in nature and 'hugs' the funnel wall. Due to the inviscid nature of the simulation, centrifugal force kept the flow away from the axis of symmetry. In Fig. 6.2 we reproduce a typical simulation result of Hawley, Smarr & Wilson [216]. The flow is inviscid and the angular momentum of the flow at the outer boundary is chosen to be l = 3.77GM/c. The contours of constant density and the velocity vectors are shown. The figure is drawn at $t = 300GM/c^3$. Several features of the thick accretion disk, such as the accretion through the cusp, the formation of the funnel and the outflow are very clearly recognizable. A large number of simulations of the disk were subsequently carried out [202-205] to check if the thick accretion disks were unstable due to the so-called 'Papaloizou-Pringle' instability [199-201] discussed earlier (§4.8).

These simulation results are understood clearly in the light of what is discussed in §5 about the shock formation in accretion flows. In above simulations, no standing shock waves were found because the parameter space (spanned by energy and angular momentum) for which standing shocks might form were not used at the boundary. Numerical study of standing shock waves are obtained in a series of very recent simulations [220, 225, 259]. These authors use Smoothed Particle Hydrodynamics (SPH) code written in axisymmetric co-ordinate system using Paczyński-Wiita [75] potential. The shocks are found to form *exactly* where they are predicted theoretically, particularly in a one-dimensional, axisymmetric, thin disk. At the beginning of the simulation, a transient behaviour is experienced by the flow, after which the flow assumes only the supersonic branch of the analytical solution. After a small perturbation is introduced at the outer edge, a shock appeared close to the inner edge of the disk. It then traveled outwards until it reached the analytical solution where it settled down. Thus, it was clear that in the presence of perturbations (which are normal for a realistic flow), the flow chooses the solution which include shock waves (higher entropy solution). In the case where the outer boundary condition does not allow shock solution at all, the perturbation is damped out and only the shock-free transonic solution is chosen.

Figure 6.3 shows an example of the simulation of a thin accretion disk which includes standing shock waves [220]. Mach number of the flow is plotted against the radial distance (in units of the Schwarzschild radius of the central black hole). Solid curves are simulation results and the dashed curves are the supersonic and subsonic branches respectively. Two vertical dashed lines indicate locations of the analytically predicted shock transitions, the outer one being stable. After a transient phase, a shock forms close to the inner edge which then travels outward till it reaches the outer stable shock. The specific energy and the specific angular momentum were chosen to be $\mathcal{E} = 0.011c^2$ and $\lambda = 3.8GM/c$ respectively.

In the thick 2-D inflow simulations, shocks are found to form without explicit introduction of the perturbation, probably because in 2-D systems turbulence generated act as a perturbation [259]. As the simulation starts, the low angular momentum advective flow is almost freely falling till it hits the centrifugal barrier. Here, a part of the flow bounces back and the shock wave formed travels outward and settles down at a location slightly outside the location predicted by a one-and-a-half dimensional model (§5.2). This deviation is probably due to the turbulent pressure in the flow just behind the shock and/or inaccuracy of the 1.5D model which ignores the vertical component of velocity altogether. These simulations also find strong wind formation (as in the finite element methods discussed above), and the wind is found to become supersonic within a finite distance. These simulations verify all the assertions made in the theoretical work, such as the stability of the shock wave at X_{s3} and the fact that the flow does not choose a shock free solution if it has another solution which includes a shock. It also verifies that the flow with a positive energy and higher entropy would produce strong winds which may contribute to jet formation a conclusion which was also verified by subsequent self-similar models [229]. The flow passed through both the sonic points and does not switch back-and-forth from one sonic point to the other contrary to what was suggested earlier [260].

Figures 6.4-6.6 show results of a 2-Dimensional simulation after the steady state is reached. The time is $T=700GM/c^3$ [259]. Here, 60,000 particles are used in each quadrant. Figure 6.4 shows the particle distribution in which the standing shock at $X\sim 16$ is clearly visible. Note the presence of the oblique shock also. The specific energy and angular momentum used were $0.006c^2$ and 3.3GM/c respectively. Figure 6.5 shows the contours of constant Mach number. Note that the flow which is subsonic after the shock, becomes supersonic very close to the black hole. Also, winds which are originated subsonically on the disk surface, eventually become supersonic. Figure 6.6 shows the contours of constant temperature (labeled in geometric units). At the post-shock region, the temperature of the flow becomes high and the velocity becomes very low satisfying all the assumptions of a thick accretion disk (Fig. 4.4a-b). The contours in the immediate vicinity of the post-shock region indeed resemble that of a thick accretion disk. The shock heating causes a strong pressure gradient term which pushes matter out of the disk to form a wind. These solutions, particularly 1-Dimensional work which is understood more completely, can be used as 'test problems' in future for any

new numerical code which are meant to study shock waves in astrophysical conditions. These tests are expected to be more rigorous than 1-Dimensional shock-tube problems in Cartesian grid.

An important set of simulations, which pertains to the formation of the nonaxisymmetric shock waves, are carried out mainly by Kyoto group and others [142, 234-237, 261-262. In this case, the spiral shock waves are induced by the tidal force of the companion. Non-axisymmetric modes amplify and steepen to produce spiral shocks inside the disk. It was shown that spiral shocks may remove angular momentum quite efficiently and it is possible to achieve an effective $\alpha \sim 10^{-2}$. Figures 6.7(a-b) show examples of the spiral shock waves. Density contours are plotted. In both the figures the ratio (Q) of the compact object to the companion is chosen to be unity. In Fig. 6.7a, $\gamma = 1.2$ and in Fig. 6.7b, $\gamma = 5/3$ were used. Matter is injected through the inner Lagrange point on the left (cusp of the smooth curve) with sound speeds $c_o = 0.15$ (in 6.7a) and $c_o = 0.05$ (in 6.7b) respectively. (Velocities are measured in units of the Keplerian velocity of the companion and the distances are measured in units of the binary separation.) The tidal perturbation of the companion produce density waves which steepen into spiral shocks. In presence of a companion as in a binary system, usually a steady shock pattern forms. In Fig. 6.7a, a two armed spiral is formed whereas in Fig. 6.7b, a three-armed spiral is formed. However, depending upon boundary conditions (the dependence is as yet poorly understood), the number of arms may change in the same simulation. Figures 6.8(a-c) show 3-D surfaces of density plots for Q=1 and $\gamma=1.2$ case at times T=2.3, 3.2 and 3.7 respectively. This case is similar to above but the injected gas is somewhat cooler ($c_o = 0.1$). Also matter is supplied all over the outer boundary (at r = 0.65) with the angular momentum gradually increased from zero to 0.5 (0.8 would correspond to Keplerian in this unit). The number of arms changed from 2 (6.8a) to 3 (6.8b) to 2 (6.8c). The simulations are done with a code obtained from Kyoto group. When the companion is present only for a short time (e.g., just passing by), multi-armed fragmented shocks may form which may cause variabilities in active galaxies [237]. When the companion is more massive than the primary compact object, as is believed to be the case in SS433 system, the perturbation is more violent and causes variability in very short time scales [262]. Similarly, the results with $\gamma \to 5/3$ tends to be unstable and consists of fragmented and multi-armed as well. This is probably because the entropy function K(x) becomes more flat (eq. 5.30g). Theoretical results on self-similar spiral patterns have been discussed in §5.7.

6.4 Simulation of Viscous Disks

It has been realized rather recently, both from the theoretical and numerical simulation results that the process of shock formation in accretion disks depends strongly upon the viscosity [224] as well as the viscosity prescriptions [225]. As discussed in §5.3 (see, Fig. 5.3a-d), when the viscosity is increased, shock waves slowly recede from the black hole and the strength of the shock gradually diminishes. Finally, for a large

viscosity, the shock disappears and the disk becomes standard Keplerian type. Below, we present the results of the numerical simulation of viscous isothermal disks as their properties are understood reasonably well. The results with general radiative transfer are expected to be similar as suggested by theoretical considerations (§5).

A serious problem with the Shakura-Sunyaev viscosity prescription is that the efficiency of transport of angular momentum becomes very high in the post-shock region of the disk compared with the pre-shock region. To see this, consider a thin, isothermal, axisymmetric, accretion flow onto a black hole.

The radial momentum equation is (cf. eq. 5.1a):

$$\frac{\partial v_r}{\partial t} + v_r \frac{\partial v_r}{\partial r} + \frac{1}{\Sigma} \frac{\partial W}{\partial r} - \frac{\lambda^2}{r^3} + \frac{\partial \Phi}{\partial r} = 0.$$
 (6.1a)

The continuity equation is given by (cf. eq. 5.1b),

$$\frac{\partial \Sigma}{\partial t} + \frac{1}{r} \frac{\partial}{\partial r} (\Sigma r v_r) = 0. \tag{6.1b}$$

The azimuthal momentum equation is given by (cf. eq. 5.1c),

$$\frac{\partial \lambda}{\partial t} + v_r \frac{\partial \lambda}{\partial r} = \frac{1}{r \Sigma} \frac{\partial}{\partial r} (r^2 W_{r\phi}) \tag{6.1c}$$

Here, v_r and λ are the radial velocity and the azimuthal angular momentum respectively, and W, Σ and $W_{r\phi}$ are the pressure, density and the $r\phi$ component of the viscous stress tensor respectively. $\Phi(r,\theta)$ is the gravitational potential of the central object. This may be any of the pseudo-Newtonian potentials discussed in §1.3.

If one considers the solution to be steady, the time derivatives of the above equations vanish and we get the following conservation equations,

(a) Conservation of energy:

$$\mathcal{E} = \frac{1}{2}v_r^2 + a_0^2 log(\Sigma) + \frac{1}{2}\frac{\lambda^2}{r^2} + \Phi,$$
(6.2a)

(b) Conservation of baryons,

$$\dot{M} = \Sigma v_r r \tag{6.2b}$$

and,

(c) Conservation of the angular momentum

$$\dot{M}(\lambda - \lambda_e) = -r^2 W_{r\phi} \tag{6.2c}$$

Here, we have used equation of state W = const. Σ appropriate for isothermal flows and $a_0 = (W/\Sigma)^{1/2}$ is the isothermal sound speed, λ_e is the angular momentum at the inner edge of the disk. Note that this distribution suggests sub-Keplerian disks will become Keplerian at larger distance.

In an inviscid, axisymmetric flow,

$$W_{r\phi} = 0, (6.3)$$

and the location and strength of the shock is determined by the shock conditions:

(a) Temperature of the flow is constant across the shock,

$$a_{0-} = a_{0+}, (6.4a)$$

(b) Baryon flux is conserved,

$$\dot{M}_{-} = \dot{M}_{+},\tag{6.4b}$$

(c) The total pressure is balanced,

$$W_{-} + \Sigma_{-}v_{r-}^{2} = W_{+} + \Sigma_{+}v_{r+}^{2}, \tag{6.4c}$$

and,

(d) Angular momentum flux is conserved,

$$\lambda_{-} = \lambda_{+}, \tag{6.4d}$$

Here, - and + signs represent quantities in the pre-shock and post-shock flows respectively.

In the presence of viscosity, the angular momentum is transported according to eq. 6.2c. In the following subsections, we discuss how the transport process depends on the viscosity prescriptions.

Let us first consider the effects of Shakura-Sunyaev prescription of α (denoted hereafter as α_s) viscosity. In this case, we have $W_{r\phi} = \alpha_s W \frac{r}{\Omega_K} \frac{d\Omega}{dr}$, and the angular momentum distribution is obtained from [77, 224],

$$\lambda - \lambda_e = \frac{\alpha_s r^3 W}{\Omega_K \dot{M}} \frac{d\Omega}{dr} = \frac{\alpha_s r a_0}{M \Omega_K} \frac{d\Omega}{dr}, \tag{6.5}$$

where, $M = v_r/a_0$ is the Mach number of the flow, and λ_e is the angular momentum at the inner edge of the disk and Ω_K is the local Keplerian angular velocity. At the shock, since the Mach number M varies from supersonic $(M_- > 1)$ to subsonic $(M_+ < 1)$, the rate of transport of angular momentum would be quite different on both sides of the shock. In particular, in the post-shock region, the angular momentum would be transported faster and would 'pile' up as the pre-shock flow is unable to transport it away to outer radius very efficiently. Hence, the angular momentum must be discontinuous and λ_+ must be higher compared to λ_- . Thus the shock formed would be a mixture of compressional type as well as shear type ('mixed' shock).

When the viscosity is very small, transport rates of angular momentum on both sides of the shock can match and the shock can remain steady. In this case the shock

is weaker and forms farther away from the black hole. When the viscosity parameter is increased, the shock wave is driven outwards and the disk in the post-shock flow becomes Keplerian [225]. For very high viscosity, the shock disappears and the disk becomes almost Keplerian except very close to the inner edge of the disk. In Figs. 6.9(ab), we compare Mach number and angular momentum variations in viscous (solid) and inviscid (dashed) flows. The viscosity parameter is chosen to be $\alpha_s = 0.01$ everywhere in the simulation. Note that the shock in the viscous disk forms farther out. It is weaker and more spreaded out. Figure 6.9b shows that a mixed shock is formed with a jump in angular momentum at the shock $(\lambda_{+} > \lambda_{-})$. The angular momentum is super-Keplerian in the post-shock flow and almost constant in the pre-shock flow. As the α_s parameter is increased, the flow behaviour changes dramatically. Figures 6.10(a-b) show the evolution of Mach number and angular momentum when $\alpha_s = 0.1$ is chosen. Dashed curves marked $\alpha = 0$ represent solutions for inviscid flows. Successive solid curves are drawn at intervals of $\Delta t = 500$. The in-fall time-scale is $t_i = 75$ in the same unit. What clearly happens in this case is that due to higher efficiency of the transport of angular momentum in the subsonic post-shock region, angular momentum is piled up in this region. This drives the shock outwards continuously and no steady shock solution at a finite distance is possible.

To understand this behaviour, we refer to the Fig. 5.3(a-d) of §5.3 where the topological properties of the phase space in viscous flows have been discussed. It was shown that when the viscosity is high enough, a flow at a large distance has two choices. In one (higher energy) solution, the flow passes through the outer sonic point and in the other (lower energy) solution, the flow passes through the inner sonic point. The latter behaviour is clearly chosen by the system.

Results presented above indicate the following behaviour which are the general characteristics of any accretion flow (§5.4), not necessarily isothermal: (a) if the flow is provided with two choices, one shock free (low entropy or high energy) and the other with shocks (high entropy and low energy), the flow chooses the solution which includes shocks. (b) If the flow is highly viscous, it is again provided with two choices. Both are shock free, but one (with high energy and low entropy) passing through the outer sonic point and the other (with low energy and high entropy) passing through the inner sonic point, the flow chooses the latter solution. Thus generally speaking, (a) A black hole solution must be transonic, and any solution which does not satisfy this criterion must be rejected, (b) if the flow has a choice to pass through the inner sonic point without violating any physical principle, whether or not the flow has any shock wave, it would like to choose that solution.

It is possible that when the transport of angular momentum is not limited by the sound velocity so that the transport becomes efficient in the supersonic region of the flow, standing shock waves may be allowed in disks with larger α parameter as well. This can be achieved through the transport of angular momentum via Alfvén waves (in presence of magnetic fields) or through radiative transport (which is specially possible in

the hot, radiation dominated post-shock region). In the presence of efficient transport processes on either sides of the shock, the angular momentum would be continuous. Continuity of λ implies continuity of the viscous stress (cf. eq. 6.2c) and one notes that at the shock,

$$W_{r\phi-} = W_{r\phi+}. (6.6)$$

In the usual form:

$$W_{r\phi} = \nu \Sigma r \frac{\partial \Omega}{\partial r}.$$
 (6.7)

Here, ν is the kinematic viscosity coefficient, and $\Omega = \lambda/r^2$ is the local angular velocity. Since λ is assumed to be smooth and continuous, Ω is also a smooth and continuous function. One way to achieve the continuity of λ across the shock is to define the kinematic coefficient as,

$$\nu_p = \frac{\alpha_p(a_0^2 + v_r^2)}{\Omega_K} \tag{6.8a}$$

so that the viscous stress is,

$$W_{r\phi} = \frac{\alpha_p (a_0^2 + v_r^2) \Sigma r}{\Omega_k} \frac{\partial \Omega}{\partial r}.$$
 (6.8b)

In this case, the pressure balance condition (eq. 6.4c) ensures the continuity of $W_{r\phi}$. A subscript p of α is used to denote the pressure balance. One could also use the balance of the mass flux in defining the kinematic viscosity,

$$\nu_m = \frac{\alpha_m v_r}{\Omega_K} \tag{6.8c}$$

so that the viscous stress becomes,

$$W_{r\phi} = \frac{\alpha_m |v_r| \Sigma r}{\Omega_K} \frac{\partial \Omega}{\partial r}$$
(6.8d)

which also ensures continuity of $W_{r\phi}$. A subscript m of α is used to denote the mass flux balance.

Simulations using this prescription shows continuity in angular momentum even across a shock [Fig. 5.7, 68, 225]. This indicates that in the presence of efficient transport of angular momentum in the supersonic branch, shocks would exist when viscosity is relatively high. This is important since the observations of X-rays and γ -rays from black hole candidates require hot regions close to the black hole which is self-consistently provided by the post-shock flow.

In the case when the angular momentum supplied at the outer edge is Keplerian, and the viscosity is reasonably high, the flow becomes Keplerian throughout, except close to the black hole. At around the marginally stable orbit, the flow can become supersonic also. Below marginally stable radius the angular momentum transport becomes relatively inefficient and the flow accretes onto the black hole with almost

constant angular momentum [76, 225]. Figure 6.11 shows the formation of a Keplerian disk [225] in this way. In this simulation, matter is injected at the outer edge of the disk at $r_o = 100$ with angular momentum 7.00 which is close to Keplerian value at r_o . The (constant) sound speed is chosen to be $a_0 = 0.005$ and the injection velocity was $v_0 = 0.003$. $\alpha_s = 0.25$ was used in this simulation.

6.5 Simulations of Flows using Radiative Transfer

An important piece of work which includes α_s viscosity as well as the radiative transfer in a sub-Eddington Keplerian disk shows a completely different behaviour [263] than what is shown above. Evolution of the inner part of a Keplerian disk around a $3M_{\odot}$ black hole shows that the disk collapses into a thin sheet on the equatorial plane. This is expected since radiation pressure supported α_s disks are known to be unstable in viscous and thermal time scales (§3.1.4). The collapsing behaviour propagates till the outer boundary. Figure 6.12 shows the density contour of the simulation at different times (t marked in each panel). Here the length and the time units are GM/c^2 and GM/c^3 respectively. Initially, the disk is radiation pressure supported but eventually it becomes dense, cool and fluid pressure supported. The accretion rate is reduced as well. An interesting scenario can emerge in this type of disks: suppose that initially viscosity is low. Material which is injected at the outer edge cannot work their way to the black hole efficiently, and therefore accumulate. The accumulated material is not able to radiate the internal energy and becomes hot. This hotter disk is of higher pressure and of higher viscosity which causes the accumulated material to accrete catastrophically and emitting very high radiation. The disk can therefore resemble a rapid burster.

In another important simulation [264], super-Eddington flow is studied which produces a thick accretion disk. Figure 6.13 shows the density contours and unit velocity vectors in a simulation with $\dot{M}=4\dot{M}_{Edd}$ at time $t\sim6000$. Contours are labeled with densities in CGS unit. Large convective cells form on either side of the equatorial plane which drives the flow along the axis, as well as along the equatorial plane. The physical origin of the latter type of outflows is not clear. Four regions are distinguished and marked on the Figure: (A) a convective core, (B) an accretion zone, (C) a photocone and (D) a jet.

A number of simulations which include bremsstrahlung cooling have recently been carried out [227] using Smoothed Particle Hydrodynamics (SPH). The location of the shock wave is found to oscillate in a time period comparable to the in-fall time scale from the shock wave as discussed in §5.4. Fig. 6.14(a-b) show results of three-dimensional (axisymmetric) simulations with bremsstrahlung cooling process. The two figures show two different phases of oscillation of the shock and the post-shock corona. The upper halves provide the velocity vectors and the contours of constant Mach numbers (M=1 are thick curves) while the lower half provides the contours of constant density. The 'breathing' of the corona appears to take place when the cooling time-scales roughly

agree with either of the dynamical/in-fall time scales and are possibly responsible for quasi-periodic behaviours seen in galactic and extra-galactic black hole candidate spectra [227]. The post-shock halo may be responsible for the production of X-rays and γ -rays seen in spectra of galactic and extragalactic candidates.

The agreement of above results with analytical works provide strong support for the SPH simulations. One possible uncertainty could be due to the deviation of the geometry as described by a pseudo-Newtonian potential from a full general relativistic description. The theoretical problem in hand using a full general relativistic framework is not solved yet. A few preliminary tests (of spherical accretion, for instance) have been carried out recently using a relativistic SPH code [265]. For a concrete understanding of the above simulations, it is essential that the above mentioned studies be carried out using a fully general relativistic code.

7 Observational Signatures of Black Hole Accretion

7.1 Introduction

In most of the models of active galaxies, black holes are considered to be essential. A black hole is believed to be an indirect (but most relevant) participant and the catalyst of a large number of activities which take place close to the galactic nuclei. In cases where galaxies are no longer active, such as our own galaxy, the observers still look for signatures for activities which may suggest the presence of black holes. Though the interpretations are made assuming the presence of black holes, in general, they do not constitute full proofs. In an alternate model, most of the activities are supposed to be taking place due to star bursts at the galactic center [266]. This model can also explain many of the observations. We shall comment on this as we proceed.

Assuming the efficiency $\eta \sim 0.06$ to 0.40 for the conversion of the accreted mass into radiated energy, the critical mass accretion rate could be several times the Eddington rate $\dot{M}_{crit} = \frac{\dot{M}_{Edd}}{\eta} \sim 2 M_{\odot} M_{9}/\eta \text{ yr}^{-1}$, where, M_{9} is the mass of the black hole in units of $M = 10^{9} M_{\odot}$. Black hole being dense and compact, the length scale of the observable quantities, such as the intensity of emission at different wave bands should be small and typically of the order of the Schwarzschild radius $2GM/c^{2}$. Similarly, the intensity at a given band could vary in time scales of light crossing time of the horizon $\sim 2GM/c^{3}$. The stability of the direction and the superluminal behaviour of the cosmic radio jets [64, 267] are also signatures of a very powerful and stable compact object 'sitting' at the center of the jet-producing galaxies. Also, in cases where direct determination of radial velocities are possible, large velocity variation within a small region would certainly be a strong signature of a black hole nearby [4-5].

In the case of X-ray binaries, such velocity measurements are common and provide the mass function of the binary system. A successful candidate of a black hole must have $M > 3M_{\odot}$ [1, 268]. Hence a dynamical mass determination usually is the strongest criterion to fix a stellar black hole candidate [269]. The strong candidates include Cyg X-1, LMC X-3 and A0620-00 and the candidates with relatively weaker confirmation include CAL 87 and LMC X-1. A recent inclusion in this list is V404 Cygni [270] whose mass function $f(M) = 6.26M_{\odot}$ is very large and gives the candidate a mass of about $6.5M_{\odot}$ or more [271].

In last few Sections, we have discussed the theoretical nature of the accretion processes on a black hole. If a black hole is indeed present, and matter is available, then the accretion should take place, and the emission from the hot, radiating matter should be observable. The radiation could be in continuum and/or in lines. It could be stationary as well as non-stationary. If the source of matter is a single companion such as that in a stellar binary system, the angular momentum of the matter is expected to be high, but still the disk will comprise of the Keplerian disk from the accretion

through Lagrange point and a sub-Keplerian halo from the wind accretion, particularly in the case of high mass X-ray binaries. In the case of low mass X-ray binaries sub-Keplerian matter may be produced from Keplerian disk itself (Fig. 5.7). In the case of accretion onto a black hole at galactic centers, the source of matter could be winds from star clusters at distances of parsecs. These winds are expected to collide and their angular momentum may be mostly 'canceled' in the process, before they can proceed to the galactic center. This way one expects the angular momentum to be much smaller, which may further be removed by means of small viscosity or spiral density waves. The supplied matter could also be an admixture of Keplerian flows along with some low angular momentum matter. Since the present report is not a review on active galaxies (on which there are several reports such as Begelman, Blandford & Rees [64]) we shall not describe various aspects of these objects. Below, we shall review some models which require a compact black hole at the nucleus to explain the continuum spectra, line emission and the variabilities.

7.2 Continuum Emission

A dominant feature of the continuum spectrum is a hump in the spectrum near blue region known as the 'big blue bump'. This emission feature is seen in radio-weak sources as well as in many radio-loud quasars. In galactic black hole candidates, the spectra in the soft-state also has the bump is soft X-rays (see below). The 'big blue bump' in the spectrum of many QSOs as well as the soft X-ray bump in galactic black hole candidates are usually attributed to the quasi-thermal emission from accretion disks [1, 272-273], and good fits to this part of the spectrum can be obtained from standard, optically thick but geometrically thin ' α ' disk models [274-275], thick accretion disks [193], and disks incorporating shock waves in the disk [211] among others. Sun & Malkan [274] fits 60 quasars and AGNs from IR to UV region of the continuum by using standard accretion disk models [11-12] around black holes. The relativistic effects of disk inclination, including Doppler boosting, gravitational focusing and gravitational redshift on the observed spectra for both Kerr and Schwarzschild black holes are considered. The apparent disk spectrum becomes harder when the disk is viewed at high inclination angles due to the Doppler boosting and the focusing effects. The relativistic corrections are significantly higher when a rotating black hole is considered. Low red-shift Seyfert galaxies were found to require relatively low accretion rates, only a few percent of the Eddington rate, while the most luminous quasars are found to be accreting close to the Eddington rate. This model, which includes a power law emissivity in the infra-red region is an improvement over the earlier works [276] which required super-Eddington accretion rates. The model of Sun & Malkan [274] produces reasonably good fit of the spectrum. Figure 7.1, shows examples of fits in optical/UV [277] of nine typical quasars using emissions from a thin Keplerian disk and contributions from the dust (modeled as a power law in infra-red region), from starlight, from re-combination lines and Fe II lines [277].

In many cases, the standard model seems to underestimate the production of UV

intensity. In the presence of shock waves [211], UV flux produced in the post-shock region is higher compared to that produced in a standard disk. Excess UV could also be produced by cooling electrons at the shock by the soft photons from underlying disk. In above mentioned models simple black body spectrum were used to compute the spectrum. If more sophisticated radiation transfer processes are used one develops a better understanding of the emergent spectra from the entire disk. We shall discuss this below. There are several models which do not include well defined disks. For instance, it has been suggested that the blue bumps might be due to optically thin thermal emission of predominantly free-free origin [278]. Both the thermal and non-thermal models are discussed in detail by Odell, Scott & Stein [279]. The thermal disk models give a flat visual-UV region up to a maximum temperature of the disk. In the non-thermal models, the synchrotron emission from electrons coming out of the proton-proton collisions are also included. This model predicts several observed properties of the non-blazer quasars and AGNs such as a relatively flat spectrum up to a high frequency break, synchrotron losses at least comparable to the Compton losses, weak polarization and no Lyman discontinuity.

One way to verify that the active galaxies accrete through accretion disks is to measure as many line ratios as possible from the emission region [280]. These ratios should depend upon the nature of the incident spectrum and may be able to distinguish the thermal from non-thermal disk continuum emission. Different subcritically accreting disk models could also be distinguished by the polarization properties of the emitted light. In a Thomson scattering dominated region of the disk, the polarization is significantly higher than the classical limit of 11.7% [281] when scattering half-thickness of the disk is less than unity corresponding to subcritical accretion. The degree of polarization varies inversely with the optical depth in this regime and the radiation pattern is anisotropic as the optical depth decreases [282].

Some of the active galactic nuclei, especially those which are radio-quiet, show strong evidence of X-ray emission. Based upon the analysis of the Ginga data at least four (model dependent) components have been tentatively assumed to be present [283]: (i) an incident non-thermal power law component with spectral index $\alpha_X \simeq 0.9$; (ii) a broad emission excess at energies \geq 10 keV as a Compton reflected component from cold matter; (iii) fluorescent Fe-K emission line at 6.4 keV and (iv) the absorption (Fe-K) edge at 7-8 keV. ROSAT in its all sky survey has identified numerous active galactic nuclei in the soft X-ray range A consistent model should satisfy the following features [284]: (a) the 2 - 10 keV X-ray spectral index α is distributed in the range $0.4 \le \alpha_X \le 1.0$; (b) the conversion efficiency of the mass to luminous energy is about 10 percent if the X-ray luminosities of typical quasars and Seyferts are maintained over cosmological time; (c) the extension of hard X-rays of AGN into γ regime must be truncated at dimensionless photon energy $x = h\nu/m_ec^2 < 5-10$ in order not to conflict with the observations of the γ ray background. A popular model of the origin of X-rays is due to Zdziarski [285, 286]. In this model, electrons of the plasma cloud of energy $\Gamma m_e c^2$ scatter with soft photons and lose their energy to these photons whose energy,

in turn, is boosted by a factor of Γ^2 per scattering (Γ being the Lorentz factor). The high energy photons produce pairs depending upon the compactness of the interaction region. When the compactness is small, the optical depth to pair production is small enough and X-rays become observable. Thus, the observation of X-rays may testify to the existence of compact hot source of energized electrons as well as soft photon source from the underlying pre-shock cool accretion disks. The energetic electrons could also be produced from magnetic corona of the accretion disks [141]. However, interpretation of the observational results need not be unique, particularly the existence of the Compton reflection component is found to be not required by more recent analysis of Ginga data [287] In this new interpretation, the X-ray is considered to be of thermal origin. Single component thermal models [287] (as opposed to multi-component Compton reflection models [285, 288-289]) have been successfully able to explain a variety of hard X-ray sources such as the galactic black hole candidate Cyg X-1 and the Seyfert galaxy NGC 4151. Fig. 7.2a show fits of the EXOSAT, GRANAT and OSSE observations of Cyg X-1 [290] with various models [285, 287-289]. The basic conclusion is that the electron temperature of the emitting region must be of the order of a hundred keV ($\sim 10^9 \text{K}$) and the optical depth is on the order of ~ 1 . In Fig. 7.2b, the OSSE [291] and Ginga data [292] are fitted with the single component model [287]. Here, the electron temperature is about $44 \text{keV} \ (\sim 4 \times 10^8 \text{K})$. These results indicate the presence of a very compact source for most of the hard emissions.

In the spectra of the galactic black hole candidates, such as LMC X-3, LMC X-1, GS1124-38 etc, the so-called soft component can be attributed to the thermal emission from the standard disk [1]. However, GS1124-68 [293] Cyg X-1 and GX339-4 [293-295] are occasionally observed to change states: they are sometimes in the hard state (low spectral index $\alpha \sim 0.5-0.8$: $F_{\nu} \sim \nu^{-\alpha}$) and sometimes in the soft state ($\alpha > 1$). Judging from the success of the thermal models [287], it may be possible to imagine that the one does not require non-thermal processes after all. Since the hard component cannot be produced using a standard disk, the only way to produce (without invoking ad hoc components, such as corona, plasma clouds etc.) would be to produce a hot re-processing site, such as a post-shock region, close to the black hole, self-consistently. To obtain a self-consistent disk model one has to take the following points into considerations:

- (a) Some objects are sometimes in the hard state and some times in the soft state (e.g., GS1124-68, Cyg X-1, GX339-4) [293-295].
- (b) The hard and soft components may vary almost independently (GS1124-68) [293].
- (c) Sometimes the soft luminosity may vary by several orders of magnitude while leaving the spectral index almost unchanged (GS2023+338, GX339-4, GS1124-68) [293-295].
- (d) Sometimes the hard flux is seen to rise with the spectral index (NGC 4151) [292].
- (e) In general, in most of the black hole candidates, the soft state has a very weak power low hard component of spectral slope $\alpha \sim 1.5$ apart from the usual black body bump.

Perhaps it is possible to understand these observational features by a single model.

Fig. 7.3 shows a plausible accretion disk model [68, 170, 296, 297] constructed taking into account the following considerations. In a black hole binary system, the matter supply at the outer edge of the accretion disk could be a mixture of Keplerian component (with specific angular momentum distribution $l_{Kep}(r)$) from the companion and a sub-Keplerian component (with a specific angular momentum $l \lesssim l_{Kep}(r_{out})$) from the winds [170, 249-257, 296] of the companion or from the Keplerian disk itself (Fig. 5.4). In active galaxies, sub-Keplerian matter supply could come from the constantly colliding stellar winds (which is mostly devoid of angular momentum) at a distance of a few parsec away. Higher viscosity near the equatorial plane creates a Keplerian disk out of this (§6) flow but lower viscosity away from the plane leaves the flow sub-Keplerian. (Contrarywise, higher viscosity cooling dominated flow deviates from Keplerian disk close to the black hole, but low viscosity, radiatively inefficient flow deviates farther away.) At a distance r_s from the black hole, where $l \sim l_{Kep}(r_s)$, the effectively freely falling sub-Keplerian halo component forms a standing shock due to the centrifugal barrier. The post-shock halo, which acts as the boundary layer of the black hole, becomes hot as the radial kinetic energy of the in-fall is thermalized: $\rho v_r^2(r_s) \sim P \sim$ $n_H \kappa T_p$. The solution with a shock wave is preferred to the alternative shock free solution as the entropy at the inner sonic point close to the black hole is higher compared to the entropy of the shock free flow [77]. For matter with marginally stable angular momentum, the shock forms at $r_s \sim 10r_g$ ($r_g = 2GM/c^2$, the radius of the black hole) in Schwarzschild geometry. The flow remains dissipative up to the marginally stable radius $r_{ms} = 3r_g$ beyond which the flow rapidly passes through the inner sonic point [77]. For a flow around a Kerr black hole of angular momentum parameter a = 0.99, these length scales are roughly half as large. For higher angular momenta shocks form much farther away [77]. A flow in vertical equilibrium with a polytropic index $\gamma = 5/3$ has a post-shock temperature of $T_p(r_s) \sim 1.6 \times 10^{12}/x_s$, $(x = r/r_g)$. The post-shock flow becomes geometrically thick with a height $h(x_s) \sim a_+(x_s)x_s^{3/2} \sim x_s/2$ $(a_+(x))$ being the post-shock sound speed) which intercepts a few ($\lesssim 5$) percent of the soft photons from the optically thick, Keplerian component of the pre-shock accretion disk. The post-shock, optically slim region with a Thomson optical depth of $\tau_h \sim \int_{x_{ms}}^{x_s} 0.4 \rho dx$ $(\sim 1-3 \text{ for } \dot{M} \sim \dot{M}_{Edd})$ rates heats up these soft photons through inverse Compton scattering and the photons are re-emitted as hard radiations [68, 106, 108, 287, 297].

Let $L_I = f_{ds}L_{SS}$ denote the fraction of the Kepleian (i.e., Shakura-Sunyaev [11] type) disk luminosity L_{SS} of the soft radiation intercepted by the bulge of the shock [68, 297] $F_e = L_H/L_I$ denote the enhancement factor of this flux due to cooling of the electrons through inverse Comptonization [106, 108] (L_H is the hard component luminosity), and f_{sd} (~ 0.25 for a small spherical bulge) denote the fraction of L_H intercepted back by the disk. The soft component observed from a disk around the black hole candidate is therefore contributed by the original disk radiation plus the absorbed intercepted radiation: $L_S = L_{SS} + L_{SS} f_{ds} F_{ef} f_{sd} \mathcal{B}$, and $L_H \sim L_{SS} f_{ds} F_{ef}$, where $\mathcal{B} = 1 - \mathcal{A}$, \mathcal{A} being the albedo of the Keplerian disk. The enhancement factor $F_e \sim 3(T_e/3T_d)^{1-\alpha} \sim 10 - 30$ because, typically, the electron temperature $T_e \sim 50$ keV and the disk temperature $T_d \sim 5$ eV for parameters of active galaxies and $T_e \sim 150$ keV and

 $T_d \sim 100 \mathrm{eV}$ for stellar black hole candidates. Hence, one easily achieves a convergence, $f_{ds}F_ef_{sd}\mathcal{B} < 1$ since $f_{sd} \sim 0.25$, $f_{ds} \sim 0.05$, and $\mathcal{B} \sim 0.5$. Here, α is the energy index $(F_{\nu} \sim \nu^{-\alpha})$ in the the up-scattering dominated region of the hard spectra. Soft photons from the disk component in the post-shock hot region do not participate in cooling the electrons since the Keplerian and sub-Keplerian components behave identically in this region for three reasons: (1) the angular momentum of the sub-Keplerian and Keplerian components are the same at $r \lesssim r_s$; (2) $v_r \approx 0$ in the immediately post-shock region of the halo whereas $dv_r/dr \approx 0$ in the disk component — in either case the advection term $v_r dv_r/dr$ (cf. eq. 5.1a) is negligible and both the flows accrete downstream as a single component, (3) since the post-shock halo is much hotter than the Keplerian component, it is likely to evaporate the disk underneath and together they behave as a single component, though the components need not find time to mix effectively.

Figure 7.4 shows a comparison of four spectra around a black hole of mass $M=5M_{\odot}$ and the halo accretion rate $\dot{m}_h=\frac{\dot{M}_h}{\dot{M}_{Edd}}=1.0$. The disk accretion rates $\dot{m}_d=\frac{\dot{M}_d}{\dot{M}_{Edd}}$ are 1.0 (dotted), 0.1 (short dashed), 0.01 (long-dashed) and 0.001 (solid) respectively [68]. The dotted curve is overlapped with another curve (dot-dashed) including the effects of the convergent inflow in the soft-state. With the increase of the disk accretion rate, the number of soft photons intercepted by the post-shock bulge is increased, cooling this region efficiently. As a result, the temperature T_e of the electron is reduced and the energy index α is increased. The luminosity and the peak frequency of the soft component go up monotonically with \dot{m}_d . The intensity of the hard component rises with \dot{m}_d below $\nu \sim 10^{18-19} {\rm Hz}$ (corresponding energy $\sim 5-50 {\rm keV}$) but it falls at higher energies since the electrons become cooler. The ratio L_H/L_S decreases with the disk accretion rate. Increasing the halo rate \dot{m}_h increases the optical depth of the post-shock region. The spectra are hardened due to the saturation of Comptonization. Here α decreases and the hard luminosity increases. Results in the case of massive black holes are similar, since the electron temperature weaky depends on the black hole mass ($\sim M^{-0.1}$).

The transition from the hard state to soft state could be seen by plotting the spectral index as functions of the disk accretion rate (\dot{m}_d) (Fig. 7.5). Halo accretion rates are marked on curves. In the hard state, $\alpha \sim \text{constant}$, even when the disk accretion rate is increased by a couple of orders of magnitude. On the right hand side, the plots of spectral index are from the convergent accretion in the post-shock region ([68, 74, 238]) close to the black hole. The slope due to the convergent flow asymptotically approaches 1.5 for high accretion rates and therefore could represent signature of rapid motion close to the black hole. (Such a component is unexpected for a neutron star accretion as discussed in §5.) The general variation of the soft (L_S) , and hard luminosities in X-rays and γ -rays $(L_X \text{ and } L_{\gamma})$, as well as the spectral index α , as predicted by this model, (and as observed as well) is presented in Table 1. The up-arrow shows the correlation while down-arrow shows the anti-correlation. The smaller arrow shows a weaker dependence.

TABLE 1 Variations of the Observed Quantities with Accretion Rates

| | $\begin{matrix} Input \\ \rightarrow \end{matrix}$ | \dot{m}_d | \dot{m}_h |
|----------------------|--|-------------------------|---------------------------|
| Output | Row & Column | (1) | (2) |
| L_S | (1) | ↑ | ↑ |
| L_X, α | (2) | $\uparrow \uparrow a$ | $\uparrow \downarrow b,c$ |
| L_{γ}, α | (3) | $\downarrow \uparrow a$ | $\uparrow \downarrow b$ |

 $[^]a$ dependence is weaker for $\dot{m}_d \stackrel{<}{{}_\sim} 0.1$

The general agreement of the observed behaviours with the predictions from this more general model indicates we now understand the black hole accretion more completely.

7.3 Variability of AGN spectrum

An interesting way to verify the possible presence of a black hole is to identify rapid variability in emitting gases from nearby regions. An extensive study of variability is now under way and there are excellent reviews on this topic [239]. Particularly interesting are the Blazars (the BL Lacertae objects and Optically Violent Variables), which show high polarization and variability at almost all wavelengths, on time scales varying from roughly months (quiescent emission component) at wavelengths longer than 1 cm to weeks at sub-millimeter wavelengths to roughly days (flaring component) in UV and smaller wavelengths. X-rays can also vary from days to months. Clear intra-day variabilities have also been reported [239-247, 298]. In objects such as OJ287, variabilities in time scale of minutes may have been seen [299].

b dependence is weaker for $\dot{m}_h \gtrsim 1$ c $\alpha_X \sim 1-1.5, L_X/L_S \leq 10^{-3}$ when shock is absent

So far, no solid physical understanding of these variabilities has emerged yet. Several phenomenological models have been proposed in terms of multiple flares, hotspots and unstable spiral shocks in disks. In modeling the optical and UV data it has been shown that reasonable time scales for fluctuations can be achieved with dozens of spots on both the standard ' α disks' [11] and " β accretion disks" [136, 300]

using sensible parameters. Very similar models (using α disks) have been used to describe X-ray flickering as well [301].

Since the "big blue bump" in the spectrum may be due to accretion disks, it is reasonable to expect that fluctuations in the optical and in the UV bands may be associated with accretion disks also, though in BL Lac spectra no "big blue bump" is seen. Wandel & Urry [302] have claimed that in the best studied case of PKS 2155-304, a significant quasi-thermal, and thus, probably, accretion disk, component is present; however, optical polarimetry of this source implies that the disk contribution, if present at all, is quite small [303]. Another contribution to variability could come from the time dependent behaviour of the formation and evolution of spiral density waves in outer disks. Such waves may be caused by some perturber massive compared to the disk, but probably less massive compared to the central black hole [237].

At least some of the variability features in blazars could be understood assuming magnetic activities in the magnetized jets [304-305], or in magnetic coronal activities in accretion disks close to the black hole [141]. The general conclusion is that the emission must originate from a single compact region [306] of size $r \sim 10^{15}$ to 10^{17} cm and the magnetic field, which is largely turbulent [307] is $B \sim 0.1-1$ G [308]. A large number of these objects, such as, OJ287, 3C 345, BL Lac, and 3C 454.3 etc. show clear evidence of a net magnetic field aligned orthogonal to the direction of the jet axis. All these points to the evidence that a strong magnetic activity, very similar to what happens on the solar surface, must be taking place at the funnel (or chimney) wall as well. Blandford & Königl [304] suggest that if a succession of mild shocks continuously re-accelerate the electrons, the flow should be roughly isothermal, and the field perpendicular to the flow axis at the shock should vary as $B \propto r^{-1}$. This condition produces a very high field of $\sim 1 \,\mathrm{G}$ at the flaring region. In a highly variable source, such as MK421 $(t_{var} \sim 10000s)$ [309], field varies as $B = B_0 r^{-1.4}$ with $B \sim 0.2$ G. In PKS2155-304, field varies as $B = B_0 r^{-1.3}$ with $B_0 \sim 100$ G close to the core to 70 μ G at 1pc. Because of the strong evidence of the presence of magnetic fields, magnetic flares in the chimney can be considered to be major contributors to the variability. The energy deposited at each flare is about $L^3B_f^2/4\pi$. Here, L is the length scale of a typical flare and B_f is the average field on the chimney surface. The energy is released in time L/V_A , where, V_A is the Alfvén velocity $(B_f^2/4\pi\rho_f)^{1/2}$, ρ_f being the density of matter inside the chimney. With reasonable estimates of $L \sim r_g$, $B \sim 100 \, \mathrm{G}$, and $\rho \sim 10^{-14} \mathrm{gm \ cm^{-3}}$, one obtains the energy release, time-scale and the rate of release to be given by 2×10^{37} erg, 0.3d and 2×10^{34} erg s⁻¹, respectively for a black hole of $10^8 M_{\odot}$. Depending upon the size of the flares their occurrence rate will change. Thus, a large number of frequent microand mini-flares are expected inside the chimney [141].

7.4 Correlated Variabilities

In some of the well-studied objects, such as NGC 5548, NGC 4151, and Fairall 9, continuum and lines vary virtually simultaneously at optical and ultraviolet frequencies [207, 310]. Molendi, Maraschi & Stella [209] have pointed out that the propagation speed of the perturbation have to be faster than 10 per cent of the speed of light to explain variabilities with so short time lags. In a standard Keplerian accretion disk model the typical time scales on which thermal and viscous instabilities operate are very long (months or more) and thus the short time lag requirement cannot be met. Molendi, Maraschi & Stella [209] have proposed that possibly this could be due to re-processing of radiation from a hot bulge component at the center of the disk. Alternatively, it is proposed that to explain such a behaviour flow has to be only partially disk-like [208].

In the presence of a strong shock wave in an accretion disk, the post-shock region becomes very hot, and the disk is puffed up to become geometrically thick (Fig. 6.4, Fig. 7.3). Hard radiation produced at the shock would be reprocessed with 10-25 percent of interception by the pre-shock flow of the disk. Since the cool and hot components of the disk reside side by side near the shock wave, such a correlated variability may be naturally explained by this generalized disk model (§7.2).

In the case of BL Lac 0716+714, it has been observed that variabilities in radio and optical are well correlated [242, 311] and some kind of quasi periodicities are observed in time scales of 0.8d and 1.3d in the first week and of $\sim 6d$ in later weeks of observations. There is at present no reliable model of this correlation. It is possible that the strength of magnetic fields on the disk surface is well correlated with the pressure inside the disk where the flux tube is originated [141]. If, for example, the optical variabilities are caused by the formation and disappearance of the hot-spots (non-axisymmetric density perturbations) inside the disk then the radio flares caused by magnetic fields anchored with these density waves should also follow a similar variability. Indeed, if the anchored corona is also responsible for production of γ -rays, then future observations of correlation with γ -rays cannot be ruled out.

In the star-burst model of quasars [266], most of the optical and UV luminosity is supposed to be due to young stars and the observed variabilities correspond to the presence of a large number of compact supernovae remnants along the line of sight. However, this model cannot explain uncorrelated variabilities observed in the four images of the lens system Q2237+0305 [312] (which has no intrinsic variability) nor can it explain short-time scale correlated variabilities $t_{var} \lesssim 1$ week. This model also may not be able to produce observed jets in quasars which has a very accurate directionality.

7.5 Variability of Disk Line Emission

Similar to the line emissions seen in Cataclysmic variables, one would expect that if the accretion disk around a black hole also emits lines, they should show double horned patterns [313, 314]. If there is a non-axisymmetric feature on the disk, the double horned pattern need not be symmetric [212, 315]. With the movement of the feature, the emitted pattern should also move so that one obtains a temporal variation. Similarly, if the disk is well resolved so that one could observe parts of the disk at a time, then one should also expect spatial variation of the line emission. These informations certainly would provide more detailed properties of the disk as well as the properties of the central black hole.

7.5.1 Temporal Variation

The first good candidate was the permitted H_{β} emission from the broad line radio galaxy (BLRG) 3C 390.3 [316-317]. Soon thereafter, Chen, Halpern & Fillipenko [318] and Chen & Halpern [319] carefully analyzed H α emission line data for the BLRG ARP 102B and showed that the double-peaked emission could fit very well using relativistic Keplerian disk models. The H α broad emission line in yet another BLRG, 3C 322, could also be explained successfully with a very similar model [320]. In these stationary relativistic disk models, Doppler boosting implies that the short-wavelength (blue) side of the profile is brighter than the long-wavelength (red) side. Recently, a comprehensive survey of 88 BLRGs is completed [321] in which nine additional objects were found to emit line emissions which fit relativistic accretion disk model emission profiles. Figures 7.6(a-b) show fits of Chen and Halpern [319] of the broad line emissions of ARP 102B. In (a), the emissivity is assumed to be power law throughout the disk:

$$\epsilon(x) = \epsilon_0 (x/x_1)^q \quad x < x_1$$

$$= \epsilon_0 (x_1/x)^q e^{-(x-x_1)^2/x_2^2} \quad x \ge x_1$$

and in (b), local line broadening with a single power law.

$$\epsilon(x) = \epsilon_0 x^{-q}$$

is used. The fit of the broad lines is generally very good and indicates that possibly the broad lines are contributed by the disk itself. In (a), the power law parameters are $x_1 = 400GM/c^2$, $x_2 = 900GM/c^2$, the emissivity exponent is q = 3, and the inclination is $i = 32^o$. In (b), the inner edge is at $x_1 = 350GM/c^2$, outer edge is at $x_2 = 1000GM/c^2$, the emissivity exponent is q = 3.0, the inclination angle is $i = 32^o$ and the broadening velocity is $\sigma = 850 \text{ km s}^{-1}$. Subsequently, it was pointed out that in some phases, the red component from ARP 102B was found to be stronger than the blue [210]. It was also noted that the temporal variations in the blue and red peaks were not well correlated; thus the possibility of an axi-symmetric disk could be ruled out [210]. Similar model of relativistic axi-symmetric standard Keplerian disk is used to

fit 3C390.3, for example. Figure 7.7 shows this fit when the blue component is stronger then the red component [321]. The lower panel gives the residual spectrum obtained after subtraction of the theoretical fits from the observed profile. The inner and the outer edges of the emitting regions are $380GM/c^2$ and $1300GM/c^2$ respectively. The Gaussian profile broadening width is assumed to be $\sigma = 1300 \text{ km s}^{-1}$, the inclination angle is assumed to be $i = 26^{\circ}$ and the emissivity exponent is assumed to be q = 3.0. However, simple disk model for the broad emission lines from 3C390.3 was also shown to be inadequate because H_{β} emission lines are found to be quite variable. Veilleux & Zheng [322] showed that the B/R ratio does not remain greater than unity for much of the extensive period between 1974–1988 and later a more complex, bipolar origin of the temporal variability was postulated [323]. Even when B/R > 1, a Keplerian disk is often unable to raise the blue component to the level that is required by observation (Fig. 7.7). One possibility, similar to that used to explain shifting B/R ratios in CVs [324-325] would be the presence of a large hot spot on a relativistic disk. It has been recently observed [326] that the double-peaked Balmer broad emission lines for the LINER nucleus of NGC 1097, the red peak exceeds the blue, which is inconsistent with the axi-symmetric relativistic disk model [318-319].

This type of temporal variability could be naturally explained in disks which have non-axisymmetric features which either advance (or trail) with the flow [212]. Using non-axisymmetric spiral shock models (§5.7), it is found that one can fit emissions from 3C390.3 and ARP 102B at two different phases. The temporal variation seems to be due to motion of the spiral shocks with respect to the line of sight. Figures 7.8(a-b) show theoretical fits of the H_{α} data of 3C390.3 [212] at two different times. The solid curves are observed data and the dashed curves are the model fits. In Fig. 7.8(a), the 1976 data is compared and in Fig. 7.8(b), the 1980 data is compared. The inner and outer edges are chosen to be $x_1 = 200GM/c^2$, $x_2 = 900GM/c^2$, the emissivity exponent q = 2.0, inclination angle $i = 38^o$, and the broadening velocity $v_{th} = 0.0015c$.

7.5.2 Spatial Variation

Spatial resolution of the disk is now possible with the advent of small aperture space telescopes. Recent imaging results of M87 [4] and the spectroscopic results of the disk [5] indicate that there are spiral features in the disk. The spectroscopy was made pointing the telescope at seven different sites. Figure 7.9 gives the spatial variation of the line emission profiles from the spectrographic data (obtained by the Faint Object Camera) at these positions. The image is plotted assuming the systemic velocity of $\sim 1300 \, \mathrm{Km}$ of M87 from the sun. The prominent line features include [O III] $\lambda\lambda 4959 \, \mathrm{Å}$, $5007 \, \mathrm{Å}$, [S II] $\lambda\lambda 6716 \, \mathrm{Å}$, $6731 \, \mathrm{Å}$, [O I] $\lambda 6300 \, \mathrm{Å}$, $[H_{\beta}]$ $\lambda 4861 \, \mathrm{Å}$ and the blending of $[H_{\alpha}]$ $\lambda 6563 \, \mathrm{Å}$ with [N II] $\lambda\lambda 6548 \, \mathrm{Å}$, $6583 \, \mathrm{Å}$. The velocity measurements at position 5 and 6, which are taken at opposite sides of the nucleus show that the velocity of the emitting flows to be $\sim \pm 550 \, \mathrm{km \ s^{-1}}$ respectively, indicating a significant rotational velocity around the nucleus. Assuming the velocities observed to be Keplerian, the determined mass is $(2.4 \pm 0.7) \times 10^9 M_{\odot}$ and the inclination of the disk plane with the

line of sight to be $(42\pm5)^o$. These results could be further improved by assuming that the spiral features are real and with a two armed spiral shock solution (§5.7) the fits of lines are found to be reproduced only if the mass of the central black hole is chosen to be $(4.0\pm0.2)\times10^9M_\odot$ and the disk inclination angle $(42\pm2)^o$. The disks with spiral shock waves are found to be sub-Keplerian and therefore a higher mass is required to obtain the same frequency shift. Figure 7.10 shows the fit (solid) of the [O III] λ 5007Å, lines (short dashed) emitted from different positions. The same theoretical fit, upon suitable scaling, matches with observed [N II] λ 6584Å profile (dot-dashed) as well [6]. The general agreement indicates that the dissipative shocks may be real and an absence of a strong ionizing source in the system indicates that the emission could be due to shock ionization. The agreement of the spatial variation of the line profiles in M87 with theoretical models, provide the strongest evidence so far of a super-massive black hole at a galactic center. Masses could be seriously underestimated due to the inefficient sub-Keplerian disks.

Another important recent observation which provides a convincing proof of the galactic black hole model is that due to Miyoshi et al [327]. Using Very Large Baseline Array (VLBA), they observe very strong water maser lines from the molecular torus which surrounds NGC4258 and find evidence of mostly Keplerian velocity of about 1000 km s-1 at a distance of 0.13pc from the galactic center. The estimated mass of the central black hole is about $3.6 \times 10^7 M_{\odot}$. In this system matter is found to have very little radial motion (< 10 km s⁻¹) indicating the flow is primarily Keplerian in the torus. A very complex structured spiral feature (identified as a jet) has been observed in this system which also shows evidence of shock ionization [328].

7.6 Quasi-Periodic Oscillations

Many low mass X-ray binaries and X-ray pulsars are known to show quasi-periodic oscillations (QPOs). These QPO behaviour is thought to be correlated with the Z-shaped spectral states, namely, the horizontal, flaring and normal branches [329]. More recently, QPOs are observed in galactic black hole candidates such as LMC X-1, [330], GX339-4, GS1124-68 [331-333] as well. Whereas the frequencies of oscillations of the horizontal, normal and flaring branches are 20-55, 5-7 and 7-20Hz respectively, the black hole candidates show evidences of generally much lower frequencies. LMC X-1 has the centroid frequencies around 0.08Hz [331], GX339-4 has around 6-8Hz and GS1124-68 has around 3-8Hz [332]. The modulated amplitude could be as high as 5-10 percent or more.

Several models have been proposed to understand the QPOs. Beat frequency model is more promising for the horizontal branch and X-ray pulsar QPOs [334]. Particularly puzzling are the QPOs in black hole candidates, where there is no 'hard' surface which would rotate at a different speed than the inner edge of the disk. Thus, presently, there is no satisfactory explanation for these QPOs. Some proposed models

include the followings:

(a) Viscous pulsational instability model [335]: In this case, the oscillation is thought to be excited by axially symmetric acoustic modes at the transonic region of the disk close to the black hole. The frequency of oscillation is found to be around $10^3 (M/M_{\odot})^{-1}$ Hz which is too high for QPOs observed. Furthermore, the energy in the acoustic wave could be very low to produce the observed modulation of amplitude. (b) Another mechanism is 'one armed corrugation wave' generation at the inner edge of the disk where the disk oscillates vertically as a whole [336]. The frequency of oscillation is around 1-0.02 Hz for a critical accretion rate, but the problem with the observed modulation persists. (c) Yet another mechanism involves the trapped oscillation [337] which are generated closer to the inner edge of the accretion disk. These oscillations appear as there is a maxima in the epicyclic frequency. These oscillations show 1-3 percent modulation in the absence of accretion. The computation which includes accretion are to be performed in order to find the relevance of these modes. (d) A fourth mechanism is due the oscillation of the shock waves [227] close to the black holes. Centrifugally supported shock waves act as hard surfaces and the post-shock flow produces hard radiations. When the cooling time of this region roughly agrees with the in-fall time, the shock oscillates, modulating the hard-radiation by 5-15 percent.

7.7 Our Galactic Center

Since our galactic center is only about 8.5Kpc away, it would be the ideal candidate to look for the evidences of a black hole [338]. However, observation of the galactic center is very difficult because the solar system is close to the galactic plane and one has to view the center through the interstellar dust and gas. The best way to observe the center is to use wave-bands in which the attenuation is minimum, such as in radio, infra-red, hard X-rays and γ -rays.

A very good and up-to-date review on the latest observational aspects is given in Genzel, Hollenbach & Townes [7]. We shall restrict ourselves only to the basic conclusions regarding the theoretical interpretation on the nature of the central object. Figure 7.11 shows schematically different identified structures as well as distribution of mass computed from various arguments within 100pc of the galactic center. The resolution of the figure is ~ 0.01 pc, roughly the size of the unresolved Sgr A*. The major components are the stars and the stellar clusters, giant molecular clouds, Sgr A east arm, the circum-nuclear ring or disk, and the mini-spiral. Also shown are the locations of the Sgr A*, the infra-red sources IRS-7 and IRS-16. Mass within a radius of 0.1pc, is found to be a few times $10^6 M_{\odot}$ which is usually attributed to a black hole at the center.

There is indeed a major controversy regarding the nature of the massive entity (if it is a single one) in our galactic center. There is not yet a clear consensus even in identifying the galactic center. Sanders [339] argues that among many stars observed in

the central parsec region, there are several very massive and luminous blue stars with strong helium lines and fast winds. Particularly, the brightest complex in the region, IRS-16 contains about 20 such blue stars. Thus, the central activity may be dominated by the ionizing radiation from IRS-16, rather than anything associated with Sgr A*. Even if it is assumed that Sgr A* is our galactic center, there are strong arguments for and against it being a massive black hole. We wish to close this Section by presenting a few such arguments.

A major problem involves in understanding the nature and the origin of the circumstellar wind which is inferred from the broad He-I emission lines from the direction of IRS16. The broad lines indicate outflows from the galactic center with velocities of the order $v_{gw} = 500 - 700 \text{ km s}^{-1}$ and a mass loss rate of $\dot{M}_{GW} \sim 3 - 4 \times 10^{-3} M_{\odot} \text{ yr}^{-1}$ [340]. Yusuf-Zadeh & Melia [341] argue that the tail associated with the giant star IRS 7 is due to the interaction between the galactic center wind and the wind from IRS 7. The origin of the galactic wind is IRS-16. There is a general opinion that the wind originating from IRS-16 should be accreted onto Sgr A*, as it is only 0.04-0.06pc away from IRS-16. The argument goes as follows [342]:

The sound speed $a \sim (kT_{gw}/m_p)^{1/2} \sim 18 \text{ km s}^{-1} \left(\frac{T_{gw}}{40,000K}\right)^{1/2}$ within the galactic center being smaller than the outflow velocity of few hundred km s⁻¹, the accretion is initiated by a bow shock and heats the gas to $T_0 = (3m_p/16k)v_{gw}^2 \sim 7 \times 10^6 (v_{gw}/600)^2 \text{K}$. The plasma accretes almost radially after passing through a shock and all plasma within the accretion radius $r_a = 2GM/v_{gw}^2$, falls on the black hole. The accretion rate is about

$$\dot{M} \sim 10^{22} \text{gm s}^{-1} \mathcal{W} (M/10^6 M_{\odot})^2$$
 (7.1)

with

$$W = \left(\frac{v_{gw}}{600 \text{ km s}^{-1}}\right)^{-4} \left(\frac{\dot{M}_{gw}}{3.5 \times 10^{-3} \text{M}_{\odot} \text{yr}^{-1}}\right) \left(\frac{D}{0.06 \text{ pc}}\right)^{-2}$$

Here D is the deprojected distance 0.06pc of the distance between the Sgr A* and the galactic wind origin.

One can calculate the radiation emitted by the accreted matter assuming magnetic dissipation (§2). The heating rate is given by,

$$\Gamma = \frac{\dot{M}c^8}{4^4\pi G^3 M^3} \left(\frac{r_g}{r}\right)^4 \sim 3.3 \times 10^6 \beta_d W \left(\frac{M}{10^6 M_{\odot}}\right)^{-1} \left(\frac{r_g}{r}\right)^4 \text{ erg cm}^{-3} s^{-1}.$$
 (7.2)

The cooling of the gas is dominated by the synchrotron emission from the thermal electrons and bremsstrahlung emission due to e-e and e-p collisions (§2). Assuming that the electron and proton temperatures are equal, and the total gravitational potential energy goes into heating,

$$T_e \sim 10^{13} \frac{r_g}{r} K,$$
 (7.3)

till the flow reaches a distance of $r=r_i$ where heating and cooling are equal— $\Lambda \sim \Gamma$, so that for $r < r_i$ the flow is nearly isothermal. Here, r_g is the Schwarzschild radius of the black hole.

Figure 7.12 shows the fit (solid) of the observed intensity of radiation using the simple model discussed above [342]. The mass of the central black hole is chosen to be $0.9 \times 10^6 M_{\odot}$ and its distance is chosen to be 8.5kpc. The flow is assumed to begin its spherical accretion at the bow shock, which is also identified as the accretion radius. The post (bow) shock gas temperature at the accretion radius is $2 \times 10^5 r_g$ is $T_e \sim T_p \sim 7 \times 10^6 \, \mathrm{K}$. The flow becomes isothermal for $r < 10^4 r_g$. Synchrotron emission dominates the spectrum for $\nu_{\infty} \leq 10^{13} \, \mathrm{Hz}$ and luminosity at higher frequencies are entirely due to thermal bremsstrahlung. The fit with observational data [343] seems to be reasonable. This model was subsequently improved by including an exact treatment of the cyclotron/synchrotron emissivity that is valid for all temperatures, the actual determination of the temperature distribution in the inflow, and some effect on the spectrum should the accreting plasma have a residual angular momentum, possibly forming a disk at small radii [344]. The most likely mass in this model is found to be $2 \pm 1 \times 10^6 \, M_{\odot}$ which is a factor of two higher than the earlier result.

Some authors suggest [345] that the luminosity of $7 \times 10^5 L_{\odot}$ of Sgr A* could be explained even by a standard disk model around a Kerr black hole (a > 0.9) of mass $\sim 2 \times 10^6 M_{\odot}$ provided the accretion rate is about $10^{-8.5} M_{\odot}$ yr⁻¹ and the disk is seen edge on. They rule out the possibility of having a very low mass $(< 10^3 M_{\odot})$ black hole.

A more critical approach to constrain the parameters $(M, M, \text{ and } \epsilon$ – the efficiency) is taken by Ozernoy [346] who considers diverse observations such as dynamics of spiral arm in the disk, stellar collisions close to the core, observation of high energy photons and particles, radiation spectrum of accreting winds etc. to come to the conclusion that the mass of the black hole may be much less.

From Fig. 7.11, it is clear that the central couple of parsec region contains a circum-nuclear disk of molecular gas, neutral hydrogen and dust. In it lies a clumped, a mini-spiral shaped Sgr A West, presumably tidally captured and sheared molecular cloud. Earlier attempts to associate this spiral arm with the underlying disk reveals a mass of the central black hole to be $2 \times 10^6 M_{\odot}$. However, in a recent work, Friedman et al. [347] point out that the arm is probably made up of superposition of various modes of density waves. Assuming the observed pattern is a part of two or three armed spiral, and the fact that the spiral could be traced as far in as $r \sim 0.1pc$, allows them to constrain the central point mass not to exceed $10^5 M_{\odot}$.

Another approach taken to tighten the constraint is to study the dispersion of stellar velocities. A small core radius of size ~ 0.15 pc [348] implies a very deep gravitational potential at the core in which stars with dispersion velocity $\sigma_0 \sim 100$ km

s⁻¹ (which is much smaller than the escape velocity of 600 km s⁻¹) and number density $\sim 10^8~{\rm pc^{-3}}$ constantly collide to produce massive stars. The luminosity of accretion of the ejected gas arising out of the collision of the stars would seriously constrain the central mass to $\sim 10^5 M_{\odot}$ [346]. Similar problem arises in explaining weak high energy source at or around Sgr A* as observed by ART-P and EGRET. A comparison of the observations with current models of shock acceleration of particles implies that the mass of the black hole may be as low as a few $\times 10^3 M_{\odot}$ [346]. Radio observations of Sgr A* reveals the Lorentz factor of the emitting electrons to be of the order 10^2 to 10^3 , which is possible if the central mass of the black hole is as low as about $5 \times 10^2 M_{\odot}$ [346].

Interpretations vary regarding the origin of the X-ray flux. It may be due to bremsstrahlung [342] as mentioned earlier, or it may be due to synchrotron-emitting relativistic pairs. These pairs may result from the decay of pions originating in the vicinity of the shock inside the IRS-16 wind while accreting on the galactic center. And the mass obtained by this constraint is again much less [349].

Another consideration is that the angular momentum $J_{gw} = r_a v_{gw} (2GMr_a)^{1/2} = 10^{25} M_6 \text{ cm}^2 \text{ s}^{-1}$ of the in-falling gas at a distance $r = r_a = 2GM/v_{gw}^2 \sim 7.5 \times 10^{16} M_6$ cm is much higher compared to the limiting angular momentum of a black hole $r_g c \sim 10^{22} M_6$, a disk must form whose radiation efficiency is much higher compared to the spherical Bondi accretion as assumed earlier [342]. Therefore, to explain the same efficiency, the mass of the black hole could be much smaller [346]. It is not clear however, that the angular momentum is indeed so high.

Recently, it has been argued [350] that the black hole at the galactic center may produce enough shear in the ionized flow that a weak seed field is amplified to equipartition value of about 10^5 G very close to the black hole which is then taken to outer parts of the galaxy through winds. The time scale taken to amplify to the equipartition value is around a thousand years, and therefore within the age of the galaxy, it is possible to supply the flux needed to fill the galaxy if, to a lesser extent, the local dynamo effect is allowed. One of the predictions of this model would be to find signatures of strong fields close to the center. In a parsec scale, the field should be at least four orders of magnitude higher compared to the field seen in the solar neighbourhood. Indeed, in northern arm (~ 1.5 pc) strong fields of the order of 10mG is observed [351]. In the circumnuclear disk (~ 5 pc), the field of 2mG is seen. The origin of these strong, structured field could be understood within the framework of the shear-amplification model [350].

So far, no model self-consistently studies the disk structure and radiation emitted from it around our galactic center. The detailed study of the observational results indicates that the Sgr A^* , considered to be coincident with the center of the galaxy does not show any special feature which distinguishes it from nearby stars. However, the resolution is possibly close to 10^{16} cm. It is possible that, at this resolution, one

is watching a very weakly active and starved ionized disk around the central black hole. With the presence of about two dozens of stars, which are possibly massive enough to launch density waves in the ionized disk, one would have expected some shock waves in the disk, which would be not enough to excite line emissions. Detection of these lines may distinguish the disk around Sgr A* from the stars in nearby region. Presence of quite a few mass loosing stars close to the Sgr A* indicates that matter from the winds may not have large angular momentum, since they could cancel (similar to Hoyle-Lyttleton accretion [45]) most of the angular momentum through collision. The apparent asymmetry of the bright sources (which may not be statistically significant, [7]) which supply matter to Sgr A* may cause the net angular momentum not to nullify completely. But still, one would expect accretion to take place with angular momentum orders of magnitude lower compared to the Keplerian value. In this sub-Keplerian regime, as discussed in §5, the transonic flow need not lose any energy at all. The solution with advection is perfectly stable with a very little energy emitted away. Hence the flow could be largely non-dissipative and not an efficient emitter ($\S 5$ - $\S 6$). This argument may be valid for other galactic centers as well.

A second argument that the nucleus is massive, yet inactive could be given from our knowledge of the behaviour of transonic flows as a function of the accretion rate. From eq. (5.8), it is clear that for a given mass flux, M, \mathcal{M} is inversely proportional to the square of the mass of the black hole. Let the mass of the black hole be $M = mM_{\odot}$. Assuming an optimistic accretion rate of $10^{-5}M_{\odot}\text{yr}^{-1}$, and an intermediate radiation content, $\beta \sim 0.1$, one has dimensionless $\dot{\mathcal{M}} \sim 10^{-16}/m^2$. For any reasonable mass of the black hole, m, this is too small to form an axisymmetric shock wave in the disk (Fig. 5.1). Only if the flow very close to the black hole is radiation dominated, say, if $\beta \sim 10^{-6}$ or so, $\dot{\mathcal{M}} \sim 10^4/m^2$. This is a very important regime. Because, if the mass of the black hole is around $10^6 M_{\odot}$, $\dot{\mathcal{M}} \sim 10^{-8}$, and the cooler flow falls onto the black hole after passing through the outer sonic point and no shock is expected. If the mass is around $10^5 M_{\odot}$, $\dot{\mathcal{M}} \sim 10^{-6}$ is in the region where shocks might form for some range of specific angular momentum of the disk. For even smaller black hole mass m, shock should not form but the flow is hotter and passes through the inner sonic point. Thus any indication of a strong X-ray radiation from regions of $10-100R_g\sim 10^{11-12}cm\frac{M}{10^5M_{\odot}}$ would be from shock emissions.

8 Concluding Remarks and Acknowledgments

In the past few Sections, several models of accretion flows such as the spherical Bondi flow and its variations, standard Keplerian thin disk and its variations, thick accretion disks and transonic accretion disks with or without shock waves have been discussed. There are a large number of other disk models in the literature which are mostly variations of these models. We do not have space to discuss them here. Presently, we summarize this review and add a few sentences on the future trend in modeling accretion processes.

In the 1970s, the standard accretion disk models were constructed [11, 12] largely to explain observations from the binary systems. In these systems, angular momentum supplied at the outer edge is necessarily Keplerian. Viscosity drives the inflow by removing angular momentum outwards and keeping the entire disk Keplerian in the process. Since then these disk models have also been used to explain the big blue bump observed in the continuum of active galaxies and quasars and with some success [274]. Occasionally, one invokes additional components along with the standard thin disks, such as corona, plasma cloud, absorbers, etc. in order to explain the continuum as well as variable components of X-rays and γ -rays. As we mentioned in \S 7, there are now several observations of almost zero time-lag correlated variabilities between X-rays and optical data [207] which cannot be explained by simple Keplerian disk models. The production and properties of the hard radiation and the occasional change of states by the galactic black hole candidates cannot be explained using Keplerian disks [285-296]. We also mentioned that the temporal variation of line profiles from objects, such as, ARP102B and 3C390.3 is impossible to explain by using axisymmetric disk models [212]. Recent HST observation of M87 shows clear evidence of non-axisymmetry in the ionized disk around the black hole [4-6]. These examples may support a hypothesis that accretion disks may have significant sub-Keplerian components in them as well.

That the disks need not be of 'standard' type was sensed by theoreticians even in late '70s and throughout the '80s. We discussed thick accretion disks ($\S4$), transonic accretion disks and slim accretion disks ($\S3$). In thick disks, angular momentum is assumed to be almost constant but the radial motion is ignored. In transonic disks [145], the flow is thin but the radial motion is included. In slim disks [146], matter is allowed to pass through the inner sonic point, thus improving on the standard disk model. However, in many of these models, unsuccessful attempts were made to match the flow with $Keplerian\ disks$ at some distance and the disk structure depended strongly upon the matching radius and other parameters invoked. It is also easy to argue that if matter had to accrete from a Keplerian disk from distances of parsecs by using ordinary viscous process, it would take a time comparable to Hubble time or more.

This intrinsic problem with these theoretical models, as well as problems in explaining a large number observations with Keplerian disks, may actually disappear if

one assumes that not only Keplerian (Roche lobe) but a significant amount of sub-Keplerian component (either from the wind or that originating from Keplerian disk itself) may co-accrete. If the matter starts with highly sub-Keplerian angular momentum, as probably is the case in active galaxies, its subsequent behaviour depends strongly upon the accretion rate and the viscosity in the flow [$\S\S5-6$]. If the accretion rate is small enough, the flow passes through the outer sonic point (just as a Bondi flow) and remains supersonic before falling onto a black hole. If the accretion rate is high, matter would pass through the inner sonic point. This description is valid if the entropy remains almost constant, i.e., the viscosity is small enough. Even when the flow starts with small entropy, some entropy could be generated at a shock or in the flow by viscosity which is advected along with the flow and allows the flow to pass through the inner sonic point as well. If the entropy is higher (for a given accretion rate) it is likely that strong winds may be formed from flows with positive energy [259]. Due to strong advection, the flow close to the black hole radiates with a very low efficiency as in a Bondi flow (§2, §5). This means that central black hole masses could be considerably (by a factor of 10 or more) than what is obtained from Keplerian flow considerations.

Contrary to a Newtonian star, a black hole has no hard surface. If the flow is unable to lose angular momentum efficiently, the centrifugal barrier causes the flow to have a shock close to the black hole (§5). The post-shock flow in a black hole accretion has similar properties as that of a boundary layer. This is clearly the case when the viscosity is small enough. The post-shock flow also has all the features of a thick accretion disk only more self-consistent since the radial motion is also included [218, 259]. The pre-shock flow is mainly advected towards the black hole, just as a Bondi flow, but the post-shock flow has very little radial velocity. Further in, the flow picks up radial motion and supersonically enters into the black hole. If the viscosity is high $(\alpha > \alpha_c)$, where, α_c could be any number between 0 and 1 depending on flow and cooling parameters), the stable shock disappears and the disk passes through only inner sonic point eventually becoming Keplerian at a far distance (Fig. 5.7, Fig. 6.10a-b) except close to the inner boundaries. That a Keplerian disk can form out of sub-Keplerian initial matter is no surprise. Matter accreted onto a black hole can have less specific angular momentum than what the incoming matter at the outer edge has and therefore the excess could be redistributed by the viscosity to produce a Keplerian or quasi-Keplerian disk. This also solves the so-called angular momentum problem in active galaxies and possibly requires jet models whose characteristics are not strongly tied with the Keplerian distribution in the disk. Similarly, depending on heating, cooling and viscous effects, only a sub-Keplerian disk could form, representing quiescent states of novae such as A0620-00 [352]

Thus, one may then have a thick, thin, slim or transonic (with or without shocks) disk from an initially Keplerian or sub-Keplerian inflow at large distance depending upon accretion rate and viscosity. Based on this experience, in order to explain the observed features across the electromagnetic spectrum, a generic model could be constructed for the accretion disk ($\S7.2$) which has all the 'desirable' properties of an

accretion disk around a black hole. A disk of this kind would form if there is a significant reduction of viscosity with height in the vertical direction inside the disk. Higher viscosity on the equatorial plane produces an optically thick standard Keplerian disk, which is vertically flanked by warm, optically thin halo of low angular momentum gas. Alternatively, if at the outer boundary, an admixture of Keplerian and non-Keplerian matter is supplied, the situation would be similar. The virtually inviscid halo forms a standing shock close to the black hole ($\gtrsim 10~R_q$). The post-shock flow ($T_p \sim 10^{11}~K$) heats up soft-photons coming from the disk to produce observed hard X-rays and γ rays. Such a model has the potential to explain most of the steady state as well as time dependent behaviour of the continuum and line emissions [297]. Again, the shocked halo could be replaced by a hot magnetic corona, provided one can build up a model (with entropy structure similar to that of the sun) where self-consistently coronae could be anchored [141]. Shock or no shock, we stress that the sub-Keplerian component must be present close to a black hole. This is a general feature of any viscous transonic flows [68, 76, 224, 229]. The observations seems to indicate its presence as well [Fig. 7.5, 68, 297].

Is it possible to provide THE signature of a black hole? In other words, is there a way to distinguish between a black hole candidate from a neutron star purely from the observational point of view? We have briefly discussed this issue in terms of presence and absence of the inner sonic point [§5, 77, 218]. In the case of black hole accretion the flow must be supersonic, and the bulk relativistic motion can Comptonize cooler soft-photons in an optically thick flow (soft state) to produce a power-law hard spectra [68, 297, 238, §5]. In the case of a Newtonian star, the inner sonic point does not exist, and the flow on the neutron star surface is subsonic. Thus such a hard component in the soft state should not be produced. Some observations already suggest that this weak hard component is indeed observed [353]. Perhaps there are black holes after all!

The present review article by no means claims to be a complete one. Against the wish of the author, many works had to be left out, partly due to the spatial limitation of the article size and the temporal limitation of the author and the rest is due to authors own limitation of knowledge in many of these topics. During the past years while preparing the manuscript the author is greatly benefited from discussions with several of his colleagues. He especially thanks M. Camenzind, D. Kazanas, J. Katz, R. Khanna, M. Livio, M. Malkan, L. Maraschi, F. Mayer, D. Molteni, J. Ostriker, L. Ozernoy, B. Paczyński, M. Rees, R. Rosner, H. Sponholz, L. Titarchuk, K. Thorne, S. Vainshtein, E. Vishniac and P. Wiita for helpful discussions. He is very grateful to his wife Sonali Chakrabarti for patiently reading the manuscript. Some of the material for this review has been compiled while the author was visiting the University of Chicago, Max Planck Institute of Astrophysics (Garching), Landessternwarte (Heidelberg) and the Goddard Space Flight Center. The author thanks several of his colleagues for giving him permission to reproduce their published or unpublished figures. They are: M.J. Rees (Fig. 1.1), J. Kormendy (Fig. 1.2), H. Sponholz (Fig. 1.3), L. Maraschi (Figs. 2.4-2.6, Fig. 4.1), J. Ostriker (Fig. 2.11), D. Kazanas (Figs. 2.13-2.15), S. Shapiro (Fig.

3.2), J.P. Lasota (Fig. 3.6), R. Khanna (Figs. 3.8-3.9), R. Blandford (Fig. 3.12), P. Madau (Fig. 4.7-4.10), M. Livio (Fig. 6.1), J. Hawley (Fig. 6.2), I. Hachisu (Fig. 6.7), J. Katz (Figs. 6.12-6.13), M. Malkan (Fig. 7.1), L. Titarchuk (Fig. 7.2), J. Halpern (Fig. 7.6), M. Eracleous (Fig. 7.7), A. Kochhar (Fig. 7.9) and F. Melia (Fig. 7.12). Also permissions from respective publishers are gratefully acknowledged. He thanks the members of the photography section of the Tata Institute of Fundamental Research for producing several of the glossy prints very promptly. The author thanks NASA Space Physics Theory Programme for the support of his visit to the University of Chicago and Indian National Science Academy and Deutsche Forschungsgemeinschaft for the support of his visit to Germany.

Note Added In Proof

(A) Effect of non-Keplerian accretion disk on gravitational wave emission from a binary black hole system:

Study of gravitational wave emission from compact binary systems has received a significant boost in recent years because of the realization that the detection of gravitational waves would directly identify the compact and strongly gravitating bodies, such as neutron stars and black holes. Laser Interferometric Gravitational Wave Observatory (LIGO) and Laser Interferometer Space Antenna (LISA) project instruments are being constructed to achieve these goals [354, 355]. In binary systems composed of only neutron stars and stellar black holes, quadrupole radiations from binary systems are found to be adequate [356]. However, around a massive black hole (M_1) , one needs to consider the exchange of angular momentum of the infalling compact object (in a Keplerian orbit) of mass M_2 with the accretion disk, since the disk usually deviates from Keplerian (Fig. 5.7). The orbital angular momentum loss rate due to gravitational wave would be, $R_{gw} = \frac{dL}{dt}|_{gw}$ In presence of an accretion disk co-planer with the orbiting companion, matter from the disk (with local specific angular momentum l(r), Fig. 5.7) will be accreted onto the companion at a rate close to its Bondi accretion rate (eq. 2.5). The rate at which angular momentum of the companion will be changed due to Bondi accretion from disk will be, $R_{disk} = \frac{dL}{dt}|_{disk} = \dot{M}_2(l_{Kep}(x) - l_{disk}(x))$ Here, l_{Kep} and l_{disk} are the local Keplerian and disk angular momenta respectively. Consider a special case where, $M_2 \ll M_1$ and $l_{disk} \ll l_{Kep}$. In this case, the ratio R of these two rates is,

$$R = \frac{R_{disk}}{R_{qw}} = 1.518 \times 10^{-7} \frac{\rho_{-10}}{T_{10}^{3/2}} x^4 M_8^2$$

Here, x is the companion orbit radius in units of the Schwarzschild radius of the primary, M_8 is in units of $10^8 M_{\odot}$, ρ_{10} is the density in units of 10^{-10} gm cm⁻³ and T_{10} is the temperature of the disk in units of 10^{10} K. It is clear that, for instance, at x=10, and $M_8=10$, the ratio $R\sim 0.015$ suggesting the effect of the disk could provide a significant correction term to the general relativistic loss of angular momentum. Thus, the gravitational wave emitted from such a system will also be affected. In the above example, both the disk and the gravitational wave work in the same direction in reducing angular momentum of the secondary. Alternatively, when $l_{disk}>l_{Kep}$ they act in opposite direction and may slow down the loss of angular momentum due to gravity waves [62]. In either case, the ratio R is independent of the mass of the companion black hole, as long as $M_2 << M_1$.

(B) Spectral signatures of bulk motion Comptonization close to a black hole:

As accreting gas comes closer to a black hole, it is accelerated and soft photons intercepted from Keplerian accretion disk (or, generated within by synchrotron radiation) are up-scattered by this flow [74, 238]. Signature of this up-scattered hard component

may have been observed in soft-states of black hole candidates (Figs. 7.4-7.5; [68]).

Consider a low energy photon diffusing outwards through an accelerated inflowing electron and getting scattered. The photons within trapping radius $r_{trap} \sim \dot{M}$ (Section 2) gain energy on an average and produce a hard tail. Physically, at a given scattering, the relative change in the photon energy due to bulk motion is $\Delta E/E \sim d(v/c)/d\tau_T \sim 1/\dot{m}$ but the energy loss due to recoil effect (Compton scattering) is $\Delta E/E \sim -E/m_e c^2$. For very soft photons, $E/m_e c^2 << 1$ the energy gain is important and the resulting spectrum is a power law of spectral slope $\alpha \sim 1.5$. When these two effects are comparable, a sharp cut-off is produced at $E \sim m_e c^2/\dot{m}$. In the case of neutron star accretion, the velocity v becomes zero on the star surface, which reduces the spectral slope to $\alpha \sim 0$.

References

- [1] A. Cowley, Ann. Rev. Astron. Astrophys 30 (1992) 287.
- [2] M.J. Rees, Ann. Rev. Astron. Astrophys. 22 (1984) 471.
- [3] M.J. Rees, Scientific American 263 (1990) 56.
- [4] H.C. Ford, R.J. Harms, Z.I. Tsvetanov, G.F. Hartig, L.L. Dressel, G.A. Kriss, A.F. Davidsen, R. Bohlin & B. Margon, Astrophys. J. Letters , 435 (1994) L28.
- [5] R.J. Harms, H.C. Ford, Z.I. Tsvetanov, G.F. Hartig, L.L. Dressel, R. Bohlin, G.A. Kriss, A.F. Davidsen, B. Margon & A. Kochhar Astrophys. J. Letters 435 (1994) L35.
- [6] S.K. Chakrabarti, Astrophys. J. 441 (1995) 576.
- [7] R. Genzel, D. Hollenbach & C.H. Townes, Rep. Prog. Phys. 57 (1994) 478.
- [8] J. Kormendy, Astrophys. J. 325 (1988) 128.
- [9] R.P. van der Marel, H.-W. Rix, D. Carter, M. Franx, S.D.M. White & T. de Zeeuw, Mon. Not. R. Astron. Soc. 268 (1994) 521; M. Bradley, A. Curir & F. de Felice, Astrophys. J. 381 (1991) 72.
- [10] L. Valtaoja, M.J. Valtonen & G.G. Byrd, Astrophys. J. 343 (1989) 47.
- [11] N.I. Shakura & R.A. Sunyaev, Astron. Astrophys. 24 (1973) 337.
- [12] I. Novikov & K.S. Thorne, in: Black Holes, eds. C. DeWitt and B. DeWitt (Gordon and Breach, New York, 1973).
- [13] R.W. Romani, Astrophys. J. 399 (1992) 621.
- [14] R. Narayan, T. Piran & A. Shemi, Astrophys. J.L 379 (1991) L17.
- [15] S.L. Shapiro & S.A. Teukolsky, Physical Review D 45 (1992) 2739.
- [16] S. Sigurdsson & L. Hernquist, Nature 364 (1993) 423; S.R. Kulkarni, P. Hut & S. McMillan, Nature 364 (1993) 412.
- [17] K. Croswell, Astronomy 21 (1993) 28.
- [18] A. Loeb, Astrophys. J. 403 (1993) 542.
- [19] V.I. Dokuchaev, Soviet Physics Uspekhi 34 (1991) 447.
- [20] A. Soltan, Mon. Not. R. Astron. Soc. 200 (1982) 115; A. Chokshi & E.L. Turner, Mon. Not. R. Astron. Soc. 259 (1992) 421.
- [21] T.A. Small & R.D. Blandford, Mon. Not. R. Astron. Soc. 259 (1992) 725.

- [22] G.A. Bower, D.O. Richstone, G.D. Bothun & T.M. Heckman, Astrophys. J. 402 (1993) 76.
- [23] I. Shlosman, M.C. Begelman & J. Frank, Nature 345 (1990) 679.
- [24] J.G. Hills, Nature 254 (1975) 295.
- [25] J.G. Hills, Mon. Not. R. Astron. Soc. 182 (1978) 517.
- [26] B. Carter & J.P. Luminet, Astron. Astrophys. 121 (1983) 97.
- [27] B. Carter & J.P. Luminet, Mon. Not. R. Astron. Soc. 212 (1985) 23.
- [28] J.P. Luminet & J.A. Marck, Mon. Not. R. Astron. Soc. 212 (1985) 57.
- [29] M.J. Rees, Nature 333 (1988) 523.
- [30] E.S. Phinney, in: Theory of Accretion Disks, eds. F. Meyer, W. Duschl, J. Frank & E. Meyer-Hofmeister (Kluwer, Dordrecht, 1989).
- [31] S. Sembay & R.G. West (1993) Mon. Not. R. Astron. Soc. 262 141.
- [32] W.H. Press & S. Teukolsky, Astrophys. J. 213 (1977) 183.
- [33] C.R. Evans & C.S. Kochanek, Astrophys. J. 346 (1989) L13.
- [34] N. Roos, Astrophys. J. 285 (1992) 108.
- [35] I.D. Novikov, C.J. Pethick & A.G. Polnarev, Mon. Not. R. Astron. Soc. 255 (1992) 276.
- [36] A.G. Kosovichev & I.D. Novikov, Mon. Not. R. Astron. Soc. 258 (1992) 715.
- [37] H. Sponholz, in: Workshop on Advances in Smoothed Particle Hydrodynamics, LA-UR-93-4375.
- [38] P. Laguna, W.A. Miller, W.H. Zurek & M.B. Davies, Astrophys. J. 410 (1993) L83.
- [39] J.G. Hills, Astron. J. 102 (1991) 704.
- [40] S. Mikkola & M.J. Valtonen, Astrophys. J. 348 (1990) 412.
- [41] G.A. Young, G.A. Shields & J.C. Wheeler, Astrophys. J. 212 (1977) 367.
- [42] M.J. Duncan & S.L. Shapiro, Astrophys. J. 268 (1983) 565.
- [43] C.L. Sarazin, Revs. Mod. Phys. 58 (1986) 1.
- [44] K.A. Arnaud, in: Cooling Flows in Clusters and Galaxies, ed. A.C. Fabian 31 (Kluwer, Dordrecht, 1988).
- [45] F. Hoyle & R.A. Lyttleton, Proc. Camb. Phil. Soc. 35 (1939) 592.

- [46] B.W. Murphy, H.N. Cohn & R.H. Durisen, Astrophys. J., 370 (1991) 60.
- [47] V.I. Dokuchaev, Mon. Not. R. Astron. Soc. 251 (1991) 564.
- [48] L.M. Ozernoy, in: Chemical and Dynamical Evolution of our Galaxy, ed. E. Basinska-Orzesik & M. Mayor (Geneva Observatory, Geneva, 1989).
- [49] R.H. Sanders & W. Van Oosterom, Astron. Astrophys. 131 (1984) 267.
- [50] T. Fukushige, T. Ebisuzaki & J. Makino, Publ. Astron. Soc. Japan, 44 (1992) 281.
- [51] C.G. Lacey & J.P. Ostriker, Astrophys. J. 299 (1985) 633.
- [52] P. Hut & M.J. Rees, Mon. Not. R. Astron. Soc. 259 (1992) 27p.
- [53] M. Morris, Astrophys. J. 408 (1993) 496.
- [54] J.R. Ipser & R.H. Price, Astrophys. J. 216 (1977) 578.
- [55] S. Collin-Souffrin, Astron. Astrophys. 243 (1991) 5.
- [56] D.J. Hegyi, E.W. Kolb & K.A. Olive, Astrophys. J. 300 (1986) 492.
- [57] J. Mcdowell, Mon. Not. R. Astron. Soc. 217 (1985) 77.
- [58] J.R. Bond & B.J. Carr, Mon. Not. R. Astron. Soc. 207 (1984) 585.
- [59] T. Fukushige, T. Ebisuzaki & J. Makino, Astrophys. J. 396 (1992) L61; K.S. Thorne
 & V.B. Braginski, Astrophys. J. 178 (1976) 623.
- [60] A.V. Tutukov & L.R. Yungelson, Mon. Not. R. Astron. Soc. 260 (1993) 675.
- [61] D.F. Chernoff & L.S. Finn, Astrophys. J. 411 (1993) L5.
- [62] S.K. Chakrabarti, Astrophys. J. 411 (1993) 610; S.K. Chakrabarti, Phys. Rev. D. (1995, submitted).
- [63] D. Molteni, G. Gerardi & S.K. Chakrabarti, Astrophys. J. 436 (1994) 249.
- [64] M.C. Begelman, R.D. Blandford & M.J. Rees, Rev. Mod. Phys 56 (1984) 255.
- [65] J.S. Kaastra & N. Roos, Astron. Astrophys. 254 (1992) 96; N. Roos, J.S. Kaastra & C.A. Hummel, Astrophys. J. 409 (1993) 130.
- [66] N.Y. Gnedin & J.P. Ostriker, Astrophys. J. 400 (1992) 1; N.Y. Gnedin, J.P. Ostriker & M.J. Rees, Astrophys. J. 438 (1995) 40.
- [67] H. Kunieda, T.J. Turner, H. Awaki, K. Koyama, R. Mushotzky & Y. Tsusuka, Nature 345 (1990) 786; L. Stella, Nature 344 (1990) 747.
- [68] S.K. Chakrabarti & L.G. Titarchuk, Astrophys. J. (1995) Dec. 20th issue.

- [69] J. Wambsganss & B. Paczyński, Astrophys. J. 397 (1992) L1.
- [70] S.L. Shapiro & S.A. Teukolsky, Black Holes, White Dwarfs and Neutron Stars—the Physics of Compact Objects (John Wiley & Sons, New York, 1983).
- [71] J.M. Bardeen, in: Black Holes, eds. C. DeWitt & B. DeWitt (Gordon & Breach, New York, 1973).
- [72] S.K. Chakrabarti, Mon. Not. R. Astron. Soc. 261 (1993) 625.
- [73] S.K. Chakrabarti & R. Khanna, Mon. Not. R. Astron. Soc. 256 (1992) 300.
- [74] R.D. Blandford & D.G. Payne, Mon. Not. R. Astron. Soc. 194 (1981) 1033; ibid.,
 194 (1981) 1041; R. Cowsik, & M.A. Lee, Proc. R. Soc. A (London), 383 (1982) 409.
- [74a] .G. Titarchuk, A. Mastichiadis & N. Kylafis, ApJ, 1996, (submitted).
- [75] B. Paczyński & P.J. Wiita, Astron. Astrophys. 88 (1980) 23.
- [76] R. Matsumoto, S. Kato, J. Fukue & A.T. Okazaki, Publ. Astron. Soc. Japan. 36 (1984) 71; J.F. Lu, Astron. Astrophys. 148 (1985) 176; S. Kato, F. Honma, R. Matsumoto, Publ. Astron. Soc. Japan 40 (1988) 709; X. Chen & R. E. Taam, Astrophys. J. 412 (1993) 254.
- [77] S.K. Chakrabarti, Theory of Transonic Astrophysical Flows (World Scientific, Singapore, 1990).
- [78] U. Anzer, G. Börner, & J.J. Monaghan, Astron & Astrophys., 176 (1987) 235; R.E.
 Davies & J. Pringle Mon. Not. R. Astro. Soc. (1980) 599
- [79] S. Shapiro & A.P. Lightman, Astrophys. J. 204 (1976) 555.
- [80] H. Bondi, Mon. Not. R. Astron. Soc. 112 (1952) 195.
- [81] I. Shima et al. Mon. Not. R. Astro. Soc., 217 (1985) 367.
- [82] J.M.T. Thompson & H.B. Stewart, Nonlinear Dynamics and Chaos (John Wiley & Sons Ltd., 1985).
- [83] K.S. Thorne, Mon. Not. R. Astron. Soc. 194 (1981) 439.
- [84] V.F. Shvartsman, Sov. Astron. A.J. 15 (1971) 377.
- [85] S.L. Shapiro, Astrophys. J. 180 (1973) 531.
- [86] S.L. Shapiro, Astrophys. J. 185 (1973) 69.
- [87] F.C. Michel, Astrophys. Sp. Sci. 15 (1972) 153.
- [88] M.C. Begelman, Mon. Not. R. Astron. Soc. 185 (1978) 847.
- [89] R.A. Flammang, Mon. Not. R. Astron. Soc. 199 (1982) 833.

- [90] R.A. Flammang, Mon. Not. R. Astron. Soc. 206 (1984) 589.
- [91] J.M. Blondin, Astrophys. J. 308 (1986) 755.
- [92] M.H. Soffel, Astron. Astrophys. 116 (1982) 111.
- [93] J.P. Ostriker, R. McCray, R. Weaver & A. Yahil, Astrophys. J. 208 (1976) L61.
- [94] L. Maraschi, R. Roasio & A. Treves, Astrophys. J. 253 (1982) 312.
- [95] M. Colpi, L. Maraschi & A. Treves, Astrophys. J. 280 (1984) 319.
- [96] A. Wandel, A. Yahil & M. Milgrom, Astrophys. J. 282 (1984) 53.
- [97] M.G. Park, Astrophys. J. 354 (1990) 64.
- [98] L. Nobili, R. Turolla & L. Zampieri, Astrophys. J. 383 (1991) 250.
- [99] M.G. Park & J.P. Ostriker, Astrophys. J. 347 (1989) 679.
- [100] M.C. Begelman & T. Chiueh, Astrophys. J. 332 (1988) 872.
- [101] P. Mészáros, Astron. Astrophys. 44 (1975) 59.
- [102] J.R. Ipser & R.H. Price, Astrophys. J. 255 (1982) 654.
- [103] J.R. Ipser & R.H. Price, Astrophys. J. 267 (1983) 371.
- [104] G.B. Rybicki & A.P. Lightman, Radiative Processes in Astrophysics (John Wiley & Sons, New York, 1979).
- [105] A.R. Masters, Ph. D. Thesis, University of Illinois, (1978).
- [106] R.A. Sunyaev & L.G. Titarchuk, Astron. Astrophys. 86 (1980) 121; R.A. Sunyaev
 & L.G. Titarchuk, Astron. Astrophys. 143 (1985) 374
- [107] L.A. Pozdnyakov, I.M. Sobol' & R.A. Sunyaeve, Astrophys. Sp. Sci. Rev. 2 (1983)
 89; A. Zdziarski, J. Astrophys. 294 (1985) L79.
- [108] L.G. Titarchuk & Y. Lyubarskij, Astrophys. J. (1995), in press.
- [109] L. Spitzer, Physics of Fully Ionized Plasma, (Interscience, New York, 1962).
- [110] T.A. Weaver, Phys. Rev. 13 (1976) 1563.
- [111] A.P. Lightman & A. Zdziarski 319 (1987) 643; A.P. Lightman, Astrophys. J. 253 (1982) 842.
- [112] R. Svensson, Astrophys. J. 258 (1982) 321.
- [113] R. Svensson, Astrophys. J. 258 (1982) 335.
- $[114]\,$ A.P. Lightman, A. Zdziarski & M.J. Rees, Astrophys. J. 315 (1987) L113.

- [115] E.V. Levich & R.A. Sunyaev, Astron. & Astrophys. 15 (1971) 363.
- [116] D. Mihalas & B.W. Mihalas, Foundation of Radiation Hydrodynamics (Oxford university press, Oxford, 1984).
- [117] L.L. Cowie, J.P. Ostriker & A.A. Stark, Astrophys. J. 226 (1978) 1041.
- [118] V. Moncrief, Astrophys. J. 235 (1980) 1038.
- [119] K.M. Chang & J.P. Ostriker, Astrophys. J. 288 (1985) 428.
- [120] R.F. Stellingwerf & J. Buff, Astrophys. J. 260 (1982) 755.
- [121] A. Babul, J.P. Ostriker & P. Mészáros, Astrophys. J. 347 (1989) 59.
- [122] D. Kazanas & D.C. Ellison, Astrophys. J. 304 (1986) 178.
- [123] A.R. Bell, Mon. Not. R. Astron. Soc. 182 (1978) 147.
- [124] A.R. Bell, Mon. Not. R. Astron. Soc. 182 (1978) 443.
- [125] J.G. Kirk & P. Schneider, Astrophys. J. 322 (1987) 256.
- [126] J.G. Kirk & P. Schneider, Astrophys. J. 315 (1987) 425.
- [127] R.D. Blandford & D. Eichler, Phys. Rep. 174 (1987) 2.
- [128] R.J. Prothero & D. Kazanas, Astrophys. J. 265 (1983) 620.
- [129] D. Eichler, Astrophys. J. 277 (1984) 429.
- [130] D.C. Ellison & D. Eichler, Astrophys. J. 286 (1984) 691.
- [131] J.H. Krolik, C.F. McKee & C.B. Tartar, Astrophys. J. 249 (1981) 422.
- [132] A. Wandel & A. Yahil, Astrophys. J. (Letters) 295 (1985) L1.
- [133] J.M. Blondin & A. Königl, Astrophys. J. 323 (1987) 451.
- [134] J. Pringle, Ann. Rev. Astron. Astrophys. 19 (1981) 137; J. Frank, A.R. King & Raine, D.J., Accretion Power in Astrophysics (Cambridge University Press, Cambridge, 1991); A.P. Lightman & D.M. Eardley, Astrophys. J. 187 (1974) L1; R.D. Blandford, in: Active Galactic Nuclei, eds. R.D. Blandford, H. Netzer & L. Woltjer (Springer-Verlag, Berlin, 1990).
- [135] F. Meyer & E. Meyer-Hofmeister, Astron. Astrophys. 104 (1981) L10.
- [136] D.N.C. Lin & G. Shields, Astrophys. J. 305 (1986) 28; J.K. Cannizzo, Astrophys. J. 385 (1992) 94.
- [137] R.E. Pudritz & C.A. Norman, Astrophys. J. 301 (1986) 571.

- [138] F.V. Coroniti, Astrophys. J. 244 (1981) 587; A.A. Galeev, R. Rosner & G.S. Vaiana, Astrophys. J. 229 (1979) 318; D.M. Eardley & A.P. Lightman, Astrophys. J. 200 (1975) 187.
- [139] S.A. Balbus & J.F. Hawley, Astrophys. J. 376 (1991) 214; S.A. Balbus & J.F. Hawley, Astrophys. J. 376 (1991) 223.
- [140] E.T. Vishniac & P. Diamond, Astrophys. J. 347 (1989) 435.
- [141] S.K. Chakrabarti & S. D'Silva, Astrophys. J. 424 (1994) 138; S. D'Silva & S.K. Chakrabarti, Astrophys. J. 424 (1994) 149.
- [142] K. Sawada, T. Matsuda & I. Hachisu, Mon. Not. R. Astron. Soc. 219 (1986) 75.
- [143] S.L. Shapiro, A.P. Lightman & D.M. Eardley, Astrophys. J. 204 (1974) 187; N.I.
 Shakura & R.A. Sunyaev, Mon. Not. R. Astron. Soc. 175 (1976) 613; D.G. Payne & D.M. Eardley, Astrophys. J. 19 (1977) 39.
- [144] T.R. White & A.P. Lightman, Astrophys. J. 340 (1989) 1024.
- [145] B. Paczyński & G. Bisnovatyi-Kogan, Acta Astron. 31 (1981) 283; B. Muchotrzeb & B. Paczyński, Acta Astron. 32 (1982) 1.
- [146] M.A. Abramowicz, B. Czerny, J.P. Lasota & E. Szuszkiewicz, Astrophys. J. 332 (1988) 646.
- [147] R.D. Blandford & D.G. Payne, Mon. Not. R. Astron. Soc. 199 (1982) 883.
- [148] M. Camenzind, in: Accretion Disks and Magnetic Fields in Astrophysics, ed. G. Belvedere (Kluwer, Dordrecht, 1989).
- [149] A. Königl, Astrophys. J. 342 (1989) 208.
- [150] S.K. Chakrabarti & P. Bhaskaran, Mon. Not. R. Astron. Soc. 255 (1992) 255.
- [151] J. Contopoulos & R.V.E. Lovelace, Astrophys. J. 429 (1994) 139.
- [152] S.H. Lubow, J.C.B. Papaloizou & J. Pringle, Mon. Not. R. Astron. Soc. 267 (1994) 235.
- [153] M. Wardle & A. Königl, Astrophys. J. 410 (1993) 218.
- [154] J. Ferreira & G. Pelletier, Astronom. Astrophys. 276 (1993) 637.
- [155] J. Heyvaerts & C.A. Norman, Astrophys. J. 347 (1989) 1055.
- [156] R.V.F. Lovelace, J.C.L. Wang & M.E. Sulkanen, Astrophys. J. 315 (1987) 504;
 J.C.L. Wang, M.E. Sulkanen & R.V.E. Lovelace, Astrophys. J. 355 (1990) 38.
- [157] R. Khanna & M. Camenzind, Astron. Astrophys. 263 (1992) 401.
- [158] R. Khanna & M. Camenzind, Astrophys. J. Letters 435 (1994) L129.

- [159] R. Khanna, Ph. D. Thesis, University of Heidelberg (1993).
- [160] E.J. Weber & L. Davis, Jr. Astrophys. J. 148 (1967) 217.
- [161] S.K. Chakrabarti, Mon. Not. R. Astron. Soc. 246 (1990) 134.
- [162] M. Takahashi, S. Nitta, Y. Tatematsu, A. Tomimatsu, Astrophys. J. 363 (1990) 206; P. Englmaier, Diploma Thesis, University of Heidelberg (1993).
- [163] R. Penrose, Nouvo cemento, 1, (1969) 252
- [164] D. Christodoulou, Phys. Rev. Lett., 25 (1970) 1596
- [165] R.L. Znajek, Mon. Not. R. Astron. Soc., 185 (1978) 833
- [166] K.S. Thorne, R. Price, & D.A. MacDonald, (1986) Black Holes the Membrane Paradigm, Yale University Press, New Haven
- [167] R. Wald, Physical Rev. D. 10 (1974) 1680
- [168] R.D. Blandford, & R.L. Znajek, Mon. Not. R. Astron. Soc. 179 (1977) 433
- [169] D.A. Macdonald & K.S. Thorne, Mon. Not. R. Astron. Soc. 198 (1982) 345
- [170] S.K. Chakrabarti, in Numerical Simulations in Astrophysics, Eds. J. Franco, S. Lizano, L. Aguilar & E. Daltabuit (Cambridge University Press: Cambridge, 1994).
- [171] L. Maraschi, C. Reina & A. Treves, Astrophys. J. 206 (1976) 295.
- [172] D. Lynden-Bell, Phys. Scripta, 17 (1978) 185.
- [173] D. Lynden-Bell, Nature, 223 (1969) 690.
- [174] M. Kozlowski, M. Jaroszynski & M.A. Abramowicz, Astron. Astrophys. 63 (1978) 209.
- [175] M. Abramowicz, M. Jaroszynski & M. Sikora, Astron. Astrophys. 63 (1978) 221.
- [176] M.A. Abramowicz, M. Calvani, & L. Nobili, Astrophys. J. 242 (1980) 772.
- [177] B. Paczyński & M. Abramowicz, Astrophys. J. 253 (1982) 897.
- [178] S.K. Chakrabarti, in: Active Galactic Nuclei, ed. J.E. Dyson (University of Manchester Press, 1984).
- [179] S.K. Chakrabarti, Astrophys. J. 288 (1985) 1.
- [180] S.K. Chakrabarti, Comments on Astrophys. 4 (1990) 209.
- [181] J.L. Tassoul, Theory of Rotating Stars (Princeton University Press, New Jersey, 1978).

- [182] J.H. Hunter & R.E. Wilson, Astrophys. J. 302 (1986) 11.
- [183] S.K. Chakrabarti, Mon. Not. R. Astron. Soc. 250 (1991) 7.
- [184] S.K. Chakrabarti, Mon. Not. R. Astron. Soc. 245 (1990) 747.
- [185] S.K. Chakrabarti, in: Accretion Processes in Astrophysics, J. Audouze & J. Tran Thanh Van (Editions Frontierès, Paris, 1986).
- [186] S.K. Chakrabarti, in: Big Bang, Active Galactic Nuclei and Supernovae, eds. S. Hayakawa & K. Sato (Universal Academy Press, Inc., Tokyo, 1988).
- [187] S.K. Chakrabarti, L. Jin & W.D. Arnett, Astrophys. J. 313 (1987) 674; S.K. Chakrabarti, Astrophys. J. 324 (1988) 391.
- [188] S.K. Chakrabarti, J. Astrophys. Astron. 9 (1988) 49.
- [189] S. Nishida, Y. Eriguchi & A. Lanza, Astrophys. J. 401 (1992) 618; S. Nishida & Y. Eriguchi, Astrophys. J 427 (1994) 429.
- [190] A. Lanza, Astrophys. J. 389 (1992) 141.
- [191] K. Arai & M. Hashimoto, Astron. Astrophys. 254 (1992) 191; M. Hashimoto, Y. Eriguchi, K. Arai & E. Müller, Astron. Astrophys. 268 (1993) 131; Y. Eriguchi & E. Müller, Astrophys. J. 418 (1993) 666.
- [192] J. Fukue, Publ. Astron. Soc. Japan 34 (1982) 163; S.K. Chakrabarti, Astrophys. J. 303 (1986) 582.
- [193] P. Madau, Astrophys. J. 327 (1988) 116.
- [194] M.J. Rees, M.C. Begelman, M.C., R.D. Blandford & E.S. Phinney, Nature 295 (1982) 17.
- [195] M. Sikora & M. Zbyszewska, Mon. Not. R. Astron. Soc. 212 (1985) 553; F. Takahara & M. Kusunose, Prog. Theor. Phys. 73 (1985) 1390.
- [196] M.C. Begelman, M. Sikora & M.J. Rees, Astrophys. J. 689 (1987) 698.
- [197] C.J. Hogan & J.H. Applegate, Nature 330 (1987) 236.
- [198] I.F. Mirabel & Rodriguez, L.F. Nature 371 (1994) 46.
- [199] J.C.B. Papaloizou & J.E. Pringle, Mon. Not. R. Astron. Soc. 208 (1984) 721;
 J.C.B. Papaloizou & J.E. Pringle, Mon. Not. R. Astron. Soc. 213 (1985) 799.
- [200] P. Goldreich, J. Goodman & R. Narayan, Mon. Not. R. Astron. Soc. 221 (1986) 339.
- [201] O.M. Blaes, Mon. Not. R. Astron. Soc. 216 (1985) 553.
- $[202]\,$ W.H. Zurek & W. Benz, Astrophys. J. 308 (1986) 123.

- [203] J.F. Hawley & O.M. Blaes, Mon. Not. R. Astron. Soc. 225 (1987) 677.
- [204] Y. Kojima, Prog. Theor. Phys. 75 (1986) 251.
- [205] O.M. Blaes, Mon. Not. R. Astron. Soc. 227 (1987) 975; Hawley, J.F, Astrophys. J. 381 (1991) 496.
- [206] O. Gat & M. Livio, Astrophys. J. 396 (1992) 542.
- [207] J. Clavel, et al. Mon. Not. R. Astron. Soc. 246 (1990) 668; B.M. Peterson et al. Astrophys. J. 368 (1991) 119.
- [208] E. Rokaki, S. Collin-Souffrin & C. Magnan, Astron. & Astrophys. 272 (1993) 8.
- [209] S. Molendi, L. Maraschi & L. Stella, Mon. Not. R. Astron. Soc. 255 (1992) 27.
- [210] J.S. Miller & B.M. Peterson, Astrophys. J. 361 (1990) 98.
- [211] S.K. Chakrabarti & P.J. Wiita, Astrophys. J. 387 (1992) L21.
- [212] S.K. Chakrabarti & P.J. Wiita, Astrophys. J., 434 (1994) 518.
- [213] T.E. Holzer & W.I. Axford, Ann. Rev. Astron. Astrophys. 8 (1970) 31; A. Ferrari,
 E. Trussoni, R. Rosner & T. Tsinganos, Astrophys. J. 294 (1985) 397.
- [214] E.P.T. Liang & K.A. Thompson, Astrophys. J., 240 (1980) 271.
- [215] J.F. Hawley, L.L. Smarr & J.R. Wilson, Astrophys. J. 277 (1984) 296.
- [216] J.F. Hawley, L.L. Smarr & J.R. Wilson, Astrophys. J. Suppl. 55 (1985) 211.
- [217] J. Fukue, Publ. Astron. Soc. Japan 39 (1987) 309.
- [218] S.K. Chakrabarti, Astrophys. J. 347 (1989) 365.
- [219] M. Abramowicz & S.K. Chakrabarti, Astrophys. J. 350 (1990) 281.
- [220] S.K. Chakrabarti & D. Molteni, Astrophys. J. 417 (1993) 671.
- [221] K. Nobuta & T. Hanawa, Publ. Astron. Soc. Japan, 46 (1994) 257.
- [222] K. Nakayama, Mon. Not. R. Astron. Soc. 259 (1992) 259.
- [223] R. Yang & M. Kafatos, Astron & Astrophys. 295 (1995) 238.
- [224] S.K. Chakrabarti, Mon. Not. R. Astron. Soc. 340 (1989) 7; S.K. Chakrabarti, Mon. Not. R. Astron. Soc. 243 (1990) 610.
- [225] S.K. Chakrabarti & D. Molteni, Mon. Not. R. Astron. Soc. 272 (1995) 80.
- [226] S.K. Chakrabarti, Astrophys. J. (1995, submitted).
- [227] D. Molteni, H. Sponholz & S.K. Chakrabarti, Astrophys. J. (1995).

- [228] S.H. Langer, G. Chanmugam & G. Shaviv, Astrophys. J. Letters 245 (1981) L23.
- [229] R. Narayan & I. Yi, Astrophys. J. 428 (1994) L13.
- [230] M.A. Abramowicz, X. Chen, S. Kato, J.P. Lasota, & O. Regev, Astrophys. J. 438 (1995) L37.
- [231] A. Wandel & E.P. Liang, Astrophys. J., 380 (1991) 84.
- [232] S.K. Chakrabarti, Astrophys. J. 350 (1990) 275.
- [233] H. Sponholz & D. Molteni, Mon. Not. R. Astron. Soc. 271 (1994) 233.
- [234] T. Matsuda, M. Inoue, K. Sawada, E. Shima & K. Wakamatsu, Mon. Not. R. Astron. Soc. 229 (1987) 295
- [235] M.L. Różyczka & H.C. Spruit, Theory of Accretion Disks, eds. F. Meyer, W. Duschl, J. Frank & E. Meyer-Hofmeister (Kluwer, Dordrecht, 1989).
- [236] H.C. Spruit, Astron. Astrophys. 184 (1987) 173.
- [237] S.K. Chakrabarti & P.J. Wiita, Astrophys. J. 411 (1993) 602.
- [238] L.G. Titarchuk, A. Mastichiadis, N. Kylafis, Astrophys. J. (1995, sumbitted)
- [239] H.R. Miller & P.J. Wiita, eds. Active Galactic Nuclei (Berlin, Springer Verlag, 1991).
- [240] M.T. Carini, H.R. Miller & B.D. Goodrich, Astron. J. 100 (1990) 347
- [241] M.T. Carini, H.R. Miller, J.C. Noble, & A.C. Sadun, Astron. J. 101 (1991) 1196.
- [242] A. Quirrenbach et al. Astrophys. J. 372 (1991) L71.
- [243] A. Treves et al. Astrophys. J. 341 (1982) 733.
- [244] A. Lawrence, M.G. Watson, K.A. Pounds & M. Elvis, Nature 325 (1987) 694.
- [245] I. McHardy, in: Proc. 23rd ESLAB Symp. on Two Topics in X-Ray Astronomy, eds. J. Hunt & B. Battrick (ESA SP-296, 1989).
- [246] R.G. Abraham & I. McHardy, in: Proc. 23rd ESLAB Symp. on Two Topics in X-Ray Astronomy, eds. J. Hunt & B. Battrick (ESA SP-296, 1989).
- [247] T.P. Krichbaum, A. Quirrenbach & A. Witzel, in: Variability of Blazars, eds. E. Valtaoja & M. Valtonen (Cambridge, Cambridge Univ. Press, 1992).
- [248] S.K. Chakrabarti, Astrophys. J. 362 (1990) 406.
- [249] E. Shima et al. Mon. Not. R. Astron. Soc. 217 (1985) 367.
- [250] T. Matsuda, M. Inoue & K. Sawada, Mon. Not. R. Astron. Soc. 226 (1987) 785.

- [251] R. Taam & B. Fryxall, Astrophys. J. 331 (1988) L117
- [252] J.M. Blondin, T.R. Kallman, B. Fryxall, & R.E. Taam, Astrophys. J. 371 (1990) 684.
- [253] T. Matsuda, N. Sekino, K. Sawada, E. Shima, M. Livio, U. Anzer, G. Börner, Astron. & Astrophys. 248 (1991) 301
- [254] M. Matsuda, T. Ishii, N. Sekino, K. Sawada, E. Shima, M. Livio, U. Anzer, U. Mon. Not. R. Astron. Soc. 255 (1992) 183.
- [255] T. Ishii, T. Matsuda, E. Shima, M. Livio, U. Anzer, G. Börner, Astrophys. J. 404 (1993) 706
- [256] M. Livio, N. Soker, T. Matsuda & U. Anzer, Mon. Not. R. Astron. Soc. 253 (1991) 633
- [257] M. Livio, 1991, in Evolutionary Processes in Interacting Binary Stars, eds. Y. Kondo et al. (Dordrech); M. Ruffert, Astrophys. J. 427 (1994) 342; M. Ruffert & W.D. Arnett, Astrophys. J. 427 (1994) 351.
- [258] J.R. Wilson, Astrophys. J. 173 (1978) 431.
- [259] D. Molteni, G. Lanzafame & S.K. Chakrabarti, Astrophys. J. 425 (1994) 161.
- [260] M.A. Abramowicz & W.H. Zurek, Astrophys. J. 246 (1981) 314.
- [261] K. Sawada & T. Matsuda, Mon. Not. R. Astron. Soc. 255 (1992) 17p.
- [262] S.K. Chakrabarti & T. Matsuda, Astrophys. J. 390 (1992) 639.
- [263] G.E. Eggum, F.V. Coroniti & J.I. Katz, Astrophys. J. 323 (1987) 634.
- [264] G.E. Eggum, F.V. Coroniti & J.I. Katz, Astrophys. J. 330 (1988) 142.
- [265] P. Laguna, W.A. Miller & W.H. Zurek, Astrophys. J. 404 (1993) 678.
- [266] R.J. Terlevich & B.J. Boyle, Mon. Not. R. Astron. Soc. 262 (1993) 491.
- [267] A.H. Bridle & R.A. Perley, Ann. Rev. Astron. Astrophys. 22 (1984) 319.
- [268] G. Baym & C.J. Pethick, Ann. Rev. Astron. Astrophys. 17 (1979) 415.
- [269] B. Paczński, Astron. Astrophys. 34 (1974) 161.
- [270] J. Casares, P.A. Charles & T. Neylor, Nature 355 (1992) 614.
- [271] A.R. King, Astrophys. J. 260 (1993) L5.
- [272] G. Shields, in: Pittsburgh Conference on BL Lac Objects, ed. A. Wolfe (Univ. Pittsburgh Press, 1978).

- [273] M. Malkan, Astrophys. J. 254 (1982) 22.
- [274] W.H. Sun & M.A. Malkan, Astrophys. J. 346 (1989) 68.
- [275] A. Laor, Mon. Not. R. Astron. Soc. 246 (1990) 369.
- [276] M. Malkan, Astrophys. J. 268 (1983) 582.
- [277] M. Malkan, in: Dynamics of Astrophysical Disks, ed., J.A. Sellwood (Cambridge University Press, Cambridge, 1989).
- [278] R.R.J. Antonucci, in: Supermassive Black Holes, ed. M. Kafatos, (Cambridge University Press, Cambridge, 1988).
- [279] S.L. Odell, H.A. Scott & W.A. Stein, Astrophys. J. 313 (1987) 164.
- [280] S. Veilleux & D.E. Osterbrock, Astrophys. J. Supp. Ser., 63 (1987) 295; J.H.
 Krolik & T.R. Kallman, Astrophys. J., 324 (1988) 714.
- [281] S. Chandrasekhar, Radiative Transfer, (Dover Publications, New York, 1960)
- [282] K.C. Phillips & P. Mészáros, Astrophys. J. 310 (1986) 284.
- [283] K.A. Pounds et al., Nature 344 (1990) 132; K. Nandra & K.A. Pounds, Mon. Not.
 R. Astron. Soc. 268 (1994) 405.
- [284] C.D. Dermer, Astrophys. J. 335 (1988) L5.
- [285] A.A. Zdziarski, Astrophys. J. 305 (1986) 45.
- [286] A.A. Zdziarski, G. Ghisellini, I.M. George, R. Svensson, A.C. Fabian, C. Done, Astrophys. J. 363 (1990) L1.
- [287] L.G. Titarchuk, Astrophys. J. 434 (1994) 570.
- [288] F. Haardt, C. Done, G. Matt & A.C. Fabian, Astrophys. J. 411 (1993) L95.
- [289] F. Haardt & L. Maraschi Astrophys. J. 380 (1991) L51.
- [290] C. Done, J.S. Mulchaey, R.F. Mushotsky & K.A. Arnaud 395 (1992) 275; D.A. Grabelsky et al. in Proc. First Compton Observatory Symp., ed. M. Friedlander, N. Gehrels & D.J. Macomb (AIP: New York, 1993); L. Solatti et al. Astron. & Astrophys. 253 (1992) 145.
- [291] M. Maisack, et al. Astrophys. J. 407 (1993) L61.
- [292] T. Yaqoob, et al. Mon. Not. R. Astron. Soc. 262 (1993) 435; T. Yaqoob, T. Mon. Not. R. Astron. Soc. 258 (1992) 198
- [293] K. Ebisawa, et al. Publ. Astron. Soc. Japan 46, (1994) 375.

- [294] Y. Tanaka in the *Proceedings of the 23rd ESLAB symposium*, vol. 1, p.3 (ESA, Paris) (1989).
- [295] Y. Ueda, K. Ebisawa, & C. Done, Publ. Astron. Soc. Japan, 46 (1994) 107.
- [296] S.K. Chakrabarti in Proceedings of 17th Texas Symposium (New York Academy of Sciences, New York, 1995).
- [297] S.K. Chakrabarti, L.G. Titarchuk, D. Kazanas & K. Ebisawa, A & A, (1995) (in press).
- [298] L.M.J. Brown et al. Astrophys. J. 340 (1989) 129.
- [299] L.O. Takalo, Vistas in Astronomy (1994); E. Valtaoja & M. Valtonen, eds. Variability of Blazars (Cambridge University Press: Cambridge, 1992).
- [300] A. Wandel & V. Petrosian, Astrophys. J. 329 (1988) L11; P.J. Wiita, H.R. Miller, N. Gupta & S.K. Chakrabarti, in Variability of Blazars, eds. E. Valtaoja & M. Valtonen (Cambridge, Cambridge Univ. Press, 1992); P.J. Wiita, H.R. Miller, M.T. Carini & A. Rosen in: Structure and Emission Properties of Accretion Disks, IAU Colloq. 129, eds. C. Bertout et al. (Gif sur Yvette: Editions Frontières, 1991).
- [301] X.-H. Zhang & G. Bao, Astron. Astrophys. 246 (1991) 21.
- [302] A. Wandel & C.M. Urry, Astrophys. J. 367 (1991) 78.
- [303] P.S. Smith & M.L. Sitko, Astrophys. J. 383 (1991) 580.
- [304] R.D. Blandford & A. Königl, Astrophys. J. 232 (1979) 34.
- [305] A. Königl & A.R. Choudhuri, Astrophys. J. 289 (1985) 173.
- [306] W.K. Gear et al. Astrophys. J. 304 (1986) 295.
- [307] T.W. Jones et al. Astrophys. J. 290 (1985) 627.
- [308] W.K. Gear, et al. Astrophys. J. 291 (1985) 511.
- [309] J. Brodie, S. Bowyer & A. Tennant, Astrophys. J. 318 (1987) 175.
- [310] J. Clavel, et al. Astrophys. J. 393 (1992) 113.
- [311] S. Wagner, F. Sanchez-Pons, A. Quirrenbach & A. Witzel, Astron. Astrophys. 235 (1990) L1.
- [312] M.J. Irwin, R.L. Webster, P.C. Hewett, R.T. Corrigan & R.I. Jedrzejewski, Astronomical J. 98 (1989) 1989.
- [313] J. Smak, Acta Astron. 31 (1981) 25.
- [314] K. Horne & T. Marsh, Mon. Not. R. Astron. Soc. 218 (1986) 761.

- [315] W. Bunk, M. Livio & F. Verbunt, Astron. Astrophys. 232 (1990) 371.
- [316] J.B. Oke, in: Superluminal Radio Sources, ed. J.A. Zensus & T.J. Pearson (Cambridge Univ. Press, Cambridge, 1987).
- [317] E. Pérez, M.V. Penston, C. Tadhunter, E. Mediavilla & M. Moles, Mon. Not. R. Astron. Soc. 230 (1988) 353.
- [318] K. Chen, J.P. Halpern & A. Fillipenko, Astrophys. J. 339 (1989) 742.
- [319] K. Chen & J.P. Halpern, Astrophys. J. 344 (1989) 115.
- [320] J.P. Halpern, Astrophys. J. 365 (1990) L51.
- [321] M. Eracleous & J.P. Halpern, Astrophys. J. Suppl. 90 (1994) 1.
- [322] S. Veilleux & W. Zheng, Astrophys. J. 377 (1991) 89.
- [323] W. Zheng, S. Veilleux & S.A. Grandi, Astrophys. J. 381 (1991) 418.
- [324] J. Smak, Acta Astron. 19 (1969) 155.
- [325] S.-S. Huang, Astrophys. J. 171 (1972) 549.
- [326] T. Storchi-Bergmann, J.A. Baldwin & A.S. Wilson, Astrophys. J. 410 (1993) L11.
- [327] M. Miyoshi et al., Nature 373 (1995) 127.
- [328] G. Cecil, A.S. Wilson & R. B. Tully, Astrophys. J. 390 (1989) 365.
- [329] G. Hasinger & van der Kliss, M. Astronomy & Astrophys., 225 (1989) 79.
- [330] K. Ebisawa, K. Mitsuda & H. Inoue, Publ. Astron. Soc. Jap. 41 (1990) 519.
- [331] T. Dotani et al. Astrophys. J., 350 (1990) 395.
- [332] T. Dotani, in *Frontiers of X-ray Astronomy*, (1992) Ed. Y. Tanaka & K. Koyama (Universal Academy Press, Inc.)
- [333] S.A. Grebenev, R.A. Sunyaev, M.N. Pavlinsky, & I.A. Dekhanov, (1992) in Frontiers of X-ray Astronomy, Ed. Y. Tanaka & K. Koyama (Universal Academy Press, Inc.)
- [334] L.M. Alpar & G. Shaham, Nature 316 (1985) 239.
- [335] S. Kato et el. Publ. Astron. Soc. Jap. 231 (1988) 37
- [336] S. Kato, Publ. Astron. Soc. Jap. 43 (1991) 95.
- [337] M. Nowak & R.V. Wagoner, Astrophys. J. 418 (1993) 183.
- [338] D. Lynden-Bell & M.J. Rees, Mon. Not. R. Astron. Soc. 152 (1971) 461.

- [339] R.H. Sanders, Nature 359 (1992) 131.
- [340] D.N.B. Hall, S.G. Kleinmann & N.Z. Scoville, Astrophys. J. 262 (1982) L53.
- [341] F. Yusef-Zadeh & F. Melia, Astrophys. J. 385 (1992) L41.
- [342] F. Melia, Astrophys. J. 387 (1992) L25.
- [343] K.Y. Lo in AIP conference proceedings No. 155, ed. D.C. Becker (New York, AIP, 1987); G.H. Rieke & M.J. Rieke, Astrophys. J. 330 (1988) L33; R.I. Sunyaev et al. 1994, Preprint.
- [344] F. Melia, Astrophys. J. 426 (1994) 577.
- [345] H., Falcke, P.L. Biermann, W.J. Duschl & P.G. Mezger, Astron. & Astrophys. 270 (1993) 102.
- [346] L. Ozernoy, in: The Nuclei of Normal Galaxies: Lessons From the Galactic Center. eds. R. Genzel & A. Harris (1994) in press.
- [347] A. Fridman, O. Khoruzhii, L. Lyakhovich, L. Ozernoy & L. Blitz, Astrophys. J. (1994) submitted.
- [348] A. Eckart, R. Genzel, R. Hoffman, B.J. Sams & L.E. Tacconi-Garman, Astrophys. J. 407 (1993) L77.
- [349] A. Mastichiadis & L. Ozernoy, Astrophys. J. 426 (1994) 599.
- [350] S.K. Chakrabarti, R. Rosner & S.I. Vainshtein, Nature 368 (1994) 434.
- [351] D.K. Aitken, S. Gezari, C.H. Smith, M. McCaughrean & Roche, P.F. Astrophys. J. 380 (1991) 419.
- [352] J.E. McClintock, K. Horne, R.A. Remillard, Astrophys. J. 442 (1995) 358.
- [353] R.A. Sunyaev et al, Astron. Lett. 20 (1994) 777
- [354] K.S. Thorne, in *Three Hundred Years of Gravitation* edited by S.W. Hawking and W. Israel (Cambridge: Cambridge University Press, 1987).
- [355] K. Danzmann et al. in Laser Interferometer Space Antenna for Gravitational Wave Measurements, (1993) ESA (Max-Planck-Institute für Quantenoptic).
- [356] L. Blanchet, T. Damour, B.R. Iyer, C.M. Will and A.G. Wiseman, Phys. Rev. Lett. 74 (1995) 3515.
- [354] K.S. Thorne, in *Three Hundred Years of Gravitation* edited by S.W. Hawking and W. Israel (Cambridge: Cambridge University Press, 1987).
- [355] K. Danzmann et al. in Laser Interferometer Space Antenna for Gravitational Wave Measurements, (1993) ESA (Max-Planck-Institute für Quantenoptic).

[356] L. Blanchet, T. Damour, B.R. Iyer, C.M. Will and A.G. Wiseman, Phys. Rev. Lett. 74 (1995) 3515.

Figure Captions

- Fig. 1.1: Possible evolutionary routes which produce massive black holes at galactic centers (reproduced with permission from the Annual Review of Astronomy and Astrophysics [2]).
- Fig. 1.2: Velocity dispersion σ and stellar rotation velocity V along the major axis and the nuclear bulge component of M31. Rapid increase of dispersion velocity at $r \sim 0$ indicates the presence of a massive compact object of at least ten million solar mass. The Figures are reproduced from Kormendy [8].
- Fig. 1.3: Gradual deformation of a star of mass $1M_{\odot}$ passing close to a black hole of mass $10^4 M_{\odot}$. Here, β is the ratio of the Roche radius to the periastron distance r_p . The star is totally disrupted when β is close to or greater than 1 [37].
- Fig. 1.4: Effective potential felt by an orbiting particle with various specific angular momenta around a Schwarzschild black hole (solid and short-dashed curves) and a Newtonian Star (long-dashed curve). Solid curves are drawn with marginally stable (lower) and marginally bound (upper) angular momenta respectively.
- Fig 1.5: Effective potential felt by an orbiting particle with various specific angular momenta around a Kerr black hole (a = 0.95). Solid curves are drawn with marginally stable (lower) and marginally bound (upper) angular momenta respectively.
- Fig. 2.1(a-b): Variation of Mach number with distance in a Bondi flow around a Newtonian star. (a) n = 3, (b) n = 3/2. Contours are of constant $\dot{\mathcal{M}}$. \mathcal{E} is chosen to be 0.01 throughout. In (a), only curves ABC and A'BC' are physically significant transonic solution. The other solutions such as DD' or EE' are not transonic. FF' and GG' are unphysical. In (b), the critical curve passes through r=0.
- Fig. 2.2: Various types of critical points are schematically drawn. A critical point is 'center' type or 'O'-type if the trajectories in the phase space are closed around that point. If the trajectories intersect with slopes of opposite signs, the critical point is 'saddle' type, or 'X'-type; if slopes are of same sign it is of 'nodal' type. If trajectories spiral around the point indefinitely, it is a 'spiral' type point.
- Fig. 2.3: Nature of critical points in the parameter space spanned by b and c for a harmonic oscillator problem. Parabolic curve $D = b^2 4ac = 0$ separates various types of critical points (when in $x \dot{x}$ plane). R and I represent real and imaginary axes. Dots drawn in the R I plane represent locations of eigenvalue λ on that plane. For D < 0, points are center type or 'O'-type if b = 0 and spiral type if $b \neq 0$. For D = 0, points are inflected nodal type where the slopes of both the trajectories are the same.

- For D > 0, points are 'nodal' type if c > 0 (both slopes are of same sign), straight line c = 0 (one slope is zero), saddle type or 'X'-type if c < 0 (slopes are of opposite signs). Gravity and viscosity in an accretion flow play roles similar to negative stiffness and damping.
- Fig. 2.4(a-c): Temperature variation of the electrons and protons as functions of the logarithmic radial distance. The black hole mass is chosen to be $10M_{\odot}$ and (a) $\dot{M}=10^{16}$ gm s⁻¹, (b-c) $\dot{M}=10^{18}$ gm s⁻¹ In (c), the electron proton coupling term is artificially increased by a factor 20 to show the effect of strong cooling. Figures are reproduced from Colpi, Maraschi & Treves [95].
- Fig. 2.5(a-d): Spectrum of radiation emitted from electrons in a spherical accretion flow at a rate of (a) 10^{16} gm s⁻¹ (b) 10^{18} gm s⁻¹ on a black hole of mass (a-b) $10 M_{\odot}$ and at a rate of (c) 10^{23} gm s⁻¹ (d) 10^{25} gm s⁻¹ on a black hole of mass (c-d) $10^{8} M_{\odot}$. Also shown in the inset is the γ -ray spectrum due to π^{0} decay. Figures are reproduced from Colpi, Maraschi & Treves [95].
- Fig. 2.6: Variation of L_{γ} with the accretion rate in a spherical accretion onto a $10M_{\odot}$ black hole. The maximum occurs at around $\tau_T \approx 0.3$. Figures are reproduced from Colpi, Maraschi & Treves [95].
- Fig. 2.7: A typical accreting solution in optically thick flows near the critical point is shown in dashed line [77, 89]. The solution of \hat{L}_s (solid curves) blows off at $u = a_s$ as k = 0 at that point. A complete solution which satisfies the condition that it should pass through the point $u = a_s$ where C = 0, asymptotically merges with the \hat{L}_s curves.
- Fig. 2.8: A complete solution of general relativistic optically thick Bondi Flow [77, 89]. Cross marks are the critical points and the open circle marks are the sonic points. The parameters chosen in CGS units are $M=3M_{\odot},~\dot{M}=2.954\times10^{-5}M_{\odot}yr^{-1},~\hat{L}_{\infty}=9.795\times10^4L_{\odot},~\hat{L}_{s,\infty}=9.795\times10^4L_{\odot},~\rho_{\infty}=1.878\times10^{-9}g~cm^{-3},~T_{\infty}=4.313\times10^5K,$ $a_{s,\infty}=8.303\times10^{-3}\times c,~a_{c,\infty}=2.814\times10^{-4}\times c,~[p_{gas}/p_{rad}]_{\infty}=1.532\times10^{-3}.$
- Fig. 2.9: A comparison of results of the 'self-consistent' spherical accretion models in the literature. The dimensionless accretion rate \dot{m} is plotted against the dimensionless luminosity. See text for the explanation of the symbols.
- Fig. 2.10: Region of the parameter space showing stationary spherical accretion solutions which include shock waves [119] (open circles). Also presented are the self-consistent shock solutions of Babul, Ostriker and Mészáros [121] (filled circles). The high and low (or no) pair density regions are as well.
- Fig. 2.11(a-d): Variations of (a) velocity, (b) temperature, (c) density and (d) Mach

- numbers in a specific case, clearly showing the formation of a standing shock at a few $\times 10^6 r_g$. Black hole of $1M_{\odot}$, luminosity (in units of Eddington luminosity) of 0.01 and efficiency $\eta = 0.003$ are chosen. Dashed curve in (a) shows free-fall velocity and the dashed curve in (b) shows the virial temperature for comparison. Figures are reproduced from Chang & Ostriker [119].
- Fig. 2.12: A cartoon diagram of a plane parallel shock wave. u_{-} and u_{+} are the mean velocities of the scattering centers in the pre-shock and post-shock regions.
- Fig. 2.13: Variation of the compression ratio $r = \beta_-/\beta_+$ as a function of the Mach number (solid) when losses are included. Also shown are the ratio r for adiabatic flows with $\gamma = 4/3$ (dotted) and $\gamma = 5/3$ (dashed). The Figure is reproduced from Kazanas & Ellison [122].
- Fig. 2.14: Variation of the efficiency of conversion of kinetic energy flux to the flux of relativistic particles (Q), and the ratio of downstream relativistic particle pressure to ram pressure (η) as function of the Mach number M_1 . The Figure is reproduced from Kazanas & Ellison [122].
- Fig. 2.15: Comparison of luminosities as predicted by the shock acceleration model (solid lines) as a function of the shock location X_1 and the model (open circles for quasars and crosses for Seyferts) of Wandel & Yahil [132] as functions of the central black hole mass. The Figure is reproduced from Kazanas & Ellison [122].
- Fig. 3.1: Equipotential surfaces of a compact binary system with mass ratio $M_1/M_2 = 1/3$. Distances are in units of GM_1/c^2 . Five points of four distinct types marked as L_1 , L_2 , L_3 and L_4 are the so-called Lagrange points where Φ_{eff} is locally or globally an extremum. Roche lobe overflow occurs when matter from M_2 fills its lobe (right section of the figure-of-eight formed by the innermost contour) and passes through L_1 to the star M_1 on the left.
- Fig. 3.2: Two annular sections of a thin accretion disk are drawn at radii r and $r + \Delta r$ to illustrate how matter is accreted from $r + \Delta r$ to r after angular momentum is transported from r to $r + \Delta r$ through the action of the viscous stress f_{ϕ} . The Figure is reproduced from Shapiro & Teukolsky [70].
- Fig. 3.3: Integral radiation spectrum of the standard disk for different accretion rates \dot{M} and viscosity parameters α . Upper curves are for the critical rate $\dot{M}_{crit} = 3 \times 10^{-8} \frac{0.06}{\eta} M_{\odot}$ yr⁻¹ with $\eta = 0.06$ and the lower curves are for an accretion rate a hundred times smaller. 'BB' refers to the emission of black body radiation at local disk temperature.
- Fig. 3.4: Region of a disk having a negative slope $(d(\nu \Sigma)/d\Sigma < 0)$ would be viscous

unstable and disk accretion takes a limit cycle behaviour ABCD. In AB and CD the slopes are positive and the disk is stable.

- Fig. 3.5: Schematic diagram showing the origin of Balbus-Hawley instability inside a differentially rotating disk in presence of vertical and toroidal flux tubes.
- Fig. 3.6: A few self-consistent angular momentum distributions inside disks which are supposed to be Keplerian at large distances. Accretion rate $\dot{m} = \frac{\dot{M}}{\eta \dot{M}_{Edd}} = 50$ is chosen. The distribution depends upon the radial distance where the disk is matched with a Keplerian disk. The Figure is taken from Abramowicz et al. [146].
- Fig. 3.7: Meridional cross section of a self-similar disk (long dashed), the Alfvén surface (short dashed) and the field lines and associated outflows (solid) in the ψ , ξ plane for the parameters: n = 0.5, $C_1 = 4 \times 10^{13}$, $r_0 = 3 \times 10^{13}$, $\rho_{i0} = 10^{-16} \mathrm{gm \ cm^{-3}}$, $B_0 = 0.019$ G, $\alpha = 9.0$, $\beta = 9.0$, and $\epsilon = 0.1$. The field lines are advected with the flow inside the disk, pushed away by centrifugal force of the outgoing matter just outside the disk and subsequently collimated due to 'hoop' stress [150].
- Fig. 3.8(a-b): Calculated poloidal fields B_p (solid lines) and currents j_P (dashed lines) with (a) even and (b) odd symmetries inside a disk. These are examples of solutions which do not require dynamo if sufficient fields are fed from outer edge. They can probably match jet solutions outside the disk as is schematically shown here. The Figure is reproduced from Khanna & Camenzind [157].
- Fig. 3.9: Poloidal flux Ψ at t=4.6 times the diffusion time scale as obtained from self-excited dynamo effects around a Kerr black hole (a=0.98). The box represents the disk. These solutions may match with jet solutions outside the disk. The Figure is reproduced from Khanna & Camenzind [158]
- Fig. 3.10: Contours of constant \mathcal{E} and L in the (r_c, u_c) plane showing the existence of five critical points in a magnetized flow around a Schwarzschild black hole. Solid contours are drawn for L = 1.2, 1.8, 2.2345, 3.0, and the dashed contours are drawn for $\mathcal{E} = 1.2$, 1.8, 2.355, 2.8 respectively [77, 161].
- 3.11(a-f): Contours of constant $\dot{\mathcal{M}}$ depicting all the solution topologies of the magnetized disks and winds [77, 161]. (a) $L=10^{-4}$, $\mathcal{E}=2.0$, (b) L=1.0, $\mathcal{E}=-0.5$, (c) L=1.0, $\mathcal{E}=1.8871$, (d) L=1.7, $\mathcal{E}=-2.0$, (e) L=1.7, $\mathcal{E}=0.0$, (f) L=1.7, $\mathcal{E}=4.0$. Important point to note here is that the fast magnetosonic point is located at a finite distance (c) which causes outflows to be superfast supermagnetosonic at a finite distance. This property is important for magnetized jet solutions.
- Fig. 3.12: Schematic diagram showing the Blandford-Znajek process of extraction

of energy from the black hole. See text for details. The Figure is reproduced from Blandford & Znajek [168].

Fig. 4.1(a-b): Variation of angular velocity ω and radial velocity $v=v_r$ in units of the Keplerian angular velocity $(\omega_K=(GM/r_0^3)^{1/2})$ and the free-fall velocity $v_K=(GM/r_0)^{1/2}$ at the inner edge of the disk r_0 . (a) $\dot{M}_c=L_{Edd}/\eta$ with $\eta=GM/2r_0$, the efficiency factor. (b) \dot{M}_c is 25 times higher. The dashed curves are Keplerian for comparison. The Figures are reproduced from Maraschi et al. [171].

Fig. 4.2: Schematic representation of the typical angular momentum distribution inside a thick accretion disk around a black hole (dashed). Keplerian distributions around a Schwarzschild black hole (solid) and around a Newtonian star (dash dotted) are shown for comparison. Inner edge of the disk is located at r_i and the center of the disk is located at r_c .

Fig. 4.3: An equipotential surface of a barotropic thick accretion disk is schematically shown along with the chimney (or funnel) along the axis. The directions of the gravitational force, centrifugal force, the net force along the effective gravity, and the force due to pressure gradient are shown with arrows. An equipotential surface is formed by the tangent vectors normal to the directions of the pressure balance.

Fig. 4.4(a-b): Equipotential surfaces in Schwarzschild geometry (a) and in Newtonian geometry (b) are shown. I and C denote the inner edge (cusp) and the center of the disk respectively. In Newtonian geometry, the equipotentials are always closed and no cusp is formed.

Fig. 4.5: Central temperature and density of a thick accretion disk [185] as functions of the ratio of the gas pressure to the total pressure β . In abscissa, mass of the central black hole is shown. In the region marked $\tau < 1$, the optical depth (due to Thomson scattering) is less than unity and the radiation pressure supported disk is impossible. In the region marked 'self-gravity', the mass of the disk is higher compared to the mass of the central black hole and various instabilities may develop in the disk.

Fig. 4.6: Keplerian distribution of an accretion disk when the mass of the disk is three percent (short dashed), five percent (medium dashed) and ten percent (long dashed) as heavy as the central compact object [188]. Here, the entire mass is assumed to be concentrated close to the disk center located at $r_c \sim 9.0$.

Fig. 4.7: Temperature distributions in a thin disk (dotted curve) and in thick disk (dashed curve) are compared for the same central mass and accretion rate. This Figure is reproduced from Madau [193].

- Fig. 4.8: Disk spectra at inclination angles (a) 90° , (b) 50° , (c) 25° and (d) 0° are compared showing the obscuring effects of the funnel. This Figure is reproduced from Madau [193].
- Fig. 4.9: Specific luminosities at various observed frequencies are compared: $log(\nu)$ is equal to (a) 15.5, (b) 16.0, (c) 16.5 and (d) 17 respectively. In optical and ultraviolet, the specific luminosity is almost independent of the angle, but at higher frequencies the dependence is very strong due to the funnel. This Figure is reproduced from Madau [193].
- Fig. 4.10: Comparison of the thin disk spectrum (dashed curve) with the spectra of a thick disk: the spectrum without the reflection effects (solid), with reflection effects (dotted), with a sum-of-black-body assumption (dash-dotted). Compared to a thin disk, the thick disk (with reflection effects) produces orders of magnitude more emission at higher frequencies. This Figure is reproduced from Madau [193].
- Fig. 5.1: Variation of the energy \mathcal{E} with the accretion rate $\dot{\mathcal{M}}$ (a measure of entropy for a given mass flux) when the angular momentum is kept fixed and is equal to 1.675. Flow with parameters from the segment AB passes through the innermost 'X'-type critical point and flow with parameters from the segment CD passes through the outermost 'X'-type critical point. Typical Rankine-Hugoniot shock transitions in accretion (s_1s_2) and in winds (w_1w_2) are shown [77, 218]. The "swallow-tail" singularity is produced due to the projection effects.
- Fig. 5.2: Example of the solution of an accretion flow. At the sonic point, the Mach number is 0.93. Contours are of constant accretion rate $\dot{\mathcal{M}}$. Shock locations are: $x_{s_1}=2.437, \ x_{s_2}=3.419, \ x_{s_3}=18.862, \ x_{s_4}=57.592$. The inner and the outer critical points, denoted by I and O, are located at $x_i=2.800$ and $x_o=34.580$ respectively. The solution which includes a shock is shown by arrows [77, 218]. The shock transition at x_{s_2} is unstable. X_{s_1} is possible of neutron stars. x_{s_4} is unphysical.
- Fig. 5.3(a-d): Phase space trajectories and the shock locations in a viscous isothermal disk. (a) $\alpha = 0.01$, and (b) $\alpha = 0.02$. (c-d): Plot of M and $\frac{1}{M}$ as functions of the logarithmic distance to show the shock locations in a dissipative flow. Parameters are the same as in (a) and (b) respectively. In (c), there are two shock locations, the one close to the black hole is unstable in accretion and the one away from the black hole is stable. In (d), when the viscosity is higher, only the unstable one remains [77, 224]. Also shown in (d), two shock-free branches of the solution out of which the flow chooses the one passing through the inner sonic point.
- Fig. 5.4(a-b): Classification of various disks around a black hole into a single framework [218]. Regions I,W,A,O respectively describe the parameter space for which (I) the flow passes through only the inner sonic point, (W) may have shocks in winds but no-shock

in accretion, (A) may have shocks in accretion but no-shock in winds, and (O) only through outer sonic points. In (b), A and W are further classified. Region between long dashed curve and central curve BF will have shocks and the post-shock region will lie between the dotted curve and the central solid curve BF [218].

- Fig. 5.5 Energy vs. entropy density is plotted for $\lambda_{in} = 1.65$, viscosity parameter $\alpha = 0$, 0.4, 0.8 and cooling parameter $f = (Q_+ Q_-)/Q_+ = 0$, 1 (as marked) and for polytropic index $\gamma = 4/3$ (left) and 5/3 (right, moved towards left by a factor of 10) respectively at all possible sonic points. The branches of type AMB pass through inner sonic point x_{in} and the branches of type CMD pass through outer sonic point x_{out} and a solution with a shock must connect two such points with the condition that $E(x_{in}) \leq E(x_{out})$ along with $s(x_{in}) \geq s(x_{out})$ [226].
- Fig. 5.6: Example of a shock solution in presence of viscosity, heating and cooling. Here $Q_-/Q_+=0.5$, $\alpha=0.05$ and angular momentum at the inner edge 1.6 is chosen. The vertical dashed curve at $X_{s3}=13.9$ represents the stable shock. $\alpha_c=0.1$ and $\gamma=4/3$ in this case.
- Fig. 5.7: Ratio of the disk angular momentum to Keplerian angular momentum in three different cases. In case marked 'A', the flow becomes sub-Keplerian before becoming super-Keplerian close to the black hole. In case marked 'B', the disk becomes sub-Keplerian and remained so before entering the black hole. In case marked 'C', the disk becomes Keplerian, then passed through a standing shock at $r = 13.9r_g$ before entering the black hole [68].
- Fig. 5.8: Examples of shock solution (logarithmic Mach number against radial distance) in presence of power law cooling effects: $\Lambda \sim \rho^2 T_b^{\alpha}$. The solid curve is for $\alpha_b = 0.5$ and the long-dashed curve is for $\alpha_b = 0.6$. The short-dashed curve is without cooling effects. Higher cooling produces weaker shocks closer to the black hole.
- Fig. 5.9: Examples of MHD shock formation in accretion. Solutions are shown in arrows and shock transitions are shown in vertical dashed lines. The parameters are: L = 1.45, $\mathcal{E} = 0.2$, $\dot{\mathcal{M}}_{-} = 0.4857$, $\dot{\mathcal{M}}_{+} = 0.5074$, $r_{s} = 1.0995$, r_{s} being the location of the shock. The dashed curves are the contours of constant slow magnetosonic wave velocities [77, 161].
- Fig. 5.10: Relative positions of two spiral shocks (thick solid curves) at ψ_{s1} and ψ_{s2} and two sonic surfaces (thin dashed curves) at ψ_{c1} and ψ_{c2} are schematically shown. The shocks as well as the sonic surfaces are separated by $\delta\psi = \pi$ $(n_s = 2)$, and $0 \le \epsilon \le 1$ measures the position of the shock relative to the sonic surface downstream [77, 248].
- Fig. 5.11(a-b): Example of a two-armed spiral shock solution. (a) Variation of Mach

number with the spiral angle at a given radial distance. Dashed vertical lines (at ψ_{s1} and ψ_{s2}) are the shock transitions. Crosses represent locations of the sonic surfaces (at ψ_{c1} and ψ_{c2}). (b) Variation of the velocity coefficients $q_j(\times 10)$ with the spiral angle. The parameters are: B=-1.0, $q_{2c}=0.02$, n=6.1840, $\epsilon=0.7274$, $M_-=1.0394$, $M_+=0.8909$ [77, 248]. The flow is seen to be highly sub-Keplerian (for Keplerian, $q_2=1$).

- Fig. 6.1: Density contours at different times during the accretion of nearly isothermal winds ($\gamma = 1.005$). The shock cone is seen to exhibit 'flip-flop' property before settling down in the symmetry axis. The Figure is reproduced from Matsuda et al. [254].
- Fig. 6.2: An example of early simulation of an inviscid, constant angular momentum (l = 3.77GM/c) flow showing the formation of a thick accretion disk. The contours of constant density and the velocity vectors are shown. The figure is drawn at $t = 300GM/c^3$ and is taken from Hawley, Smarr and Wilson [216].
- Fig. 6.3: An example of the simulation of a thin accretion disk which includes a standing shock wave [220]. Mach number of the flow is plotted against the radial distance. Results at different times are shown in solid curves. Analytical solution is shown as a dashed curve with vertical shock transition. The flow forms the shock at the predicted location.
- Fig. 6.4: Pseudo-particles in a smoothed particle hydrodynamics simulation of a two-dimensional sub-Keplerian angular momentum flow. A standing shock is formed at $X \sim 16$. Note the presence of the oblique shocks also. The specific energy and angular momentum used were $0.006c^2$ and 3.3GM/c respectively. There are 60,000 particles in this simulation [259].
- Fig. 6.5: Contours of constant Mach number in the two dimensional flow. Note that the flow which is subsonic after the shock, becomes supersonic very close to the black hole. Also, the wind originated subsonically on the disk surface becomes supersonic farther away [259].
- Fig. 6.6: Contours of constant temperature (in geometric units). At the shock location, the temperature of the flow becomes high and the velocity becomes very low thus satisfying all the conditions of a thick accretion disk [75]. The contours in the immediate vicinity of the post-shock region resemble that of a thick accretion disk (Fig. 4.4). The pre-shock flow is primarily advected like Bondi flow whereas the post-shock flow is rotation dominated [259].
- Fig. 6.7(a-b): Examples of the spiral shock waves in early numerical simulations. Density contours are plotted. The ratio (Q) of the compact object to the companion is chosen to be unity. In (a), $\gamma = 1.2$ and a two armed spiral is formed, whereas in

(b), $\gamma = 5/3$, a three-armed spiral is formed. Number of arms depends on boundary conditions of the problem. Matter is injected at the inner Lagrange point L_1 . These figures are taken from Sawada, Matsuda & Hachisu [142].

Fig. 6.8(a-c): Evolution of the density waves for Q=1 and $\gamma=1.2$ case at times (a) T=2.3, (b) 3.2, and (c) 3.7 respectively. This case is similar to that shown in Fig. 6.7(a) above but the injected gas is somewhat cooler and matter is injected all over the outer boundary (at 0.65). The number of arms changes from 2 (a) to 3 (b) to 2 (c). In the same time unit, Keplerian periods at a radial distance ~ 0.2 (where the shocks are fully developed) and at the outer boundary are 0.56 and 3.3 respectively.

Fig. 6.9(a-b): Comparison of (a) Mach number and (b) angular momentum variations in viscous (solid) and inviscid (dashed) isothermal thin accretion disks. The viscosity parameter $\alpha_s = 0.01$ is chosen everywhere in the simulation. Note that the shock in the viscous disk forms farther out and is weaker and wider. The solid curve in (b) marked 'Keplerian' is the Keplerian distribution plotted for comparison. Due to the inefficiency of transfer of angular momentum in the pre-shock flow, a mixed-shock forms with higher angular momentum in the post-shock flow [226].

Fig. 6.10(a-b): Evolution of (a) Mach number and (b) angular momentum when viscosity parameter is high ($\alpha_s = 0.1$). Higher efficiency of transport of angular momentum in the post-shock region causes its accumulation in the post-shock region which drives the shock outwards. This makes the entire flow outside the inner sonic point to be subsonic, and the angular momentum distribution becomes almost Keplerian. Dashed curve marked $\alpha = 0$ represents the solution for inviscid flows [225]. In (b), Keplerian distribution is shown for comparison.

Fig 6.11: Formation of an isothermal Keplerian disk. In this simulation, particles are injected at the outer edge of the disk at $r_o = 100$ with angular momentum 7.00 which is close to Keplerian value at r_o . The (constant) sound speed is chosen to be $a_0 = 0.005$ and the injection velocity was $v_0 = 0.003$. Shakura-Sunyaev viscosity parameter $\alpha_s = 0.25$ was used in this simulation [226]. The dashed Keplerian distribution is shown for comparison.

Fig. 6.12 Evolution of a sub-critical, initially radiation pressure supported, Keplerian disk. Density contours of the simulation at different times are shown in different panels in which the time t (since the commencement of the simulation) is also noted. Length and time units are GM/c^2 and GM/c^3 respectively. In the first panel, the disk is radiation pressure supported, but subsequently it becomes cooler, dense and gas pressure supported. The Figure is reproduced from Eggum, Coroniti and Katz [263].

Fig. 6.13: Evolution of a super-critical viscous flow which produces a geometrically thick disk. $\dot{M} = 4\dot{M}_{Edd}$ was used. Density contours and unit velocity vectors are shown

at $t \sim 6000$ unit after the commencement of the simulation. Contours are labeled with densities in CGS units. Four regions: (A) a convective core, (B) an accretion zone, (C) a photocone and (D) a jet are distinguished and marked. The Figure is reproduced from Eggum, Coroniti and Katz [264].

Fig. 6.14(a-b): Example of 'breathing' of accretion disks in presence of bremsstrahlung cooling and accretion shock. The post-shock hot corona cools in a time scale comparable to the in-fall time and the shock oscillates [227]. The figures show two different epochs of this oscillation. Upper half shows velocity vectors and Mach number contours and the lower half shows the velocity contours.

Fig. 7.1: Examples of fitting optical/UV region of nine typical quasars using emissions from a thin standard Keplerian disk, and contributions from the dust (modeled as a power law in infra-red region), from starlight, from re-combination lines and Fe II lines. This Figure is reproduced from Malkan [277].

Fig. 7.2(a-b): Fits of hard X-rays and γ -ray data with the Comptonization models: (a) EXOSAT, GRANAT and OSSE observation of Cyg X-1 [290] and (b) OSSE and Ginga data of NGC4151 [291-292]. In (a), histogram is the result of [288], dashed curve is the result of [289], solid curve is the analytical solution [287], the dash-dot-dot curve is from [285]. In (b), the histogram is from [287]. The Figures are reproduced from Titarchuk [287]. The thermal model provides sufficiently good fit in both of these cases.

7.3: A possible model of the accretion flow which is produced by either (a) a Keplerian/sub-Keplerian flow with vertical viscosity variation, or (b) an admixture of Keplerian and sub-Keplerian flow at the outer boundary. Soft emission comes from the Keplerian equatorial disk, whereas the X-rays to γ -rays are from the shocked component of the halo which cools by re-processing soft photons from the standard disk. Existence of various components will depend upon the accretion rate, viscosity and angular momentum [296, 297].

Fig. 7.4: Variation of the spectral properties as the accretion rate of the disk is changed: $\dot{m}_d = 0.001$ (solid), $\dot{m}_d = 0.01$ (long dashed), $\dot{m}_d = 0.1$, (short dashed) and $\dot{m}_d = 1.0$ (dotted). The accretion rate in the sub-Keplerian halo component is kept fixed at $\dot{m}_h = 1.0$. The hard component softens and the soft component brightens with \dot{m}_d . This figure is drawn for $M = 5M_{\odot}$ but should remain similar for any black hole candidate [68, 297]. The dash-dotted curve over-laid on the dotted curve represents the weaker hard component due to the convergent inflow near the black hole horizon (Newtonian computation).

Fig. 7.5: Variation of the energy index α (of the hard component between $\sim 2-50 \mathrm{keV}$) as the accretion rate of the disk \dot{m}_d is changed. Halo rates are marked. Plots on the

left-side are due to post-shock hot flow, and those on the right side are due post-shock flow cooled by high disk accretion rate. Dashed curves are drawn where the effects of both the components may be present [68, 297].

Fig. 7.6(a-b): Fits of broad line emission features from ARP 102B using a relativistic Keplerian disk model. In (a), the continuous emissivity is used and in (b) local broadening is used. Figures are reproduced from Chen & Helpern [319].

Fig. 7.7: Fit of 3C390.3 is presented using relativistic Keplerian disk model. This Figure is taken from Eracleous & Helpern [321]. Lower panel shows the residual spectrum.

Fig. 7.8(a-b): Fits (dashed) of the H_{α} data (solid) of (a) 1976 and of (b) 1980. The parameters are: $x_1 = 200GM/c^2$, $x_2 = 900GM/c^2$, q = 2.0, $i = 38^o$, $v_{th} = 0.0015c$ [212].

Fig. 7.9: Spatial variation of the line emission profiles from the ionized disk of M87 taken by the Faint Object Camera (FOS) of Hubble space telescope. This Figure is reproduced from Harms et al. [5]. The vertical dashed lines are drawn at positions [O III] $\lambda\lambda5007\text{Å}$, [N II] $\lambda\lambda6584\text{Å}$ to show that red and blue shifts of lines at different positions.

Fig. 7.10: Fits (solid) of the [O III] $\lambda\lambda5007\text{Å}$, lines (short dashed) emitted from different positions. The same theoretical fit, upon suitable scaling, matches with observed [N II] $\lambda\lambda6584\text{Å}$ profile (dot-dashed) as well. The good fit indicates that the flow may be strongly non-Keplerian [6].

Fig. 7.11: Various identified structures and mass distribution within 100pc of our galactic center.

Fig. 7.12: Fit of the observed luminosity [343] using magnetized spherical accretion model [342]. Emission dominates the spectrum for $\nu_{\infty} \leq 10^{13} \text{Hz}$ and luminosity at higher frequencies are entirely due to thermal bremsstrahlung. Mass of the central black hole is chosen to be $0.9 \times 10^6 M_{\odot}$. The Figure is reproduced from Melia [342].

This figure "f1p1.gif" is available in "gif" format from:

This figure "f2p1a.gif" is available in "gif" format from:

This figure "f2p1b.gif" is available in "gif" format from:

This figure "f3p1.gif" is available in "gif" format from:

This figure "f4p1.gif" is available in "gif" format from:

This figure "f5p1.gif" is available in "gif" format from:

This figure "f6p1.gif" is available in "gif" format from:

This figure "f7p1.gif" is available in "gif" format from:

This figure "f1p2.gif" is available in "gif" format from:

This figure "f2p2.gif" is available in "gif" format from:

This figure "f3p2.gif" is available in "gif" format from:

This figure "f4p2.gif" is available in "gif" format from:

This figure "f5p2.gif" is available in "gif" format from:

This figure "f6p2.gif" is available in "gif" format from:

This figure "f7p2a.gif" is available in "gif" format from:

This figure "f7p2b.gif" is available in "gif" format from:

This figure "f1p3.gif" is available in "gif" format from:

This figure "f2p3.gif" is available in "gif" format from:

This figure "f3p3.gif" is available in "gif" format from:

This figure "f4p3.gif" is available in "gif" format from:

This figure "f5p3.gif" is available in "gif" format from:

This figure "f6p3.gif" is available in "gif" format from:

This figure "f7p3.gif" is available in "gif" format from:

This figure "f1p4.gif" is available in "gif" format from:

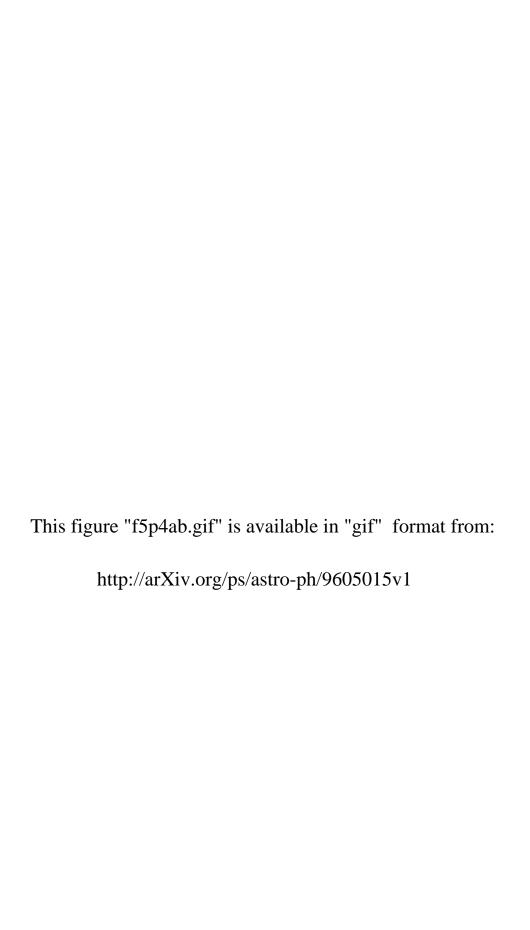
This figure "f2p4.gif" is available in "gif" format from:

This figure "f3p4.gif" is available in "gif" format from:

This figure "f4p4.gif" is available in "gif" format from:

This figure "f4p4a.gif" is available in "gif" format from:

This figure "f4p4b.gif" is available in "gif" format from:



This figure "f6p4.gif" is available in "gif" format from:

This figure "f7p4.gif" is available in "gif" format from:

This figure "f1p5.gif" is available in "gif" format from:

This figure "f2p5.gif" is available in "gif" format from:

This figure "f3p5.gif" is available in "gif" format from:

This figure "f4p5.gif" is available in "gif" format from:

This figure "f5p5.gif" is available in "gif" format from:

This figure "f6p5.gif" is available in "gif" format from:

This figure "f7p5.gif" is available in "gif" format from:

This figure "f2p6.gif" is available in "gif" format from:

This figure "f3p6.gif" is available in "gif" format from:

This figure "f4p6.gif" is available in "gif" format from:

This figure "f5p6.gif" is available in "gif" format from:

This figure "f6p6.gif" is available in "gif" format from: http://arXiv.org/ps/astro-ph/9605015v1

This figure "f7p6.gif" is available in "gif" format from:

This figure "f3p7.gif" is available in "gif" format from:

This figure "f4p7.gif" is available in "gif" format from:

This figure "f5p7.gif" is available in "gif" format from:

This figure "f6p7a.gif" is available in "gif" format from:

This figure "f6p7b.gif" is available in "gif" format from:

This figure "f7p7.gif" is available in "gif" format from:

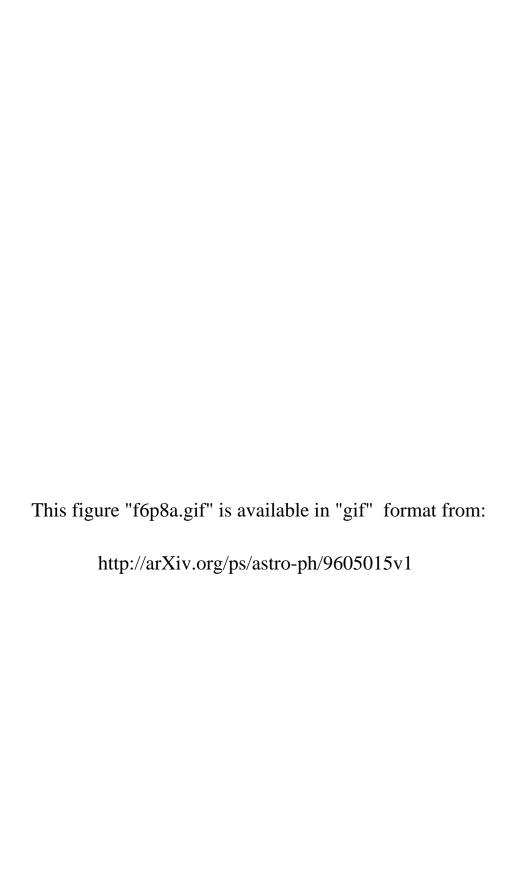
This figure "f2p7n8.gif" is available in "gif" format from:

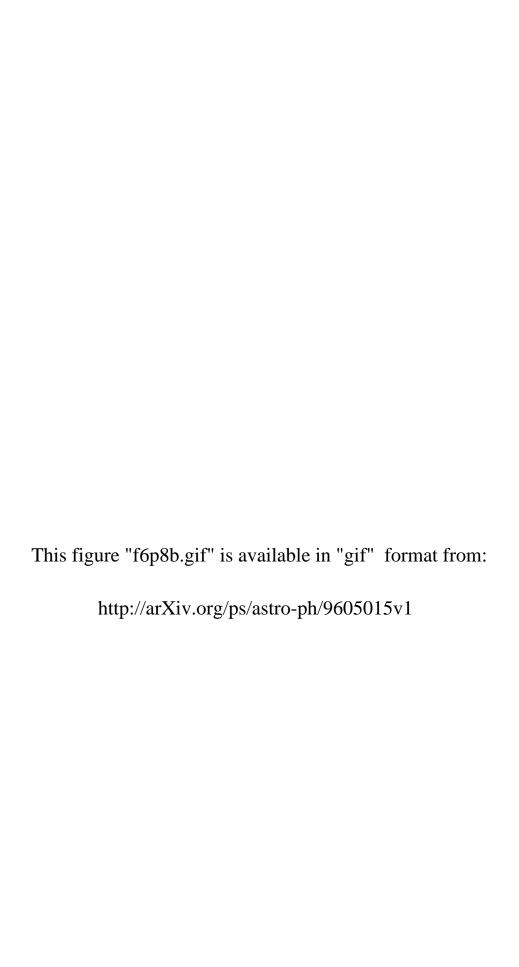
This figure "f3p8a.gif" is available in "gif" format from:

This figure "f3p8b.gif" is available in "gif" format from:

This figure "f4p8.gif" is available in "gif" format from:

This figure "f5p8.gif" is available in "gif" format from:





This figure "f6p8c.gif" is available in "gif" format from: http://arXiv.org/ps/astro-ph/9605015v1

This figure "f7p8a.gif" is available in "gif" format from:

This figure "f7p8b.gif" is available in "gif" format from:

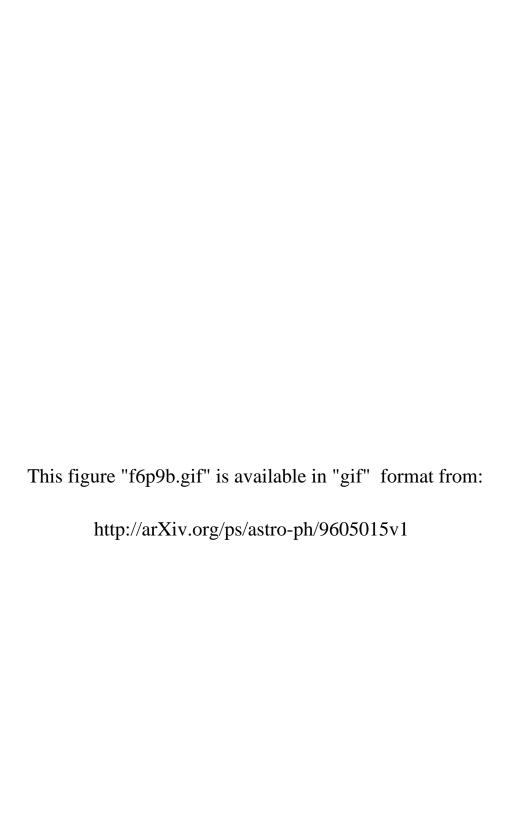
This figure "f2p9.gif" is available in "gif" format from:

This figure "f3p9.gif" is available in "gif" format from:

This figure "f4p9.gif" is available in "gif" format from:

This figure "f5p9.gif" is available in "gif" format from:

This figure "f6p9a.gif" is available in "gif" format from:



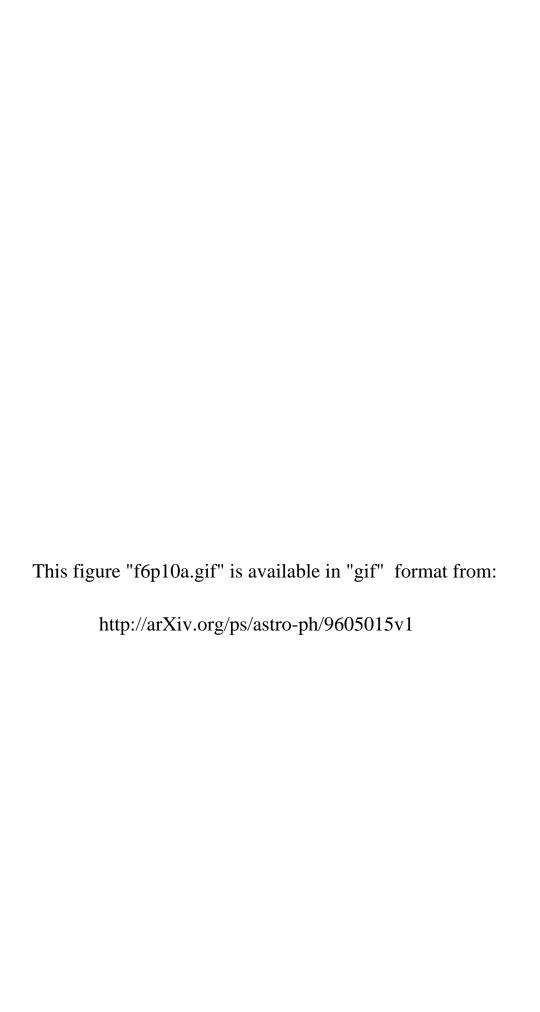
This figure "f7p9.gif" is available in "gif" format from:

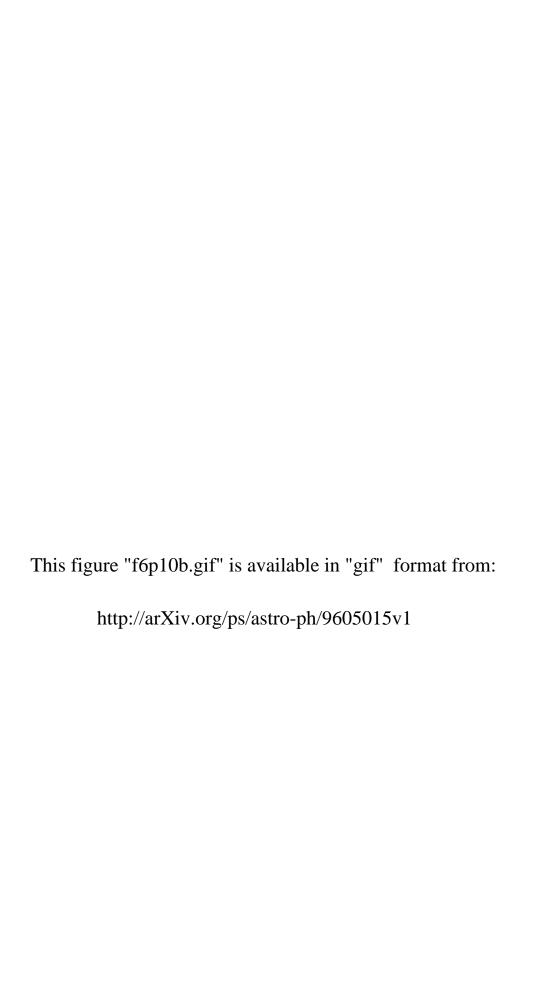
This figure "f2p10.gif" is available in "gif" format from:

This figure "f3p10.gif" is available in "gif" format from:

This figure "f4p10.gif" is available in "gif" format from:

This figure "f5p10.gif" is available in "gif" format from:





This figure "f7p10.gif" is available in "gif" format from:

This figure "f2p11.gif" is available in "gif" format from:

This figure "f3p11.gif" is available in "gif" format from:

This figure "f5p11a.gif" is available in "gif" format from: http://arXiv.org/ps/astro-ph/9605015v1

This figure "f5p11b.gif" is available in "gif" format from: http://arXiv.org/ps/astro-ph/9605015v1

This figure "f6p11.gif" is available in "gif" format from:

This figure "f7p11.gif" is available in "gif" format from:

This figure "f2p12.gif" is available in "gif" format from:

This figure "f3p12.gif" is available in "gif" format from:

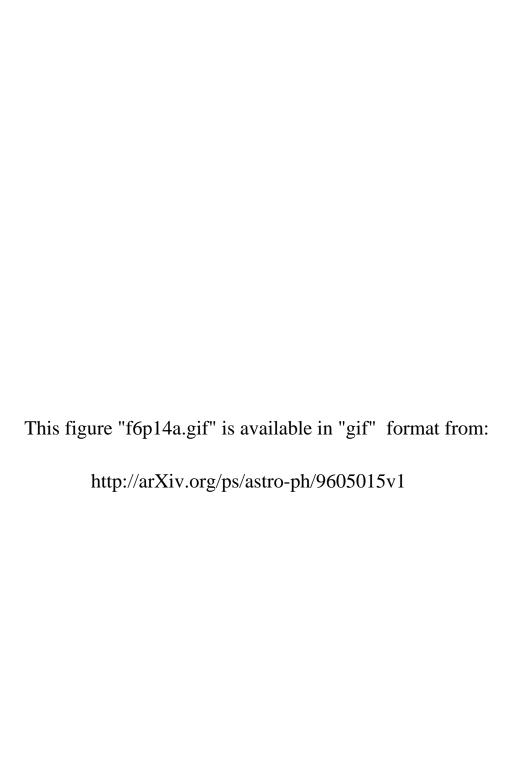
This figure "f6p12.gif" is available in "gif" format from:

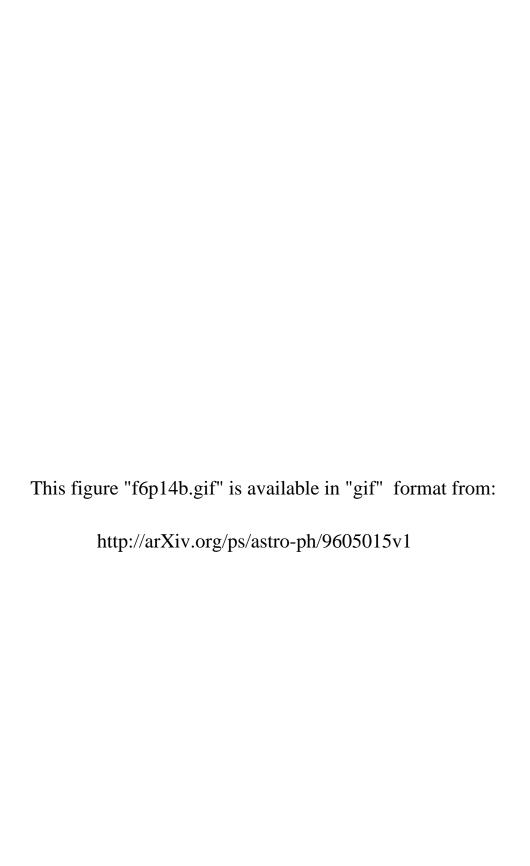
This figure "f7p12.gif" is available in "gif" format from:

This figure "f2p13.gif" is available in "gif" format from:

This figure "f6p13.gif" is available in "gif" format from:

This figure "f2p14.gif" is available in "gif" format from:





This figure "f2p15.gif" is available in "gif" format from: